



<https://theses.gla.ac.uk/>

Theses Digitisation:

<https://www.gla.ac.uk/myglasgow/research/enlighten/theses/digitisation/>

This is a digitised version of the original print thesis.

Copyright and moral rights for this work are retained by the author

A copy can be downloaded for personal non-commercial research or study,
without prior permission or charge

This work cannot be reproduced or quoted extensively from without first
obtaining permission in writing from the author

The content must not be changed in any way or sold commercially in any
format or medium without the formal permission of the author

When referring to this work, full bibliographic details including the author,
title, awarding institution and date of the thesis must be given

Enlighten: Theses

<https://theses.gla.ac.uk/>
research-enlighten@glasgow.ac.uk

Dry etched III-V semiconductors for nanoelectronics

A Thesis submitted to
the Faculty of Engineering of the
University of Glasgow for the degree of
Doctor of Philosophy

by

Rebecca Mei Kwan Cheung B.Sc. (Eng.)

April 1990

ProQuest Number: 11007355

All rights reserved

INFORMATION TO ALL USERS

The quality of this reproduction is dependent upon the quality of the copy submitted.

In the unlikely event that the author did not send a complete manuscript and there are missing pages, these will be noted. Also, if material had to be removed, a note will indicate the deletion.



ProQuest 11007355

Published by ProQuest LLC (2018). Copyright of the Dissertation is held by the Author.

All rights reserved.

This work is protected against unauthorized copying under Title 17, United States Code
Microform Edition © ProQuest LLC.

ProQuest LLC.
789 East Eisenhower Parkway
P.O. Box 1346
Ann Arbor, MI 48106 – 1346

Acknowledgements

I wish to express my gratitude to Professor J. Lamb for the provision of departmental laboratory and computing facilities, and to my supervisor Professor C.D.W. Wikinson; Professor S.P. Beaumont and Dr. S. Thoms for their invaluable advice and encouragement throughout this work.

I am also grateful for the advice and assistance given by Professor J. Chapman of the Natural Philosophy Department during the TEM analysis along with the conscientious efforts of the final year project student A. Birnie. Thanks are also due to Dr. U.J. Cox, Dr. M. Watt and Dr. C.M. Sotomayer-Torres, and S. D. Pan for their collaboration in the work on specular X-ray reflectivity, Raman scattering and X-ray photoelectron spectroscopy respectively.

The excellent technical support provided by all the technical staff at Glasgow University during this project is gratefully acknowledged. In particular, D. Gourlay, A. Stark, H. Wallace, D.S. Macintyre, R. Darkin, D. Clifton, J. Cochran and G. Boyle.

I would also like to express my gratitude to my manager Dr. D.P. Kern at IBM Thomas J. Watson Research Centre, Yorktown Heights; and to Dr. S.A. Rishton, Dr. K.Y. Lee, Dr. Y.H. Lee, Dr. T.P. Smith III, Dr. T.H.P. Chang, Dr. C.M. Knoedler, Dr. E. Kratschmer and H.E. Luhn for their invaluable advice, continual support and care which made my short stay in the U.S. an enlightening experience.

Thanks are also due to Dr. C. R. Stanley at Glasgow University and Dr. W. Wang at Columbia University for providing the MBE materials.

I also wish to express my appreciation to the Croucher foundation for financial support during the three years of research at Glasgow University.

Special thanks go to all my fellow research students and friends at Glasgow who have made my stay in this part of the world a memorable one, in particular, K. McIlvaney, J. Tang, J. Bell, H. Arnott, A. Jennings, I. Thayne,

N.Cameron, J.Adams, D.Lau, P.Chu, T.Krauss and A.Jeziarski; and especially to my office mates R.K.Henderson and M.A.Foad with whom I shared many interesting philosophical discussions.

I also wish to express my personal thanks to Ray and Irene Hutchins, Nancy and Bill Mackie, and Chris and Judy Wilkinson for their understanding and encouragement, especially towards the final stages of this work; and to my flatmates N. Hamlaoui and C.Wild for their warmth and kindness making flat-sharing an enjoyable experience.

Finally, I wish to express my gratitude to my family for what seemed like an everlasting support and encouragement during my years of study in the U.K., and in particular, to K.Kwok for his patience and understanding for the past years.

Summary

The purpose of this work was to try to identify the amount, degree and physical nature of the damage caused on both the surface and sidewalls of reactive ion etched GaAs and AlGaAs nanostructures using a variety of complimentary characterisation techniques, and to develop low damage high resolution dry etch processes for GaAs and AlGaAs. The gases investigated included SiCl_4 , CH_4/H_2 and $\text{CCl}_2\text{F}_2/\text{He}$. Two new methods of etching GaAs anisotropically by magnetron radio-frequency and electron cyclotron resonance radio-frequency reactive ion etching employing $\text{CCl}_2\text{F}_2/\text{He}$, and the use of a novel gas mixture CH_4/H_2 to reactive ion etch GaAs in the conventional radio-frequency mode were developed. It was found to be important to distinguish between surface and sidewall damage, and both were characterised using electrical, optical as well as analytical techniques. In particular, two novel processes were developed using high resolution fabrication techniques for the construction of sidewall Schottky diodes and electron transparent thin wire specimens to allow the amount of sidewall damage to be estimated and its nature to be realised through diode characteristic measurements and transmission electron microscopy analysis. To investigate the surface damage caused after etching, techniques such as Schottky diode performance, integrated band-gap photoluminescence, Raman scattering and X-ray photoelectron spectroscopy were employed; and for the first time, the usefulness of specular X-ray reflectivity for the identification of surface damage was explored. Sidewall damage was examined using room and low temperature conductivity, and low temperature magnetoconductance of n^+ GaAs quantum wires, sidewall Schottky diode characteristics and transmission electron microscopy on thin wire specimens. The dependence of surface and sidewall damage on etch time and etch power was also studied.

Papers which arose from this work

- 1) G.F.Doughty, S.Thoms, R.Cheung, C.D.W.Wilkinson, "Dry etching damage to GaAs and InP", 6th int. conference on ion and plasma assisted techniques, Brighton, U.K., May, 1987, p.284-289
- 2) R.Cheung, S.Thoms, S.P.Beaumont, G.Doughty, V.Law, C.D.W.Wilkinson, "Reactive ion etching of GaAs using a mixture of methane and hydrogen", Electronics Letters, 1987, **23**, p. 857-859
- 3) M.Watt, C.M.Sotomayer-Torres, R.Cheung, C.D.W.Wilkinson, H.E.G.Arnott, S.P.Beaumont, "Raman scattering investigations of the damage caused by reactive ion etching of GaAs", presented at the 3rd Int. Conf. on Superlattices, Microstructures and Microdevices, Chicago, Aug.1987; Superlattices and Microstructures, **4**, p.243-244, 1988
- 4) S.Thoms, I.McIntyre, S.P.Beaumont, M.Al-Mudares, R.Cheung and C.D.W.Wilkinson, "Fabrication of quantum wires in GaAs/AlGaAs heterolayers", J. Vac. Sci. Tech., **B6**, p.127-130, 1988
- 5) M.Watt, C.M.Sotomayer-Torres, R.Cheung, C.D.W.Wilkinson, H.E.G.Arnott, S.P.Beaumont, "Raman scattering of reactive ion etched GaAs", presented at the IOP Solid State Conf., Bristol, Dec.1987 and Proceedings of Quantum Electronics 8, St. Andrews, Sept,1987; Journal of Modern Optics, **35**, p.365-370, 1988
- 6) R.Cheung, S.Thoms, I.McIntyre, C.D.W.Wilkinson, S.P.Beaumont, "Passivation of donors in electron-beam lithographically defined nanostructures after methane/hydrogen reactive ion etching", presented at the 32nd international conference on Electron, Ion, and Photon beams, Florida, 1988; J. Vac. Sci. Technol., **B6**, p.1911-1914, 1988
- 7) R.Cheung, Y.H.Lee, C.M.Knoedler, K.Y.Lee, T.P.Smith III, D.P.Kern, "Sidewall damage in n^+ GaAs quantum wires from reactive ion etching", App. Phys. Letts., **54**, p.2130-2132, 1989
- 8) R.Cheung et al., "A comparison of damage in the dry etching of GaAs by conventional reactive ion etching and by reactive ion etching with an electron cyclotron resonance generated plasma", paper presented at the 33rd international conference on Electron, Ion, and Photon beams, Monterey, CA, 1989; J. Vac. Sci. Technol. **B7** p.1462-1466, 1989
- 9) R.Cheung, A.Birnie, J.N.Chapman, S.Thoms and C.D.W.Wilkinson, "Evaluation of dry etch damage by direct TEM observation", paper presented at the 15th international conference on Microlithography, Microcircuit Engineering, Cambridge, 1989
- 10) W.Hansen, T.P.Smith III, D.P.Divincenzo, K.Y.Lee, Y.H.Lee and R.Cheung; "Quantum fluctuations in n^+ GaAs wires with invasive probes", preprint paper submitted to EP2DS8 Conference, 1989

Contents

Chapter 1 Introduction

1.1 General introduction	1
1.2 Thesis outline	1
1.3 References	3

Chapter 2 Electron beam processing, dry etching and damage

2.1 Introduction	4
2.2 Pattern definition	4
2.2.1 Electron beam lithography	5
2.2.2 Electron beam lithography (E.B.L.) system	5
2.2.3 Positive resist	6
2.2.4 Negative resist	7
2.3 Pattern transfer	7
2.3.1 Metallisation	7
2.3.2 Etching	8
2.4 Dry etching	9
2.4.1 Ion beam etching and its variations	9
2.4.2 Plasma etching (barrel)	10
2.4.3 Plasma etching (planar)	10
2.4.4 Reactive ion etching	11
2.4.4.1 Plasma surface interactions	12
2.5 Dry etching damage	14
2.6 Reactive ion etching of GaAs in silicon tetrachloride (SiCl_4)	15
2.6.1 Chemistry	15
2.6.2 Machine	17
2.7 Reactive ion etching of GaAs in a mixture of methane and hydrogen (CH_4/H_2)	
2.7.1 Chemistry	17
2.7.2 Machine	19
2.8 References	20

Chapter 3 Reactive ion etching of GaAs and Al_{0.3}Ga_{0.7}As using SiCl₄
and damage characterisation

3.1 Introduction	24
3.2 Etch rate dependence on power density and pressure in the RIE of GaAs and Al _{0.3} Ga _{0.7} As	24
3.2.1 Experimental	25
3.2.2 Results and Discussion	25
3.3 Microscopic relation between flow rate and etch rate in the reactive ion etching of GaAs	27
3.4 Characterisation of damage induced in GaAs and Al _{0.3} Ga _{0.7} As after RIE	29
3.4.1 Surface damage - Schottky diode characteristic	
3.4.1.1 Theory	29
3.4.1.2 Experimental	32
3.4.1.3 Results and Discussion	33
3.4.2 Low temperature integrated band-gap photoluminescence measurement	34
3.4.2.1 Theory	35
3.4.2.2 Experimental	36
3.4.2.3 Results and Discussion	37
3.4.3 Raman Scattering	38
3.4.4 X-ray photoelectron spectroscopy (XPS) analysis	40
3.4.4.1 Theory	40
3.4.4.2 Experimental	41
3.4.4.3 Results and Discussion	42
3.5 Sidewall Damage	43
3.5.1 Development of the fabrication of sidewall Schottky diode	44
3.5.1.1 Experimental	44
3.5.1.2 Preliminary data	46
3.5.2 Effect of an hydrochloric acid (HCl) boil	48
3.5.3 Results and Discussion	48
3.6 Conclusions	50
3.7 References	52

Chapter 4 Development and damage characterisation of reactive ion etching of GaAs in CH₄/H₂

4.1 Introduction	56
4.2 Development of RIE of GaAs using CH ₄ /H ₂	56
4.2.1 Experimental	56
4.2.1.1 Resolution tests	56
4.2.2 Reactive ion etching	57
4.2.2.1 Conditioning of the etch chamber	58
4.2.3 Results and Discussion	59
4.2.3.1 Masks	59
4.2.3.2 Etching	59
4.3 Damage characterisation	61
4.3.1 Hydrogen passivation and the effect of annealing	61
4.3.2 Surface damage - Electrochemical profiling	
4.3.2.1 Experimental	62
4.3.2.2 Results and Discussion	63
4.3.3 Schottky diode characteristics	63
4.3.3.1 Theory	63
4.3.3.2 Experimental	64
4.3.3.3 Results and Discussion	65
4.3.4 Low temperature integrated band-gap photoluminescence measurements	
4.3.4.1 Theory	66
4.3.4.2 Experimental	66
4.3.4.3 Results and Discussion	66
4.3.5 Sidewall damage - Conductivity of n ⁺ GaAs quantum wires	68
4.3.5.1 Theory	69
4.3.5.2 Experimental	69
4.3.5.3 Preliminary data	73
4.3.5.4 Results and Discussion	74
4.4 Conclusions	76
4.5 References	78

Chapter 5 Development and damage characterisation of magnetron and electron cyclotron resonance radio frequency (rf) reactive ion etching using $\text{CCl}_2\text{F}_2/\text{He}$

5.1 Introduction	81
5.2 Dry etching	81
5.2.1 Magnetron (MAG) and electron cyclotron resonance (ECR) rf reactive ion etching	81
5.2.2 Development of MAG and ECR RF RIE of GaAs using $\text{CCl}_2\text{F}_2/\text{He}$	83
5.2.2.1 Reactor configuration	83
5.2.2.2 Experimental	84
5.2.2.3 Results and Discussion	84
5.2.3 Conventional radio frequency reactive ion etching of GaAs using $\text{CCl}_2\text{F}_2/\text{He}$	86
5.3 Sidewall damage - n^+ GaAs quantum wires	87
5.3.1 Material design	87
5.3.2 Device design	88
5.3.3 Quantum wires fabrication	88
5.3.3.1 Electron beam lithography system (VS-6)	88
5.3.3.2 Ohmic contact and alignment marks level	89
5.3.3.3 Wires level	90
5.3.3.4 Bonding pads level	91
5.3.4 Experiment	91
5.3.4.1 Resolution tests	91
5.3.4.2 Pattern layout	92
5.3.4.3 Dry etching	92
5.3.5 Room temperature conductivity measurement	93
5.3.5.1 Experimental	93
5.3.5.2 Results and Discussion	93
5.3.6 Low temperature transport measurement	96
5.3.6.1 Experimental	96
5.3.6.2 Theory	97
5.3.6.3 Results and Discussion	99
5.4 Surface damage characterisation	100
5.4.1 Schottky diode characteristics	101

5.4.1.1 Experimental	101
5.4.1.2 Results and Discussion	101
5.4.2 X-ray photoelectron spectroscopy (XPS) analysis	102
5.4.2.1 Experimental	102
5.4.2.2 Results and Discussion	103
5.5 Conclusions	105
5.6 Appendix	105
5.7 References	107

Chapter 6 Other novel dry etch damage characterisation techniques

6.1 Introduction	111
6.2 Surface damage - Specular X-ray reflectivity	111
6.2.1 Theory	112
6.2.2 Experimental	114
6.2.3 Results and Discussion	115
6.3 Sidewall damage - Transmission electron microscopy	118
6.3.1 Theory	119
6.3.2 Experimental	124
6.3.2.1 Electron microscopy	124
6.3.2.2 Fabrication	126
6.3.3 Results and Discussion	130
6.3.3.1 Sidewall damage	130
6.4 Conclusions	134
6.5 References	135

Chapter 7 Conclusions 137

Chapter 1 Introduction

1.1 General introduction

In the past 20 years, electronic devices based on GaAs/AlGaAs have been reduced from an initial millimeter scale to the present sub-micron size. This reduction in device dimension enable the possibility of improvements in their operation^{1.1,1.2}. Moreover, quantum structures in this sub-micron size regime allow fundamental limits imposed by quantum mechanics and statistical physics to be exploited^{1.3-1.6} and are potentially of importance for the development of new electronic devices. The fabrication of these nanostructures such as quantum wires, dots^{1.3-1.6} and various transistor schemes^{1.7-1.11} require advanced pattern definition and transfer techniques. At the moment, the most common way to produce these structures involves the use of electron beam lithography followed by dry etching. While the use of dry etching is essential due to the isotropic nature of conventional wet etching techniques, the action of the energetic ions and reactive radicals bombarding the surfaces and sidewalls of the etched structures during dry etching can cause damage directly or indirectly to the semiconductor thus degrading the material's electrical and optical performance. Therefore, the present work is concerned with the identification of the amount, degree and nature of the possible damage caused on both surfaces and sidewalls of the etched structures in GaAs and AlGaAs after reactive ion etching using a variety of electrical, optical and analytical characterisation techniques and the development of low damage dry etch processes suitable for the application of high resolution fabrication.

1.2 Thesis outline

Chapter 2 gives a brief account of electron beam lithography in the application of high resolution pattern definition along with the various techniques of pattern transfer. The use and mechanism involved in dry etching, in particular, reactive ion etching (RIE) are discussed in more detail. The possible sources and reduction of damage in dry etching and some proposed chemistry in the RIE of GaAs using SiCl₄ and CH₄/H₂ are presented.

In Chapter 3, RIE of GaAs and Al_{0.3}Ga_{0.7}As using SiCl₄ are

investigated. In addition, the surface damage is examined using Schottky diode characteristics, low temperature integrated band-gap photoluminescence and Raman scattering measurements; possible identification of the nature of this damage employing X-ray photoelectron spectroscopy is presented. A novel process for constructing Schottky diode onto the sidewall of the etched structures for an estimation of the induced sidewall damage is described.

Chapter 4 involves the development of a high resolution reactive ion etch process using a mixture of CH_4/H_2 for GaAs. The passivative nature of the atomic hydrogen, the damage caused on the etched surface and the effect of annealing are studied using electrochemical profiling, Schottky diode characteristics and low temperature integrated band-gap photoluminescence measurements, and these effects on the sidewalls are characterised by measuring the conductance and cut-off widths of n^+ GaAs quantum wires.

Chapter 5 reports on the work carried out in IBM Thomas J. Watson Research Centre, Yorktown Heights for four months during the course of this project. It involves the development of magnetron and electron cyclotron resonance rf RIE of GaAs in $\text{CCl}_2\text{F}_2/\text{He}$ using optical emission spectroscopy. The damage induced on both the sidewalls and surface was characterised by applying the knowledge of the techniques acquired at Glasgow, namely, room temperature conductivity of n^+ GaAs quantum wires, Schottky diode performance and X-ray photoelectron spectroscopy. In addition, the low temperature conductance of the n^+ GaAs wires and their rms amplitude in the Universal Conductance Fluctuations are investigated.

Chapter 6 presents two novel analytical damage characterisation techniques: specular X-ray reflectivity and transmission electron microscopy (TEM). In the case of TEM, using high resolution patterning techniques, a novel structure which allow sidewall damage to be studied was developed.

Finally, findings based on the present work and some suggestions for future work are given in Chapter 7.

1.3 References

- 1.1) W.Patrick, W.S Mackie, S.P.Beaumont, C.D.W.Wilkinson and C.H.Oxley; IEEE Elect. Dev. Letts. **EDL-6** p.471, 1985
- 1.2) K.Y.Lee, J.Frost, C.R.Stanley, W.Patrick, W.S.Mackie, S.P.Beaumont and C.D.W.Wilkinson; J.Vac.Sci.Technol. **B5** p.322, 1987
- 1.3) A.Scherer and H.G.Craighead; Appl. Phys. Letts. **49** p.1284, 1986
- 1.4) H.van Houten, B.J. van Wees, M.G.J.Heijman and J.P.Andre; Appl. Phys. Letts. **49** p.1781, 1986
- 1.5) T.P.Smith III, K.Y.Lee, C.M.Knoedler, J.M.Hong and D.P.Kern; Phys. Rev. B **38** p.2172, 1988
- 1.6) M.A.Reed, J.N.Randall, R.J.Aggarwal, R.J.Maty, T.M.Moore and A.E.Wetsel; Phys. Rev. Letts. **60** p.535, 1988
- 1.7) W.D.Goodhue, G.D.Johnson and T.H.Windhorn; in Proc. of the Conf. on GaAs and Related Compounds, edited by W.T.Lindley (Institute of Physics, Bristol) p.349, 1987
- 1.8) C.L.Chen and K.D.Wise; IEEE Trans. on Elect. Dev. **ED-29** (10) p.1522, 1982
- 1.9) S.Kuroda, T.Mimura, M.Suzuki, N.Kobayashi, K.Nishiuchi, A.Shibatomi and M.Abe; IEEE GaAs IC Symp. Tech. Dig. p.125, 1984
- 1.10) P.M.Solomon, C.M.Knoedler and S.L.Wright; IEEE Elect. Dev. Letts. **EDL-5** p.379, 1984
- 1.11) M.Heiblum, D.C.Thomas, C.M.Knoedler and M.I.Nathan; Appl. Phys. Letts. **47** p.1105, 1985

Chapter 2 Electron beam processing, dry etching and damage

2.1 Introduction

This chapter gives an overview of the technology used in the fabrication of nano-structures: pattern definition using electron beam lithography and resists, and pattern transfer using metallisation and dry etching techniques. Mechanisms associated with dry, in particular, reactive ion etching and the possible damage caused by RIE are discussed.

2.2 Pattern definition

In general, patterns can be defined onto a substrate using lithography. This is normally done by exposing an image using some type of radiation into a 'resist' layer. In the application of fabrication of structures in semiconductors and metals, a range of radiation may be used: namely, optical, x-ray, and electron and ion beams. The resolution of the various lithographic techniques differs widely depending on the size of the source, its wavelength and energy, and contributions from diffraction and scattering effects. Up to the present time, the smallest feature defined in resist is $\approx 2\text{nm}$ ^{2.1} with the use of electron beams. However, the ultimate resolution of electron beam lithography is limited by the electron beam size (the smallest at present $\approx 2\text{nm}$) and scattering from lateral secondary electrons which lead to the proximity effect^{2.2-2.4}. While advantages in particle scattering, exposure efficiency and chemical possibilities may make ion beam lithography of importance in the future, the presently available ion sources and optics do not allow the focussing of an ion beam to less than 30nm. Electron beam lithography has been used throughout this work both at Glasgow University and at IBM Yorktown Heights (Ch.6). The process and the lithography system used at Glasgow University will be described briefly below as details can be found in the theses of Rishton^{2.4}, Mackie^{2.5} and Binnie^{2.6}.

2.2.1 Electron beam lithography

In electron beam lithography, a focused electron beam is deflected in a controlled manner over an electron sensitive material (usually a polymer) known as a resist. The irradiation modifies the molecular structure of the resist such that when immersed in a developer, the development process selectively dissolves either the exposed areas (positive resist) or the unexposed areas (negative resist). This process is known as pattern definition and is illustrated in figure 2.1.

2.2.2 Electron beam lithography (E.B.L.) system

At Glasgow, the electron beam lithography was carried out using a Philips PSEM 500 Scanning Electron Microscope which has been modified into a very high resolution Electron Beam Lithography (E.B.L.) system. The modifications enable the beam deflection coils to be driven under external software control. This is achieved using an Olivetti computer to drive a scan generator which contains two 16 bit digital to analogue converters. The converters are used to 12 bit accuracy to obtain a 4096 by 4096 pixel exposure field. The essential features of the Philips vector scan electron beam lithography machine are as follows:

- a) a filament electron source with associated magnetic lenses giving electron spot sizes ranging from 8nm to 1 μ m
- b) variable accelerating voltage from 1.5 to 50kV
- c) a specially fitted transmission detector for Scanning Transmission Microscopy (STEM)
- d) a fully eucentric goniometer on which a specimen can be positioned in the X and Y directions in 1 μ m steps and rotated with an accuracy of 1/68th of a degree
- e) X- and Y- electronic beam shifters for fine positioning in the X and Y directions of up to + 10 μ m
- f) X- and Y- varymag control which allows the magnification and therefore frame size in the X and Y directions to be increased continuously by a factor between 1 and 2.5
- g) beam blanking which, when activated, deflects the beam into an aperture thus avoiding unwanted exposure.

Exposure pattern files are developed on an Olivetti computer using a computer aided design software package (DE). The design aid was developed by S. Thoms at Glasgow University for pattern data preparation and allows multi-level mask design. After the design files are generated, they are then stored in floppy disks for future use. The PSEM based E.B.L. system is shown in figure 2.2.

2.2.3 Positive resist

At Glasgow, the positive resists used were polymethylmethacrylate (PMMA) with molecular weights of 185,000 and 350,000. Two resist systems were employed:

- 1) 1 μ m thick layer 185,000 MW PMMA
- 2) a bilayer resist system consisting typically of a 20nm thick layer of 350,000 MW PMMA on a 100nm thick 185,000 MW PMMA layer.

Resist (1) is obtained by spinning 15% PMMA (BDH) in chlorobenzene at 5K rpm for 60s. For resist (2), 4% PMMA (BDH) in o-xylene and then 4% PMMA (Elvacite) in o-xylene are spun for 60s at 6Krpm respectively. The bottom layer is baked at 180°C for at least one hour before coating on the top resist layer. Both resist systems are hardened by baking at 180°C for at least one hour before exposure. It is necessary to bake the resists overnight at 180°C if they are to be used as wet etch masks.

Resist (1) (thicker layer) is used for low resolution patterning while the bilayer resist is suitable for defining high resolution patterns. After exposure, the thick resist is developed in 1:1 Isopropylalcohol (IPA):Methylisobutylketone (MIBK) for 45s at 23°C and the bilayer resist in 3:1 IPA:MIBK for 20s at 23°C; followed by a 30s rinse in IPA for both resist systems. As PMMA is a positive resist, it is characterised by a reduction of molecular weight owing to chain scission of the molecules on exposure to the electron beam, therefore, the development process preferentially dissolves the exposed areas leaving behind a resist stencil on the substrate. Both resist systems develop into undercut profiles which facilitate better lift-off. In the case of resist (1) when well exposed, the undercut profile results from the divergence of the electron beam by electron scattering as it passes

through the resist film^{2.4}, see figure 2.3a). The undercut in resist (2) arises because the lower resist layer is more sensitive to the electron beam than the top layer, therefore, when the resist is developed, more material is dissolved from the bottom layer, leaving an undercut profile^{2.7} as shown in figure 2.3b).

2.2.4 Negative resist

The negative resists used were Philips High Resolution Negative Resist (HRN)^{2.8} and Polyimide (preimidized Ciba-Geigy XU218 dissolved in 35:65 acetophenone:xylene)^{2.9}. For high resolution patterning, 8% HRN is spun coated on the substrate at 6K rpm for 60s to give a thickness of 0.1 μ m and baked at 120°C for 20 minutes. After exposure, the resist is developed in MIBK for 30s at 23°C, then rinsed twice in IPA for 30s. For low resolution work, 15% HRN of 0.25 μ m thick, (with the same spinning and development procedures as for 8% HRN) and 10% polyimide were used. In the case of 10% polyimide, the solution is spun on at 6K for 60s to give a thickness of 0.35 μ m and baked at 180°C for at least 2 hours; overnight if the polyimide is to be used as a mask for wet etching. After exposure, the polyimide is developed in acetophenone:xylene, 65:35 at 23°C. In contrast to PMMA, the molecular weight of the areas exposed to the electron beam in negative resist increases due to the cross linking of the molecules. On development, the areas which are not exposed are dissolved.

2.3 Pattern transfer

2.3.1 Metallisation

Once the patterns have been defined by electron beam lithography, they were subsequently transferred into the solid substrate using metallisation, more often known as lift-off, and either wet or dry etching techniques.

In the case of positive resist, the developed resist layer can be used directly as an etch mask or a pattern can be transferred by evaporating metal onto the

resist stencil, then, the lift-off process is carried out in acetone, which dissolves the remaining resist leaving the deposited metal on the substrate^{2.10}. The metal can then be used as an etch mask for dry etching. A number of metals were used, namely: nichrome, gold/paladium and titanium, as these metals have a relatively small grain size suitable for high resolution patterning.

The use of negative resists are generally due to its economy of processing since the molecules are crosslinked on exposure, therefore after development, the areas which has been exposed are not dissolved. This remaining resist can then be used as a mask for etching. Different techniques of pattern transfer are illustrated in figure 2.4.

2.3.2 Etching

In general, when transferring patterns into solid substrate, material can be removed in two ways: wet or dry etching. In wet etching, material is removed by immersing the substrates in the required chemicals for an appropriate time whereas in dry etching, material is removed by a chemical gas. While wet etching often has the advantage of being selective (defined as the ratio of etch rates between two materials) and fast, it usually leads to an isotropic etch profile (see figure 2.5a) because the etch front moves at the same rate in the vertical as well as in the horizontal direction. On the other hand, dry etching is capable of producing very anisotropic profiles, figure 2.5b). Wet etching can also produce anisotropic etching in crystalline materials, this occurs when the etch rate along different crystallographic orientations vary by a large extent^{2.11}. However, the difficulty in obtaining good uniformity and the critical adherence of the mask to the substrate surface in wet etching renders dry processing more desirable over wet etching. But clearly, as the dimensions of electronic devices and quantum structures shrink to the nano-metric scale, the need for producing anisotropic profiles is of prime importance in their fabrication, and therefore, the development and use of dry etching techniques are essential. But there is one potential problem associated with the use of dry etching, that is, the presence of energetic ions which bombard the substrate can cause damage to the material. The following chapters will contain investigations of this damage using a variety of characterisation techniques. At present, an account of the variations in the dry etching techniques available, in

particular, mechanisms associated with the etching process and damage in reactive ion etching will be discussed.

2.4 Dry etching

There are many configurations of dry etching, including: ion beam etching (IBE), plasma etching (PE) [barrel and planar], reactive ion etching (RIE), reactive ion beam etching (RIBE), chemically assisted ion beam etching (CAIBE), radical assisted ion beam etching (RBIBE), chemically assisted reactive ion beam etching (CARIBE), magnetron ion etching (MIE), magnetron reactive ion etching (MRIE), and electron cyclotron resonance reactive ion etching (ECR-RIE). In these processes, material is removed by either subjecting the surface to reactive radicals and ions generated in a plasma, or by bombarding the surface with an energetic beam of ions/reactive ions. In the next sections, ion beam etching and variations of it, and plasma etching (barrel and planar) will be described briefly; a more detailed account will be given for reactive ion etching since the present characterisation is mostly concerned with RIE; and magnetron reactive ion etching and electron cyclotron resonance reactive ion etching will be discussed in chapter 5.

2.4.1 Ion beam etching and its variations

In ion beam etching (IBE), an inert gas is ionised by a hot filament. It is then drawn out into a beam through a series of grid and accelerated through an acceleration grid to a specific energy. The ions pass from the gun into the etch chamber in the form of a beam which impinges onto the substrate and material is removed by physical sputtering^{2.12-2.17}. Chamber pressures below (5-10)mTorr are usually employed with ion energies in the range of 100-1000eV. However, since the etch mechanism is solely physical, most materials have a similar etch rate and consequently etch selectivity is poor. Nevertheless, this can be improved by the use of a reactive gas instead of an inert one. This is known as reactive ion beam etching (RIBE)^{2.17-2.19,2.34}. The etching process then becomes a combination of physical sputtering and chemical reaction at the surface thus enhancing the etch rate and through a proper choice of reactive gas, selectivity can also be improved. But the introduction of reactive gases into the ion source can cause a reduction in

lifetime of the exposed filaments and grids. This then leads to a variant of RIBE, which is chemically assisted ion beam etching (CAIBE) or also known as ion beam assisted etching (IBAE). In this configuration, inert gas is fed into the ion gun as in IBE, but a reactive gas is admitted just in front of the substrate. In this way, the etch rate and etch selectivity can be enhanced compared with IBE. Moreover, since the angles of incidence of the inert beam and the reactive gas can be independently varied, the process can be easily controlled and a wide range of etch profiles can be achieved 2.20-2.23; this technique also eliminates the problem of short gun lifetime. There also exists a newly developed etching technique using a combined radical beam and ion beam etching (RBIBE)2.24 which uses a microwave excited radical beam combined with an inert ion beam. This differs from CAIBE in that the reactive etch gas is microwave excited, and etch rates have been observed to be higher than using CAIBE.

2.4.2 Plasma etching (barrel)

In barrel plasma etching, rf power, usually at 13.56MHz frequency, is applied to the barrel shaped reactors via external capacitive or inductive coupling. Normally, the samples sit in the glow on an insulating (often quartz) holder surrounded by the cylindrical column of plasma. This configuration is characterised by a high operating pressure ≈ 1 Torr and the etching results solely from the chemically reactive species created in the plasma diffusing into the substrate region. Therefore, the process is highly selective, but isotropic in nature. In this work, the barrel etcher was mainly used for stripping resist in an oxygen plasma.

2.4.3 Plasma etching (planar)

In planar plasma etching, the etch chamber consists of two parallel electrode plates. The bottom electrode is grounded and the top electrode is driven by an r.f. generator (either 13.56MHz or low frequency, 0-100kHz), connected through a capacitor and an impedance matching circuit, see figure 2.6. The sample is normally mounted on the grounded electrode. An etchant gas is fed into the etch chamber which is kept under a pumped evacuated environment. Free electrons in the chamber gain energy from the applied r.f. power which lead to the ionisation of

some of the feed-gas molecules and consequently, a plasma is created. The gas is chosen such that it dissociates to produce reactive radicals which will react with the substrate material to be etched. Because of the r.f. cycle, the ions and electrons are alternately accelerated towards the r.f. driven electrode. But as the electrons have a higher mobility than the ions, more electrons are drawn towards the electrode during the positive half of the cycle compared with the number of ions drawn during the negative half of the cycle. However, the net d.c. current to this capacitively coupled electrode must be zero, that is, the total ion and the total electron charge reaching the electrode during each cycle must be equal. This leads to the formation of an equilibrium whereby a negative d.c. voltage component is developed across a dark space region (plasma sheath) which separates the main plasma from the powered electrode. The potential distribution established is shown in figure 2.6, where V_p is the plasma potential. (Since the total ion and the total electron charge reaching the electrode during each cycle are equal, insulating substrates can be etched without charging effects.)

In plasma etching, because the sample being etched is placed on the grounded electrode, the ions bombarding the etched surface is of relatively low energy ($< 50\text{eV}$). In addition, relatively high chamber pressures in the range 0.1 to 10 Torr are usually used. This implies that as the ions and reactive radicals are accelerated across the plasma sheath, they suffer many collisions, and their momentum is randomised. Hence in general, the etching process is isotropic due to the non-directionality of the low energy ions bombarding the etch surface, but highly selective because of the chemical nature of the reactive radicals.

2.4.4 Reactive ion etching

Reactive ion etching is very similar to planar plasma etching except that the bottom electrode, where the sample is situated, is now the driven electrode (at 13.56MHz), see figure 2.7. In addition, the bottom electrode is smaller in area than the top electrode leading to an asymmetrical configuration. Since the plasma potential can be determined by the following expression^{2.25}:

$$V_2 = V_1 / (A_2/A_1)^4 \quad (2.1)$$

where V_1 is the potential difference between the powered electrode and the plasma and V_2 the potential difference between the grounded electrode and the plasma and A_2/A_1 is the ratio of the respective electrode areas, the accelerating field for the ions near the sample is greatly enhanced. The resultant potential distribution is shown in figure 2.7. The negative d.c. voltage component (described in the previous section) in this configuration is developed across the bottom electrode (where the sample is situated) and is largely increased. This results in the bombarding ions having a higher mean energy ($\approx 300-1000\text{eV}$) compared to plasma etching, corresponding to the negative d.c. bias ($-V_{\text{dc}}$) with an oscillating component. However, with a high frequency (13.56MHz), this oscillating component is small. Furthermore, the pressure used in reactive ion etching is rather less than that used for plasma etching, being in the range 5-100 mTorr. Hence, the mean free path of the ions is increased so that they are not randomised in direction while traversing the plasma sheath. The above features such as the driven electrode being the bottom one where the sample is placed, electrode asymmetry and low pressure operation all lead to an enhancement in the energy and directionality of the ions bombarding the etch surface, thus increasing the degree of anisotropy obtained in RIE. (Note that increasing the power density in RIE also increases the ion energies.) However, since RIE utilises both chemical and physical etch mechanisms, while the energetic ions bombarding the sample may cause physical damage to the material, contribution to damage from etch chemistry is also possible. Therefore, in order to gain a fuller understanding of the induced damage, knowledge of the fundamental processes involved during etching concerning the roles of reactive radicals and ion bombardment is beneficial and will be discussed in the following section.

2.4.4.1 Plasma surface interactions

There are basically four processes which occur in reactive ion etching (and plasma etching). They are the 'production' of reactive species in the plasma, 'adsorption' of the reactants on the substrate surface, 'reaction' with the surface material and 'desorption' of the reaction products.

The generation of reactive species in the plasma are due to the collisions of electrons with the etch gas molecules whose rate R is given by:

$$R = kn_e N \quad (2.2)$$

where n_e is the electron concentration and N the concentration of the reactant. k is the rate coefficient which is a function of the reaction cross section and the electron distribution function. However, accurate expressions for these parameters are usually not available and therefore, R can only be determined qualitatively, e.g. via Langmuir probe measurements^{2.26-2.28}.

Before any reaction can take place on the substrate surface, the reactive radicals have to be adsorbed at surface sites. After the reaction has taken place, the reaction product has to be desorbed from the surface again. Often in an etching process, the rate limiting step (which determines the etch rate of a particular material) is governed by one of these mechanisms and its identification vary depending on the chemical system. In reactive ion etching, since the gases chosen are such that they will adsorb and react with the substrate, the rates of adsorption and reaction will be finite but fast, a more important parameter to note is the desorption rate, which is related to the vapor pressure of the etch products, the higher the vapour pressure, the faster the desorption rate. However, the presence of ion bombardment in RIE can also play an important role in the etching process. While the ions can etch the substrate by physical sputtering processes, (as in IBE), there are also three other ways in which the ions can participate in enhancing an etching reaction:

1) on an adsorption/reaction level, by creating surface damage. Ion bombardment serves to create or enhance reactive sites on the substrate surface. While the former mechanism implies no reaction will take place in areas without ion bombardment and has been used to explain why GaAs was only etched in the presence of argon ions in an IBAE study using molecular Cl_2 by Balooch et. al.^{2.29}; the effect of enhancement of adsorption was observed by Coburn et. al.^{2.30} by independently controlling the impingement of Ar^+ and XeF_2 on silicon. Moreover, a mechanism involving the creation of surface damage has been proposed for the production of anisotropy^{2.31}, as long as the ions are directional, as in the case of RIE.

2) on a desorption level, by chemically enhanced physical sputtering. Ion bombardment can stimulate or increase the rate of desorption and help remove

reaction products held on the substrate surface^{2.32}. In particular, the rate of desorption of GaF₃ have been found to be the rate limiting step in the reactive ion etching of GaAs using CCl₂F₂^{2.33}, and similarly, GaCl_x in the RIE of GaAs in Cl₂^{2.34}, RIBE in Cl₂^{2.35}, and IBAE in Ar⁺ and Cl₂^{2.20,2.29}.

2.5 Dry etching damage

In dry processing, the action of the energetic ion bombardment can cause damage on the material being etched. In ion beam etching, the crystal can suffer a high degree of damage since the etch mechanism is purely physical. Studies on the damage induced in GaAs and GaAs/AlGaAs structures by ion beams have been carried out by a number of workers^{2.12,2.36-2.42}. Since all variants of ion beam etching involve the introduction of a reactive gas resulting in the addition of a chemical component during etching, the damage caused in those configurations is expected to be lower, and has been demonstrated by various authors^{2.42-2.45,2.20}. In this work, damage characterisation has been carried out mostly in the area of reactive ion etching, although magnetron and electron cyclotron resonance RIE have also been investigated. While in general, it is expected that a reactive component in etching can reduce the induced damage, it can become an indirect cause of damage, as will be shown later. Reduction of damage is also possible by passivation of defects^{2.46-2.48} or by using very low ion energies^{2.42,49-50,70}. It is important at this point to note that damage can occur both on the surface and sidewalls of etched structures. This effect is illustrated in figure 2.8. In RIE, while the surface may suffer physical damage from the bombardment of directional ions and reactive radicals and/or chemical damage from the reactive radicals, effects from the non-directional ions and reactive radicals and possibly redeposition^{2.71-73} from the bottom surface can also contribute to the causes of damage induced on the sidewalls. The study and minimisation of sidewall damage is at least as important as surface damage in applying dry etching techniques to fabricate electronic devices with nano-metric dimensions. Although there has been many investigations on RIE surface damage^{2.44,45,51-56}, outwith Glasgow, less effort has been directed towards sidewall damage studies^{2.48,49,57,58}. These studies will be discussed in detail later. A variety of electrical, optical and analytical characterisation techniques can be used to investigate damage^{2.50-55,59,60}. It is, in fact, essential that complimentary techniques are used in order to obtain both quantitative and

qualitative information about the damaged layer due to the different depth resolution and origin of sensitivity associated with the different techniques as will be shown later.

2.6 Reactive ion etching of GaAs in silicon tetrachloride (SiCl₄)

2.6.1 Chemistry

Stern et. al.^{2.61-62} were the first workers reported to use SiCl₄ for the high resolution reactive ion etching of GaAs and InP; 20nm wide patterns, defined by electron beam lithography, were transferred into GaAs using NiCr as the dry etch mask. At pressure around 20mT and a lower power than was used in this work, crystallographic etching in the (100) orientation in GaAs using this etch gas has also been observed^{2.63,64}. Furthermore, using optical emission spectroscopy, the type of products excited in a SiCl₄ microwave plasma were monitored by Rowe^{2.65} who found that SiCl₄ gas is broken down to SiCl⁺, SiCl₂ and Cl⁺. Since the Cl⁺ reactive radicals excited in the SiCl₄ plasma are believed to be responsible for the etching of GaAs, it is highly possible that the type of etch mechanism and products produced in the SiCl₄ process are similar to the species produced from studies of the ion-assisted etching of GaAs using molecular Cl₂ and argon ions^{2.29,66}. In Balooch's experiment^{2.29}, etching of GaAs in molecular chlorine was observed only in the presence of argon ion bombardment. Using a Cl₂ flux of 1×10^{17} molecules/cm²s to impinge on the GaAs surface, they observed AsCl₃⁺, AsCl₂⁺, AsCl⁺, GaCl₃⁺, GaCl₂⁺ and GaCl⁺ ions, and suggested that they had arisen from AsCl₃ and GaCl₃. It was also evident, according to their data, that ion bombardment did not cause sputtering of Ga or As but instead, enhances the production and/or desorption rate of GaCl₃ leading to their belief that the rate limiting step for the etching of GaAs in their experiment is the rate of desorption of GaCl₃. On the other hand, in a similar experiment by McNevin et. al.^{2.66}, they employed a maximum Cl₂ flux of 5×10^{14} molecules/cm²s and found AsCl₃, GaCl₂, and possibly GaCl as major species leaving the GaAs surface. In addition, from their experimental data, they proposed a very different reaction model which involves the enhancement of the reaction of adsorbed Cl₂ with the arsenic on the

GaAs surface which produces AsCl₃. The difference in the reaction products observed and possibly the models proposed in the two cases may be explained by a thermodynamic analysis of the steady state chemical etching of GaAs using Cl₂ performed by McNevin^{2.67}: by minimising the Gibbs free energy and assuming that the fluxes of Ga and As leaving the surface, and the amount of Cl incident and the amount of Cl leaving the surface were equal, it was predicted that under chlorine deficient conditions, the less than fully chlorinated species, GaCl₂ will be formed while under chlorine excess conditions, the fully chlorinated species, GaCl₃ and AsCl₃ will be formed. However, this analysis only takes into account of the chemical component of etching and has been applied by McNevin et. al.^{2.66} to their ion enhanced chemical etching experiment and they found that the predicted reaction products in chemical etching (AsCl₃ and GaCl₃) were in contrast with the species AsCl₃ and the less than fully chlorinated GaCl₂/GaCl species observed experimentally. Nevertheless, the etch chemistry involved during the etching of GaAs using SiCl₄ based on the above information suggests the following:

plasma excitation



where x = 1, 2, 3 and y = 3

The vapour pressures of the reaction products (GaCl₂, GaCl₃ and AsCl₃) are plotted against temperature as shown in figure 2.9. It is clear that AsCl₃ is the most volatile, followed by GaCl₃, with the least volatile product being GaCl₂. A more detailed analysis of the microscopic relationship between the flow rate and etch rate, and the possible etch products formed in the reactive ion etching of GaAs using SiCl₄ in the present work is described in section 3.3.

At Glasgow, SiCl₄ was developed by S.Thoms as a dry etchant for the high resolution etching of GaAs^{2.57}. A useful etch mask for this etchant was found to be NiCr lifted-off from PMMA polymer resist, see section 2.3, with the ratio of GaAs etch rate to mask etch rate of > 50:1. High resolution negative resist HRN was found not to be so resistant to the etch, at best, a ratio of > 10:1 was observed.

2.6.2 Machine

The reactive ion etching system (Plasmatech RD80) used is a conventional 13.56MHz parallel plate reactive ion etcher. The anode and cathode are aluminium with hard anodisation, in particular, three NiCr pins are fitted around the perimeter of the cathode to enable d.c. voltage measurement. The cathode is 17cm in diameter and the anode to cathode area ratio is 2.8:1. The pumping system consists of an Edwards two stage rotary (mechanical) pump and a Roots blower (mechanical booster). In all experiments, the etch chamber was evacuated to a base pressure of around 10^{-3} to 10^{-4} Torr range before the samples were loaded, and the temperature of the cathode, where the GaAs samples were mounted, was kept constant at 40°C. The optimum etch condition found to give clean, vertical sidewalls and maximum reproducibility was at a power density of $0.44\text{W}/\text{cm}^2$, true volume flow rate of 9sccm, (after applying a calibrated correction factor of 0.28) and a pressure of 12mTorr giving a d.c. bias of 300V. The etch rate of GaAs etched under this condition is 200nm/min.. SEM 2.1 shows some thin GaAs ridges of widths $\approx 170\text{nm}$ etched in SiCl_4 using HRN as the etch mask.

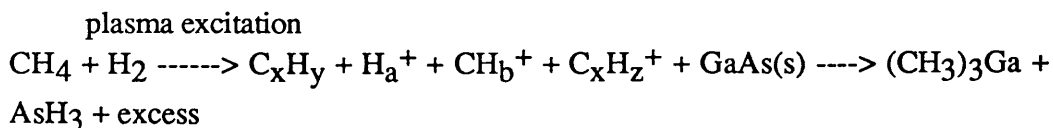
2.7 Reactive ion etching of GaAs in a mixture of methane and hydrogen (CH_4/H_2)

2.7.1 Chemistry

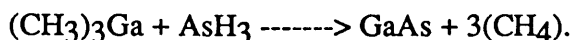
The use of CH_4/H_2 for the etching of semiconductor compound materials was first developed by Niggebrügge et. al.^{2.68}. They reported reactive ion etching of indium phosphide (InP), indium gallium arsenide (InGaAs) and the quaternary compound indium gallium arsenide phosphide (InGaAsP). By choosing the appropriate parameters, (1 to 3 Pa total pressure, volume flow rate of 15 to 20 % CH_4), a good degree of anisotropy and an excellent surface morphology was produced. A high selectivity was also brought about by using photoresist and SiO_2 as dry etch masks. However, they were unable to use this mixture to etch GaAs. With 20% CH_4 in H_2 , a power density of $0.4\text{W}/\text{cm}^2$ and pressures of 10 and 20 mTorr, very slow etch rates below 10nm/min. and considerable surface roughness were observed.

Using mass spectrometry, a detailed analysis of the plasma species present during the reactive ion etching of InP with CH₄/H₂ has been studied by Schmid^{2.69}. The mass spectra of neutral compounds with and without the plasma are depicted in figures 2.10a) and b). Ethine, ethene, ethane and molecules with carbon chains of higher order appear as products formed in the plasma. The spectrogram of positive plasma ions were also taken and is shown in figure 2.11. It is a common belief that the chemistry of the RIE of InP in a CH₄/H₂ plasma relies on the formation of phosphine and group III alkyls. Indeed phosphine was clearly resolved by mass spectroscopy as a neutral compound as well as in ionic state as shown in figure 2.12. Although the limited resolution of the mass spectrometer did not allow the identification of group III etching products, the author believes that the similar dependence of the InP etch rate and the concentration of neutral products on total pressure (figure 2.13) suggests that the methyl radicals play an important role in the etching mechanism.

Unfortunately, no such detailed analysis has been done in the etching of GaAs using CH₄/H₂, nonetheless, it is likely that the etch chemistry involved with GaAs is similar to InP and may be written as follows:



where x = 1, 2; y = 2, 4, 6; a = 2, 3; b = 3, 4, 5; z = 2, 4, 5, 6. This is similar to the inverse metal organic chemical vapour deposition (MOCVD) process. In MOCVD, the reactant products, (CH₃)₃Ga and AsH₃ are transported in a H₂ carrier gas to the growth zone where GaAs is formed through the chemical reaction:



A plot of vapor pressure vs. temperature is shown in figure 2.14 illustrating the volatility of the products of the suggested reaction.

2.6.2 Machine

The reactive ion etching machine used was also a conventional 13.56MHz parallel plate reactive ion etcher, (Electrotech BRS Plasma-fab 340) with an anode/cathode ratio of 3.3:1. Both electrodes are made of aluminium with titanium oxide coated on the cathode which is 17cm in diameter. The pumping system used and the base pressure acquired are the same as in the RD80 RIE machine. The temperature of the cathode, where the GaAs samples were situated, was kept constant at 30°C. Section 4.2 describes the optimum condition developed for the high resolution etching of GaAs using this mixture.

2.8 References

- 2.1) M.Mochel, C.Humphreys, J.Eades, J.Mochel and A.Petturd; *Appl. Phys. Letts.* **42** p.38, 1983
- 2.2) D.F.Kyser; *J.Vac.Sci.Technol.* **B1** p.1391, 1983
- 2.3) N.Jamoto and R.Shimizu; *J. Appl. Phys.* **54** p.3855, 1983
- 2.4) S.A.Rishton; Ph.D. thesis, Glasgow University, 1984
- 2.5) W.S.Mackie; Ph.D. thesis, Glasgow University, 1984
- 2.6) C.E.Binnie; Ph.D. thesis, Glasgow University, 1985
- 2.7) S.P.Beaumont, T.Tamamura and C.D.W.Wilkinson; in *Proc. Int. Conf. on Microlithography*, Amsterdam, edited by R.P.Kramer, Delft University Press, 1981
- 2.8) Data sheet from P.W.Whipps, Philips Redhill Lab., Surrey. 'Negative-acting electron beam resist: type HRN and HSN', 1980
- 2.9) W.Patrick, W.S.Mackie, S.P.Beaumont and C.D.W.Wilkinson; *J.Vac.Sci.Technol.* **B4(1)** p.390, 1986
- 2.10) 'Electron-beam technology in micro-electronic fabrication', edited by G.R.Brewer, Academic, New York, 1980
- 2.11) K.E.Bean; *IEEE Trans. Electron. Dev.* **ED-25** p.1185, 1978
- 2.12) Y.X.Wang and P.H.Holloway; *J.Vac.Sci.Technol.* **B2(4)** p.613, 1984
- 2.13) J.W.Coburn; *J.Vac.Sci.Technol.* **13(5)** p.1037, 1976
- 2.14) P.G.Glöersen; *J.Vac.Sci.Technol.* **12(1)** p.28, 1975
- 2.15) 'Erosion and Growth of Solids Stimulated by Atom and Ion Beams', edited by G.Kiriakidis, G.Carter and J.L.Whitton, 1986
- 2.16) P.Sigmund; *Phys. Rev.* **184** p.383, 1969
- 2.17) 'VLSI Electronics Microstructure Science', Vol. 8, edited by N.G.Einspruch and D.M.Brown, Academic Press, 1984
- 2.18) H.Kinoshita T.Ishida and K.Kaminishi; *Appl. Phys. Letts.* **49(4)** p.204, 1986
- 2.19) K.Asakawa and S.Sugata; *J.Vac.Sci.Technol.* **A4(3)** p.677, 1986
- 2.20) M.W.Geis, G.A.Lincoln, N.Efremow and W.J.Piacentini; *J.Vac.Sci.Technol.* **19(4)** p.1390, 1981
- 2.21) G.A.Lincoln, M.W.Geis, L.J.Mahoney, A.Chu, B.A.Vojak, K.B.Nichols, W.J.Piacentini, N.Efremow and W.T.Lindley; *J.Vac.Sci.Technol.* **20(3)** p.786, 1982
- 2.22) J.D.Chinn, A.Fernandez, I.Adesida and E.D.Wolf; *J.Vac.Sci.Technol.* **A1(2)** p.701, 1983

- 2.23) J.D.Chinn and E.D.Wolf; *J.Vac.Sci.Technol.* **B3(1)** p.410, 1985
- 2.24) J.A.Skidmore, L.A.Coldren, E.L.Hu, J.L.Merz and K.Asakawa; *J.Vac.Sci.Technol.* **B6(6)** p.1885, 1988
- 2.25) H.R.Koenig and L.I.Maissel; *IBM J. Res. Dev.* **14** p.168, 1970
- 2.26) I.Langmuir and M. Mott-Smith; *Phys. Rev.* **28** p.727, 1926
- 2.27) C.Steinbrüchel; *J. Electrochem. Soc.* **130** p.648, 1983
- 2.28) Y.H.Lee, J.E.Heidenreich III and G.Fortunato; *J.Vac.Sci.Technol.* **A7** p.903, 1989
- 2.29) M.Balooch and D.R.Olander; *J.Vac.Sci.Technol.* **B4(4)** p.794, 1986
- 2.30) J.W.Coburn and H.F.Winters; *J. Appl. Phys.* **50(5)** p.3189, 1979
- 2.31) D.L.Flamm and V.M.Donnely; *Plasma Chem. Plasma Proc.* **1** p.317, 1981
- 2.32) J.L.Mauer, J.S.Logan, L.B.Zielinski and G.S.Schwartz; *J.Vac.Sci.Technol.* **15** p.1734, 1978
- 2.33) R.E.Klinger and J.E.Greene; *J. Appl. Phys.* **54(3)** p.1595, 1983
- 2.34) E.L.Hu and R.E.Howard; *J.Vac.Sci.Technol.* **B2(1)** p.85, 1984
- 2.35) R.A.Barker, T.M.Mayer and R.H.Burton; *Appl. Phys. Letts.* **40(7)** p.583, 1982
- 2.36) Y.Yuba, T.Ishida, K.Gamo and S.Namba; *J.Vac.Sci.Technol.* **B(6)** p.253, 1988
- 2.37) C.M.Knoedler, L.Osterling and M.Heiblum; *J. Appl. Phys.* **65** p.1800, 1989
- 2.38) T.L.Cheeks, M.L.Roukes, A.Scherer and H.G.Craighead; *Appl. Phys. Letts.* **53(20)** p.1964, 1988
- 2.39) A.Scherer, H.G.Craighead, M.L.Roukes and J.P.Harbison; *J.Vac.Sci.Technol.* **B6(1)** p.277, 1988
- 2.40) C.S.Wu, D.M.Scott, W.X.Chen and S.S.Lau; *J. Electrochem. Soc.* **132(4)** p.918, 1985
- 2.41) K.Yamasaki, K.Asai, K.Shimada and T.Makimura; *J. Electrochem. Soc.* **129(12)** p.2760, 1982
- 2.42) S.W.Pang, M.W.Geis, N.N.Efremow and G.A.Lincoln; *J.Vac.Sci.Technol.* **B3(1)** p.398, 1985
- 2.43) K.Nagata, O.Nakajima and T.Ishibashi; *Jpn. J. of Appl. Phys.* **25(6)** p.L510, 1986
- 2.44) S.W.Pang, G.A.Lincoln, R.W.McClelland, P.D.DeGraff, M.W.Geis and W.J.Piacentini; *J.Vac.Sci.Technol.* **B1(4)** p.1334, 1983
- 2.45) S.W.Pang; *J. Electrochem. Soc.* **133(4)** p.784, 1986

- 2.46) J.S.Wang, S.J.Fonash and S.Ashok; IEEE Electron Device Letts. **4** p.4326, 1983
- 2.47) S.J.Pearton, A.J.Tavendale and E.M.Lawson; Radiation Effects, **79** p.21, 1983
- 2.48) R.Cheung, S.Thoms, I.McIntyre, C.D.W.Wilkinson and S.P.Beaumont; J.Vac.Sci.Technol. **B6** p.1911, 1988
- 2.49) R.Cheung, Y.H.Lee, C.M.Knoedler, K.Y.Lee, T.P.SmithIII and D.Kern; Appl. Phys. Letts. **54** p.2130, 1989
- 2.50) H.F.Wong, D.L.Green, T.Y.Liu, D.G.Lishan, M.Bellis, E.L.Hu, P.M.Petroff, P.O.Holtz and J.L.Merz; J.Vac.Sci.Technol. **B6** p.1906, 1988
- 2.51) S.J.Pearton, U.K.Chakrabarti and W.S.Hobson; J. Appl. Phys. **66(5)** p.2061, 1989
- 2.52) S.Semura, H.Saitoh and K.Asakawa; J. Appl. Phys. **55(8)** p.3131, 1984
- 2.53) K.L.Seaward, N.J.Moll, D.J.Coulman and W.F.Stickle; J. Appl. Phys. **61(6)** p.2358, 1987
- 2.54) S.J.Pearton, M.J.Vasile, K.S.Jones, K.T.Short, E.Lane, T.R.Fullowan, A.E.Von Neida and N.M.Haegel; J. Appl. Phys. **65(3)** p.1281, 1989
- 2.55) N.Yabumoto and M.Oshima; J. Electrochem. Soc. **132(9)** p.2224, 1985
- 2.56) C.M.Knoedler, L.Osterling and H.Shtrikman; J.Vac.Sci.Technol. **B6** p.1573, 1988
- 2.57) S.Thoms, S.P.Beaumont, C.D.W.Wilkinson, J.Frost and C.R.Stanley; Microcircuit Engineering 1986, edited by H.W.Lehmann and Ch. Bleicker (North-Holland, Amsterdam, 1986), p.249
- 2.58) S.W.Pang, W.D.Goodhue, T.M.Lyszczarz, D.J.Ehrlich, R.B.Goodman and G.D.Johnson; J.Vac.Sci.Technol. **B6(6)** p.1916, 1988
- 2.59) M.Watt, C.M.Sotomayer-Torres, R.Cheung, C.D.W.Wilkinson, H.E.G.Arnot and S.P.Beaumont; J. of Modern Optics, **35(3)** p.365, 1988
- 2.60) R.Cheung, A.Birnie, J.N.Chapman, S.Thoms and C.D.W.Wilkinson; Microcircuit Engineering, paper presented at the 15th international conference on Microlithography, Microcircuit Engineering, Cambridge, 1989
- 2.61) M.B.Stern and P.F.Liao; J.Vac.Sci.Technol. **B1(4)** p.1053, 1983
- 2.62) M.B.Stern, H.G.Craighead, P.F.Liao and P.M.Mankiewich; Appl. Phys. Letts. **45(4)** p.410, 1984
- 2.63) J.Z.Li, I.Adesida and E.D.Wolf; Appl. Phys. Letts. **45(8)** p.897, 1984
- 2.64) J.Z.Li, I.Adesida and E.D.Wolf; J.Vac.Sci.Technol. **B3(1)** p.406, 1985
- 2.65) M.D.Rowe, 5th Int. Conf. on Ion and Plasma Assisted Techniques (IPAT),

p.87, 1985

2.66) S.C.McNevin and G.E.Becker; J. Appl. Phys. **58(12)** p.4670, 1985

2.67) S.C.McNevin, internal report of AT&T Bell Lab., Murray Hill, New Jersey.

2.68) U.Niggebrügge, M.Klug and G.Garus; Proc. 12th Int. Symp. on GaAs and Related Compounds; Inst. Phys. Conf. Ser. no.79, p.367, 1986

2.69) H.Schmid; Proc. 6th Int. Conf. Ion and Plasma Assisted Techniques, Brighton, U.K. p.98, 1987

2.70) R.Cheung, Y.H.Lee, K.Y.Lee, T.P.Smith III, D.P.Kern, S.P.Beaumont and C.D.W.Wilkinson; J.Vac.Sci.Technol. **B7(6)** p.1462, 1989

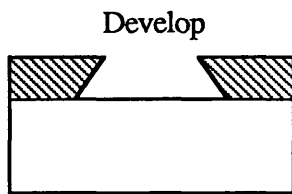
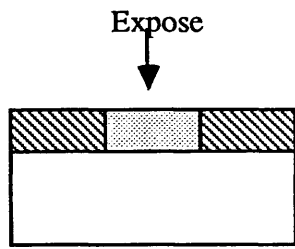
2.71) H.W.Lehmann, L.Krausbauer and R.Widmer; J.Vac.Sci.Technol. **14(1)** p.281, 1977

2.72) P.G.Glöersen; J.Vac.Sci.Technol. **12** p.28, 1975

2.73) P.G.Glöersen; Sol. State Technol. **19(4)** p.68, 1976

2.74) CRC Handbook of Chemistry and Physics; 1986-87

Positive resist



Negative resist

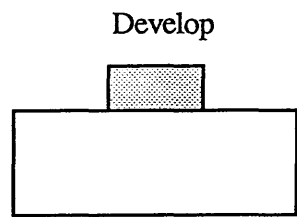
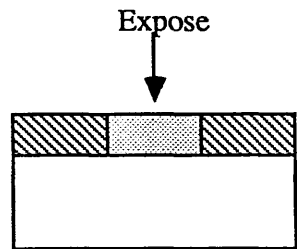


Figure 2.1 Illustration of the pattern definition process using positive and negative resists

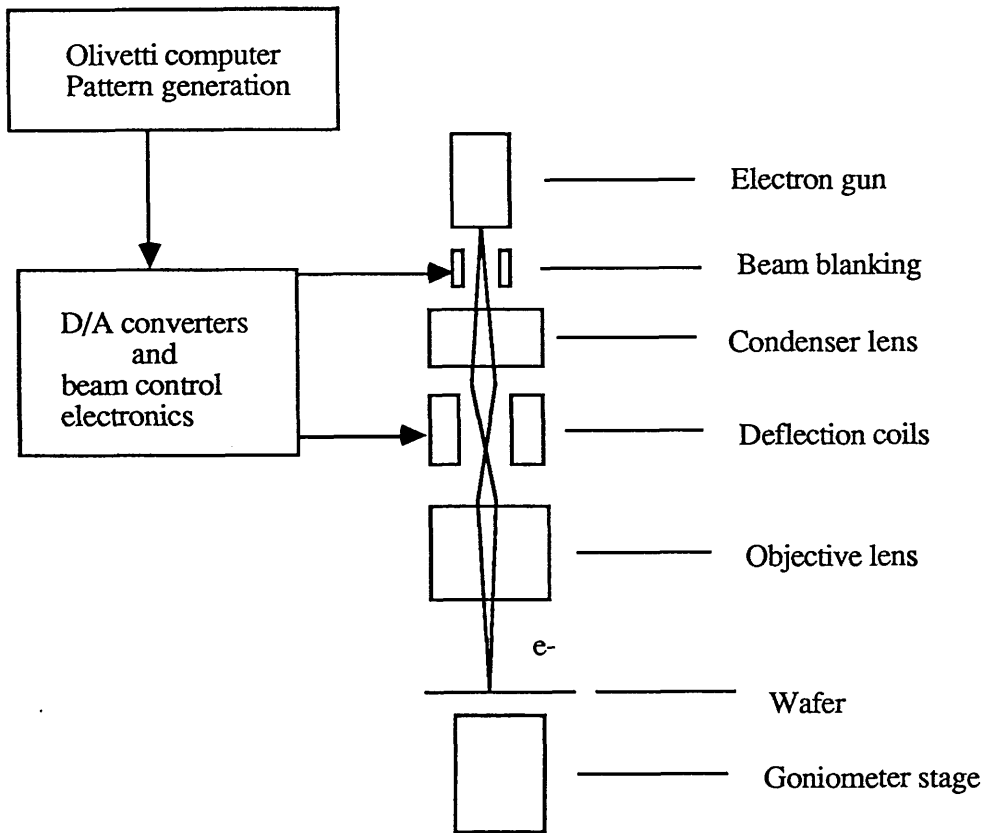
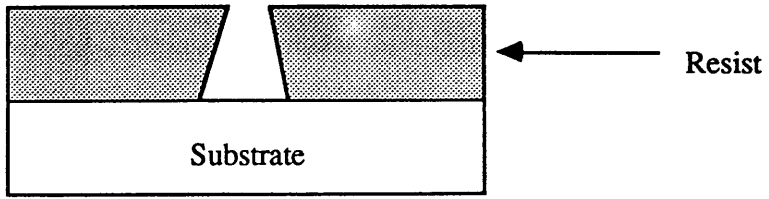
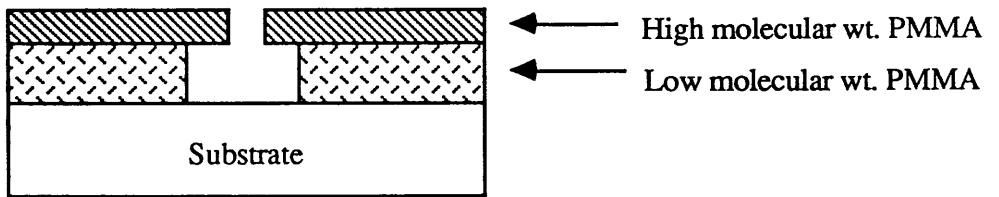


Figure 2.2 The PSEM based high resolution E.B.L.system at Glasgow University



(a)

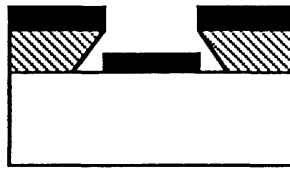


(b)

Figure 2.3 Developed profiles of a) thick ($1\mu\text{m}$) PMMA and b) bilayer resist system

Metallisation

Metallise

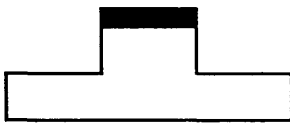


Lift-off

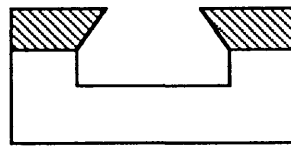


Etching

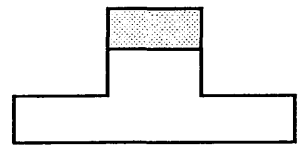
Dry etch substrate
using metal mask



Dry etch substrate
using positive resist



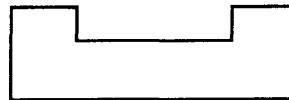
Dry etch substrate
using negative resist



Remove metal



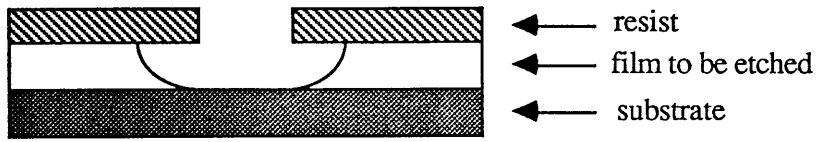
Remove resist



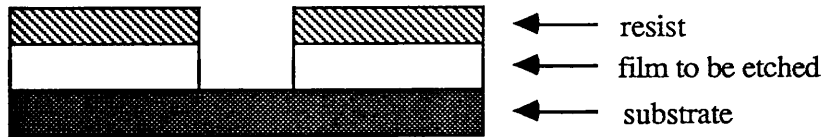
Remove resist



Figure 2.4 showing the various techniques of pattern transfer



a) Isotropic etch profile after wet etching



b) Anisotropic etch profile after dry etching

Figure 2.5 showing the resultant etch profiles after wet and dry etching

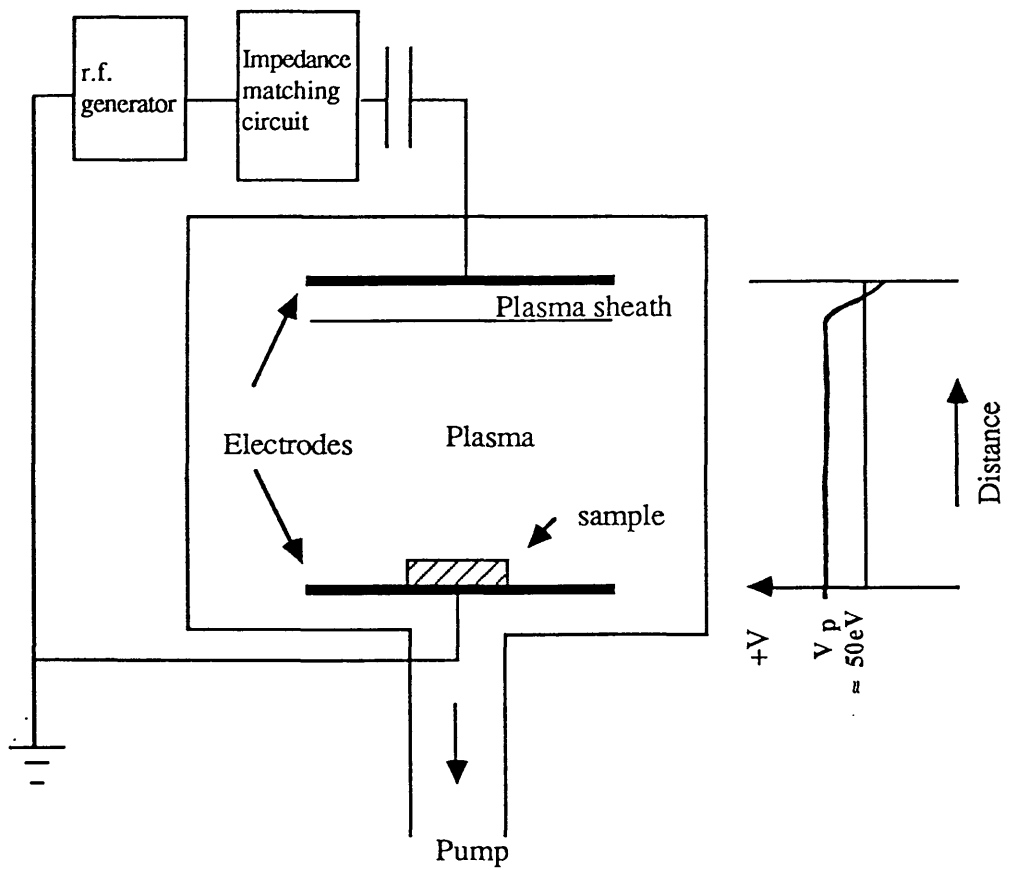


Figure 2.6 Planar plasma system and its potential distribution

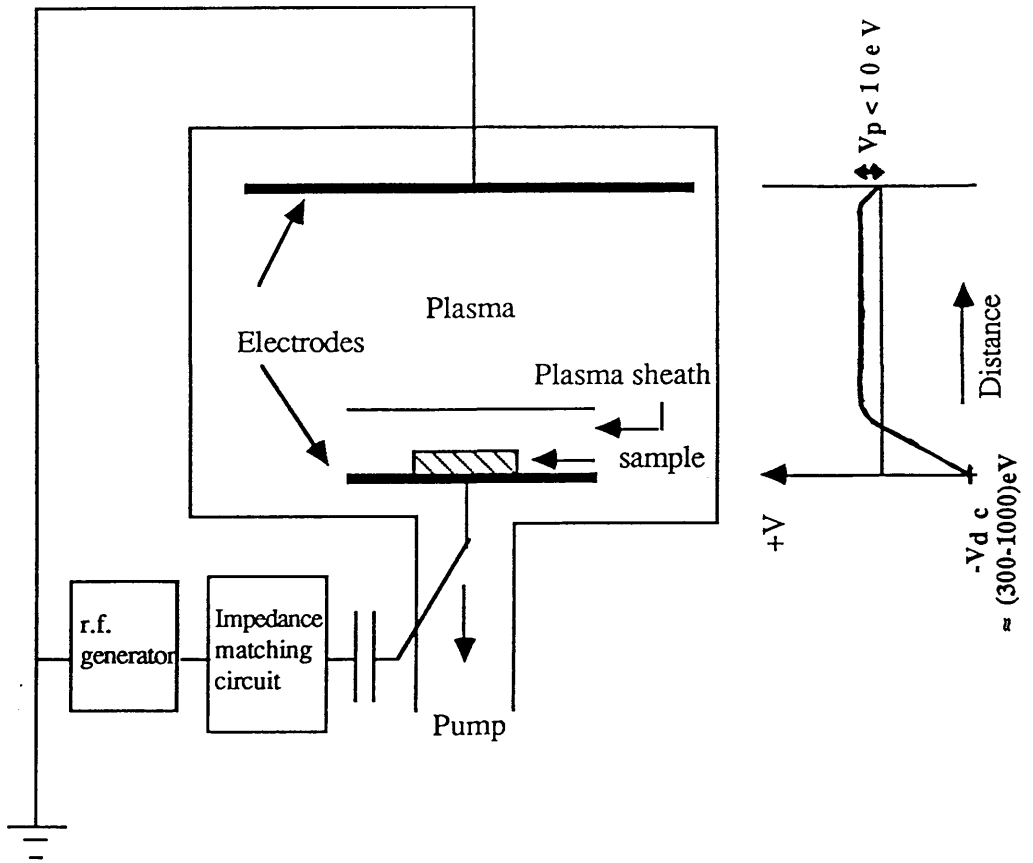


Figure 2.7 Reactive ion etching and its potential distribution

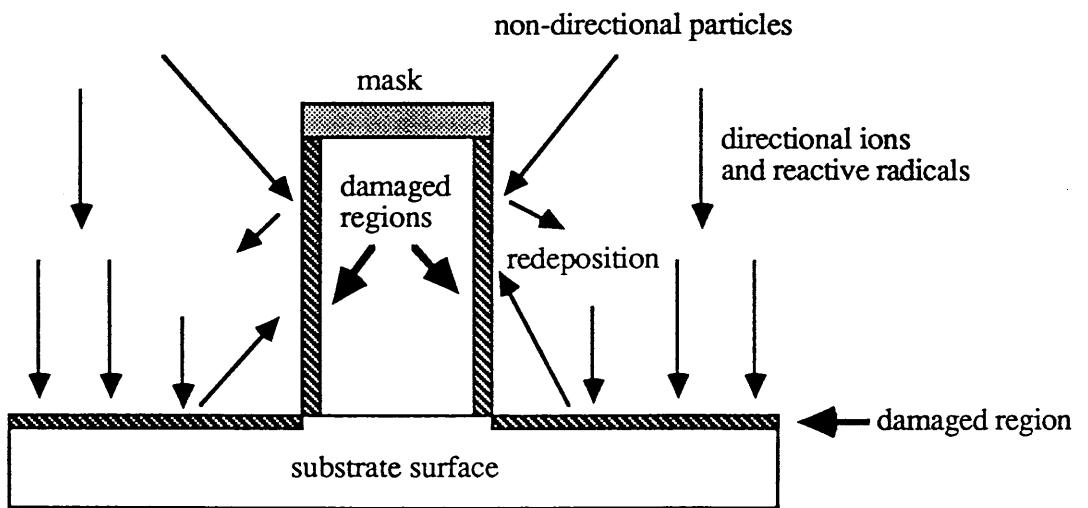


Figure 2.8 Possible causes of RIE surface and sidewall damage, see text.

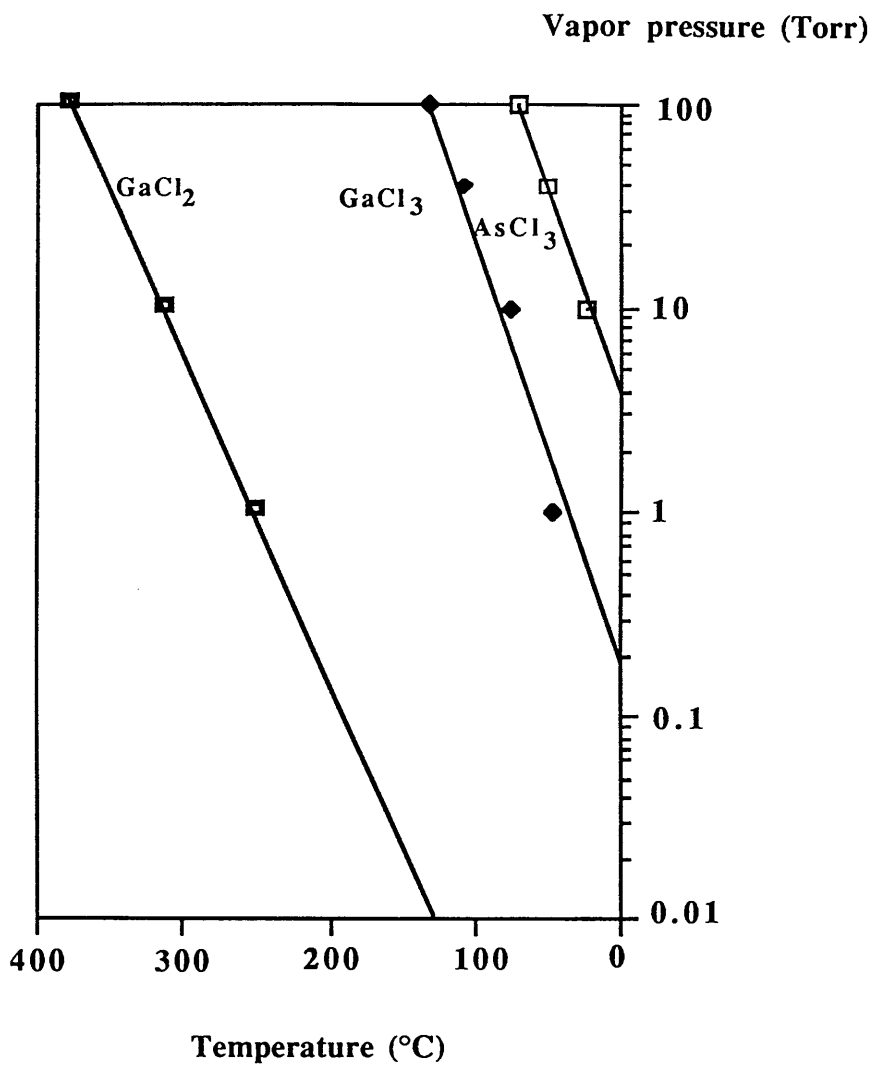
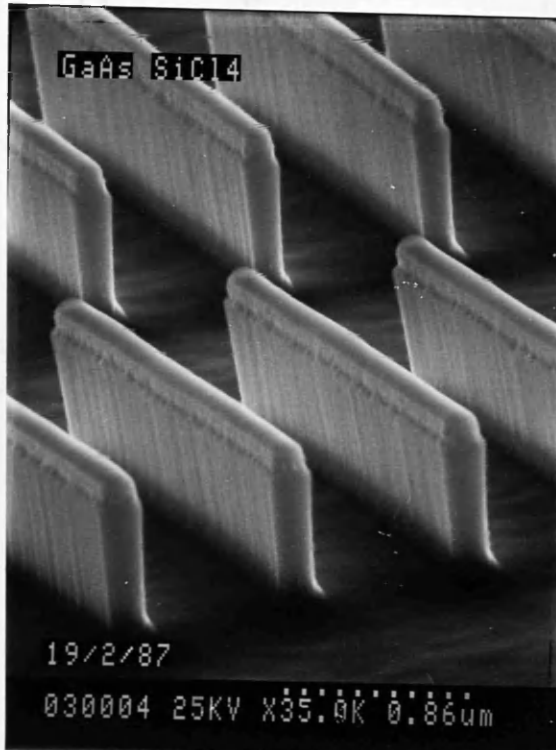


Figure 2.9 Vapour pressures of GaCl₃, GaCl₂ and AsCl₃ (ref. 2.74)



SEM 2.1 GaAs ridges fabricated by reactive ion etching using SiCl_4 under the optimum conditions: power density $0.44\text{W}/\text{cm}^2$, 12mT total pressure, 300V d.c. bias and 9scm volume flow rate, with the HRN mask still remaining on the wires

Figure 2.11 Spectrogram of positive plasma ions (with the same process parameters as fig. 2.10) (After Schmidt ref. 2.69).

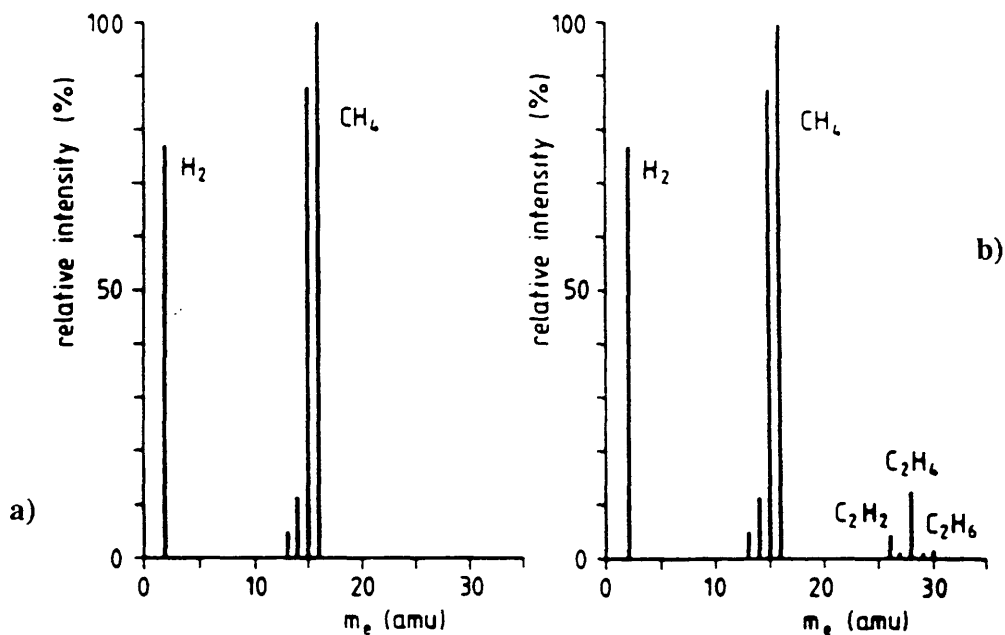


Figure 2.10 Spectrograms of neutral species a) without and b) with plasma

(20% CH_4 in H_2 ; flow rate 25sccm; pressure 2.6Pa; power density $0.4W/cm^2$) (After Schmid ref. 2.69)

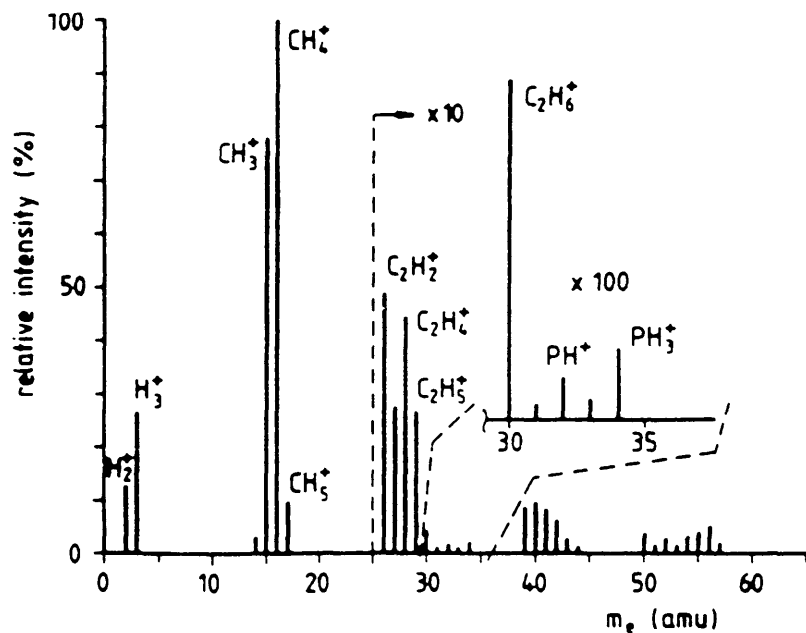


Figure 2.11 Spectrogram of positive plasma ions (with the same process parameters as fig. 2.10) (After Schmid ref. 2.69)

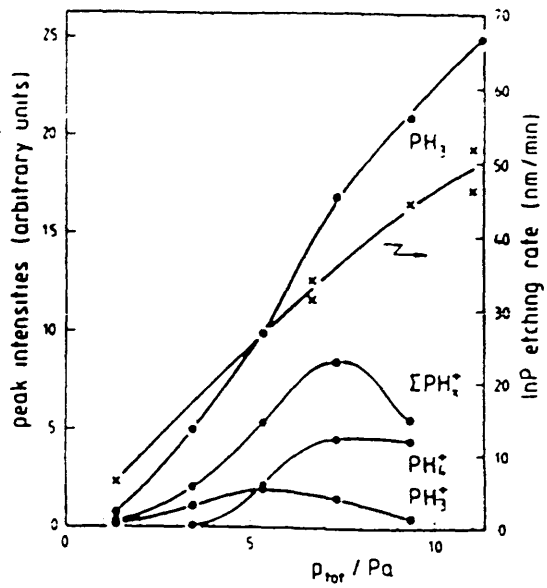


Figure 2.12 InP etch rate and intensities of neutral and ionic phosphorous compounds vs. total pressure (6% CH₄ in H₂; power density 0.4W/cm²; flow 25scem) (After Schmid ref. 2.69)

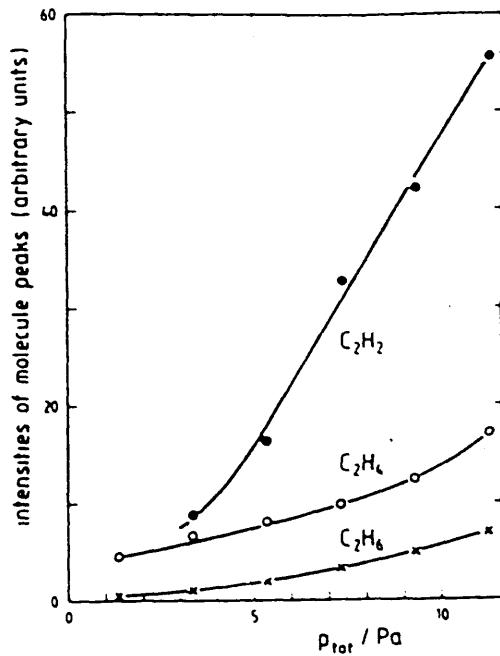


Figure 2.13 Dependence of neutral products concentration on pressure (same process parameters as fig.2.12) (After Schmid ref. 2.69)

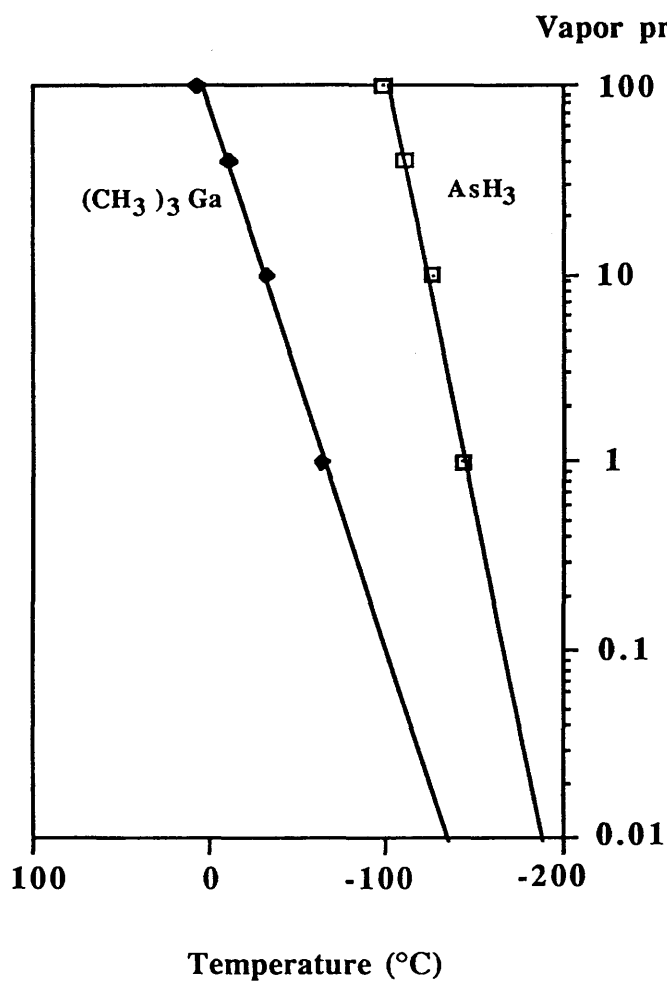


Figure 2.14 Vapor pressures for $(\text{CH}_3)_3\text{Ga}$ and AsH_3 (ref. 2.74)

Chapter 3 Reactive ion etching of GaAs and Al_{0.3}Ga_{0.7}As using SiCl₄ and damage characterisation

3.1 Introduction

This chapter investigates the reactive ion etching of GaAs and Al_{0.3}Ga_{0.7}As using SiCl₄. Damage characterisation on the etched surface was performed using quantitative electrical and optical techniques such as Schottky diode performance, integrated band-gap photoluminescence and Raman scattering; analytical X-ray photoelectron spectroscopy was also employed to study the chemical bonding on etched surfaces. A novel fabrication process was developed to allow Schottky diodes to be constructed on the etched sidewalls so that the damage inflicted on the sidewalls may be estimated.

3.2 Etch rate dependence on power density and pressure in the RIE of GaAs and Al_{0.3}Ga_{0.7}As

The reactive ion etching of GaAs employing SiCl₄ has been developed at the University of Glasgow by S. Thoms previously^{3.1} and using a power density of 0.44W/cm², 12mT total pressure with a volume flow rate of 9sccm, vertical sidewalls and smooth surfaces were obtained suitable for fabrication of structures in the nano-metric scale. While it has been demonstrated that SiCl₄ can be used to reactive ion etch aluminium^{3.2} through the formation of AlCl₃ compounds, the technique has also been investigated by Salimian et. al.^{3.17} for the reactive ion etching of GaAs/AlGaAs and applied to the fabrication of optical waveguides^{3.15} and quantum wires in GaAs/AlGaAs heterolayers by etching through the AlGaAs layer^{3.16}. Moreover, the etch rate ratio between GaAs and Al_xGa_{1-x}As has been studied by a number of workers using a variety and mixture of gases, etch parameters and systems to obtain either equi-rate or selective etching for the fabrication of optoelectronic devices and transistor structures^{3.3-3.11}. In this section, the etch rate dependence on power density and pressure around the optimum condition in the etching of both GaAs and Al_{0.3}Ga_{0.7}As using SiCl₄ has been investigated.

3.2.1 Experimental

Throughout the work of this chapter, the GaAs used was a $2 \times 10^{17} \text{cm}^{-3}$ Si-doped epitaxial layer of thickness $1 \mu\text{m}$ on an n^+ substrate, and the AlGaAs material was of 30% aluminium and 70% gallium composition doped with $1 \times 10^{17} \text{cm}^{-3}$ silicon of thickness $1 \mu\text{m}$, on a $2 \mu\text{m}$ thick $2 \times 10^{18} \text{cm}^{-3}$ Si-doped GaAs, grown by molecular beam epitaxy on an n^+ substrate, (provided by University of Nottingham); the $\text{Al}_{0.3}\text{Ga}_{0.7}\text{As}$ was capped with 20nm of undoped GaAs. In order to characterise the etch rate, the wafers were scribed to $5 \times 5 \text{mm}^2$ chips and half covered with 15% PMMA BDH positive resist before etching. The GaAs capping layer was left on the AlGaAs to avoid oxidation from air. After etching, the resist was removed in acetone and the etch depths were measured using a Talystep. The reactive ion etching was carried out using the Plasmatech RD80 etcher described in section 2.5.2. To investigate the shape of the structures after etching, NiCr of 30nm thick lifted-off from a double layer PMMA polymer resist (section 2.2.2) was used as a dry etch mask for both materials since NiCr has been found to be a good etch mask for GaAs in SiCl_4 rendering a ratio of GaAs etch rate to mask etch rate of $> 50:1$ ^{3.1}.

3.2.2 Results and discussion

Initially, $\text{Al}_{0.3}\text{Ga}_{0.7}\text{As}$ patterned with NiCr lines were reactive ion etched under the optimum conditions developed for GaAs and results showed that vertical sidewalls were produced. Quantum wires in GaAs/AlGaAs heterolayers have been fabricated under similar etching conditions^{3.16}. Figure 3.1 shows the graph of etch depth vs. time for both GaAs and $\text{Al}_{0.3}\text{Ga}_{0.7}\text{As}$ reactive ion etched in SiCl_4 at a power density of $0.44 \text{W}/\text{cm}^2$, 9sccm, 12mT, 300V d.c. bias. Similar etch rates and an induction period of 5 seconds were observed for both materials. Since the GaAs cap was left on the AlGaAs, the induction period is believed to be the time taken to remove the native oxides on the GaAs surface and has been observed by others in the reactive ion etching of $\text{GaAs}/\text{Al}_x\text{Ga}_{1-x}\text{As}$ ^{3.8,3.9}. It is well known that $\text{Al}_x\text{Ga}_{1-x}\text{As}$ oxidises readily in the presence of oxygen and Al_2O_3 is an involatile product which is believed to hinder the etching process; because of this, the etch rate of $\text{Al}_x\text{Ga}_{1-x}\text{As}$ has been found by others using various gases to be slower than

GaAs^{3.3,3.8}. Moreover, this characteristic has been used to obtain a selective etch for GaAs in RIBE using Ar/O₂^{3.18} and in RIE by adding O₂ to a BCl₃/Ar gas mixture^{3.6}. In this work, similar etching rates for GaAs and Al_{0.3}Ga_{0.7}As were measured. While the prevention of Al_{0.3}Ga_{0.7}As oxidation through the presence of the capped GaAs layer before etching may explain this observation, this result also suggests that the amount of oxygen present in the etching chamber during etching does not cause a high level of Al_{0.3}Ga_{0.7}As oxidation, at least to the degree of which may effect the etching rate in the presence of ion bombardment, see below.

Figure 3.2 shows the etch rate and sidewall profile dependence on power density for both GaAs and Al_{0.3}Ga_{0.7}As reactive ion etched in SiCl₄ at a constant pressure of 12mT with power densities varying from 0.08W/cm² to 0.44W/cm². An increase in etch rate with power density is observed. Since the etch mechanism in reactive ion etching is a chemical as well as a physical one, it is likely that increases in radical generation and ion bombardment with power density are responsible for the corresponding increase in the measured etch rate. For both materials, overcut sidewalls are observed at power densities below 0.44W/cm² while at a power density of 0.44W/cm², vertical sidewalls are present. Thus it may appear that the verticality observed at higher power density is largely due to a higher degree of ion bombardment during etching, though the possibility of a higher reaction probability with the sidewalls from the larger radical generation at high power densities could not be ruled out. Similar etch rates are measured for GaAs and Al_{0.3}Ga_{0.7}As, this data is consistent with those reported by Salimian et. al.^{3.17}. In this work, although the Al_{0.3}Ga_{0.7}As was prevented from oxidation by leaving on the GaAs cap layer, low concentrations of oxygen may be present in the etcher during etching which may cause the formation of Al₂O₃. In a RIE study by Nagasaka et. al.^{3.8}, they found that AlGaAs was not etched with a Cl₂ plasma and a CCl₄ plasma etches AlGaAs with a slow rate, but fast and an equal rate of etching between GaAs and AlGaAs was obtained using a suitable mixture of Cl₂ and CCl₄. This they attributed to the possibility of the removal of Al₂O₃ which could have been formed on top of the AlGaAs substrate or during etching by the CCl₃⁺ ions. A similar etch mechanism was also suggested by Tamura et. al.^{3.3} using BCl₃-Cl₂ as the etch gas. It is possible, therefore, that the etching mechanism of Al_{0.3}Ga_{0.7}As in SiCl₄ resembles that in BCl₃-Cl₂ and CCl₄-Cl₂, and in this case, the SiCl_x⁺ ions would be responsible for the removal of the low level of involatile

Al_2O_3 thus enabling the Cl^+ to react with the underlying $\text{Al}_{0.3}\text{Ga}_{0.7}\text{As}$.

By varying the feed gas flow rate, the etch rate and sidewall profile dependence on gas pressure for GaAs and $\text{Al}_{0.3}\text{Ga}_{0.7}\text{As}$ etched in SiCl_4 from 5mT to 32mT at a constant power density of $0.44\text{W}/\text{cm}^2$, 300V d.c. bias was investigated, see figure 3.3. At a gas pressure above 12mT, an increase in etch rate and undercut profiles are observed for both materials. At higher pressure conditions, a larger reactive radicals generation and the development of a lower self d.c. bias are expected. Although the increase in etch rate may be explained by the larger radical generation, the undercut profiles could be a result of both the larger radical generation and the shorter mean free path of the ions associated with a lower d.c. bias^{3.78}. On the other hand, at lower pressure conditions, while both the larger self d.c. bias developed and the lower radical generation may account for the vertically etched sidewalls observed, the dominant role of ion bombardment in the etch mechanism in this pressure regime is suggested from the slight increase in etch rate at pressures below 12mT.

3.3 Microscopic relation between flow rate and etch rate in the reactive ion etching of GaAs

The etch rate dependence on the volume flow rate of SiCl_4 in the reactive ion etching of GaAs has been studied and figure 3.4 shows such dependence for power densities $0.44\text{W}/\text{cm}^2$ and $0.88\text{W}/\text{cm}^2$. The volume flow rate was varied from 2.8 to 11.6 sccm (with a corresponding chamber pressure change of 4 to 16mT). An increase in etch rate with gas flow rate is evident with a higher etch rate observed at higher power density. While the larger concentration of reactive radicals generated with an increase in gas flow rate may explain the similar trends of etch rate increase observed, the larger etch rate measured at $0.88\text{W}/\text{cm}^2$ may result from both the higher generation of reactive radicals and the larger d.c. bias developed at a higher power density. More information on the effect of gas flow rate on etch rate on a microscopic level both experimentally and theoretically is possible by calculating the following assuming the etch reactions which occur are those proposed in section 2.6.1. Experimentally, by taking the area of the GaAs exposed to a plasma to be $a \times b \text{ cm}^2$ with an etch rate of $c \text{ cm}/\text{min.}$, the volume of the GaAs

etched per minute is therefore $a \times b \times c \text{ cm}^3$. Since the density of GaAs is $2.21 \times 10^{22} \text{ molecules/cm}^3$, the number of GaAs molecules etched per minute can then be determined. To calculate the experimentally available Cl (in sccm) for reaction, the following assumptions may be made:

- a) the feed gas ionisation efficiency in conventional reactive ion etching is $\approx 0.01\%$, (see section 5.2.1)
- b) in an emission spectroscopic study of a SiCl_4 plasma by Rowe^{3.12}, 22% Cl atoms were measured to have been produced from the ionised SiCl_4
- c) according to a study of ion-assisted reactions using a steady state molecular and modulated ion beam by Balooch et. al.^{3.13} where a Cl_2 flux was used to react with GaAs, some 8% reaction probability was measured by monitoring the reduction in the intensity of the reflected Cl_2 beam when an argon ion beam was turned on.

At standard temperature pressure, $1\text{sccm} = 2.69 \times 10^{19} \text{ molecules/min.}$ and therefore, the available Cl (in sccm) for reaction can be converted to atoms/min.. In theory, if the reactant products produced under steady state conditions are assumed to be GaCl_3 and AsCl_3 , since they are the most volatile reactant products and have been observed by Balooch et.al.^{3.13}, this would result in 6 Cl atoms reacting with 1 GaAs molecule. Hence, a comparison between the theoretically determined and the experimental result of the Cl atoms available per minute for the GaAs molecules consumed per minute for a power density of 0.44W/cm^2 may be plotted and is shown in figure 3.5. Clearly, in the regime of flow rates considered, the plasma is operating under chlorine deficient conditions. In a thermodynamic study of GaAs chemical etching using Cl_2 at a temperature of 300K by McNevin^{3.14}, it was predicted that the dependence of the relative chlorination of the reactant products on the amount of chlorine available for reaction, leading to the formation of different reactant species. In the situation where chlorine is deficient, i.e. there is not enough chlorine to react with all of the Ga and As atoms, a competition for the limited amount of available chlorine results and consequently, the less than fully chlorinated species As, GaCl_2 or GaCl are formed. In contrast, when there is excess chlorine, i.e. there is more than enough chlorine to react with all of the Ga and As, the formation of the fully chlorinated species AsCl_3 and GaCl_3 are expected, as in the present theoretical assumption. Therefore, if the formation of reactant products were assumed to be GaCl_2 or GaCl and AsCl_3 instead of GaCl_3 and AsCl_3 ; i.e. 5 or 4 Cl atoms to 1 GaAs molecule, a similar graph of Cl atoms

available/min. vs. GaAs molecules consumed/min. may be plotted and is shown in figure 3.6. In this case, GaCl₂ and GaCl are most likely to be formed corresponding to flow rates of 11.6sccm and 7.2sccm respectively. Hence, in the flow rate regime where the plasma is normally operated, i.e. 9sccm; the formation of the less chlorinated species GaCl₂ and GaCl and possibly As may be expected. However, it is worth noting that the 8% reaction probability assumed from Balooch et. al.^{3.13} is probably an underestimated value. Although their estimation was taken in the presence of ion bombardment, as would be the case in RIE, it was the Cl₂ reaction probability which was being measured rather than the Cl reaction probability. It has been found that the Cl radicals adsorb much more easily on the GaAs surface than the Cl₂ molecule^{3.19} and that enhanced etching of GaAs has been observed using Cl radicals rather than Cl₂ in the presence of ion bombardment^{3.20}. Therefore, information on the Cl reaction probability would have been more useful for the present calculation since the Cl radicals are responsible for the reactive ion etching of GaAs in a SiCl₄ plasma. An additional uncertainty between Balooch's and this experiment concerns with the different effects of ion bombardment contributed by different ions^{3.30,3.32,3.77} in ion-assisted reactions. So overall, such type of calculation should be taken with caution - but does reveal that chlorine deficiency is not improbable.

3.4 Characterisation of damage induced in GaAs and Al_{0.3}Ga_{0.7}As after reactive ion etching

The characterisation techniques used to investigate the degree and nature of damage caused on the semiconductor surface include measurement of ideality factor of Schottky diodes, low temperature integrated band-gap photoluminescence, X-ray photoelectron spectroscopy and Raman scattering. To quantify the degree of damage induced on the sidewall, a novel technique was developed by fabricating a Schottky diode onto the sidewall of the etched structure.

3.4.1 Surface damage - Schottky diode characteristic

3.4.1.1 Theory

The transport mechanisms which determine the conduction properties of Schottky barriers under forward bias for an n-type semiconductor are shown schematically in figure 3.7, where ϕ_b is the height of the barrier measured from the metal Fermi energy level, V_d is the diffusion voltage or "band bending", and ξ is the energy difference between the conduction band and the semiconductor Fermi level; while the inverse processes occur under reverse bias. The basic mechanisms are:

- a) emission of electrons from the semiconductor over the top of the barrier into the metal,
- b) quantum-mechanical tunneling through the barrier,
- c) recombination in the space-charge (depletion) region, and
- d) recombination in the neutral region.

When process a) described above is the dominant transport mechanism in a Schottky diode, the diode can be considered as nearly ideal, $n \approx 1$ (see derivation below); while processes b), c) and d) cause departures from the ideal behaviour, $n \gg 1$; n is commonly known as the ideality factor.

Furthermore, there are two ways in which the electrons can be emitted over the Schottky barrier in mechanism a) described above. Before the electrons are emitted over the barrier into the metal, they must first be transported from the interior of the semiconductor to the interface. In traversing the depletion region of the semiconductor, their motion is governed by the usual mechanisms of diffusion and drift in the electric field of the barrier. When they arrive at the interface, their emission into the metal is controlled by the number of Bloch states in the metal which can communicate with states in the semiconductor. These two processes are effectively in series, and the current is determined predominantly by whichever causes the larger impediment to the flow of electrons. According to the diffusion theory of Wagner^{3.21} and Schottky et.al.^{3.22}, the first of these processes is the limiting factor whereas in the thermionic-emission theory of Bethe^{3.23}, the second is more important. However, in Roderick's analysis^{3.24} of Smith's experimental data^{3.25} on GaAs diodes, it was shown that the forward current in these diodes at room temperature is almost certainly limited by thermionic emission provided the forward bias is not too large. This conclusion was further confirmed by Gol'dberg et. al.^{3.26}. In addition, contributions to the electron transport across the GaAs

Schottky junction through recombination in the depletion region (process c) due to the short lifetime of the electrons, and tunnelling through the barrier (process b) because of their very small effective mass ($m^* = 0.07m$) seem to play significant roles in making the fabrication of ideal GaAs diodes ($n = 1$) very difficult; however, n of the order of 1.04 can generally be achieved^{3.27-3.34}. Furthermore, the effects of quantum-mechanical tunneling appear to be very sensitive in the reverse bias configuration when measuring the reverse leakage current, as will be shown in section 4.3.2.3.

Therefore, assuming the electron transport mechanism from GaAs into the metal is attributed almost entirely to thermionic emission, the current-voltage characteristic of a practical diode is given by^{3.38}:

$$I = I_0 \exp \{eV/nkT\} \{1 - \exp[-eV/kT]\} \quad (3.1)$$

$$\text{where } I_0 = A^{**}T^2 \exp \{-e\phi_b/kT\} \times \text{area} \quad (3.2)$$

where A^{**} is the Richardson constant modified to take into account of the effective mass, quantum-mechanical reflection and phonon scattering of the electrons ($8.6A.K^{-2}cm^{-2}$), T is the absolute temperature and n is the ideality factor; $n \geq 1$.

When $V > 3kT/e$, equation 3.1 approximates to:

$$I = I_0 \exp \{eV/nkT\} \quad (3.3)$$

A straight line results when $\ln I$ is plotted against V for small forward bias ($\approx 0.5V$), and the ideality factor n is calculated from the slope of the graph, see figure 3.8. If large values of n are calculated or $\ln I$ against V plots are non-linear, the diode is far from ideal probably due to the presence of a thick interfacial layer or to recombination in the depletion region via localised centres, traps. This measurement of the ideality factor from Schottky diodes as a quantitative study of the degree of damage induced on the semiconductor surface after dry etching have been used widely by a number of workers^{3.27-3.37}.

3.4.1.2 Experimental

The material configurations used for GaAs and $\text{Al}_{0.3}\text{Ga}_{0.7}\text{As}$ diode fabrication have been described in section 3.2.1. Ohmic contacts were prepared on the back surface of the wafers by alloying 100nm:20nm:50nm of Au₈₈Ge₁₂:Ni:Au in an Ar:H₂ 95:5 ambient at 325°C for 1 minute, which is the composition optimised for low temperature ohmic contacts formation^{3,39}. To avoid any surface oxide, the wafers were etched in NH₃:H₂O; 4:16 for 60s before evaporation. Normally, HCl:H₂O; 1:1 would have been used as a wet etch to remove the surface oxide, but in this case, since the HCl in the mixture would react with the Al in the $\text{Al}_{0.3}\text{Ga}_{0.7}\text{As}$ to produce AlCl₃, an alternative surface oxide etch was chosen. A piece of thin wire was also mounted in the middle of the wafers before evaporation to ensure a discontinuity so that the conductance of the ohmic contacts can be tested after annealing. The wafers were then scribed into 3 x 3 mm² chips. Six chips from each material were processed of which one was used as a control sample. The others were reactive ion etched in SiCl₄ for 30s at varying power densities from 0.08W/cm² to 0.44W/cm² at a chamber pressure of 12mT, volume flow rate 9sccm. To investigate the damage dependence on etch time, three samples from the GaAs wafer were reactive ion etched in SiCl₄ for 30s, 60s, 90s, and 120s with a power density of 0.44W/cm², 12mT pressure and a volume flow rate of 9sccm. The etching machine used has been described in section 2.6.2. For the AlGaAs material, the GaAs capped layer was left on the $\text{Al}_{0.3}\text{Ga}_{0.7}\text{As}$ for the samples which were subjected to dry etching; the GaAs cap on the control sample was removed in H₂O₂:NH₃; 40:1 for 2s, a selective GaAs to AlGaAs wet chemical etch with an etch rate of $\approx 1\mu\text{m}/\text{min}$. After etching, a single layer of 15% PMMA in chlorobenzene (185,000MW) $\approx 1\mu\text{m}$ thick was spun onto the chips at 5K rpm and baked at 180°C overnight. Windows of area 5 x 5 μm^2 in the resist were exposed with an electron beam at 0.25 μm spot size at 50kV in a 1.56 x 1.18 mm frame. After exposure, the exposed resist was developed in 1:1 MIBK:IPA for 60s at 23°C followed by a 30s rinse in IPA. Native oxides on all samples were removed by NH₃:H₂O; 4:16 for 60s followed by a 30s rinse in deionised water before diode evaporation. The Schottky diodes were formed by evaporating 60nm-Ti/50nm-Au and subsequently, lift off was performed in acetone. The I-V characteristics of the diodes were measured using an HP 4145A semiconductor parameter analyser.

However, a high density of oval defects were present on the $\text{Al}_{0.3}\text{Ga}_{0.7}\text{As}$ material. While the formation of these defects during the molecular beam epitaxial growth of GaAs and $\text{Al}_x\text{Ga}_{1-x}\text{As}$ is a well known effect^{3.40-3.44}, their origin still remain a controversial topic. The long oval axis of these defects all lie along the $\langle 1\bar{1}0 \rangle$ direction with densities ranging from $10^3 - 10^5 \text{ cm}^{-2}$. They are commonly proposed to result from spitting of globules of material from the group III (e.g. Ga) element effusion cells^{3.42-3.44} and there is increasing effort directed towards their reduction^{3.45-3.47}. The defect density of the present material was determined using the optical microscope and was measured to be approximately $8 \times 10^5 \text{ cm}^{-2}$. Therefore, the area of the openings in the resist was chosen to reduce the probability of fabricating the diodes onto these defects. It is also assumed that the resistance of the additional $\text{Al}_{0.3}\text{Ga}_{0.7}\text{As}/\text{GaAs}$ interface is negligibly small compared with the metal/ $\text{Al}_{0.3}\text{Ga}_{0.7}\text{As}$ interface so that the Schottky characteristics measured would be a valid assessment of the state of the metal/ $\text{Al}_{0.3}\text{Ga}_{0.7}\text{As}$ interface.

3.4.1.3 Results and discussion

Figure 3.9 shows a graph of ideality factor vs. power density for GaAs and $\text{Al}_{0.3}\text{Ga}_{0.7}\text{As}$ reactive ion etched in SiCl_4 at 12mT for 30s in a volume flow rate of 9sccm with power densities varying from 0.1 W/cm^2 to 0.44 W/cm^2 . The control GaAs and $\text{Al}_{0.3}\text{Ga}_{0.7}\text{As}$ samples exhibit ideality factor of values 1.04 and 1.14 respectively. The higher ideality factor measured for the $\text{Al}_{0.3}\text{Ga}_{0.7}\text{As}$ sample is attributed to the ease of oxidation of the Al and the quality of the MBE growth. Nonetheless, a valid comparison may be made since the state of the dry etched surfaces would be relative to that of the wet etched. In a recent damage study by Pearton et. al.^{3.48}, higher ideality factors have also been measured on both unetched and etched AlGaAs surfaces compared with GaAs surfaces. In this work, the n values measured for the etched GaAs and $\text{Al}_{0.3}\text{Ga}_{0.7}\text{As}$ surfaces show an increase from their unetched samples, this implies the state of the semiconductor surfaces has been deteriorated electrically after etching, probably from the introduction of interface traps. A monotonic increase in the measured n values towards higher power densities is observed, this may be a result of more energetic ion bombardment associated with higher power densities. It is worth noting that the

relative increase in the ideality factors for the etched $\text{Al}_{0.3}\text{Ga}_{0.7}\text{As}$ surfaces is higher than the etched GaAs surfaces, this is an indication of more degraded $\text{Al}_{0.3}\text{Ga}_{0.7}\text{As}$ than GaAs surfaces after etching. However, since Al is very easily oxidised, it is not entirely clear whether the result of more degraded $\text{Al}_{0.3}\text{Ga}_{0.7}\text{As}$ surface after etching is due to more damage caused during the etching process, or because of more susceptible surface reactions (e.g. oxygen uptake) from an equally deteriorated surface after etching. A similar trend is observed for both semiconductors producing a minimum n value at a power density of around $0.22\text{W}/\text{cm}^2$. A dramatic increase in the measured ideality factor is also evident at around $0.1\text{W}/\text{cm}^2$ power density. This seemed a surprising result in a low power density regime with a low level of ion bombardment. However, according to figure 3.1, this corresponds to a regime where no measurable etch depth resulted. Therefore, deposition appears to be a likely cause for the high ideality factors measured.

Figure 3.10 shows a graph of measured ideality factor as a function of etch time. The deteriorative effect of the damage layer appears to have saturated after 30s of etching. It is possible that this is a result of the simultaneous production and removal of the surface damage layer, since the substrate surface is being etched constantly. It is also worth noting that a similar effect was observed in some recent experiments using CH_4/H_2 as the etch gas^{3.79}. On the other hand, in an RIE study using $\text{CCl}_2\text{F}_2/\text{He}$ by Knoedler et. al.^{3.80}, they found that the surface damage increased with overetch time. However, their substrate configuration contained an AlAs etch stop layer, which was different from this work; and their investigation was concerned with the damage caused in the underlying GaAs after having reached the AlAs etch stop layer as a function of overetch time, rather than etch time. This data is significant in that while they observed an increase in GaAs surface damage with etch time without removal of the substrate surface (due to the AlAs etch stop layer), no such dependence is evident from this work with continuous removal of the substrate surface.

3.4.2 Low temperature integrated band-gap photoluminescence measurements

The optical performance of the unetched and reactive ion etched GaAs surfaces in SiCl_4 was investigated by low temperature integrated band-gap photoluminescence measurements.

3.4.2.1 Theory

Photoluminescence can be defined as the optical radiation emitted by a physical system resulting from excitation to a nonequilibrium state by irradiation with light. Three processes may be distinguished:

- a) creation of electron-hole pairs by absorption of the exciting light,
- b) radiative recombination of electron-hole pairs, and
- c) nonradiative recombination caused by centres such as deep traps, impurities and defects from the sample.

Figure 3.11a) shows the energy (E) vs. wavevector ($k=2\pi p/h$) diagram for the photoluminescence process for a perfect (i.e. without nonradiative recombination centres) direct band gap semiconductors such as GaAs, where p is the momentum and h Planck's constant. The electron-holes pairs are created by the absorption of a photon having energy $hf > E_g$, where E_g is the value of the forbidden energy gap, which is 2.24×10^{-19} J, or 1.4eV for GaAs. Recombination of the photo-excited electron-hole pairs then occur, emitting light with energy of the forbidden gap with maximum intensity. However, in the case where nonradiative recombination centres are present, which are normally deep states situated in the middle of the energy gap, some electron-holes pairs will still recombine with energy E_g but the output intensity will be decreased, since some of the radiation will be lost through the nonradiative deep centres. This situation is illustrated in figure 3.11b).

Clearly, b) and c) are competing processes in a damaged sample while process b) will be larger in an undamaged one. In integrated band-gap photoluminescence, it is the measurement of the difference in intensity of the resultant light emitted from processes b) and c) which gives an indication of the state of the semiconductor surface. This technique has been used by Namba et. al.^{3.49} and Kawabe et. al.^{3.40} to study the effect of rf sputter etching and ion milling by argon respectively on Si-doped GaAs with a He-Cd laser.

Since the exciting light is absorbed in creating electron-hole pairs, the greatest excitation of the sample is near the surface; the resulting carrier distribution is both inhomogeneous and not in equilibrium. In attempting to regain homogeneity and equilibrium, the excess carriers will diffuse away from the surface while being depleted by both radiative and nonradiative recombination processes. Therefore, most of the excitation of the semiconductor is restricted to a region within an absorption length of the illuminated surface; for the He-Ne laser employed in the present experiment, the absorption length in GaAs is 270nm.

The photoluminescence measurements are carried out at around 15K. The need for this low temperature is that in order to obtain information about the quantity of the nonradiative deep centres which might be present in the semiconductor, any electrons recombining in these states must not be re-ionised themselves. At temperatures much greater than 0K, the otherwise recombined electrons will be thermally liberated from all traps and defects, making the analysis insensitive to the presence of these centres.

3.4.2.2 Experimental

The GaAs used for this photoluminescence study was a $2 \times 10^{17} \text{cm}^{-3}$ Si-doped GaAs epitaxial layer of $1 \mu\text{m}$ on an n^+ substrate. In this experiment, four GaAs samples of area $4 \times 4 \text{mm}^2$ were prepared. Three of which were reactive ion etched in SiCl_4 using the etcher described in section 2.6.2 at a total pressure of 12mT, volume flow rate 9sccm for 30s with power densities 0.44W/cm^2 , 0.22W/cm^2 and 0.08W/cm^2 . The remaining unetched chip served as a control sample.

The photoluminescence equipment used was one which has been set up by the molecular beam epitaxy group at Glasgow University. A schematic diagram of the system is shown in figure 3.12. The sample is mounted on a nickel plated copper block which is fixed to a metal support rod using adhesive/acetone and the temperature is lowered from ambient down to 15K by a commercial refrigeration cryostat system. The laser power output is nominally 27mW at 6328\AA . Any infra

red radiation is blocked by the KG3 filter. The laser beam is chopped at 40Hz, a value which optimises the operating signal/noise conditions for the germanium detector. Mirrors M1, M2 and M3 are coated with dielectric giving 99.9% reflectivity at 45° angle of incidence and 6328Å wavelength. The laser beam is then directed towards the focussing lenses L1 and L2 by mirrors M1 and M2, which are fixed in position, before arriving at M3, which is adjustable over a small angle to allow the beam to be incident on a sample of minimal size 1mm². The beam diameter at the sample can be focussed to less than 0.5mm. Due to the transmission losses from the filter, mirrors and lenses, the peak power which reaches the sample is reduced to 15mW. In practice, the average incident power on the sample is further reduced to 7.5mW since the chopped beam has a mark/space ratio of 1:1. The output light from the sample is then focussed and directed through the vertical input slit of the monospectrometer. In all experiments, the scan rate and the range of wavelengths scanned have been kept constant at 500Å/min. and from 7500Å to 18,000Å respectively. The output of the germanium detector is detected by a lock-in phase sensitive detector and amplified before the spectrum is recorded on a chart recorder.

3.4.2.3 Results and discussion

Figure 3.13a) shows the photoluminescence spectrum for the unetched GaAs sample excited by the He-Ne laser at 15K. The main peak at 831nm is due to process b) described above through donor-acceptor and band to acceptor transitions; the small peak at 850nm is a phonon sideband of the main peak. The 820nm peak is due to excitons. The spectra of the GaAs samples reactive ion etched at power densities 0.44W/cm², 0.22W/cm² and 0.08W/cm² are shown in figure 3.13b) - d) respectively. It is evident that the intensity of the main peaks for all power densities have decreased from their original spectrum indicating a deterioration of the semiconductor surface optically after etching. A more useful graph of the normalised luminescence intensity to the unetched sample may be plotted against power densities and is shown in figure 3.14. A higher normalised PL intensity is observed at a power density of 0.22W/cm² compared with 0.44W/cm² implying less non-radiative recombination centres are introduced to the GaAs surface after etching at 0.22W/cm²; this is probably related to the lower ion energies associated with lower power densities. Very low luminescence resulted at

a power density of $0.08\text{W}/\text{cm}^2$ indicating a highly degraded semiconductor surface after etching. In this power regime, deposition is believed to occur, see figure 3.1. It is worth noting that these optical measurements correlate very well with the electrical Schottky characteristics observed in the previous section.

3.4.3 Raman scattering

Raman scattering was also used to evaluate the possible structural damage induced in GaAs after reactive ion etching. The experiments were carried out in collaboration with the low temperature group of University of Glasgow and details of the theory, experiment, and discussion of results can be found in Ch.6 of the Ph.D thesis of Morag Watt, 1989 and ref. 3.51-3.52. Therefore, only a brief account on part of the experimental results which verify the usefulness of this technique and correlation with other experimental measurements will be presented here.

The material used was a $2 \times 10^{17} \text{ cm}^{-3}$ Si-doped GaAs epitaxial layer of $1\mu\text{m}$ thick on an n^+ substrate. Similar to the photoluminescence experiment, four GaAs samples of area $4 \times 4 \text{ mm}^2$ were prepared. Three of which were reactive ion etched at a total pressure of 12mT, volume flow rate 9 sccm for 30s with power densities $0.44\text{W}/\text{cm}^2$ (100W), $0.22\text{W}/\text{cm}^2$ (50W) and $0.08\text{W}/\text{cm}^2$ (20W). The remaining unetched chip served as a control sample. These samples were studied with various laser lines from a Coherent krypton-ion laser in order to change the penetration depth of the light and therefore, probe different depths in the GaAs which allowed evaluation of the depth dependence of the damage.

The Raman spectrum of the GaAs (001) surface is well documented in the literature^{3.53,3.55}. The feature arises from the interaction between the electromagnetic field of the incident laser light and the variation in the crystal potential caused by the quantised lattice vibrations (phonons). The dominant features of the GaAs Raman spectrum are the longitudinal optical (LO) phonons and the transverse optical (TO) phonons which occur at 292 and 269 cm^{-1} respectively. The observable peaks for any given scattering geometry are determined by Raman group-theoretical selection rules. The selection rules for GaAs, in backscattering

geometry, show that only the LO phonons are allowed to scatter while the TO mode contribution is forbidden by symmetry^{3.55}. However, in the presence of damage or strain in the crystal, the selection rules are destroyed and as a result, the TO mode will appear^{3.56}. Therefore, the measurement of the variation in the TO mode intensity will give an indication of the degree of structural damage caused by RIE. This technique has been used by other workers to study the inflicted crystalline damage on GaAs surfaces after dry etching^{3.56-3.58} and ion implantation^{3.58-3.60}.

The Raman spectra of the unetched and etched GaAs samples excited from a light wavelength of 4825Å with a penetration depth of 350Å^{3.61} are shown in figure 3.15. It is clear that the selection rules are obeyed very well for the unetched control sample where scattering from the LO mode but no corresponding feature from the TO phonon is observed. The other etched samples show different behaviour in that the TO mode is present in each spectrum. This suggests that the etch process has disordered the crystal and relaxed the selection rules. The ratio of TO:LO intensities are compared for the etched samples giving a value of 0.3 for the sample etched at 0.44W/cm² (100W), 0.17 for the 0.22W/cm² (50W) sample and 0.40 for the 0.08W/cm² (20W) sample. While the sample reactive ion etched at 0.08W/cm² (20W) exhibits the highest TO:LO ratio suggesting a largely disordered crystal, it appears that this is the etch condition at which deposition was believed to occur (see sections 3.4.1.3 and 3.4.2.3) and indeed, the surface produced on this sample was particularly bad, being dull and rough, even to the naked eye. Therefore, it is highly possible that the enhanced TO:LO ratio observed in the spectrum of this sample arose less from the greater intrinsic damage inflicted into the crystal and more from the overall reduction in intensity of the allowed scatter, it is certain that the LO phonon intensity from this sample was far less than any of the other three samples. In the case of the other two samples, the 0.44W/cm² sample showed a larger TO:LO ratio than the 0.22W/cm² sample without degradation of the overall spectral intensity. This can be regarded as evidence that the 0.44W/cm² sample suffered more crystalline damage than the 0.22W/cm² sample. This result is significant in that it correlates very well with both Schottky diode and photoluminescence measurements conducted on similarly etched GaAs surfaces (sections 3.4.1.3 and 3.4.2.3). In order to acquire a quantitative estimate of the size of the damaged region, the Raman spectra of the samples were taken at different penetration depths by varying the light excitation wavelength. The Raman spectra of

the control, $0.22\text{W}/\text{cm}^2$ (50W) etched and $0.44\text{W}/\text{cm}^2$ (100W) etched samples recorded with an excitation wavelength of 5309\AA with penetration depth 650\AA are shown in figure 3.16. It is evident that a TO mode is observed for the $0.44\text{W}/\text{cm}^2$ sample while for the $0.22\text{W}/\text{cm}^2$ sample, it has disappeared. This change is indicative of crystalline damage that lies close to the surface of the material. As the penetration depth is increased, the scattering volume is increased and the contribution to the scattered signal from the surface region is reduced. It is worth noting that the Raman spectrum of the $0.44\text{W}/\text{cm}^2$ etched GaAs sample recorded with 6471\AA exciting light with a penetration depth of 1450\AA exhibited only an LO phonon with no evidence of a TO phonon suggesting that the contribution of the damage layer after reactive ion etching at $0.44\text{W}/\text{cm}^2$ is still significant up to a thickness scale of 650\AA but no longer so on a scale of 1450\AA .

3.4.4 X-ray photoelectron spectroscopy (XPS) analysis

In order to investigate the nature of the modified GaAs surface after etching, XPS analysis was carried out on both unetched and reactive ion etched GaAs in SiCl_4 .

3.4.4.1 Theory

XPS is one of the many important surface analytical techniques available and many reviews have been written^{3.62,3.63}. Essentially, in XPS, X-rays are used to eject electrons by raising each electronic energy level from its original value by the amount of the photon energy $h\nu$, while the number and kinetic energy of these photoemitted core level electrons are measured. The relevant energy conservation equation is:

$$h\nu + E_{\text{tot}}^i = E_{\text{kin}} + E_{\text{tot}}^f(k) \quad (3.4)$$

where E_{tot}^i is the total energy of the initial state, E_{kin} is the kinetic energy of the photoelectron, and $E_{\text{tot}}^f(k)$ is the total final energy of the system after ejection of the

photoelectron from the k th level. The binding energy of the photoelectron is defined as the energy required to remove it to infinity with a zero kinetic energy. In XPS measurements $E_B^V(k)$, the binding energy of an electron in the k th level referred to the local vacuum level, is defined as:

$$E_B^V(k) = E_{\text{tot}}^f - E_{\text{tot}}^i \quad (3.5)$$

giving

$$h\nu = E_{\text{kin}} + E_B^V(k) \quad (3.6)$$

Generally, in the study of semiconductors, binding energies are expressed relative to the Fermi level. The exact binding energy for an electron in a given element depends on the chemical environment of that element. This is because in a given core level, the energy of an electron in this core state is determined by the Coulomb interaction with the other electrons and the attractive potential of the nuclei, any change in the chemical environment of the element will involve a spatial redistribution of the valence electron charges of this atom and the creation of a different potential will be seen by a core electron. This redistribution affects the potential of the core electrons and results in a change in their binding energies. Therefore, in addition to the identification of the particular elemental species associated with certain electron binding energies, analysis of the exact peak positions can indicate the chemical binding state of these elements. This technique has been used by a number of workers to study the chemical binding state on the GaAs surface after ion implantation using Si^{2+} ions^{3.64} and reactive ion etching employing a variety of gases^{3.65-3.69}. Since the X-rays only have a penetration depth of $\approx 5\text{nm}$, XPS is a purely surface sensitive technique. A variant from XPS is angle resolved XPS in which the angle of the detector of the output electrons is changed whereby the depth of the modified surface may be probed^{3.69,3.70,3.35}.

3.4.4.2 Experimental

The material used for the XPS study was a $2 \times 10^{17}\text{cm}^{-3}$ Si-doped GaAs

layer of 1 μ m thick grown on an n⁺ substrate by molecular beam epitaxy. Due to the time slots available on the XPS equipment, it was only possible to carry out measurements on two samples. Therefore, two chips of area 5 x 5 mm² were prepared. One was reactive ion etched in SiCl₄ at a power density of 0.44W/cm², 12mT total pressure, 9sccm volume flow rate for 30s, while the other served as a control sample.

The actual XPS experiment was carried out in collaboration with the Department of Physics of the University of Strathclyde. The experimental equipment is similar to the one used at Harwell laboratory, see section 5.4.2.1, except that the output data was taken as analogue signals and was plotted simultaneously on a graph plotter instead of being digitally recorded in a computer. The kinetic energies for the recorded spectra were scanned from 1485eV to 1188eV.

3.4.4.3 Results and discussion

The XPS spectra taken from the unetched and etched GaAs samples are shown in figure 3.17a) and b) respectively. The peaks at binding energies 19.5eV and 41.3eV from the unetched GaAs sample are due to signals from Ga(3d) and As(3d) and are indicative of the presence of Ga to As bonds^{3.81,82}. An additional peak in the As(3d) signal at binding energy 44.2eV is observed on the GaAs surface which has been reactive ion etched. This peak is commonly resolved as arsenic - oxygen bonding^{3.65-69,83}, the observation of this peak is a result of the presence of As₂O₃ on the substrate surface.

The ratio of the concentration of Ga/As may be estimated using the approximation that the area under Ga(3d) / area under As(3d) is proportional to the concentration of Ga / concentration of As^{3.71}. In this simple analysis, it is assumed that the photoelectron peaks have about the same energy, their photopeak efficiencies and photoelectric cross-sections are about equal. Under this assumption, the area under the Ga(3d) signal / the area under the As(3d) signal for the unetched sample was measured to be 0.98 while for the etched sample, it was 1.14. This suggests that the reactive ion etched GaAs sample has become deficient

in As after etching. While this is a rather crude analysis compared with the one carried out in section 5.4.2.2, it still appears that both As_2O_3 and an As deficiency are present for the reactive ion etched GaAs sample. Oxygen uptake and Ga-rich surfaces after the reactive ion etching of GaAs employing other gases have also been observed by various workers^{3.67-3.70} (also see section 5.4.2.2). In the present work, the reactant products in the reactive ion etching of GaAs in SiCl_4 are GaCl_x and AsCl_x , and because of the higher vapour pressures associated with AsCl_x products, it is likely that they will vapourise faster than the GaCl_x products, leaving behind a Ga-rich surface. However, the importance of ion bombardment in increasing the production and/or desorption rate of the etch products, as has been demonstrated by McNevin et. al.^{3.72} and Balooch et. al.^{3.13}, must not be overlooked. Moreover, it is possible that the diode characteristics measured in section 3.4.1 is a result of this defective layer containing As vacancies and As_2O_3 , since it has been reported that As vacancies in GaAs behave as donors^{3.73,74} and this type of donor defect layer has been suggested to cause enhancement in the tunneling transport across GaAs Schottky diodes thus increasing the ideality factors and decreasing the barrier height measured after rf sputter etching^{3.37} and ion sputtering^{3.27,29,35}. Furthermore, Robinson^{3.75} concluded that the larger ideality factor resulting from the interfacial oxide in a metal/semiconductor junction is a consequence of the creation of interface states coincident with the formation of the native oxide, which in turn cause an interface charge which increases the probability of conduction by tunneling. However, the possibility of creation of other defects (e.g. As and Ga antisites, interstitials and complexes) cannot be ruled out. Since the XPS data suggests the existence of As vacancies and the electrical properties suggest the presence of a donor layer, it may be concluded that As vacancies dominate the damage layer. This damaged layer can behave as traps or strain thus leading to the low output of luminescence and the presence of the symmetry forbidden TO mode in Raman scattering observed for the etched surfaces.

3.5 Sidewall damage

A novel characterisation technique was developed in order to estimate the amount of damage induced on the sidewall of etched structures. This is possible by constructing a Schottky diode directly onto the etched sidewall and measuring its ideality factor.

3.5.1 Development of the fabrication of sidewall Schottky diode

3.5.1.1 Experimental

Material and fabrication outline

The starting material was a $2 \times 10^{17} \text{cm}^{-3}$ Si-doped GaAs epitaxial layer of $0.5 \mu\text{m}$ thick grown by molecular beam epitaxy on a semi-insulating GaAs substrate. The wafer was diced into $5 \times 5 \text{ mm}^2$ chips and nine (3×3) device patterns were defined by electron beam lithography using the converted Philips PSEM 500 scanning electron microscope, see section 2.2.2. The lithographic steps consists of three levels, the design of which are shown in figures 3.18a) - c). First, the sample was cleaned for 30s in trichloroethylene for 30s, then rinsed in acetone for 30s, followed by isopropanol alcohol (IPA) for 30s. Ohmic contact and alignment marks were prepared by alloying Au-Ge-Ni-Au at 325°C , figure 3.18a). The next stage defines the mask for etching a ridge into the semi-insulating substrate, figure 3.18b). Both polymeric high resolution negative resist and metal (NiCr) were tried as dry etch masks with NiCr rendering better results, see section 3.5.1.2. Subsequently, Schottky diode was fabricated by evaporating $60\text{nm}:60\text{nm}$ Ti:Au onto one side of the ridge. The third level defines an opening to provide access to the ohmic contact for probing and lines for isolation amongst the devices, see figure 3.18c).

Ohmic and alignment level

Single layer 15% PMMA in chlorobenzene (185,000 MW) $\approx 1 \mu\text{m}$ thick was spun onto the chip and baked at 180°C overnight. The ohmic and alignment pattern was exposed with a $0.125 \mu\text{m}$ spot at 50kV in a $1.56 \times 1.18 \text{ mm}$ frame. After exposure, the resist was developed in 1:1 MIBK:IPA for 60s at 23°C for 60s followed by a 30s rinse in IPA. Ohmic contacts were made by evaporating $100\text{nm}:20\text{nm}:50\text{nm}$ of $\text{Au}_{88}\text{Ge}_{12}:\text{Ni}:\text{Au}$ on the exposed areas and annealed at 325°C for in an $\text{Ar}:\text{H}_2$ 95:5 ambient for 60s. Lift off was performed in acetone. See figure 3.19a).

Masking level

Two types of etch masks were tried, namely: a polymeric high resolution negative resist and metal (NiCr) mask. In the case of polymeric resist, 15% HRN of 0.25 μm thick was spun onto the sample and baked for 20 mins.. The masking area was exposed with a 0.125 μm spot size at 50kV in a 1.56 x 1.18 mm frame. After exposure, the resist was developed in MIBK for 30s at 23°C, then rinsed twice in IPA for 30s. The sample was then ready for dry etching. In the case of metal mask, more processing steps were required. To open the masking area for etching, 15% PMMA was spun onto the sample, baked, exposed and developed in the same way as in the ohmic level with the exposed pattern being the masking level. After development, NiCr of 80nm thick was evaporated onto the exposed area and lift off was performed in acetone. The sample was then ready for dry or wet etching, see figure 3.19b).

Sidewall Schottky diode

Since the HRN resist is an insulator, the sample processed with this mask would be ready for the fabrication of sidewall Schottky diode after etching. On the other hand, if NiCr was used as dry etch mask, its removal was required after etching and was carried out using HCl:H₂O 4:1 for 2 minutes. Subsequently, evaporation of 150nm of SiO₂ at 60° to the sample was necessary in order to avoid contribution of conductance from the surface of the epitaxial layer, see figure 3.19c). In both cases, the Schottky diode was fabricated by evaporating 60nm:60nm Ti: Au: at 60° to the sample, see figure 3.19d). Before diode fabrication, the samples were subjected to HCl:H₂O 1:1 for 30s, a chemical etch to remove surface oxide, followed by a rinse in deionised water.

Opening of ohmic contacts and device isolation level

In order to facilitate probing to the devices, it was necessary to make access to the ohmic contacts and to isolate the devices from one another. To do this, 18% PMMA of 2 μm thick was spun onto the samples and baked overnight, the thicker resist used was to avoid subsequent wet etch attack. The area around the ohmic contact and the isolation lines were exposed with a 0.125 μm spot size at 50kV in a 1.56 x 1.18 mm frame. After exposure, the resist was developed in

MIBK:IPA 1:1 for 60s at 23°C. After development, the gold which would be exposed was removed in a gold etch, iodine/potassium iodide (I₂/KI) 1:1 by weight for 50s. If HRN resist was used as a dry etch mask, the Ti which was underneath the gold would be removed in HF for 10s in a cold bath, an O₂ plasma would then be used to strip the HRN for half an hour and the 18% PMMA would be removed in acetone. In the case of metal mask, both Ti and SiO₂ would be removed in HF:H₂O 3:1 in a cold bath for 50s and the 18% PMMA in acetone. This process along with the final diode structure is illustrated in figure 3.19e). Since the result of the wet etches which contain HF rely largely upon the resistancy of the 18% PMMA resist, they were carried out in a cold bath as the resist is more resistant to wet etch attack at lower temperatures, see section 3.5.1.2 below.

Alignment

The alignment scans for aligning to the registration marks (in the first level) are shown in figure 3.20a) and b). The squares are used for coarse alignment while the outline of the "T" shape is used for fine alignment. The scans are scanned at a rate of 2μs per pixel and the alignment was carried out by adjusting the X-Y varymag, the stage rotation and the beam shifters.

Etching

The gas used for reactive ion etching was SiCl₄ with 9sccm volume flow rate, 0.44W/cm² power density, 12mT total pressure for 3 mins.. The chemical etch used for wet etching was HCl:H₂O₂ in the ratio 20:1 for 16s.

3.5.1.2 Preliminary data

Initially, the sidewall Schottky diodes were fabricated using HRN as dry etch masks and their ideality factors were measured to be around 1.153. However, there were some problems associated with this fabrication method. Detail observation of the devices using both optical and scanning electron microscopes revealed the shrinkage of the HRN resist after etching (see also section 4.3.5.2) thus exposing ≈ 100nm of unetched GaAs on the top surface of the etched structure

before diode evaporation, see SEM 3.1. This implies the diode characteristics are due to both the 100nm of unetched surface and 500nm of the etched sidewall. Alternatively, a metal mask can be used for dry etching. Therefore, another sample was processed using NiCr as the dry etch mask and very satisfactory etching resulted producing vertical sidewalls and a smooth etched surface with no problem of mask shrinkage, see SEM 3.2. After the removal of NiCr in HCl:H₂O 4:1 for 2 mins., SiO₂ of 150nm thick was evaporated at 60° to the sample in order to insulate the top conducting GaAs surface. The effect of shadowing after evaporation is shown in SEM 3.3. Subsequently, Ti/Au is evaporated at 60° to the other side of the sample, see SEM 3.4. In practice, the shadowing effect from the previous layer of SiO₂ can cause a discontinuity in the Ti/Au layer as shown in SEM 3.5. In this case, an additional evaporation of ≈ 50nm of Au is needed to ensure good contact. In the final step of wet etching for the removal of Au, Ti, and SiO₂, the sample was scribed into 3 chips. One was used for wet etching at room temperature and the ideality factor measured for the sidewall diodes on this chip were 2.471. However, further examination of the sample in the scanning electron microscope revealed holes on the Ti/Au layer, see SEM 3.6. This is believed to be due to wet etch attack from the HF mixture during the removal of Ti and SiO₂ and may account for the high ideality factor measured. Therefore, the remaining chips were wet etched at low temperature ≈ 3°C and the final surface did not appear to have been attacked, see SEM 3.7, and the ideality factor was measured to be 1.827.

Figure 3.21 shows the I-V characteristics of the sidewall diodes fabricated using both HRN and NiCr as dry etch masks. In this case, the NiCr masked sample was wet etched at 3°C. It is evident that more current flows through the diode fabricated using HRN compared with metal mask. In particular, at a forward bias of 3V, the surface current was measured to equal half the sidewall current. The graph of ln I vs. V for the same samples is shown in figure 3.22 giving ideality factors of 1.152 for the HRN masked and 1.827 for the NiCr masked samples. It is likely that the higher current and the lower ideality factor measured for the HRN masked sample are due to contributions from both the sidewall and part of the unetched top GaAs surface as a consequence of the shrinkage of the resist after etching and therefore, the NiCr masked sample which was wet etched at low temperature offers a more valid result.

3.5.2 Effect of an hydrochloric acid (HCl) boil

There is evidence that by boiling a sample patterned with quantum dots which have been fabricated with reactive ion etching using SiCl_4 in similar etching conditions as those considered in this work in concentrated HCl, a reduction in dot size is observed^{3,76}. Therefore, it appeared that the effect of the HCl boil initiated the removal of some material from around the etched dot. To investigate whether this would have any effect on the characteristics of the diodes, two reactive ion etched GaAs samples were prepared for both surface and sidewall Schottky diode fabrication. After etching, both samples were boiled in concentrated HCl for half an hour before diode evaporation.

3.5.3 Results and discussion

A summary of the ideality factors measured for both surface and sidewall Schottky diodes having been treated by a) wet etch in $\text{HCl}:\text{H}_2\text{O}_2$ 20:1; b) reactive ion etch in SiCl_4 at $0.44\text{W}/\text{cm}^2$, 12mT; c) reactive ion etch in SiCl_4 at $0.44\text{W}/\text{cm}^2$, 12mT, with a 30mins. boil in concentrated HCl; is shown in figure 3.23. As expected, both wet etched samples show very low n values at around 1.05 implying very little appreciable damage is caused. The process of reactive ion etching increases the n value of the surface diode to 1.172 and that of the sidewall diode to 1.54. While this suggests that a higher degree of modification to the GaAs etched sidewall is produced compared with the etched surface after reactive ion etching in SiCl_4 , it is not possible to conclude whether the larger degradation is due to a thicker sidewall damaged layer or a more severely damaged one. Nevertheless, this seemed a rather surprising result since in reactive ion etching, the ions produced in the plasma are accelerated directionally towards the substrate surface and therefore, the surface exposed to this directional physical energetic bombardment is expected to be more susceptible to the occurrence of physical damage. However, it is also possible for damage to be produced by the chemical component of etching, for example, a more volatile etch product may vaporise faster than a less volatile one thus leaving behind a stoichiometric surface after etching. In addition, the final vaporisibility of the products may be affected by their desorption rate, which in turn is related to the degree of ion bombardment. From the present experimental data, it is inadequate to pinpoint the nature of this damage layer. Additional analytical

techniques such as XPS (see sections 3.4.4 and 5.4.2) and transmission electron microscopy (TEM) (see section 6.3) are needed to reveal more of the physical nature of the damaged layer. Nonetheless, it appears that its deteriorative effect is more prominent on the sidewall than on the surface. This may be explained by the fact that during etching, the material on the substrate (probably damaged) surface is constantly being removed by ions and reactive radicals and therefore, whatever damage is being induced is also being removed at the same time, see section 3.4.1.3. On the other hand, although the sidewall surface is not exposed to the directional bombardment of the ions, because it is not being etched constantly, any damage caused by the bombardment of ricocheting atoms or the chemical component of etching will remain on the sidewall and probably increase with time (see section 5.3.5.2). Moreover, the structure of the sidewall may also be very susceptible to redeposition effects^{3,84-86} from the bottom surface, which may contribute to the modified layer observed. At this point, it is worth mentioning that the larger damage observed on the sidewalls in this section could be a result of the sidewall damage dependence on etch time, (evidence of which can be found in section 5.3.5.2), since the sidewall structure was etched for 3 mins. and only 30s for the surface. The effect of the concentrated HCl boil after etching on the ideality factors measured are also shown in figure 3.23. The n values for both diodes were measured to have decreased from their values after dry etching giving 1.11 for the surface and 1.20 for the sidewall diodes. This implies the state of the GaAs has been recovered to some extent after the acid boil. From the previous evidence of a reduction in dots sizes measured after the acid boil, see section 3.5.2, it may appear that some material has been removed, but no further information as to the nature of the removed material can be obtained from this experiment. However, it may be speculated that if Ga-rich surface and sidewalls were present after RIE, which is evident both from the XPS data on the reactive ion etched surface (see section 3.4.4.3), and the data suggested from TEM analysis on the etched sidewall (see section 6.3.3.1), these Ga-rich surfaces and sidewalls may have reacted with the HCl producing gallium chloride ions, hence giving a better GaAs surface. It is also worth noting that a larger decrease in n value is observed for the sidewall diode compared with the surface, which may be indicative of a more chemically damaged sidewall.

3.6 Conclusions

- 1) The etch rates and sidewall profile dependence on power density and gas pressure in the RIE of both GaAs and $\text{Al}_{0.3}\text{Ga}_{0.7}\text{As}$ using SiCl_4 were investigated. Results suggest the presence of a low level of O_2 in the etcher during etching and the importance of ion bombardment in the etch mechanism.
- 2) The etch rate was observed to increase with flow rate in the RIE of GaAs in SiCl_4 . Comparison of theoretical and experimental calculation in a microscopic level indicates that the standard etch conditions operate under a Cl deficient state and as a result, the less chlorinated species GaCl_2 and GaCl and possibly As may be expected.
- 3) The ideality factors of both etched GaAs and $\text{Al}_{0.3}\text{Ga}_{0.7}\text{As}$ surfaces were observed to increase with power densities implying more interface traps are introduced at higher power densities. In addition, more degraded $\text{Al}_{0.3}\text{Ga}_{0.7}\text{As}$ surfaces were evident before and after etching.
- 4) While the ideality factors of etched GaAs surfaces in this work in which the substrate surface is constantly being etched did not exhibit dependence on etch time, surface damage dependence on overetch time was observed by others^{3,80} with an etch stop layer. See no.8).
- 5) The output photoluminescence intensity decreases with power density increase implying more non-radiative recombination centres are introduced after etching with higher power densities. This data is consistent with the electrical measurements conducted on the etched surfaces.
- 6) More structural damage is also evident from the emergence of the TO phonon mode in Raman scattering measurements at higher etch power densities consistent with previous electrical and optical measurements and at a power density of $0.44\text{W}/\text{cm}^2$, the thickness of the damage layer appear to be significant up to a thickness scale of 650\AA but no longer so on a scale of 1450\AA .
- 7) XPS data suggests that the damage layer contains As vacancies and As_2O_3 . Such a surface layer can contribute to the behaviour of a charged layer, traps, or

strain which may explain the electrical and optical characteristics observed on the etched surfaces.

8) A novel process for fabricating sidewall Schottky diode was developed. Comparison of sidewall and surface diode characteristics indicate that more damage is induced on the sidewall of the etched structures. However, since the surface damage has been found to saturate with etch time (no.4)) and the sidewall damage dependent on etch time (Ch.5), the more damaged sidewall could be a manifestation of etch time dependence.

3.7 References

- 3.1) S.Thoms, S.P.Beaumont, C.D.W.Wilkinson, J.Frost and C.R.Stanley; *Microcircuit Engineering 1986*, edited by H.W.Lehmann and Ch. Bleicker (North-Holland, Amsterdam, 1986), p.249
- 3.2) M.Sato and H.Nakamura; *J.Vac.Sci.Technol.* **20(2)** p.186, 1982
- 3.3) H.Tamura and H.Kurihara; *Jpn. J. of Appl. Phys.* **23 (9)** p.L731, 1984
- 3.4) C.M.Knoedler and T.F.Kuech; *J.Vac.Sci.Technol.* **B4(5)** p.1233, 1986
- 3.5) H.Yamada, H.Ito and H.Inaba; *J.Vac.Sci.Technol.* **B3(3)** p.884, 1985
- 3.6) A.Scherer, H.G.Craighead and E.D.Beebe; *J.Vac.Sci.Technol.* **B5(6)** p.1599, 1987
- 3.7) S.S.Cooperman, H.K.Choi, H.H.Sawin and D.F.Kolesar; *J.Vac.Sci.Technol.* **B7(1)** p.41, 1989
- 3.8) H.Nagasaka, H.Okano and N.Motegi; *Proc. Symp. Dry Process*, p.79, 1982
- 3.9) K.Hirosaka, T.Mimura and K.Joshin; *Jpn. J. of Appl. Phys.* **20(11)** p.L847, 1981
- 3.10) K.Asakawa and S.Sugata; *J.Vac.Sci.Technol.* **B3(1)** p.402, 1985
- 3.11) M.Uchida, S.Ishikawa, N.Takado and K.Asakawa; *IEEE J. of Quantum Electronics*, **24(11)** p.2170, 1988
- 3.12) M.D.Rowe, 5th Int. Conf. on Ion and Plasma Assisted Techniques (IPAT), p.87, 1985
- 3.13) M.Balooch, D.R.Olander and W.J.Siekhaus; *J.Vac.Sci.Technol.* **B4(4)** p.794, 1986
- 3.14) S.C.McNevin, internal report of AT&T Bell Lab., Murray Hill, New Jersey.
- 3.15) G.J.Sonek, L.J.Zhong, E.D.Wolf and J.M.Ballantyne; *J of Lightwave Technol.* **LT-3(5)** p.1147, 1985
- 3.16) S.Thoms, I.McIntyre, S.P.Beaumont, M.Al-Mudares, R.Cheung and C.D.W.Wilkinson; *J.Vac.Sci.Technol.* **B6(1)** p.127, 1988
- 3.17) S.Salimian and C.B.Cooper III; *J. Electrochem. Soc.* **136(8)** p.2420, 1989
- 3.18) H. Kinoshita, T.Ishida and K.Kaminishi; *Appl. Phys. Letts.* **49(4)** p.204, 1986
- 3.19) K.Asakawa and S.Sugata; *J.Vac.Sci.Technol.* **A4(3)** p.677, 1986
- 3.20) J.A.Skidmore, L.A.Coldren, E.L.Hu, J.L.Merz and K.Asakawa; *J.Vac.Sci.Technol.* **B6(6)** p.1885, 1988
- 3.21) C.Wagner; *Phys. Z.* **32** p.641, 1931
- 3.22) W.Schottky and E.Spenke; *Phys. Z.* **113** p.367, 1939
- 3.23) H.A.Bethe; M.I.T. Radiation Lab. Report, 1942

- 3.24) E.H.Roderick; J. Phys. D, **5** p.1920, 1972
- 3.25) B.L.Smith; Ph.D Thesis, Manchester University, 1969
- 3.26) Y.A.Gol'dberg, D.N.Nasledov and B.V.Tsarenkov; Soviet Phys. Semicond. **9** p.337, 1975
- 3.27) C.S.Wu, D.M.Scott, W.X.Chen and S.S.Lau; J. Electrochem. Soc. **132(4)** p.918, 1985
- 3.28) Y.X.Wang and P.H.Holloway; J.Vac.Sci.Technol. **A2(2)** p.567, 1984
- 3.29) P.Kwan, K.N.Bhat, J.M.Borrego and S.K.Ghandhi; Solid State Electronics, **26(2)** p.125, 1983
- 3.30) S.W.Pang, M.W.Geis, N.N.Efremow and G.A.Lincoln; J.Vac.Sci.Technol. **B3(1)** p.398, 1985
- 3.31) S.W.Pang, G.A.Lincoln, R.W.McClelland, P.D.DeGraff, M.W.Geis and W.J.Piacentini; J.Vac.Sci.Technol. **B1(4)** p.1334, 1983
- 3.32) S.W.Pang; J. Electrochem. Soc. **133(4)** p.784, 1986
- 3.33) D.E.Aspnes and A.Heller; J.Vac.Sci.Technol. **B1(3)** p.602, 1983
- 3.34) R.Cheung, S.Thoms, S.P.Beaumont, G.Doughty, V.Law and C.D.W.Wilkinson, Electron. Letts. **23** p.857, 1987
- 3.35) Y.X.Wang and P.H.Holloway; J.Vac.Sci.Technol. **B2(4)** p.613, 1984
- 3.36) S.Ashok; Int. Symp. on VLSI Technol. Systems and Applications, Proc. of Technical Papers, p.102, 1985
- 3.37) K.Yamasaki, K.Asai, K.Shimada and T.Makimura; J. Electrochem. Soc. **129(12)** p.2760, 1982
- 3.38) E.H.Roderick; Metals-semiconductor contacts, Clarendon Press, Oxford, 1980
- 3.39) W.Patrick, W.S.Mackie, S.P.Beaumont and C.D.W.Wilkinson; Appl. Phys. Letts. **48** p.986, 1986
- 3.40) F.Alexandre, L.Goldstein, G.Leroux, M.C.Joncour, H.Thibierge and E.V.K.Rao; J.Vac.Sci.Technol. **B3(4)** p.950, 1985
- 3.41) A.C.Papadopoulo, F.Alexandre and J.F.Bresse; Appl. Phys. Letts. **52(3)** p.224, 1988
- 3.42) R.A.Stall, J.Zilko, V.Swaminathan and N.Schumaker; J.Vac.Sci.Technol. **B3(2)** p.524, 1985
- 3.43) S.Matteson and H.D.Shih; Appl. Phys. Letts. **48(1)** p.47, 1986
- 3.44) C.T.Lee and Y.C.Chou; J. of Crystal Growth, **91** p.169, 1988
- 3.45) C.E.C.Wood, L.Rathbun, H.Ohno and D.DeSimone; J. of Crystal Growth, **51** p.299, 1981

- 3.46) T.J.Mattord, V.P.Kesan, D.P.Neikirk and B.G.Streetman; *J.Vac.Sci.Technol.* **B7(2)** p.214, 1989
- 3.47) D.G.Schlom, W.S.Lee, T.Ma and J.S.Harris,Jr.; *J.Vac.Sci.Technol.* **B7(2)** p.296, 1989
- 3.48) S.J.Pearton, U.K.Chakrabarti and W.S.Hobson; *J. Appl. Phys.* **66(5)** p.2061, 1989
- 3.49) S.Namba, M.Kawabe, N.Kanzaki and K.Masuda; *J.Vac.Sci.Technol.* **12(6)** p.1348, 1975
- 3.50) M.Kawabe, N.Kanzaki, K.Masuda and S.Namba; *Appl. Optics*, **17(16)** p.2556, 1978
- 3.51) M.Watt, C.M.Sotomayer-Torres, R.Cheung, C.D.W.Wilkinson, H.E.G.Arnot and S.P.Beaumont; *Superlattices and Microstructures*, **4(2)** p.243, 1988
- 3.52) M.Watt, C.M.Sotomayer-Torres, R.Cheung, C.D.W.Wilkinson, H.E.G.Arnot and S.P.Beaumont; *J. of Modern Optics*, **35(3)** p.365, 1988
- 3.53) M.Holtz, R.Zallen, O.Brafman and S.Matteson; *Phys. Rev.* **B37** p.4609, 1988
- 3.54) G.Abstreiter, E.Bauser, A.Fischer and K.Ploog; *Appl. Phys.* **16** p.345, 1978
- 3.55) F.H.Pollak and R.Tsu; *Proceedings of SPIE - The Int. Soc. for Optical Eng. 'Spectroscopic Characterisation Techniques for Semiconductor Technology'*, **452** p.26, 1983
- 3.56) S.Semura, H.Saitoh and K.Asakawa; *J. Appl. Phys.* **55(8)** p.3131, 1984
- 3.57) D.Kirillov, C.B.Cooper III and R.A.Powell; *J.Vac.Sci.Technol.* **B4(6)** p.1316, 1986
- 3.58) J.Wagner and Ch.Hoffman; *Appl. Phys. Letts.* **50** p.682, 1987
- 3.59) K.K.Tiong, P.M.Amirtharaj, F.H.Pollak and D.E.Aspnes; *Appl. Phys. Letts.* **44(1)** p.122, 1984
- 3.60) R.Ashokan, K.P.Jain, H.S.Mavi and M.Balkanski; *J. Appl. Phys.* **60(6)** p.1985, 1986
- 3.61) D.E.Aspnes and A.A.Studna; *Phys. Rev. B*, **279** p.85, 1983
- 3.62) K.Siegbahn, C.Nordling, A.Fahlman, et. al.; in *Atomic, Molecular and Solid State Structure Studied by Means of Electron Spectroscopy, ESCA*, Almquist and Wiksell Boktryckeri AB., Uppsala, 1967
- 3.63) 'Electron Spectroscopy', edited by C.R.Brundle and A.D.Baker (Academic,

New York) Vol.4, 1981

- 3.64) Z.H.Lu, A.Azelmad, Y.Trudeau and A.Yelon; *Appl. Phys. Letts.* **55(9)** p.846, 1989
- 3.65) S.Semura and H.Saitoh; *J.Vac.Sci.Technol.* **A2(2)** p.474, 1984
- 3.66) N. Vodjdani and P.Parrens; *J.Vac.Sci.Technol.* **B5(6)** p.1591, 1987
- 3.67) K.L.Seaward, N.J.Moll, D.J.Coulman and W.F.Stickle; *J. Appl. Phys.* **61(6)** p.2358, 1987
- 3.68) R.Cheung, Y.H.Lee, K.Y.Lee, T.P.Smith III, D.P.Kern, S.P.Beaumont and C.D.W.Wilkinson; *J.Vac.Sci.Technol.* **B7(6)** p.1462, 1989
- 3.69) S.J.Pearton, M.J.Vasile, K.S.Jones, K.T.Short, E.Lane, T.R.Fullowan, A.E.Von Neida and N.M.Haegel; *J. Appl. Phys.* **65(3)** p.1281, 1989
- 3.70) N.Yabumoto and M.Oshima; *J. Electrochem. Soc.* **132(9)** p.2224, 1985
- 3.71) 'Fundamentals of Surface and Thin Film Analysis', L.C.Feldman and J.W.Mayer, North-Holland, 1986
- 3.72) S.C.McNevin and G.E.Becker; *J. Appl. Phys.* **58(12)** p.4670, 1985
- 3.73) S.Y.Chiang and G.L.Pearson; *J. Appl. Phys.* **46** p.2986, 1975
- 3.74) M.Jaros and S.Brand; *Phys. Rev. B*, **14** p.4494, 1976
- 3.75) G.Y.Robinson; in 'The Physics and Chemistry of III-V Semiconductor Interfaces', edited by C.W.Wilmsen, Plenum, New York, 1983
- 3.76) H.E.G.Arnot; Private Communication, Glasgow University
- 3.77) J.D.Chinn and E.D.Wolf; *J.Vac.Sci.Technol.* **B3(1)** p.410, 1985
- 3.78) K.Suzuki, S.Okudaira and I.Kanomata; *J. Electrochem. Soc.* **126(6)** p.1024, 1979
- 3.79) M.A.Foad; Private Communication, Glasgow University
- 3.80) C.M.Knoedler, L.Osterling and H.Shtrikman; *J.Vac.Sci.Technol.* **B6** p.1573, 1988
- 3.81) C.R.Brundle and D.Seybold; *J.Vac.Sci.Technol.* **16** p.1186, 1979
- 3.82) G.Leonhardt, A.Berndtsson, J.Hedman, M.Klasson, R.Nilsson and C.Nordling; *Phys. Status Solidi* **60** p.241, 1973
- 3.83) M.K.Bahl, R.D.Woodall, R.L.Watson and K.J.Irgolic; *J. Chem. Phys.* **64** p.1210, 1976
- 3.84) H.W.Lehmann, L.Krausbauer and R.Widmer; *J.Vac.Sci.Technol.* **14(1)** p.281, 1977
- 3.85) P.G.Glöersen; *J.Vac.Sci.Technol.* **12** p.28, 1975
- 2.86) P.G.Glöersen; *Sol. State Technol.* **19(4)** p.68, 1976

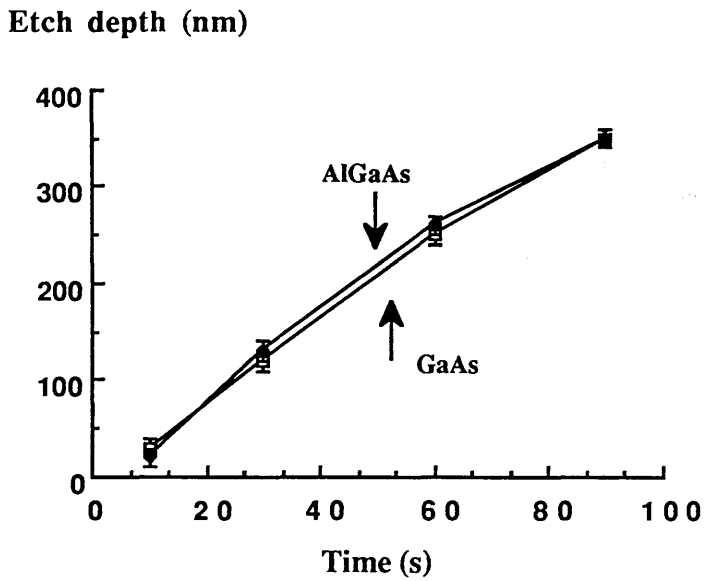
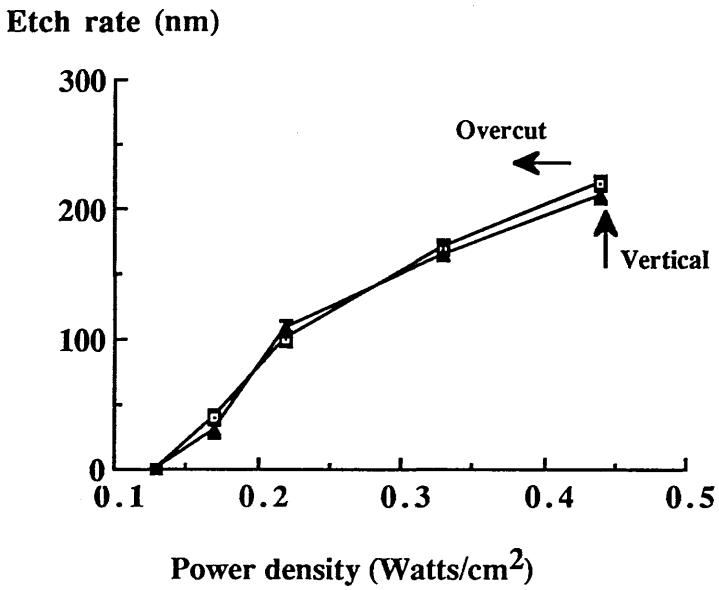


Figure 3.1 Graph of etch depth vs. time for GaAs and $\text{Al}_{0.3}\text{Ga}_{0.7}\text{As}$ reactive ion etched in SiCl_4 at power density $0.44\text{W}/\text{cm}^2$ 12mT pressure



- Etch rate of GaAs
- ▲— Etch rate of Al_{0.3}Ga_{0.7}As

Figure 3.2 Graph of etch rate and sidewall profile dependence on power density for GaAs and Al_{0.3}Ga_{0.7}As reactive ion etched in SiCl₄

Etch rate (nm)

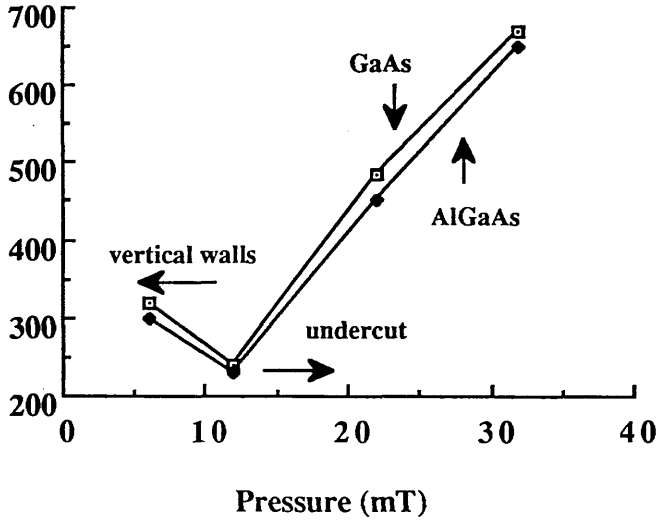


Figure 3.3 Graph of etch rate and sidewall dependence on gas pressure for GaAs and $\text{Al}_{0.3}\text{Ga}_{0.7}\text{As}$ reactive ion etched in SiCl_4

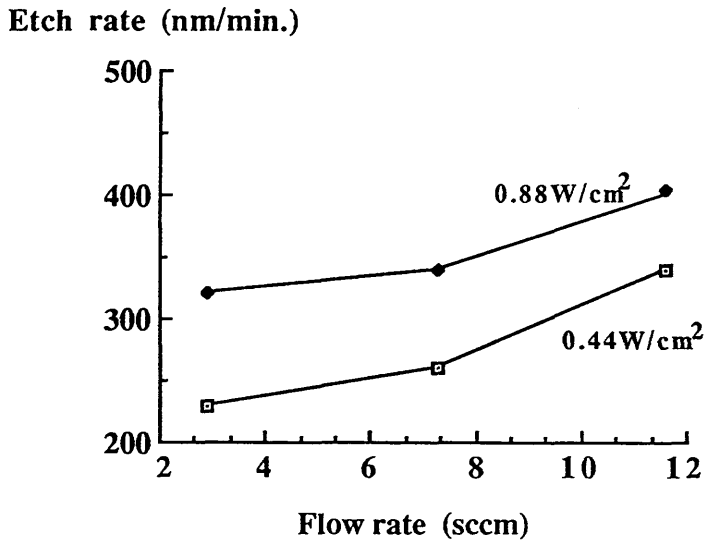
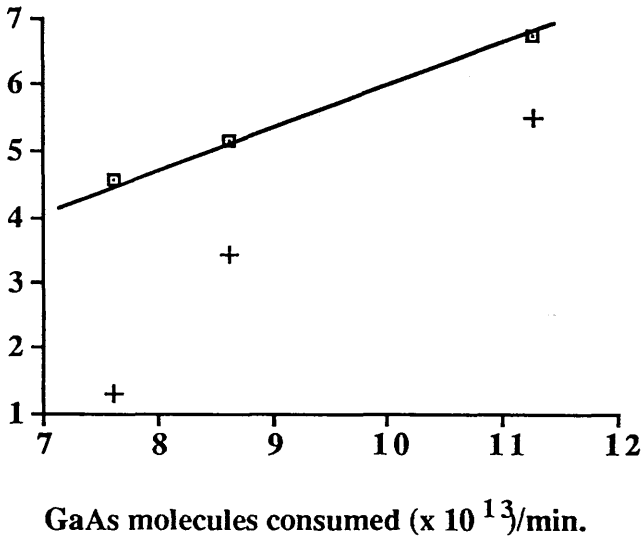


Figure 3.4 Graph of etch rate dependence on the volume flow rate of SiCl_4 in the reactive ion etching of GaAs at power densities 0.44W/cm^2 and 0.88W/cm^2

Cl atoms available ($\times 10^{14}$)/min.

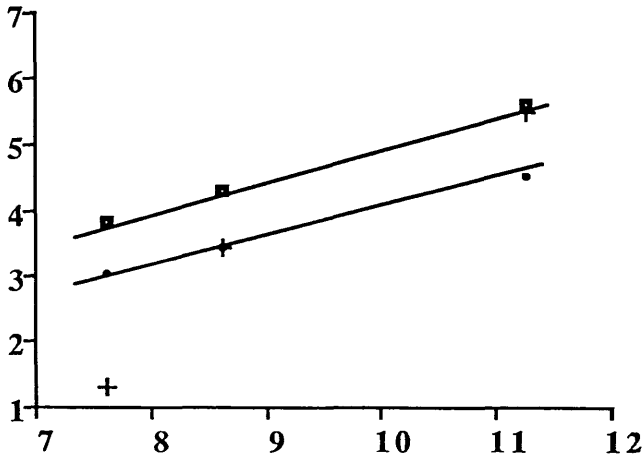


▣ Theoretical calculation

+ Experimental data

Figure 3.5 Graph of Cl atoms available vs. GaAs molecules consumed per min. with the theoretical assumption that 6 Cl atoms react with 1 GaAs molecule

Cl atoms available ($\times 10^{14}$)/min.



GaAs molecules consumed ($\times 10^{13}$)/min.

- + Experimental data
- Theoretical calculation assuming 5 Cl atoms react with 1 GaAs molecule
- Theoretical calculation assuming 4 Cl atoms react with 1 GaAs molecule

Figure 3.6 Graph of Cl atoms available vs. GaAs molecules consumed per min. assuming 5 or 4 Cl atoms react with 1 GaAs molecule

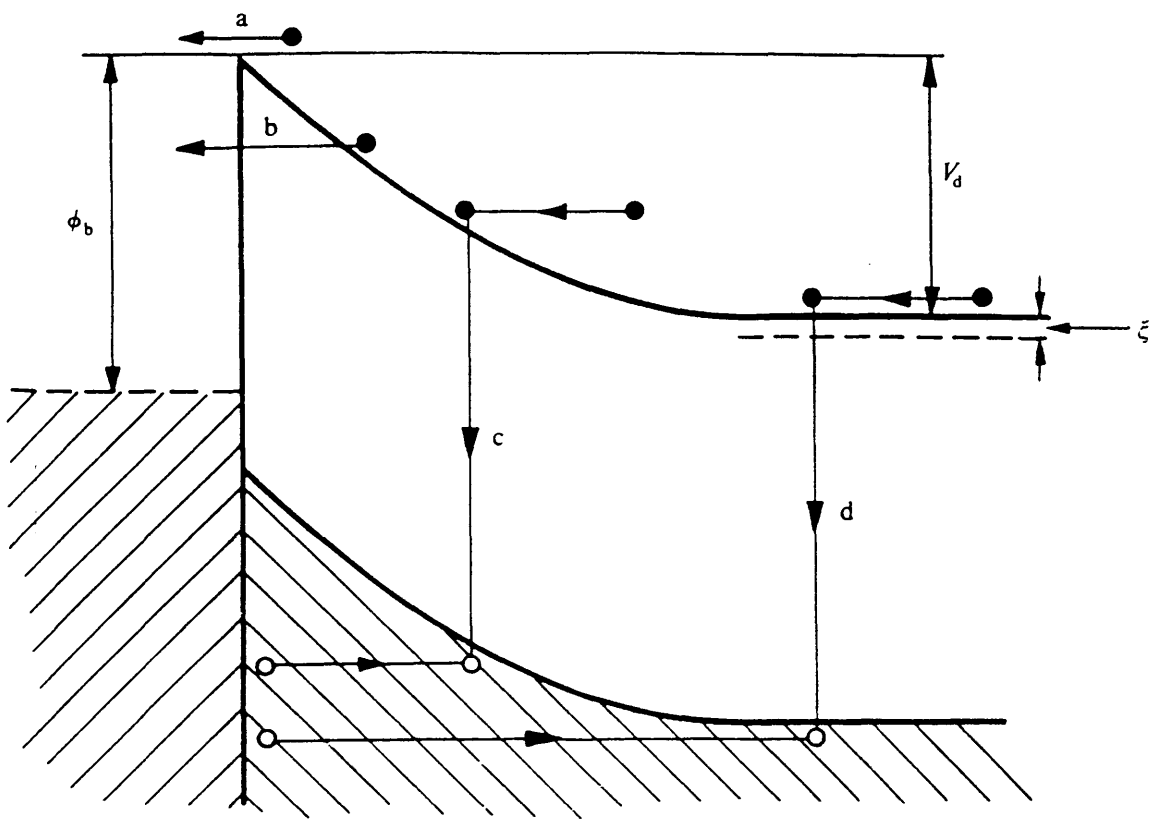


Figure 3.7 Schematic diagram of the transport mechanisms in a Schottky barrier under forward bias

[hp] ***** GRAPHICS PLOT *****

IF
(A)

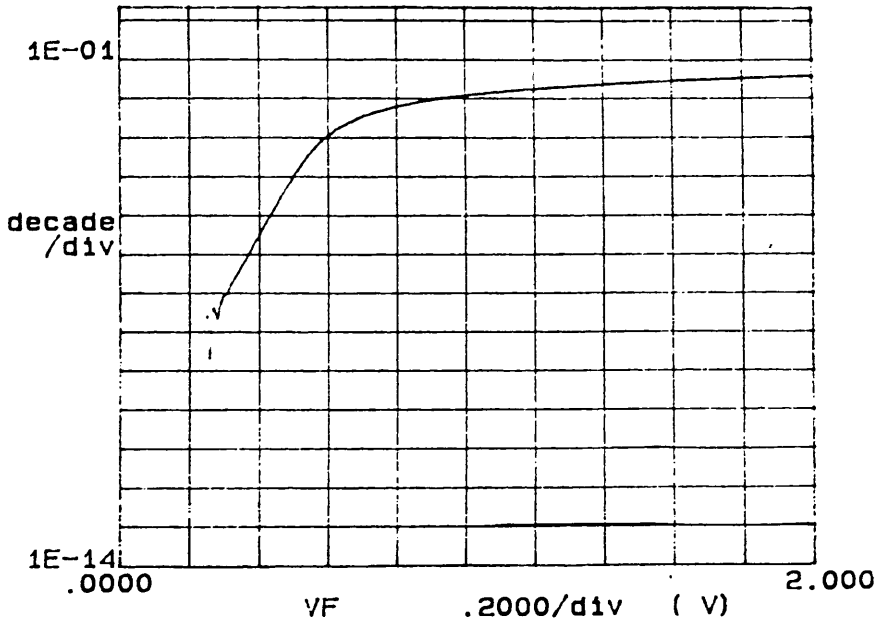


Figure 3.8 Plot of $\ln I$ against V for a GaAs Schottky diode with ideality factor 1.04

Ideality factor n

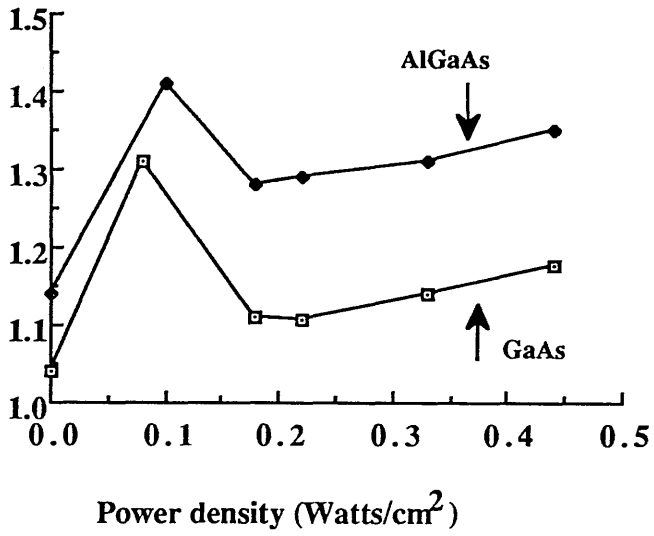


Figure 3.9 Graph of ideality factor as a function of power density for GaAs and Al_{0.3}Ga_{0.7}As reactive ion etched in SiCl₄

Ideality factor n

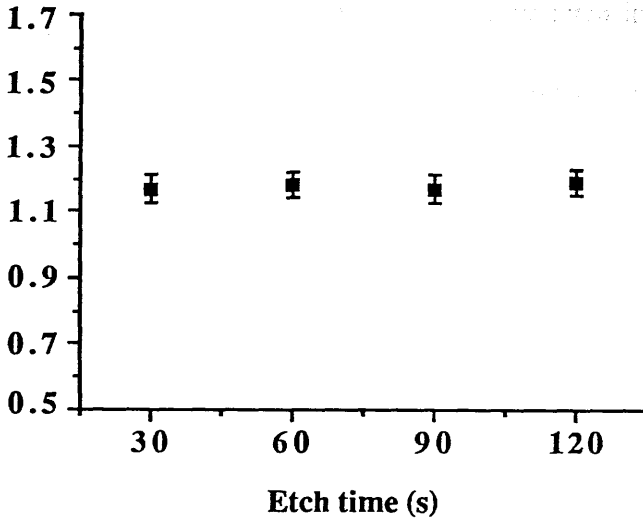


Figure 3.10 Measured ideality factor as a function of etch time for GaAs surfaces reactive ion etched in SiCl_4 at $0.44\text{W}/\text{cm}^2$, 12mT total pressure

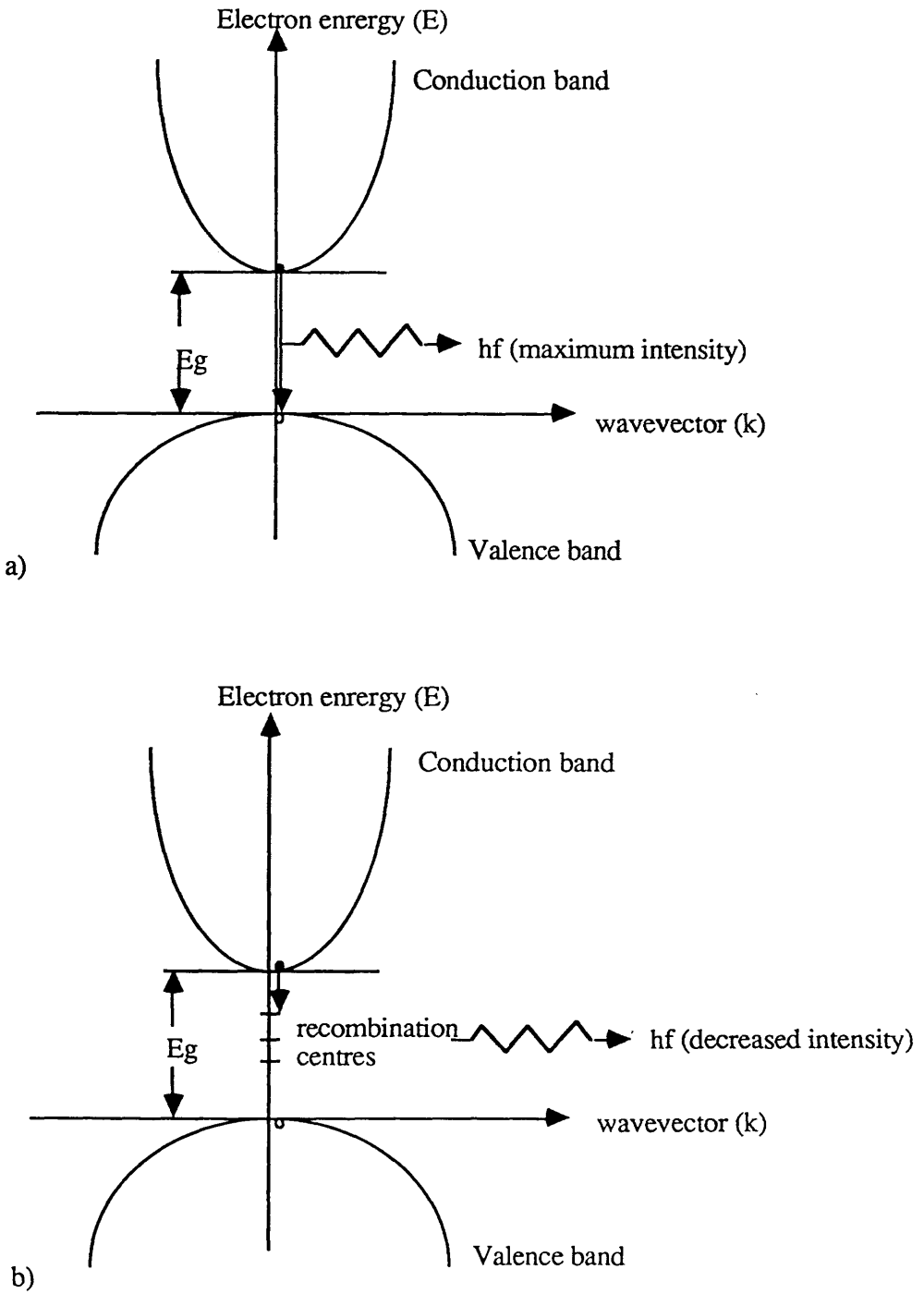


Figure 3.11 showing band diagram for photoluminescence process in a a) perfect direct band gap semiconductor b) imperfect (damaged) semiconductor with nonradiative recombination centres

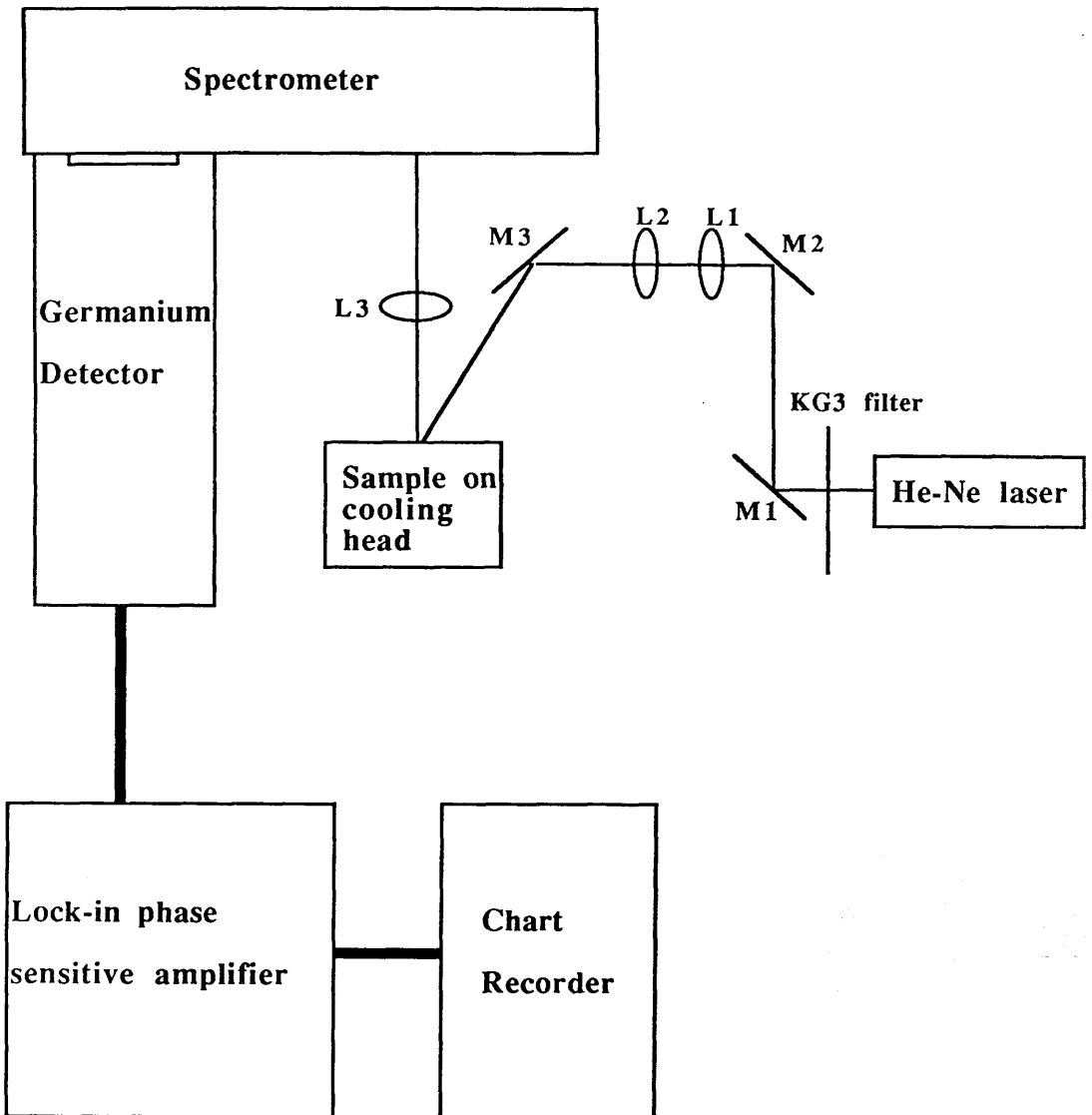


Figure 3.12 Schematic diagram of the photoluminescence system

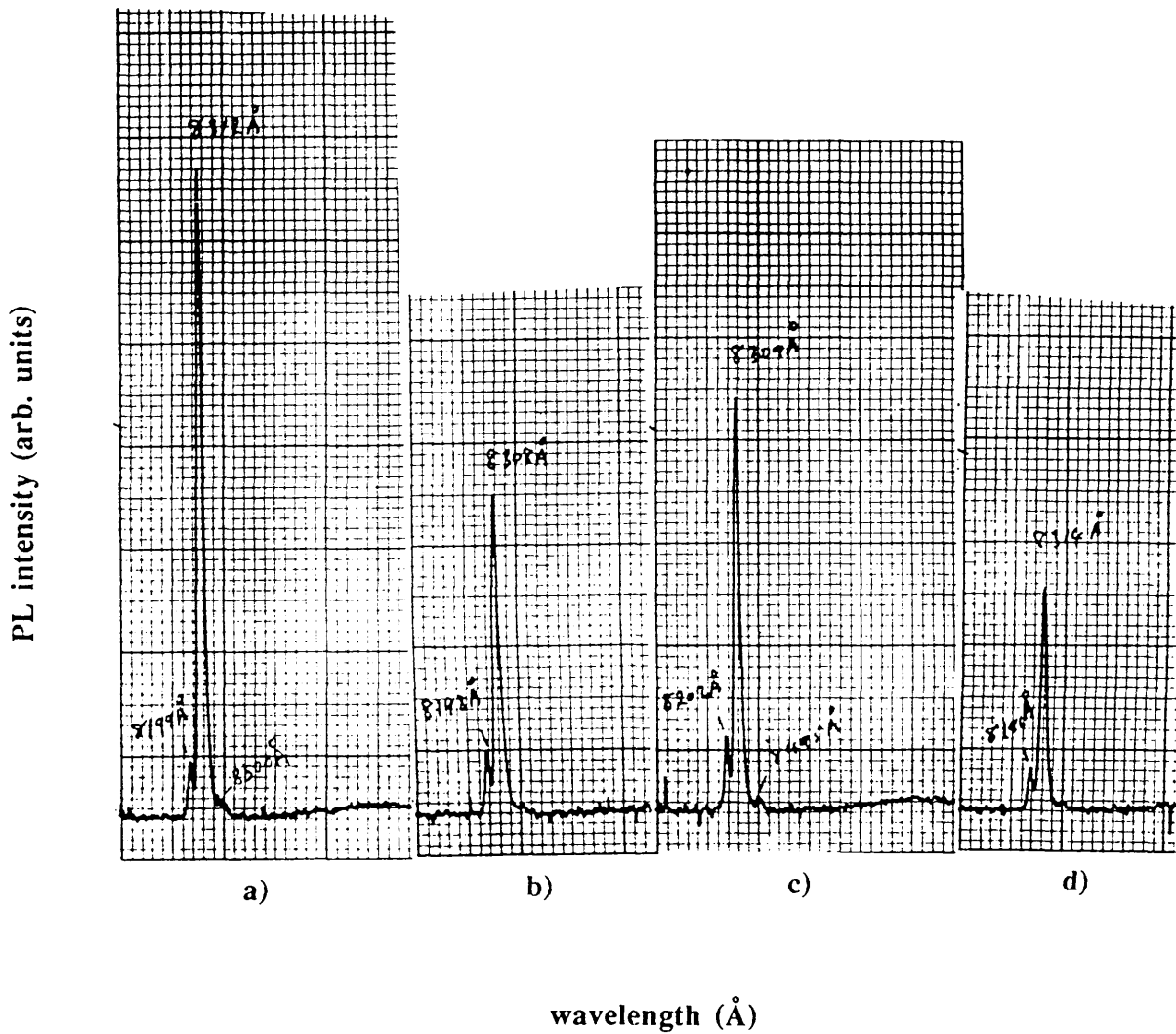


Figure 3.13 showing the photoluminescence spectra with the main transition at a wavelength of $831 \pm 1 \text{ nm}$ for a) unetched, and SiCl_4 reactive ion etched GaAs at a power density of b) 0.44 W/cm^2 , c) 0.22 W/cm^2 and d) 0.08 W/cm^2

Normalized PL intensity

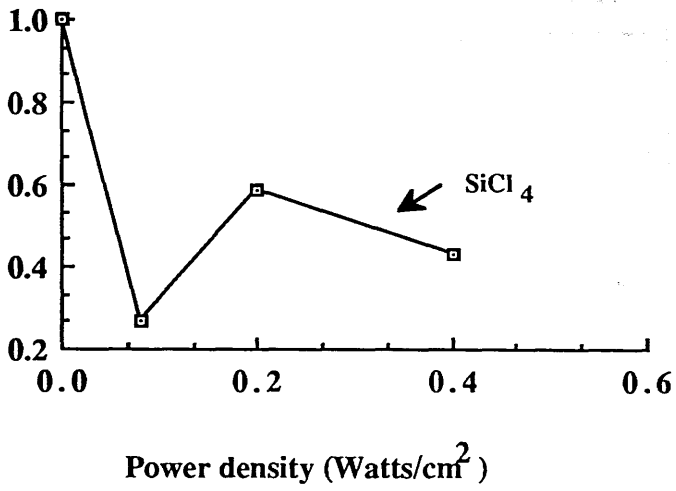


Figure 3.14 Normalised PL intensity vs. power density for GaAs surfaces reactive ion etched in SiCl₄

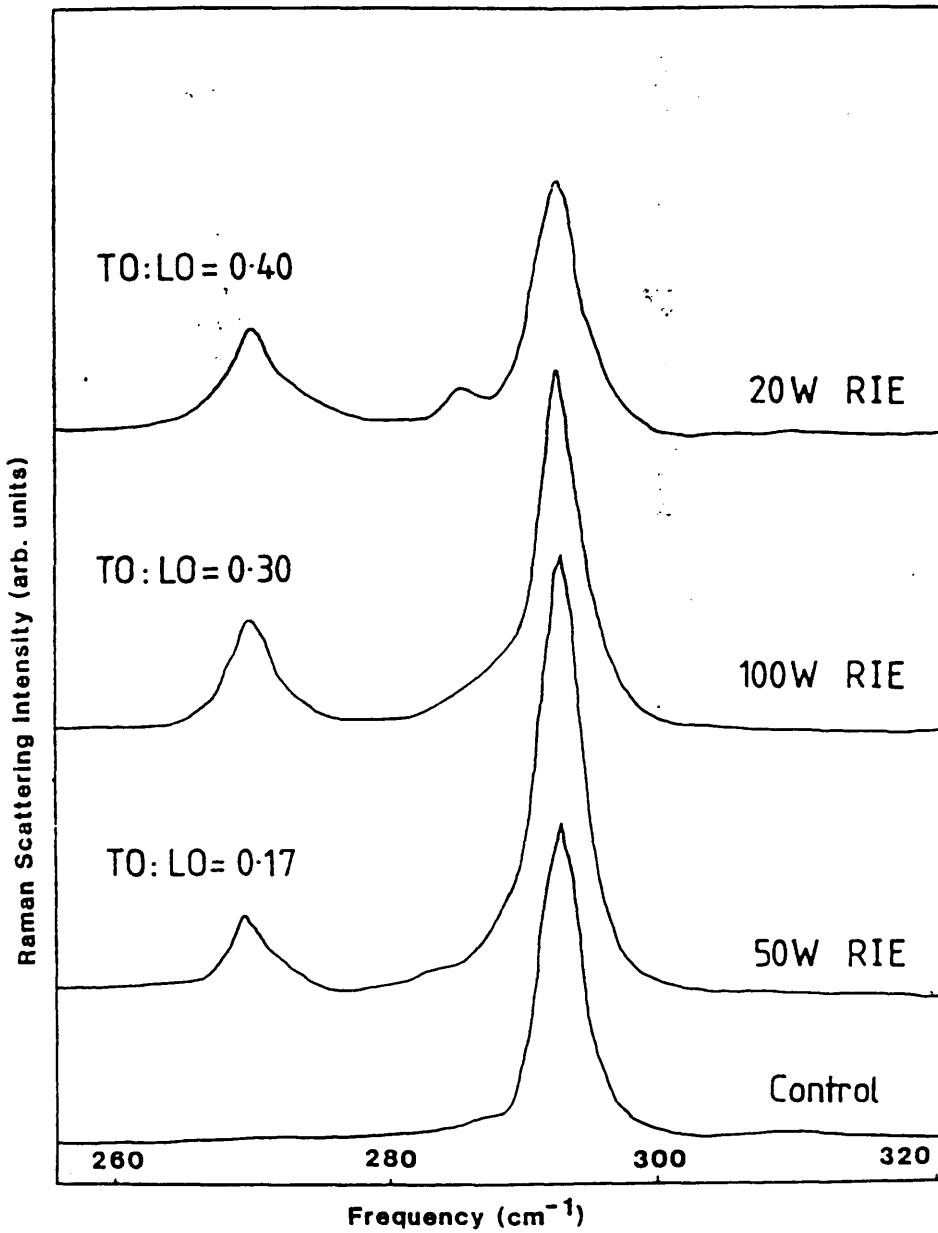


Figure 3.15 showing the Raman scattering spectra for unetched and reactive ion etched GaAs at different powers with TO:LO phonon mode ratios. Excitation wavelength was 4825Å (After M.Watt Ph.D thesis, 1988)

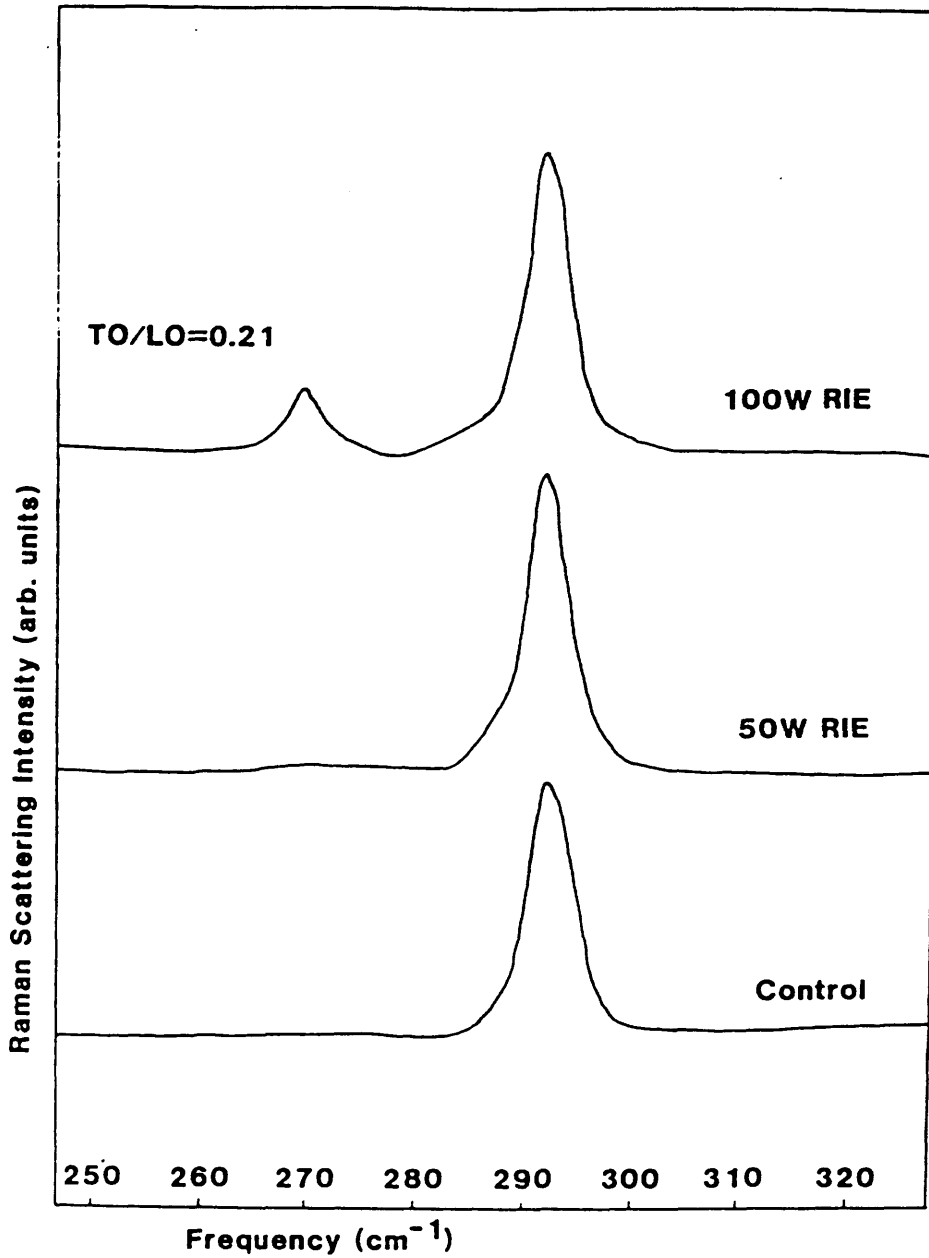


Figure 3.16 Raman scattering spectra of unetched and reactive ion etched GaAs at different powers with TO:LO phonon mode ratio. Excitation wavelength was 5309Å (After M.Watt Ph.D thesis, 1988)

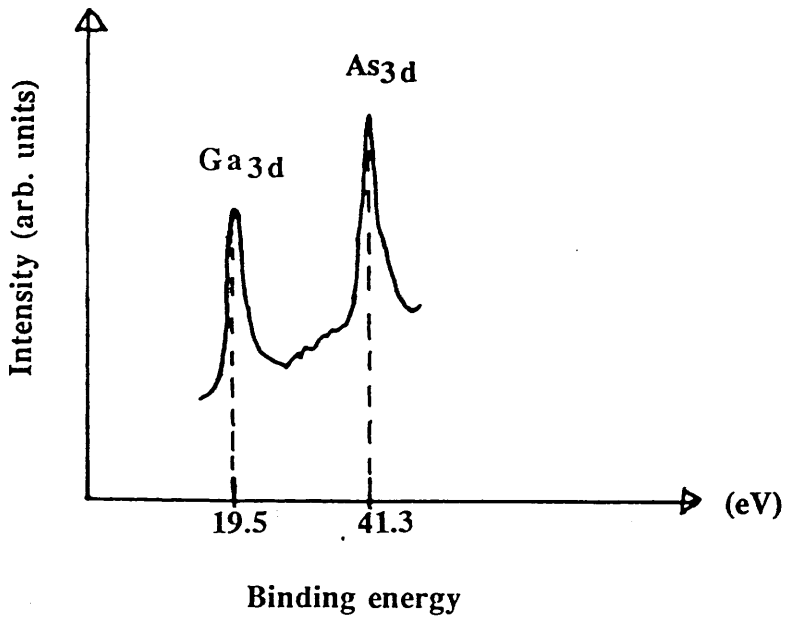


Figure 3.17a) XPS spectra of unetched GaAs

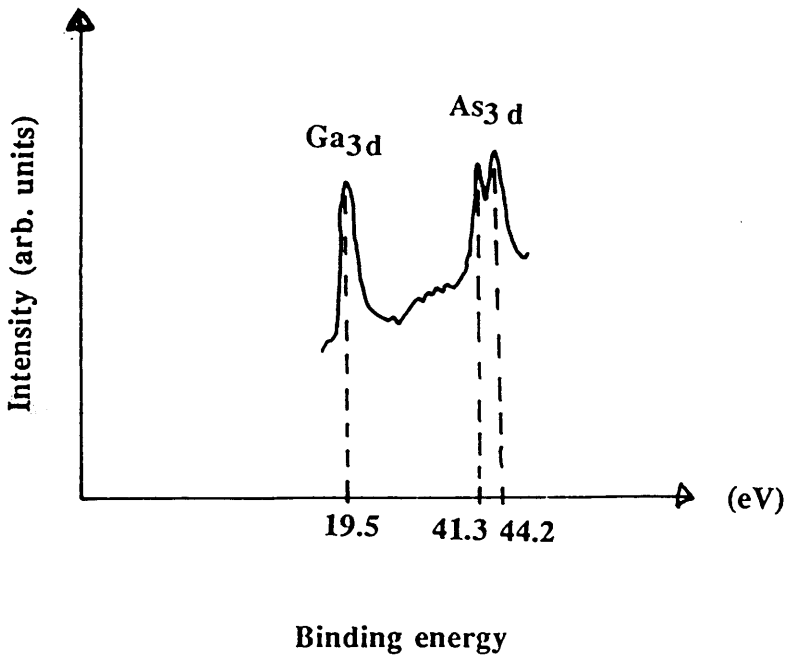


Figure 3.17b) XPS spectra of reactive ion etched GaAs in SiCl₄ at 0.44W/cm²

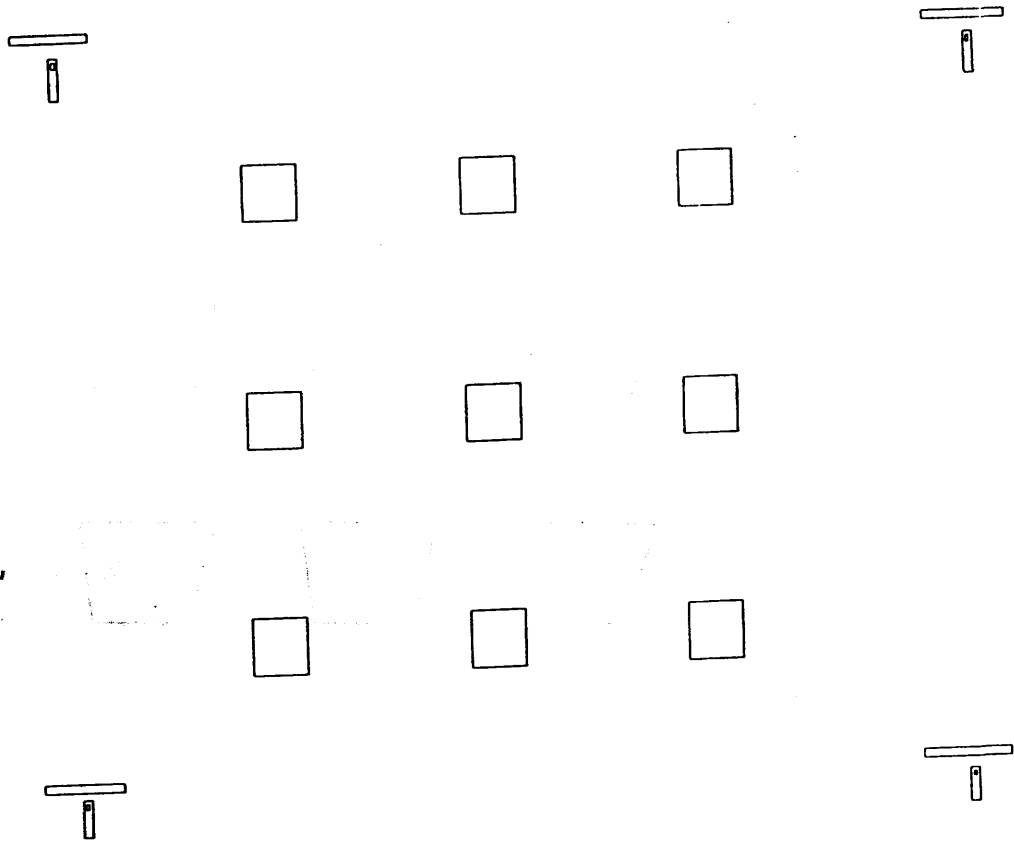


Figure 3.18a) Ohmic and alignment level in the fabrication of sidewall Schottky diode

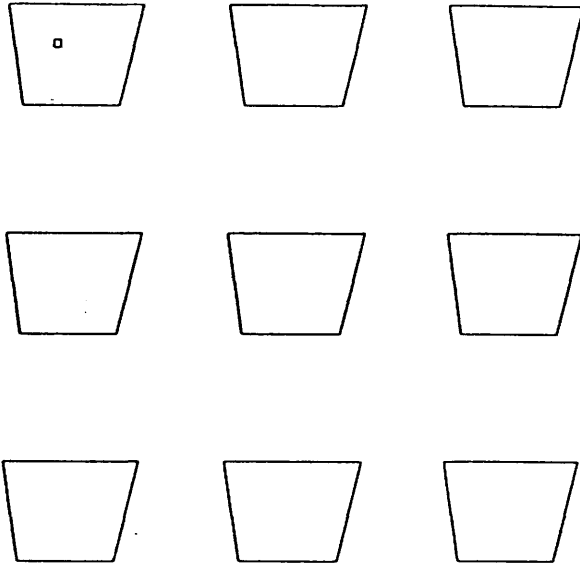


Figure 3.18b) Masking level in the fabrication of sidewall Schottky diode

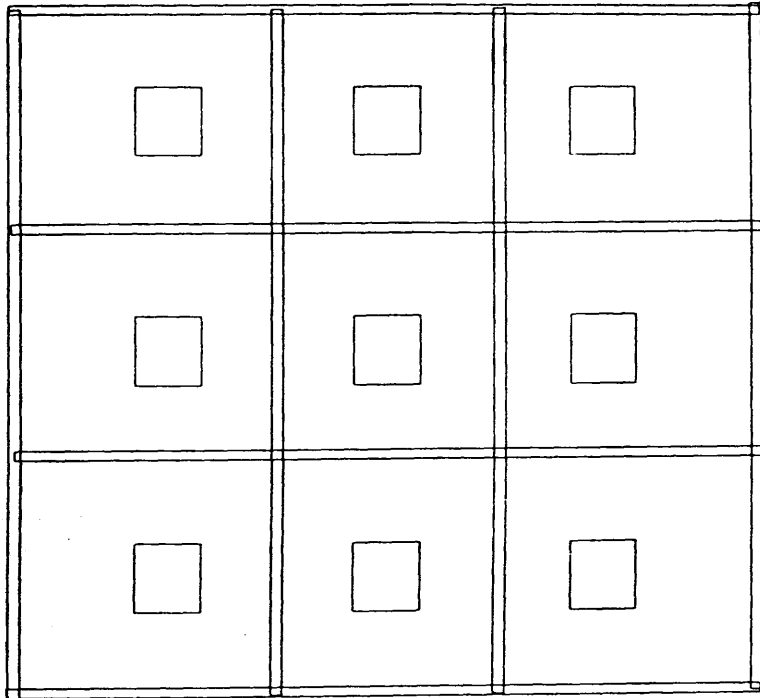
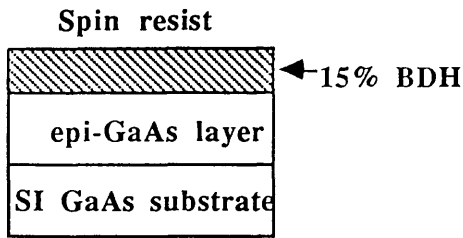
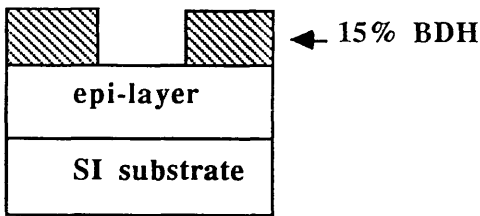


Figure 3.18c) Opening of ohmic contacts and device isolation level in the fabrication of sidewall Schottky diode

Ohmic and alignment level



Expose and develop



Evaporate, lift-off, anneal

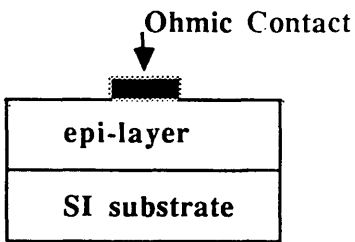
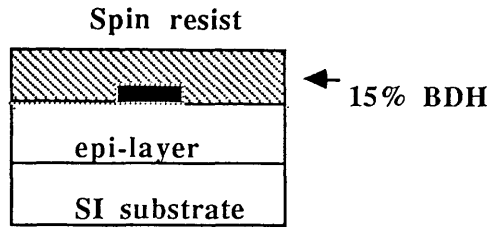
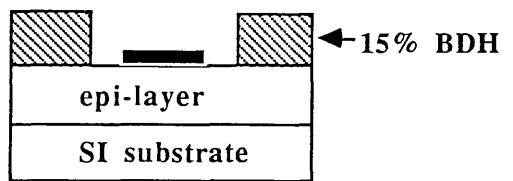


Figure 3.19a)

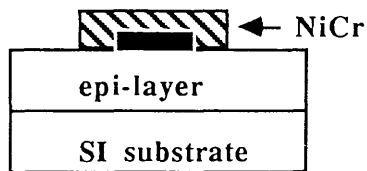
Masking level



Expose and develop



Evaporate and lift-off



Dry etch

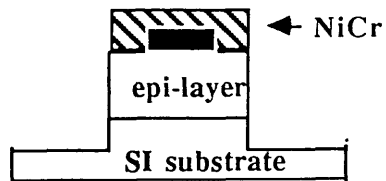


Figure 3.19b)

Open ohmic contacts and isolation level

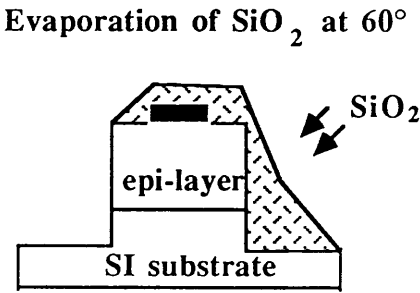
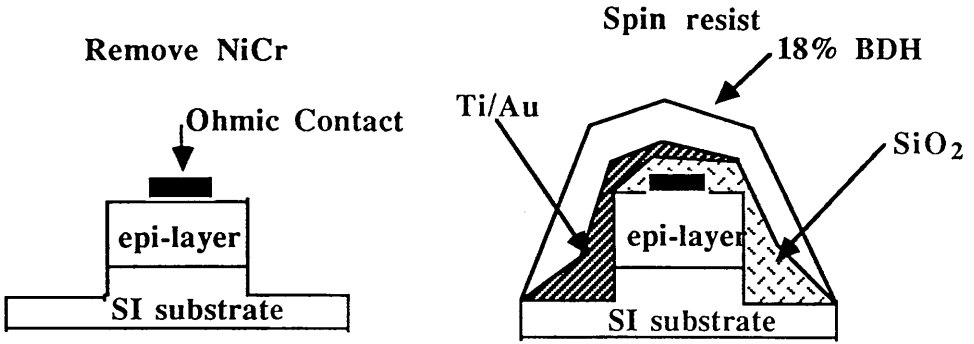


Figure 3.19c)

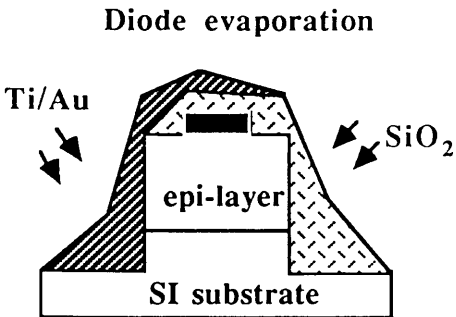
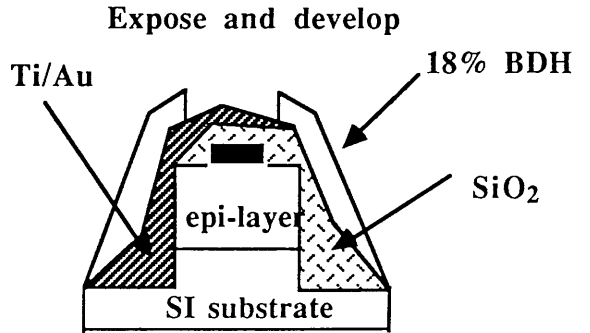
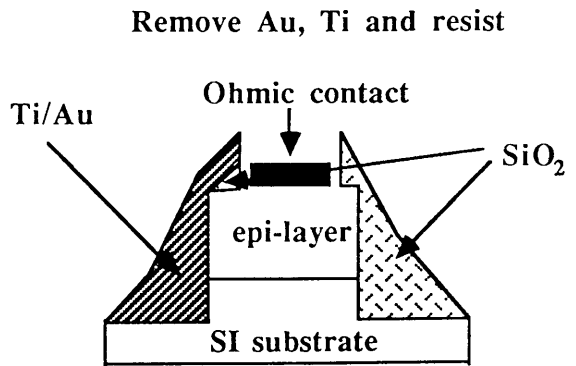


Figure 3.19d)



Final sidewall diode structure

Figure 3.19e)

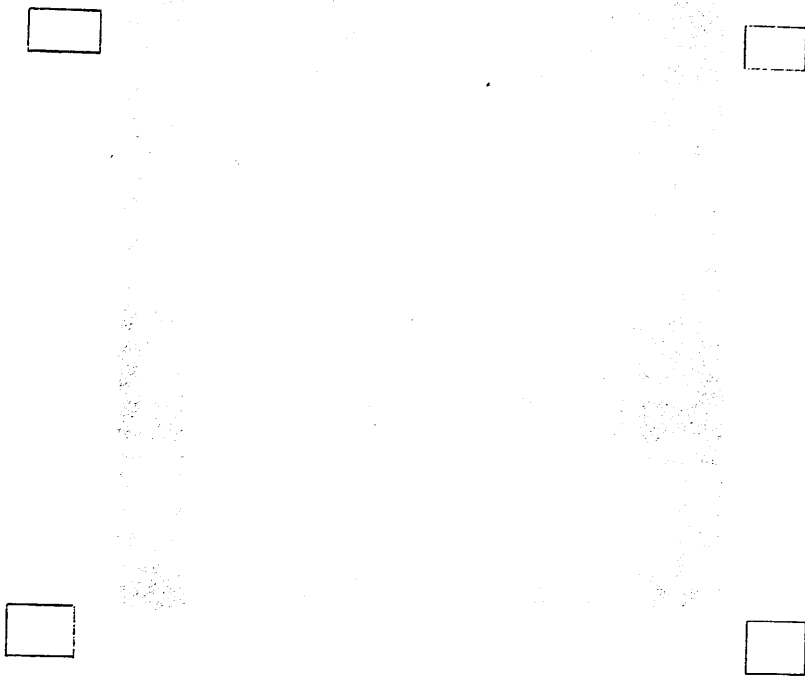


Figure 3.20a) Coarse alignment scan

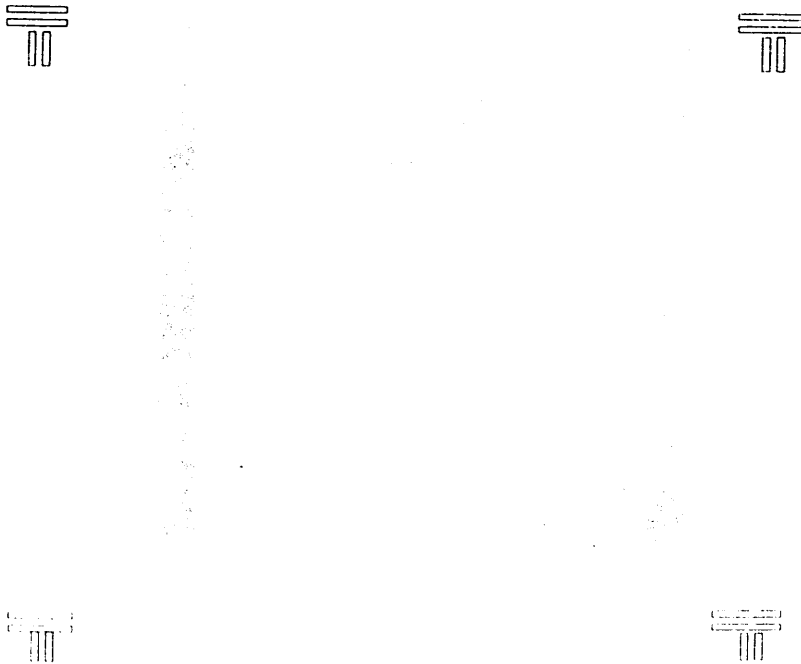


Figure 3.20b) Fine alignment scan



SEM 3.1 showing the shrinkage of HRN resist after reactive ion etching during sidewall Schottky diode fabrication



SEM 3.2 Using NiCr as dry etch mask resulted in very satisfactory etching with no problem of mask shrinkage



SEM 3.3 Effect of shadowing after the evaporation of SiO_2 at 60° during sidewall Schottky diode fabrication



SEM 3.4 The result of the subsequent evaporation of Ti/Au at 60° from the other side (on top of the SiO_2)



SEM 3.5 Discontinuity due to the shadowing effect from the underlying SiO_2 layer after Ti/Au evaporation



SEM 3.6 The presence of holes in the Ti/Au layer due to wet chemical attack



SEM 3.7 shows the final structure of a sidewall Schottky diode

Figure 3.7 shows the final structure of a sidewall Schottky diode. The image displays the cross-section of the diode, showing the Schottky contact on the sidewall and the underlying layers. The structure is characterized by a series of parallel, vertically oriented layers, indicating a high degree of alignment and control in the fabrication process.

***** GRAPHICS PLOT *****

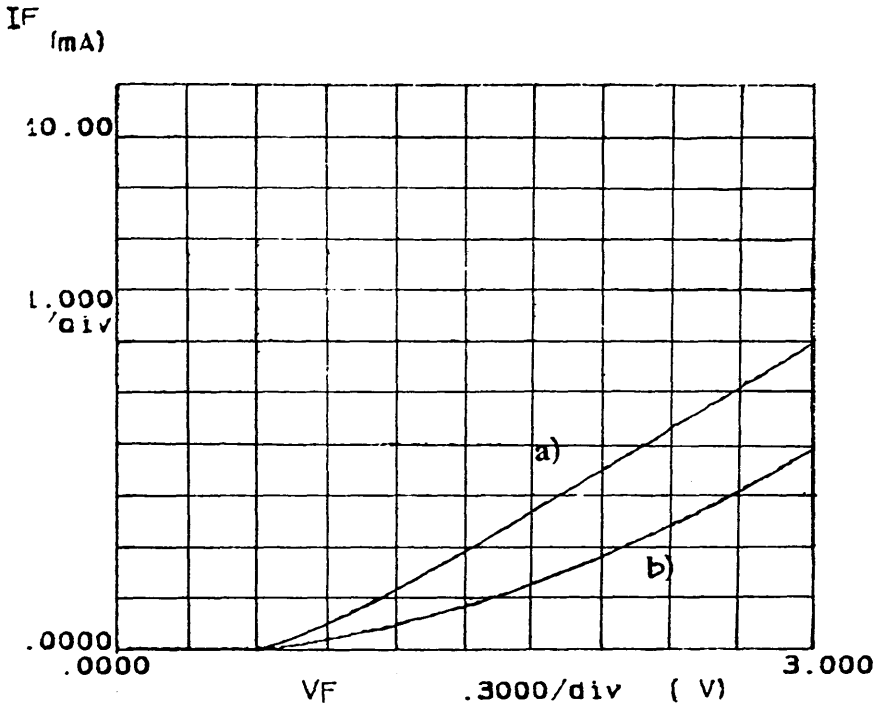


Figure 3.21 I-V characteristics showing the difference in current flow in the sidewall diodes using a) HRN and b) NiCr as dry etch masks

***** GRAPHICS PLOT *****

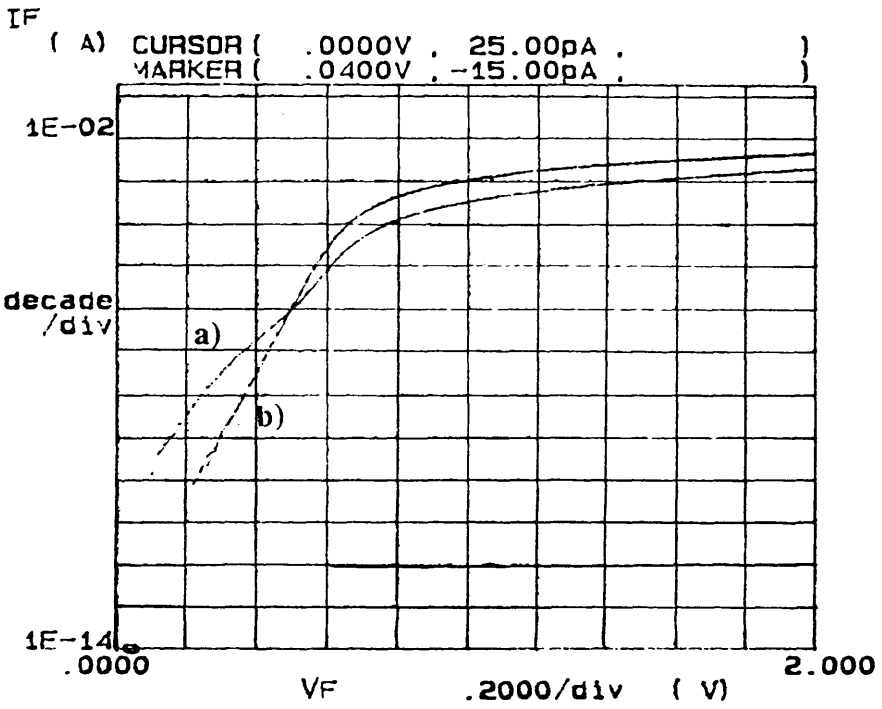
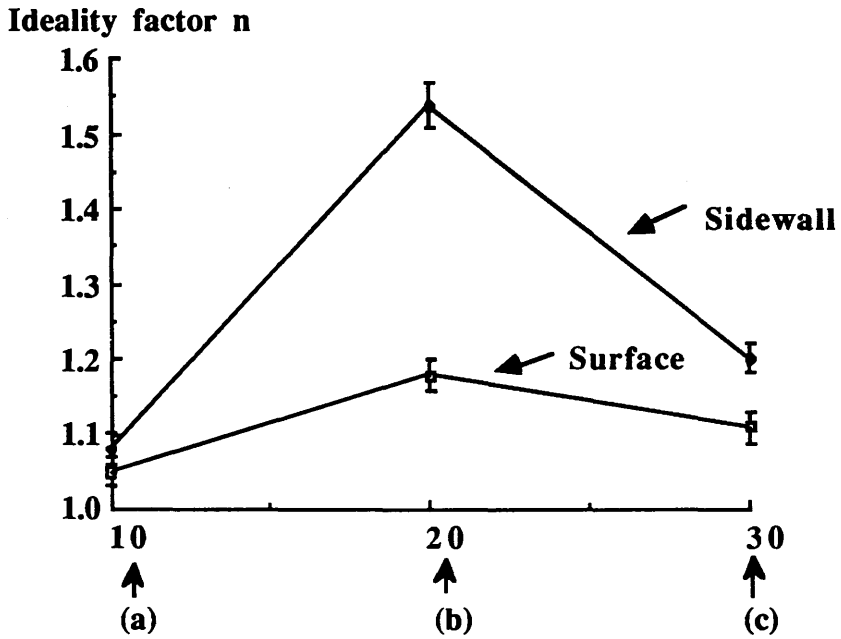


Figure 3.22 $\ln.I$ vs. V characteristics for a) HRN masked and b) NiCr masked sidewall diodes



- a) Control wet etch HCl : H₂O₂ 20:1
- b) Reactive ion etched in SiCl₄
- c) RIE in SiCl₄ and boiled in conc. HCl

Figure 3.23 Comparison between sidewall and surface damage after RIE in SiCl₄ and the effect of conc. HCl boil

Chapter 4 Development and damage characterisation of reactive ion etching of GaAs in CH₄/H₂

4.1 Introduction

This chapter is concerned with the development of the reactive ion etching of GaAs using CH₄/H₂; in addition, both damage and passivation effects caused by etching on the surface and sidewalls of etched structures are characterised employing electrical and optical techniques.

4.2 Development of reactive ion etching of GaAs using CH₄/H₂

4.2.1 Experimental

In order to develop the high resolution etching of GaAs using CH₄/H₂, a suitable dry etch mask has to be produced. Initially, single layer 15% polymethylmethacrylate (PMMA) positive resist (with molecular weight 185,000) was tried for low resolution etching. GaAs samples were half patterned with the resist and subsequently reactive ion etched. Although inspection of the etched sample under the Hitachi S800 scanning electron microscope (SEM) showed a high degree of reacted polymer (a blue residue) on the resist after etching, which was neither removable by soaking in acetone, nor in an O₂ plasma, the etched surface was very smooth. Therefore, various metals and negative resist were tried, the necessary fine metal lines were patterned using electron beam lithography and lift-off. After etching, the etch depths were measured using a Taly-step stylus.

4.2.1.1 Resolution tests

Resolution tests were carried out using the positive resist and the lift-off process described in sections 2.2 and 2.3. The double layer resist was exposed by an electron beam using a converted Phillips PSEM 500 scanning electron

microscope (SEM) (section 2.2.2) at 8nm spot of 50keV energy in a (25 x 19) μm frame. The exposure doses used were as follows:

- 1) 2000-10,000 $\mu\text{C}/\text{cm}^2$ for the 1-pixel lines;
- 2) 1000-5000 $\mu\text{C}/\text{cm}^2$ for the 2-pixel lines;
- 3) 800-2500 $\mu\text{C}/\text{cm}^2$ for the 4-pixel lines;
- 4) 400-1250 $\mu\text{C}/\text{cm}^2$ for the 8-pixel lines;
- 5) 350-500 $\mu\text{C}/\text{cm}^2$ for the 16-pixel lines;
- 6) 320-370 $\mu\text{C}/\text{cm}^2$ for the 40-pixel lines.

SEM 4.1 shows the 1-pixel Ti lines of linewidths 450 \AA -550 \AA with exposure doses from 2000-3500 $\mu\text{C}/\text{cm}^2$ on a GaAs sample. SEM 4.2 shows the entire exposure test pattern with the smallest Ti lines with linewidths at 400 \AA exposed at 2000 $\mu\text{C}/\text{cm}^2$ for 1-pixel and 1000 $\mu\text{C}/\text{cm}^2$ for 2-pixel. In order to test the degree of etch resistancy of the various masks, 8% HRN negative resist and different metal lines were fabricated on GaAs samples using this resolution test pattern and subsequently reactive ion etched in CH_4/H_2 .

4.2.2 Reactive ion etching

The RIE machine used was an Electrotech SRS Plasmafab 340 and has been described previously in section 2.7.2.

Initially, a large number of etching conditions within the parameter space^{4.1} was tried in order to find the correct feed gas composition and etch condition to provide the anisotropy needed for high resolution applications. Thereafter, the change in etch rate as the power density was varied about the optimum condition was studied; with a constant power density of 0.4W/cm², the effect of gas composition on etch rate and sidewall profile was observed by varying the H₂ flow rate while fixing the flow rate of CH₄ at 6.9sccm while maintaining a constant total pressure of 14mT. A residual gas analyser (RGA) was also employed to investigate the type and concentration of gases present in the exhaust gas. The RGA was fitted in a separately pumped chamber about 1 meter away from the main chamber. A sample of the exhaust gas is admitted through a needle valve and is ionised by a gauge head before entering the analysing chamber. The ions in the

chamber are then separated by their molecular weight and displayed on the screen of the control unit. In this way, the type of gaseous species present in the main chamber can be monitored by detecting their ion signals.

4.2.2.1 Conditioning of the etch chamber

Normally, after two to three reactive ion etch runs in CH_4/H_2 , the etch chamber is contaminated with polymeric material deposited from the CH_4/H_2 plasma. Since carbon and oxygen impurities is believed to strongly influence the plasma confinement as discussed by McCracken and Stott^{4.2} and it has been demonstrated that the use of hydrogen plasma cleaning and conditioning can remove these impurities^{4.3}, it was decided to clean the chamber using a H_2 plasma with a flow rate of 25sccm, $0.6\text{W}/\text{cm}^2$ power density and a pressure of 10mT. However, after 30minutes of cleaning, the polymeric material still remained. Therefore, it was decided to try to remove the carbon-containing compounds first with an O_2 plasma for 30 minutes with a flow rate of 25sccm, $0.2\text{W}/\text{cm}^2$ power density and a pressure of 15mT, followed by a H_2 clean for 30 minutes. This arrangement rendered very satisfactory results. In order to quantify the cleaning process, RGA signals were taken from the various stages during a H_2 clean. Figure 4.1 shows the RGA spectra with the addition of hydrogen gas after 30 minutes of cleaning in an oxygen plasma. Apart from the ions from the H_2 gas observed at molecular weights 1, 2 and 3g; the ions of H_2O at 17g and 18g, and carbon-containing compounds at 28g are clearly evident. Figures 4.2a) - d) show the RGA signals after 10 minutes, 15 minutes, 25 minutes and 30 minutes of H_2 plasma cleaning. The concentration of the ions from the water and carbon-containing compounds are observed to decrease as the duration of cleaning increases; after 30 minutes, most of the impurities are removed. Therefore, throughout this work, the etch chamber was preconditioned with O_2 and H_2 before etch runs were carried out.

4.2.3 Results and discussion

4.2.3.1 Masks

Two classes of mask were considered, namely metals and polymer resists. Metallic masks of gold/palladium (Au/Pd), nichrome (NiCr) and titanium (Ti) were tried. However, after etching, the Au/Pd and NiCr masks exhibited pyramid shaped profiles. Similar profiles have been observed when other metals were sputtered by high energy inert ions^{4.4} indicating a similar process occurring on these masks. On the other hand, Ti did not appear to have been sputtered, instead, an etch ratio to GaAs of $\approx 20:1$ after reactive ion etching in CH_4/H_2 was observed. It is possible that this is a result of the lower sputtering yield associated with Ti compared with other metals as reported by Laegreid and Wehner^{4.5}. Polymeric resists 8% HRN and 15% PMMA were also tried. 8% HRN was also observed to have been sputtered while a polymeric material which was not removable either in acetone or an O_2 plasma resulted when 15% PMMA was used.

4.2.3.2 Etching

The etch condition which produced the vertical sidewalls needed for high resolution application was found to be $0.4\text{W}/\text{cm}^2$ power density, 14mT total gas pressure, CH_4 volume flow rate of 6.9sccm with a CH_4 to H_2 gas ratio of 1:5, rendering an etch rate of $20\text{nm}/\text{min}$.^{4.6} SEM 4.3 shows a micrograph of a thin rib of width 30nm on a very smooth surface etched under these conditions using a 50nm thick Ti mask. The change in etch rate as the power density was varied about the optimum condition is shown in figure 4.3. The etch rate was found to increase with power density. While this observation may be due to the increase in reactive radical generation with increasing power densities, contribution from an enhanced ion-assisted processes as a result of more energetic ion bombardment (see section 2.4.4.) at higher power densities cannot be ruled out. At power densities below $0.2\text{W}/\text{cm}^2$, no etching but rather polymer deposition was observed. This is probably due to the presence of less energetic ions at such low power densities leading to a build up of the less volatile reactant products on the substrate surface thus inhibiting the etching process. Etch profiles are also dependent on power

density, changing from overcut at low power to vertical profiles at higher power. Although the vertical profile observed is probably because of the effects from the more energetic and directional ions at higher power densities, it is also possible that at higher power densities, more reactive radicals will be available to react with the sidewalls of the etched structures. Reverse explanations may also apply to the overcut profiles observed at lower power densities with lower radical generation and less energetic ion bombardment. However, it is difficult to distinguish, from this experiment alone, the dominant effect which affects the profile dependence, it is probably a combination of both physical and chemical contributions, especially in RIE. Experiments whereby the chemical and physical components during etching can be independently controlled are beneficial for this type of etch mechanism study^{4.7-4.9}.

Figure 4.4 shows the dependence of etch rate and sidewall profile on feed gas composition with the power density and total gas pressure being kept constant at 0.4W/cm^2 and 14mT respectively. An initial experiment in pure H_2 showed a very slow etch rate of 6nm/min. , as observed by Chang et al.^{4.10}. As the concentration of CH_4 was increased, the etch rate also increased to a maximum of 20nm/min. at a ratio of $1:5 \text{CH}_4:\text{H}_2$, then decreased with additional CH_4 . It is possible that the decrease in etch rate at low methane concentration is a consequence of an inadequate generation of $(\text{CH}_3)_3$ species for reaction. On the other hand, the decrease in etch rate at high methane concentration may be due to an excess generation of methyl species, leading to the formation of long chain polymers which may deposit on the surface of the GaAs surface, thus inhibiting the etching process. This explanation is further supported by the formation of a deposit with increased CH_4 concentration which is removable in an O_2 plasma. This suggests that a polymeric film is formed, which is a common occurrence with hydrocarbons in a gaseous discharge^{4.11}.

Overcut profiles were observed in both high and low CH_4 concentration regimes. While the overcut phenomena observed in the high CH_4 concentration regime may be a result of a high level of methyl species generated leading to redeposition of polymeric material onto the sidewalls of the etched structures, it is somewhat surprising to observe overcut profiles in the low CH_4 concentration regime since with a lower concentration of CH_4 , less methyl species would be generated.

It is worth noting that recently, GaAs etch rates of up to 45nm/min. has been demonstrated by increasing the CH₄ molecular concentration in the CH₄/H₂ gas mixture using Shipley positive photoresist S1718-J5 in a Plasma Technology RIE80 system^{4.12}.

4.3 Damage characterisation

The amount and nature of damage induced after CH₄/H₂ etching was characterised by a number of techniques. However, the damage measurements were complicated by the effect of passivation of the donors in GaAs from the atomic hydrogen generated in the CH₄/H₂ plasma. Nonetheless, to characterise both the passivation and damage effects on the etched surface, electrochemical profiling, Schottky diode characteristics and low temperature integrated band-gap photoluminescence were used while the conductivity of n⁺ GaAs quantum wires were measured to study the etched sidewalls. Comparison tests were made by dry etching in SiCl₄ and wet etching in potassium chlorate (KClO₃).

4.3.1 Hydrogen passivation and the effect of annealing

The incorporation of hydrogen in semiconductors (e.g. Si, Ge, InP, GaAs, AlGaAs) is well documented in the literature^{4.13-4.25}. Hydrogenation occurs when the samples are subjected to exposure of a H₂ plasma, or implantation of H⁺ ions from a beam source. In n-doped GaAs, atomic hydrogen has been observed to passivate donors leading to a decrease in carrier concentration^{4.16-4.18}, increase in electron mobility^{4.14} and an increase in the photoluminescence spectra^{4.20} measured. The incorporated hydrogen is also found to passivate deep level defects such as M1, M2, M4^{4.21} and EL2^{4.23}, bulk donor defect (at E_C-0.36eV)^{4.15}, argon sputter-etch induced defects^{4.26} and non-radiative deep centres^{4.20}. Moreover, after hydrogen plasma exposure, passivation of Si donors and DX centres in AlGaAs occurs^{4.22}. Although electrical activity of the shallow donors can be restored by annealing at temperatures around 400°C for 10 minutes^{4.17,18,21}, deep levels M1, M2 and M4 remain fully passivated up to anneal temperatures around 600°C^{4.21}. From a photoluminescence study by Weber

et. al.^{4.20}, they found that while the Si donors were recoverable from passivation at anneal temperature of 400°C, the nonradiative centres were not. It follows, therefore, that there is a wide temperature window within which it is possible to regain the carrier concentration without loss of passivation of the deep level defects and non-radiative deep centres. Furthermore, the effect of hydrogenation has been demonstrated to passivate dry etched defects in Ge, Si and GaAs^{4.26-28} and has been applied to the fabrication of a field-effect transistor^{4.29}.

The type of bonding arrangements for the donor neutralization in GaAs still remains an open question although some models have been suggested^{4.13,17-20}. The fact that the activation energy for the recovery of electrical activity varies with donor species suggests that atomic hydrogen is in some way bonded to the donor ion, see figure 4.5. While some simple microscopic bonding models involving the utilisation of the extra electron from the donor leading to the formation of hydrogen to Ga-site donor (Si, Sn, and Ge) or As-site donor (Se, S, and Te) complexes have been proposed^{4.17,20}, the possibility of a hydrogen to arsenic bond, where the arsenic is supposed to sit as a first nearest neighbour of the silicon donor atom, giving rise to (SiAs₃)As-H complexes has also been suggested from infrared absorption spectroscopic studies on hydrogenated n-type silicon doped GaAs^{4.13}.

4.3.2 Surface damage - Electrochemical profiling

4.3.2.1 Experimental

The material employed was a $2 \times 10^{17} \text{cm}^{-3}$ Si-doped GaAs epitaxial layer of 1 μm thick on an n^+ substrate. For this experiment, the GaAs wafer was diced into five 6 x 6 mm² chips. The surfaces of four unpatterned GaAs samples were CH₄/H₂ etched for 2 minutes to an etch depth of $\approx 40\text{nm}$. The etch condition used was as in section 4.2.3.2. The remaining unetched chip serves as a control sample. After etching, three samples were annealed on a strip heater in a 95% Ar/ 5% H₂ ambient for 2 minutes at 200°C, 300°C and 380°C. The carrier concentration profiles of the five differently treated GaAs samples were obtained from

capacitance-voltage measurements on Schottky barrier structures formed by an electrolyte (0.1 molar Tiron solution) in contact with the samples. Instead of varying the applied voltage to change the depletion depth at which the carrier concentration is measured as in the conventional C-V profiling, this electrochemical method changes the depth (the sum of the depletion depth and the etched depth) by etching smoothly the semiconductor in a controlled way while keeping the applied voltage constant. In principal, the electrochemical profiler is able to measure profiles to an unlimited depth or very highly doped layers ($n \geq 10^{19} \text{ cm}^{-3}$) since it is not limited by the Schottky breakdown voltage.

4.3.2.2 Results and discussion

Figure 4.6 shows the carrier concentration before and after processing as a function of depth. In the unetched control sample the carrier concentration is uniform from the edge of the surface depletion region through the epilayer. After CH_4/H_2 etching, the depletion region edge has moved to a depth of $0.2\mu\text{m}$ beyond which the carrier concentration varies continuously for a further $0.1\mu\text{m}$ from $5 \times 10^{16} \text{ cm}^{-3}$ to the bulk value. Partial recovery of the carriers was possible by annealing the sample at 200°C for 2 min. and full recovery was obtained after a 300°C anneal for the same period. These results are similar with those previously reported for the depassivation of Si-doped GaAs exposed to hydrogen plasmas^{4,17}. Therefore, it appeared that the loss of carriers close to the surface was largely due to hydrogen passivation though the possibility of near surface damage could not be ruled out by this experiment alone.

4.3.3 Schottky diode characteristics

4.3.3.1 Theory

The theory concerning the estimation of surface damage by measuring the ideality factor of Schottky diodes can be found in section 3.4.1.1. In addition to measuring the ideality factor, the diode barrier height can be calculated by taking the intercept on the current axis at $V = 0$ as I_0 and substituting in equation 3.3. If large values of n are calculated or $\ln I$ against V plots are non-linear, the diode is

considered to be far from ideal probably due to the presence of a thick interfacial layer leading to an enhancement in tunneling transport or to an increase in recombination in the depletion region.

For additional information about the quality of the semiconductor surface, another useful parameter to measure in a Schottky diode is the reverse leakage current. This is carried out by applying a moderately small reverse bias ($\approx -2V$) to the metal-semiconductor junction and measuring the resultant current. In this configuration, the current contributed from quantum-mechanical tunneling, especially in the presence of additional surface charges and traps become very significant.

4.3.3.2 Experimental

The material employed for diode fabrication was a $2 \times 10^{17} \text{cm}^{-3}$ Si-doped GaAs epitaxial layer, $1 \mu\text{m}$ thick on an n^+ substrate. Ohmic contacts were prepared by alloying Ge-Au-Ni-Au at 325°C on the back surface of the wafer, see section 4.3.1.1. The GaAs wafer was then scribed into $3 \times 3 \text{mm}^2$ chips. To investigate the effect of annealing on the diode behaviour after CH_4/H_2 etching, three unpatterned GaAs chips were CH_4/H_2 etched for 2 minutes to an etch depth of $\approx 40\text{nm}$. The etch condition used was as in section 4.3.1.1. After etching, two samples were annealed on a strip heater in a 95% Ar/ 5% H_2 ambient for 2 minutes, one at 200°C and the other at 380°C . The remaining chip served as a control sample. Two other chips were processed with similar etching conditions as above only with differing power densities, $0.3\text{W}/\text{cm}^2$ and $0.6\text{W}/\text{cm}^2$. Then, a single layer of 15% PMMA in chlorobenzene ($185,000 \text{MW}$) $\approx 1 \mu\text{m}$ thick was spun onto the four chips (one serves as a control sample) at 5K rpm and baked at 180°C overnight. Openings of $10 \times 10 \mu\text{m}^2$ were made by exposing the resist with an electron beam at $0.25 \mu\text{m}$ spot at 50kV in a $1.56 \times 1.18 \text{mm}$ frame and developing the exposed resist in 1:1 MIBK:IPA for 60s at 23°C followed by a 30s rinse in IPA. Native oxides were removed by dipping the sample in 1:1 HCl: H_2O for 30s followed by a 30s rinse in deionised water. Schottky diodes were subsequently formed by 60nm-Ti/50nm-Au metallisation. The I-V characteristics were performed using an HP 4145A semiconductor parameter analyser.

4.3.3.3 Results and Discussion

A summary of the measurements derived from the I-V characteristics as a function of anneal temperature for the Schottky diodes is shown in table 4.1. After CH₄/H₂ etching, ideality factor, barrier height, turn on voltage, breakdown voltage, and reverse leakage current were increased. The effect of annealing at 200°C decreases the barrier height, turn on voltage, and breakdown voltage. At an anneal temperature of 380°C, the above parameters decrease to values comparable with the control sample. While these relative changes are attributed to the change in carrier concentration due to passivation as observed in the carrier profile measurement, the reverse leakage current is not recovered by annealing, suggesting that interface traps are generated by the CH₄/H₂ etch. The ideality factors measured at various power densities for the CH₄/H₂ etched GaAs surfaces before annealing is also shown in figure 4.7 along with the SiCl₄ etched GaAs surfaces (see section 3.4.1.3). From table 4.1 and figure 4.7, it is observed that small increases in the ideality factors are measured after CH₄/H₂ etching before and after annealing and comparing this data with the SiCl₄ etched surfaces (figure 4.7), the CH₄/H₂ etch appears to cause less damage on the GaAs surface than the SiCl₄ etch (see also section 4.3.4.3). However, from the reverse leakage current data, the presence of interface traps are clearly evident after CH₄/H₂ etching before and after annealing.

It is worth noting that arsenic deficient surfaces were found from an x-ray photoemission spectroscopy study of GaAs surface having been exposed to a multipolar hydrogen plasma^{4.30} and from a transmission electron microscopy investigation after the GaAs sample was exposed to a capacitively coupled rf H₂ plasma for 2 hours^{4.31}. However, this effect does not appear to be evident from the present measured diode characteristics since a decrease in barrier height would be expected if the GaAs surface was arsenic depleted^{4.32-4.35} (also section 5.4.2.2).

4.3.4 Low temperature integrated band-gap photoluminescence measurements

4.3.4.1 Theory - see section 3.4.2.1

4.3.4.2 Experimental

The material used for the photoluminescence study was a $2 \times 10^{17} \text{cm}^{-3}$ Si-doped GaAs epitaxial layer of $1 \mu\text{m}$ thick on an n^+ substrate. In this experiment, ten GaAs samples of $4 \times 4 \text{mm}^2$ were prepared, seven of which were reactive ion etched in CH_4/H_2 for 2 minutes at the condition described in section 4.2.3.2. After etching, two samples were annealed at 200°C , one for 2 minutes and the other for 4 minutes, while four others were annealed at 380°C for 1, 2, 3, and 4 minutes separately. The annealing procedure was carried out on a strip heater in a 95:5 $\text{Ar}:\text{H}_2$ ambient. Two other GaAs chips were also reactive ion etched by CH_4/H_2 at varying power densities of 0.3 and $0.6 \text{W}/\text{cm}^2$. No annealing was carried out on these samples. The remaining unetched chip served as a control sample. Details of the photoluminescence equipment used can be found in section 3.4.2.2.

4.3.4.3 Results and Discussion

Figure 4.8 shows a graph of integrated photoluminescence intensity (at the transition wavelength of 831nm) normalised to the unetched control sample for GaAs after reactive ion etched by SiCl_4 and CH_4/H_2 at different power densities. The PL spectra for the SiCl_4 etched surfaces can be found in section 3.4.2.3 with a more detailed explanation. In the present graph, it is evident that the samples etched by the CH_4/H_2 etching process result in much higher PL intensities at all power densities compared with the SiCl_4 process. This implies that more non-radiative deep centres are introduced by the SiCl_4 etching process than the CH_4/H_2 process. It is worth noting that this data is consistent with the Schottky diode characteristics observed in section 4.3.3.3. One possible explanation for this observation is that the deep centres introduced by the CH_4/H_2 process are constantly passivated by the atomic hydrogen since this is believed not only to bind to Si-donors but also to nonradiative deep centres^{4,20}. It has also been demonstrated that atomic hydrogen

is effective in passivating electrically active damage centres created during sputter etching of GaAs^{4.27} and that lattice damage due to ion bombardment can be self-passivating when hydrogen is present in the bombarding species when etching silicon^{4.36,42}. However, if all the nonradiative deep centres were effectively passivated by the atomic hydrogen, an overall increase in luminescence intensity should be expected for the hydrogenated samples^{4.20}; in this experiment, an overall decrease in luminescence intensity is observed. Therefore, while it is possible that the rate of introduction of deep centres by the etching process is higher than the rate of passivation by the atomic hydrogen, a reduction in the donor-related transitions resulting from the decrease in donor concentration through the effect of passivation may also contribute to the decrease in the luminescence intensity observed.

The effect of annealing on the PL output of the CH₄/H₂ etched GaAs samples were also studied. Unetched samples were also annealed to ensure the validity of this investigation. Figure 4.9 shows the normalised PL intensity vs. anneal time for the unetched and hydrogenated samples annealed at temperatures 200°C and 380°C. The unetched samples before and after annealing show PL intensities of around 1 as expected. The general trend of the data shows an increase in PL output with the anneal time in the hydrogenated samples. From a previous study by Pearton et. al.^{4.19}, the anneal process is believed to recover the donors from donor-hydrogen complexes while the activated H is either redistributed deeper in the sample or is released outwards from the sample depending on the anneal temperature; this behaviour was observed by Heddleson et. al.^{4.42} in hydrogenated silicon. In this study, while the activated H upon annealing from the de-passivated donors (from previous electrochemical and diode characteristic measurements) may indiffuse into the substrate and passivate the nonradiative centres (probably introduced by the etching process) thus causing increases in PL output to values greater than 1 with anneal time at both anneal temperatures, it is also possible for the donor-related transitions from the recovered donors to contribute to the luminescence. However, if H indiffusion was the only result of annealing, for the temperature range considered in this study, a higher PL output would be expected for the samples annealed at 380°C compared with 200°C according to a carrier recovery mechanism proposed by Chevalier et. al.^{4.18} and Pearton et. al.^{4.17} for the dissociation of Si-H bond. From their experimental data, the integrated fraction of the donor-hydrogen complexes remaining N/N_0 was found to be dependent on

the anneal temperature T and anneal time t corresponding to the equation:

$$N/N_0 = \exp - \left[\nu \exp (- E_D/kT) \right] \quad (4.1)$$

where E_D is the dissociation energy and ν is the dissociation attempt frequency. For Si-H complexes, taking ν as 10^{14}s^{-1} , E_D was found to be 2.1eV. Therefore, the smaller PL luminescence intensities observed for the samples annealed at 380°C is perhaps suggestive of the presence of a H outdiffusion process. But from this experiment, it is not possible to distinguish whether the H outdiffusion process only begins or has a faster rate at 380°C.

It is worth noting that the effect of hydrogenation and damage caused by CH_4/H_2 have also been studied recently employing thin highly-doped GaAs epilayers on semi-insulating substrate using TLM and Hall conductances techniques^{4.43-45}.

4.3.5 Sidewall damage - Conductivity of n^+ GaAs quantum wires

As already mentioned in section 2.5, compared with studies performed on dry etched surfaces, relatively little work has been carried out to investigate damage caused on the sidewalls of the etched structures. Throughout this work, two novel processes have been developed to enable sidewall damage to be investigated. The first process involves the fabrication of a Schottky diode onto the sidewall and by measuring the diode ideality factor, it is possible to estimate the amount of induced damage, see section 3.5. The second process is concerned with devising a thin wire structure to exploit the analytical techniques available in transmission electron microscopy, see section 6.3. In this section, a third technique is presented whereby through measuring the conductivity of n^+ quantum wires, the extent of damage caused on the sidewalls can be deduced. This technique was first developed by Stephen Thoms at the University of Glasgow^{4.37}.

4.3.5.1 Theory

This technique utilises the assumption that for GaAs, the expected surface depletion depth, d , for the epilayer can be found to be:

$$d = \left[\frac{2\epsilon\epsilon_0(V_{BS} - kT/q)}{q(N_D - N_A)} \right]^{1/2} \quad (4.2)$$

from Chandra et.al.^{4.38}, where ϵ is the static dielectric constant of GaAs and V_{BS} is the built in surface potential, taken as 13 and 0.6eV respectively, and $N_D - N_A$ is the net donor density. Assuming there is negligible conductance in the depletion region, for a non-damaged wire at cut-off, defined as the wire width at which the wire ceases to conduct, the wire width will be simply $2d$, where d is the depletion region. However, for a damaged wire, the additional surface states produced from the dry etch process will cause the surface depletion width to widen, as a result, at cut-off, the wire width measured will be larger, and the damage width can be seen to be $(w_0 - 2d)$, where w_0 is the cut-off width for the epilayer. This situation is illustrated in figure 4.10 by a diagram of a wet and dry etched wire along with a graph of normalised conductance \times length plotted against wire widths^{4.37}. Since no appreciable damage is expected in wet etching, the cut-off wire width is equal to $2d \approx 40\text{nm}$, for n^+ GaAs with a donor concentration of $1.2 \times 10^{18}\text{cm}^{-3}$. In the case of dry etching, the additional damage layer causes w_0 , the cut-off wire width to increase to 100nm. This implies the thickness of the damaged layer is 30nm on each sidewall after SiCl_4 reactive ion etching at 0.44W/cm^2 power density with 300V d.c.bias.

4.3.5.2 Experimental

Material and fabrication outline

For fabricating n^+ GaAs quantum wires, the starting material used was a nominally $1.5 \times 10^{18}\text{cm}^{-3}$ Si-doped, 50nm thick GaAs epitaxial layer grown on a semi-insulating substrate by molecular beam epitaxy. The wafer was diced into 5 x

5 mm chips and sixteen (4 x 4) device patterns were defined by electron beam lithography using the converted Phillips PSEM 500 scanning electron microscope (SEM), see section 2.2.2. The lithographic steps consisted of two levels: ohmic/alignment marks and wire level. First, ohmic contacts and alignment/focussing markers were prepared by alloying Ge-Au-Ni-Au at 325°C. Two sets of alignment marks were necessary, one for aligning to the whole frame and the other for aligning the wires to the rest of the pattern, see next section. The next stage defines the mask needed for the particular etchant. After the required masks have been defined, the samples were wet etched in a potassium chlorate solution (KClO₃), and reactive ion etched in SiCl₄ and CH₄/H₂. The dry etching conditions were chosen to give clean, vertical sidewalls and optimum reproducibility.

Ohmic and alignment level

Single layer 15% PMMA in chlorobenzene (185,000 MW) \approx 1 μ m thick was spun onto the 5 x 5 mm chip at 5K rpm and baked at 180°C overnight. The ohmic, alignment, and focussing patterns were exposed with a 0.125 μ m spot at 50kV in a 1.56 x 1.18 mm frame, see figure 4.11. After exposure, the resist was developed in 1:1 MIBK:IPA at 23°C for 60s followed by a 30s rinse in IPA. The metallisation consisted of 100nm:20nm:50nm of Au₈₈Ge₁₂:Ni:Cu annealed in an Ar:H₂ 95:5 ambient at 325°C for 1 minute, which is the composition optimised for low temperature ohmic contacts formation^{4.40}. Prior to metallisation, the sample was etched in HCl:H₂O 1:1 for 30s to remove any surface oxide. Lift-off was performed in acetone.

Wire level

Standard bilayer resist was spun onto the GaAs chip and subsequently developed (see section 2.2.3). The e-beam exposures were carried out with a 16nm spot size at 50kV in a 100 x 76 μ m frame. In order to avoid exposing the rest of the sample, the wires were aligned to the rest of the pattern using the small registration marks (marked 'a') as shown in the bottom middle of figure 4.11 and refocussed using the same focussing marks (marked 'focus') for each exposure; the sample

was then moved down $10\mu\text{m}$ in the y-direction, realigned using the middle registration marks before exposure. To carry out the alignment process, two fine alignment patterns are scanned, one at a time, over the sample registration marks at $2\mu\text{s}$ per pixel, see figure 4.12a) and b). The first pattern contains dots around the registration marks and is used to look for the marks. Once the marks on the sample are found to be in the vicinity of the dots, or preferably close to the registration marks of the alignment scan, the second pattern, which contains outlines of the registration marks is used for fine alignment. When the registration marks is in the middle of the outlines of the alignment scan pattern, the exposure frame is deemed to be aligned. The alignment is achieved by adjusting the X-Y varymag, the stage rotation and the beam shifters.

In order to optimise the wire design for the devices, different designs were tried:

Design 1): see figure 4.13; in this design, the wires were fabricated by evaporating Ti from the left and right sides at an angle of 45° giving a total thickness of $\approx 300\text{\AA}$, lifted off in acetone, and then reactive ion etched. The double evaporation was important since a single evaporation had been carried out [using design 4)] and no conductivity was measured. This is attributed to the discontinuity between the wire and ohmic contact, see SEM 4.4. However, even with the use of a double evaporation, some wires still exhibited Schottky behaviour, indicating the possibility of 'cracking' at the ohmic-wire junctions. Nevertheless, it was possible to take preliminary measurements on the wires which conducted. In these measurements, a rapid fall to $0\mu\text{S}$ in the conductivity (nose dive) in the graph of conductivity vs. wire width was observed, see section 4.3.5.3. This is believed to be due to the non-uniformities in the wire width near the wire-ohmic junction as shown in SEM 4.5.

Design 2): this is essentially the same as design 1 but instead of Ti, 8% HRN negative resist was used as the dry etch mask (see section 2.2.4). However, after CH_4/H_2 etching, the resist was found to have shrunk. A similar occurrence was also observed during the fabrication of GaAs sidewall Schottky diodes, see section 3.5. Because of this, it was not possible to plot the graph of conductance vs. wire width making this design not viable.

Design 3): this design is very similar to design 1), but two extra pads are placed between the ohmic and wire contact where 8% HRN resist was used to cover the junction discontinuity and to eliminate the possibility of 'cracking' at the junction, see figure 4.14. This design rendered satisfactory results and some preliminary data was taken (see section 4.3.5.3). In addition, no 'nose-diving' behaviour was observed in the graph of conductivity vs. wire width, this is perhaps indicative of the absence of wire non-uniformity. But the main drawback with this technique was the additional stage needed to pattern the HRN resist.

Design 4): this is the optimum design whereby the problems of discontinuity, 'cracking', and fluctuation of wire width at the ohmic-wire junction were solved, and the ease of processing was encouraged. This was possible by combining the use of design 3) and a double evaporation of $Ti \approx 300\text{\AA}$, see figure 4.15. In this way, no discontinuity was observed between the wire and ohmic contact as shown in SEM 4.6; the wire widths did not fluctuate as in design 1), see SEM 4.7; and the 'nose-dive' behaviour was no longer observed, see section 4.3.5.4.

Figure 4.16 and SEM 4.8 show the wire design pattern of widths varying from $0.08\mu\text{m}$ to $0.9\mu\text{m}$.

RIE in CH_4/H_2

For CH_4/H_2 etching, a ratio of one part CH_4 to five parts H_2 (by volume flow rate) at a power density of $0.4\text{W}/\text{cm}^2$, 14mT total gas pressure and a d.c. bias of 1kV was used. The etch rate of GaAs under these conditions is $20\text{nm}/\text{min.}$, see section 2.7.2 for details of the machine used.

RIE in SiCl_4

For SiCl_4 etching, a power density of $0.44\text{W}/\text{cm}^2$, 9sccm volume flow rate, 12mT total gas pressure and a d.c. bias of 300V was used. Details of the machine used can be found in section 2.6.2. A useful dry etch mask for this etchant has been found to be NiCr lifted-off from PMMA, see section 2.3.1, with a GaAs

to mask etch ratio of $>50:1$ ^{4.37}. Although high resolution negative resist HRN is not so resistant to the etch with a GaAs to mask etch ratio of $>10:1$ and has poorer resolution than PMMA (30 vs 10 nm), it was adequate for this experiment and therefore was used due to its ease of processing.

Wet etching

The wet etch used was a HCl:KClO₃ [aqueous (aq)]; 50:1 mixture, where the KClO₃ (aq) is a 1% solution by weight. In order to characterise the etch rate of this solution, 8% HRN lines were patterned (see section 2.2.4) on $6.5 \times 10^{17} \text{cm}^{-3}$ Si-doped GaAs using an electron beam with a $0.125 \mu\text{m}$ spot size at 50kV in a 0.77×0.59 mm frame. The samples were wet etched for different time durations and the depth of etch measured using a Talystep. It was found that the solution etches GaAs isotropically at a rate of $\approx 5 \text{nm/min.}$, see figure 4.17 and SEM 4.9.

Annealing

To investigate the effect of annealing on hydrogenation and damage after CH₄/H₂ etching, GaAs samples were annealed at different temperatures. The annealing procedure was carried out on a strip heater in a 95:5 Ar:H₂ ambient^{4.40}.

The conductivity measurements were performed using the four point probe technique in conjunction with an HP 4145A semiconductor parameter analyser.

4.3.5.3 Preliminary Data

Initially, with the use of design 1), a set of wires was fabricated using CH₄/H₂ reactive ion etching, most of the wires exhibited Schottky behaviour. This was attributed to the possibility of 'cracking' between the wire and ohmic contact, see section 4.3.5.2. Consequently, another set of wires was fabricated using design 3), from a plot of conductance vs. wire width shown in figure 4.18, a cut-off width of $0.4 \mu\text{m}$ was measured. This implied a large amount of damage was caused by CH₄/H₂ reactive ion etching. However, from the knowledge of the donor and

defect passivation in GaAs and other semiconductors after exposure to hydrogen plasmas^{4.13-25}, and previous damage studies carried out on the etched surfaces, see sections 4.3.2-4.3.4, it was decided to investigate further the possibility of a similar occurrence in these GaAs wires through the effect of annealing. Therefore, two sets of wires were fabricated using design 1), see section 4.3.5.2. One set was annealed at 375°C for 2 minutes and the other for 4 minutes. The conductance vs. wire width plots are shown in figures 4.19a) and b). While both plots show "nose-dive" behaviour towards 0.1µm probably as a result of the fluctuation of wire widths (see section 4.3.5.2), extrapolation of the linear parts of the graph gives a cut-off width of $\approx 0.05\mu\text{m}$, and for n^+ GaAs with a donor concentration of $1.5 \times 10^{18}\text{cm}^{-3}$, this value approaches those of damage-free wires. The different anneal times did not cause a great deal of difference in the measured cut-off widths. The enormous dependence of cut-off width on anneal temperature clearly suggests the occurrence of donor depassivation. Therefore, the cut-off width and resistivity dependence on different anneal temperatures and anneal times was investigated further using a proper wire design.

4.3.5.4 Results and Discussion

Using design 4), various sets of wires were fabricated, annealed and measured. Figure 4.20 shows a comparison of cut-off characteristics of CH_4/H_2 (before annealing), SiCl_4 , and wet etched wires. (Notice there was no more "nose-dive" behaviour as observed using design 1). The extrapolated cut-off width of the wet etched wires is $40\text{nm} \pm 10\text{nm}$. The mean value is roughly twice the surface depletion depth for material of this doping density, which is as expected since wet etching is not believed to cause appreciable surface damage. The SiCl_4 etched wires exhibit cut-off widths of $(100 \pm 5)\text{nm}$, implying a damaged region of $\approx 30\text{nm}$ on each sidewall, which agrees with previous data^{4.37}. The effect of both hydrogenation and damage for the CH_4/H_2 etched wires shifts the cut-off width to 400nm. A resistivity change is also evident from the change in gradient for the CH_4/H_2 etched wires compared with the wet etched wires. While it is likely that this is due to the graded carrier profile caused by hydrogen penetration from the sidewalls, the possibility of hydrogen diffusion through the thin Ti mask (which is thick enough to prevent etching) during etching cannot be ruled out.

The wire samples were then annealed at 200°C, 300°C, 380°C and 450°C for 2 minutes: the corresponding cut-off characteristics are plotted in figure 4.21. A cut-off width of (80±5) nm and full recovery of conductivity were obtained by annealing at 300°C for 2 minutes. Longer anneals did not reduce the cut-off width. Therefore, while the cut-off widths of depassivated CH₄/H₂ etched wires are measurably smaller than those etched by SiCl₄, it appears that the process causes ≈ 20nm of damage to each sidewall. It is worth noting that Chevalier et al.^{4.18} observed reductions in conductivity after exposures of heavily doped epilayers to hydrogen plasmas, of which only 50% could be recovered by annealing. This they attributed to near-surface damage. On the other hand, in this experiment, the carriers in the core of the wire were completely recovered, but sidewall damage is observed. Evidently the mask is capable of protecting the bulk of the wire, but not the sidewalls, from damage by the etching process. Lower conductances were measured for the wires annealed at 450°C. This is attributed to the degradation of the ohmic contacts according to measurements of TLM patterns^{4.40} fabricated on the same chip. The possibility of As vaporization is unlikely since its sublimation temperature is ≈ 613°C.

The cut-off widths of wires subjected to very short anneals were also investigated. Full recovery of carriers was found experimentally for anneal times as low as 1 second. Using Fick's law of diffusion based on the hypothesis that the rate of transfer of diffusing substance through unit area of a section is proportional to the concentration gradient measured normal to the section:

$$F = -D \, dn/dy \quad (4.3)$$

where F is the rate of transfer per unit area of section, n is the concentration of diffusing substance, y is the space coordinate measured normal to the section, and D is the diffusion coefficient, it is possible to estimate the time required to complete the depassivation process.

A schematic diagram of a quantum wire is shown in figure 4.22. The diffusion lengths and coefficients of hydrogen in GaAs as a function of anneal temperature have been determined previously by Zavada et. al.^{4.41}. Assuming all the donors in the wire are passivated, the diffusion direction of the hydrogen is in

the y-direction only and a constant diffusion coefficient; taking $n = 1.5 \times 10^{18} \text{cm}^{-3}$, $y = 50 \times 10^{-7} \text{cm}$, and $D = 0.368 \times 10^{-10} \text{cm}^2 \text{s}^{-1}$ at 300°C from ref.4.41 and substituting in equation 4.2, the flux can be calculated to be 1.1×10^{13} per unit area per second. Therefore, the time taken to depassivate the donors is given by:

$$w y \ln n / F w l = y n / F \quad (4.4)$$

and on substituting the values for y, n and F, the time is calculated to be 0.68 second, which is in agreement with the experimental data. However, it is important to note that while the above analysis assumes the direction of the hydrogen diffusion to be outward in the y-direction into the atmosphere, it is equally possible for the hydrogen to indiffuse, especially at this anneal temperature, as has been suggested by others^{4.19, 4.42} and the present surface damage studies, see section 4.3.4.

4.4 Conclusions

1) A novel RIE process was developed to etch GaAs anisotropically. Preconditioning of the etch chamber using O_2 and H_2 led to a reduction in water and carbon contaminants in the etch chamber. A suitable mask for this etch was found to be Ti which possesses a relative low sputtering yield. The etch rate and profile dependence on power density and the % of CH_4 in H_2 around the optimum etch condition were investigated.

2) From electrochemical profiling, the occurrence of atomic H_2 passivation of the Si-donors in the etched surfaces was evident from the total recovery of the carrier concentration with annealing.

3) While diode characteristics of the etched, unannealed and annealed surfaces after CH_4/H_2 RIE suggest the effects of hydrogenation, and damage in terms of interface traps, comparison with the electrical characteristics of the surfaces after SiCl_4 RIE indicate lower damage is introduced by the CH_4/H_2 process.

4) Comparison of the PL output intensities of the SiCl_4 and CH_4/H_2 etched surfaces suggests less nonradiative deep centres are introduced by the CH_4/H_2

process consistent with previous diode measurements. Such high luminescence intensities observed for the CH_4/H_2 etched surfaces are believed to be due to the passivation of the non-radiative centres by the atomic H_2 . However, the overall decrease in luminescence observed is attributed to the higher rate of introduction of non-radiative centres compared with their passivation rate. While the dependence of PL output intensities on annealing time suggests the occurrence of both donor recovery and non-radiative centre passivation, its dependence on anneal temperature indicate the presence of a H outdiffusion process.

5) The effect of hydrogenation and damage on the etched sidewalls was investigated by measuring the conductances and cut-off widths of n^+ GaAs quantum wires. Results show that while hydrogenation occurs throughout the whole wire after CH_4/H_2 etching, the effect of annealing recovers the conductance (donors) in the core of the wire, but not the sidewalls. This is indicative of the presence of sidewall damage, whose width is of the order 20nm on each sidewall.

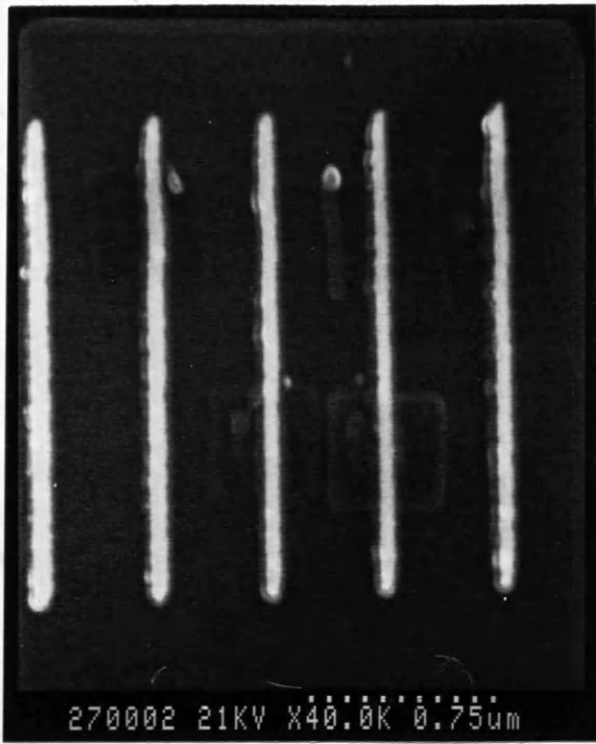
6) Theoretical calculation of the dependence of donor recovery with anneal time in these wires agrees with the experimental data.

4.5 References

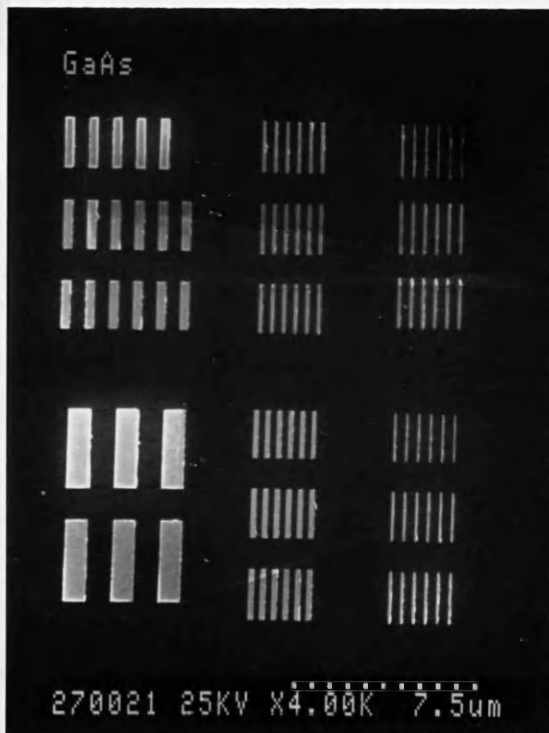
- 4.1) M.T.Mocella, M.W.Jenkins, H.H.Sawin and K.D.Allen; *Mat. Res. Soc. Proc.* **38** p.227, 1985
- 4.2) G.M.McCracken and P.E.Stott; *Nucl. Fusion*, **19** p.889, 1979
- 4.3) F. Waelbroeck, J.Winter and P.Wienhold; *J.Vac.Sci.Technol.* **A2(4)** p.1521, 1984
- 4.4) 'Ion bombardment modification of surfaces, Fundamentals and Applications', edited by O.Auciello and R.Kelly, Elsevier, 1984
- 4.5) N.Laegreid and G.K.Wehtner; *J. of Appl. Phys.* **32(3)** p.365, 1961
- 4.6) R.Cheung, S.Thoms, S.P.Beaumont, G.Doughty, V.Law and C.D.W.Wilkinson, *Electron. Letts.* **23** p.857, 1987
- 4.7) M.W.Geis, G.A.Lincoln, N.Efremow and W.J.Piacentini; *J.Vac.Sci.Technol.* **19(4)** p.1390, 1981
- 4.8) J.D.Chinn, A.Fernandez, I.Adesida and E.D.Wolf; *J.Vac.Sci.Technol.* **A1(2)** p.701, 1983
- 4.9) J.D.Chinn and E.D.Wolf; *J.Vac.Sci.Technol.* **B3(1)** p.410, 1985
- 4.10) R.P.H.Chang, C.C.Chang and S.Darack; *J.Vac.Sci.Technol.* **20** p.45, 1982
- 4.11) D.L.Flamm and V.M.Donnely; 'The Design of Plasma Etchants', *Plasma Chem. and Plasma Process.*, **1** p.317, 1981
- 4.12) V.Law and G.A.Jones; *Semiconductor Sci. Technol.* ? 1989
- 4.13) A.Jalil, J.Chevalier, J.C.Pesant, R.Mostefaoui, B.Pajot, P.Murawala and R.Azoulay; *Appl. Phys. Letts.* **50(8)** p.439, 1987
- 4.14) A.Jalil, J.Chevalier, R.Azoulay and A.Mircea; *J. Appl. Phys.* **59(11)** p.3774, 1986
- 4.15) S.J.Pearson; *J. Appl. Phys.* **53(6)** p.4509, 1982
- 4.16) S.J.Pearson, C.S.Wu, M.Stavola, F.Ren, J.Lopata and W.C.Dautremont-Smith; *Appl. Phys. Letts.* **51(7)** p.496, 1987
- 4.17) S.J.Pearson, W.C.Dautremont-Smith, J.Chevalier, C.W.Tu and K.D.Cummings; *J. Appl. Phys.* **59(8)** p.2821, 1986
- 4.18) J.Chevalier, W.C.Dautremont, C.W.Tu and S.J.Pearson; *Appl. Phys. Letts.* **47(2)** p.108, 1985
- 4.19) S.J.Pearson, J.W.Corbett and T.S.Shi; *Appl. Phys. A*, **43** p.153, 1987
- 4.20) J.Weber, S.J.Pearson and W.C.Dautremont-Smith; *Appl. Phys. Letts.* **49(18)** p.1181, 1986
- 4.21) W.C.Dautremont-Smith, J.C.Nabity, V.Swaminathan, M.Stavola, J.Chevalier, C.W.Tu and S.J.Pearson; *Appl. Phys. Letts.* **49(17)** p.1098, 1986

- 4.22) J.C.Nabity, M.Stavola, J.Lopata, W.C.Dautremont-Smith, C.W.Tu and S.J.Pearton; *Appl. Phys. Letts.* **50(14)** p.921, 1987
- 4.23) J.Lagowski, M.Kaminska, J.M.Parsey Jr., H.C.Gatos and M.Lichtensteiger; *Appl. Phys. Letts.* **41(11)** p.1078, 1982
- 4.24) N.Pan, S.S.Bose, M.H.Kim, G.E.Stillman, F.Chambers, G.Devane, C.R.Ito and M.Feng; *Appl. Phys. Letts.* **51(8)** p.596, 1987
- 4.25) T.R.Hayes, W.C.Dautremont-Smith, H.S.Luftman and J.W.Lee; *Appl. Phys. Letts.* **55(1)** p.56, 1989
- 4.26) J.S.Wang, S.J.Fonash and S.Ashok; *IEEE Electron Device Letts.* **4** p.4326, 1983
- 4.27) S.J.Pearton, A.J.Tavendale and E.M.Lawson; *Radiation Effects*, **79** p.21, 1983
- 4.28) R.Cheung, S.Thoms, I.McIntyre, C.D.W.Wilkinson and S.P.Beaumont; *J.Vac.Sci.Technol.* **B6** p.1911, 1988
- 4.29) E.Constant, N.Caglio, J.Chevalier and J.C.Pesant; *Electron. Letts.* **23(16)** p.841, 1987
- 4.30) P.Friedel, P.K.Larsen, S.Gourrier, J.P.Cabanie and W.M.Gertis; *J.Vac.Sch.Technol.* **B2(4)** p.675, 1984
- 4.31) G.S.Jackson, J.Berberman, M.S.Feng, K.C.Hsieh, N.Holonyak Jr. and J.Verdeyen; *J. Appl. Phys.* **64(10)** p.5175, 1988
- 4.32) F.H.Mullins and A. Brunnschweiler; *Solid State Electronics*, **19** p.47, 1976
- 4.33) Y.X.Wang and P.H.Holloway; *J.Vac.Sci.Technol.* **B2(4)** p.613, 1984
- 4.34) C.S.Wu, D.M.Scott, W.X.Chen and S.S.Lau; *J. Electrochem. Soc.* **132(4)** p.918, 1985
- 4.35) P.Kwan, K.N.Bhat, J.M.Borrego and S.K.Ghandhi; *Solid State Electronics*, **26(2)** p.125, 1983
- 4.36) X.C.Mu, S.J.Fonash, A.Rohatgi and J.Reiger; *Appl. Phys. Letts.* **48** p.1147, 1986
- 4.37) S.Thoms, S.P.Beaumont, C.D.W.Wilkinson, J.Frost and C.R.Stanley; *Microcircuit Engineering 1986*, edited by H.W.Lehmann and Ch. Bleicker (North-Holland, Amsterdam, 1986), p.249
- 4.38) A.Chandra, C.E.C.Wood, D.W.Woodard and L.F.Eastman; *Solid State Electronics*, **22** p.645, 1979
- 4.39) W.Patrick, W.S.Mackie, S.P.Beaumont and C.D.W.Wilkinson; *Appl. Phys. Letts.* **48** p.986, 1986
- 4.40) W.Patrick; Ph.D. thesis, 1985

- 4.41) J.M.Zavada, H.A.Jenkinson, R.G.Sarkis and R.G.Wilson; J. Appl. Phys. **58** p.3731, 1985
- 4.42) J.M.Heddleson, M.W.Horn, S.J.Fonash and D.C.Nguyen; J.Vac.Sci.Technol. **B6(1)** p.280, 1988
- 4.43) M.A.Foad; First year Ph.D. report, 1989
- 4.44) N.I.Cameron; First year Ph.D. report, 1989
- 4.45) N.I.Cameron, S.P.Beaumont, C.D.W.Wilkinson, N.P.Johnson, A.H.Kean and C.R.Stanley; paper presented at the 15th international conference on Microlithography, Microcircuit Engineering, Cambridge, 1989



SEM 4.1 Ti lines of widths 450\AA - 550\AA lifted-off from double layer PMMA resist on GaAs with electron beam exposure dosages varying from $2000\text{-}3500\mu\text{C}/\text{cm}^2$



SEM 4.2 shows the entire exposure test pattern

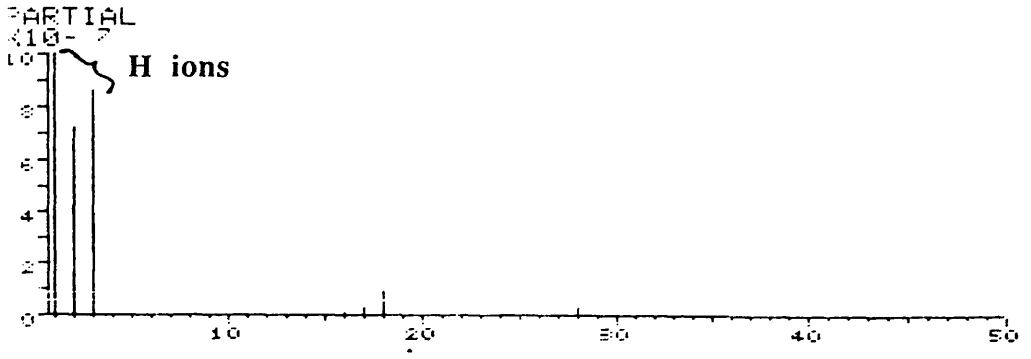


Figure 4.1 RGA signal of the chamber with the addition of H₂ gas after 30 minutes of cleaning in an O₂ plasma

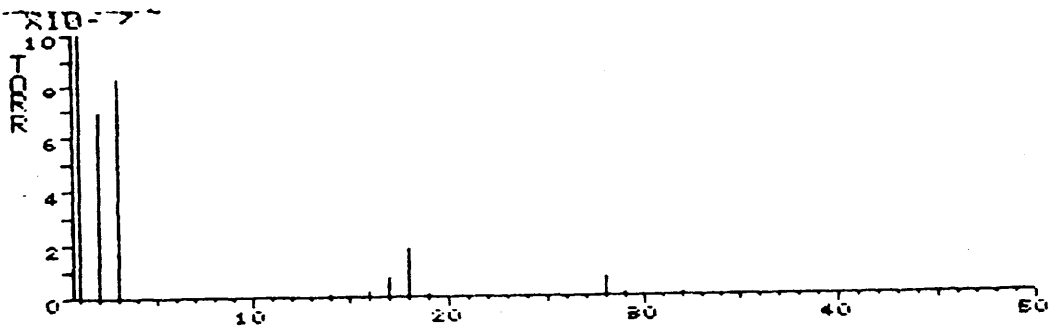


Figure 4.2a) RGA signal with H₂ plasma for 10 mins.

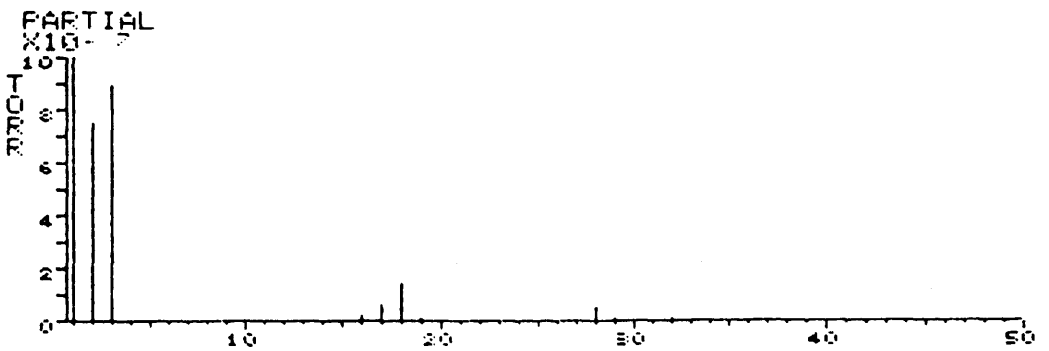


Figure 4.2b) RGA signal with H₂ plasma for 15 mins.

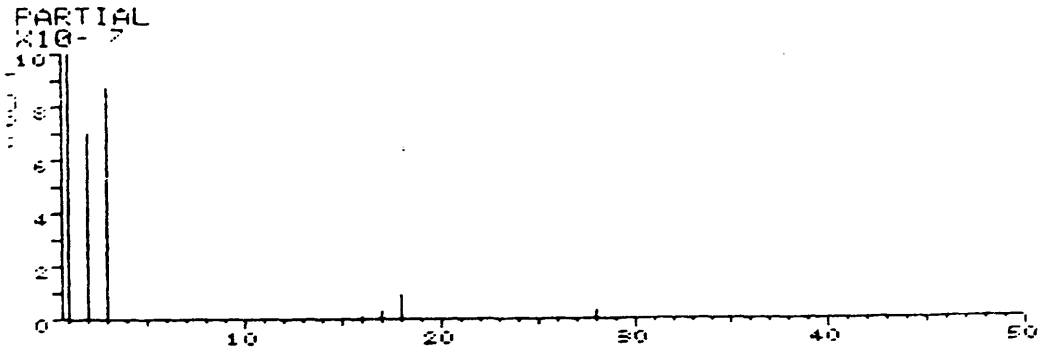


Figure 4.2c) RGA signal with H_2 plasma for 25 mins.

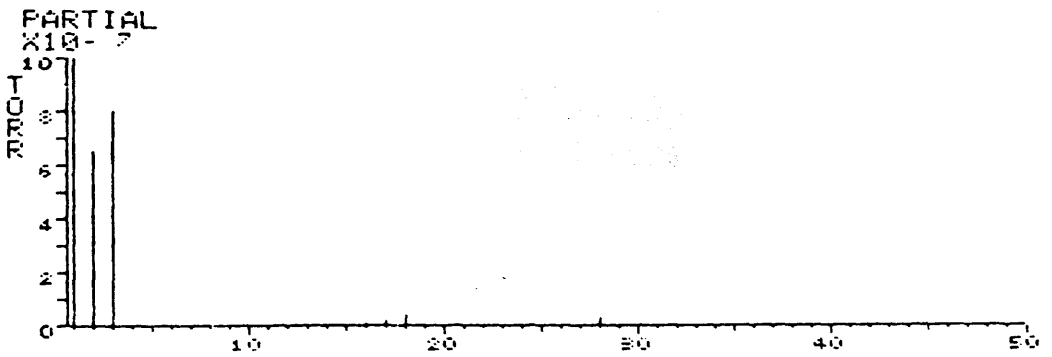


Figure 4.2d) RGA signal of the chamber after H_2 plasma for 30 mins.

Etch rate (nm/min.)



SEM 4.3 A thin GaAs rib of width 30nm fabricated by reactive ion etching in CH_4/H_2 under the optimum conditions (see text) using a 50nm thick Ti mask

Etch rate (nm/min.)

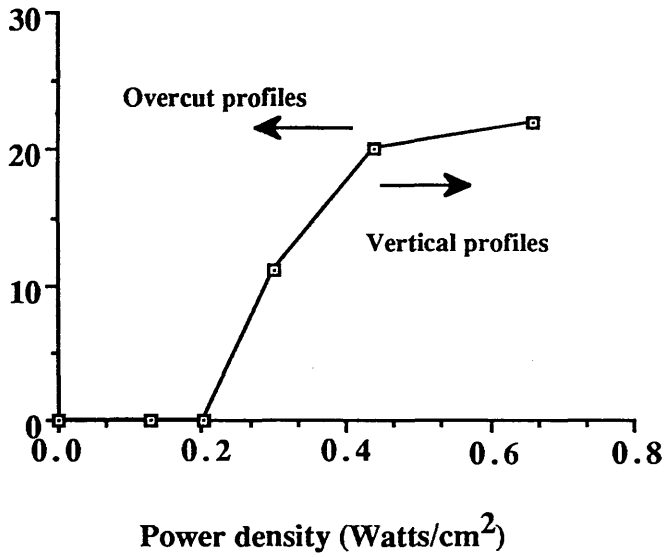


Figure 4.3 Etch rate and etch profile dependence on power density in the of RIE GaAs using CH₄/H₂

Etch rate (nm/min.)

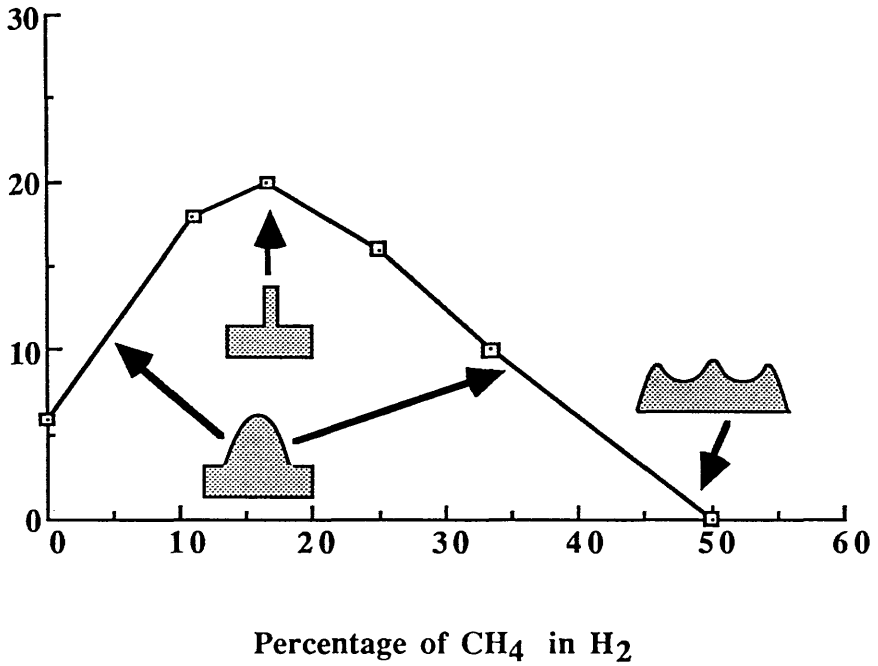


Figure 4.4 Etch rate and sidewall profile dependence on feed gas composition in the RIE of GaAs using CH₄/H₂

Power density and total gas pressure were kept constant at 0.4W/cm² and 14mTorr respectively

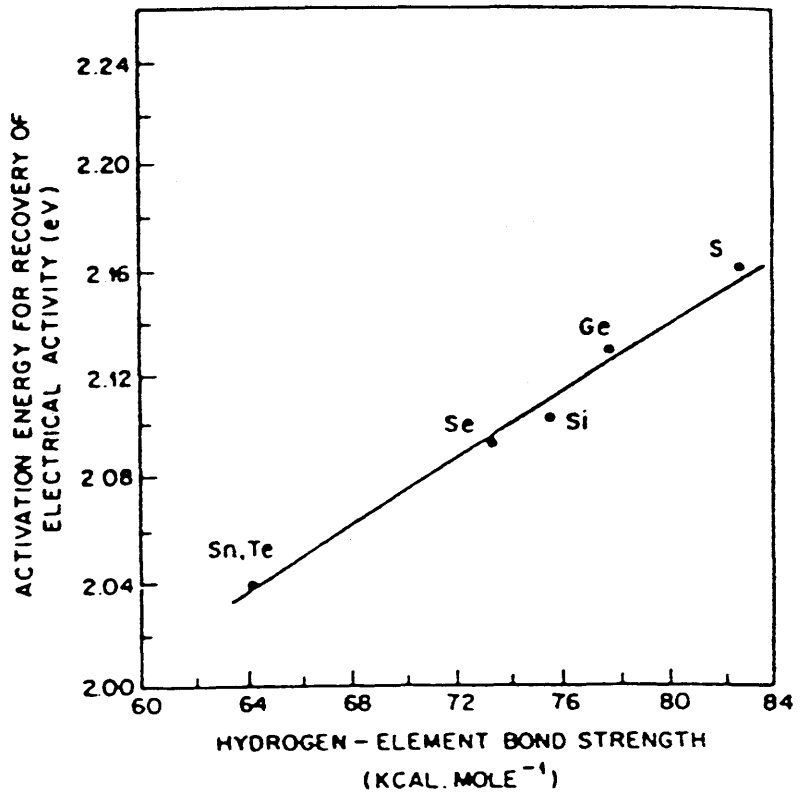


Figure 4.5 Plot of experimentally determined reactivation energies for each donor element vs. hydrogen-donor species bond strength for each element. (After Pearton et. al. ref. 4.17)

Carrier concentration (cm^{-3})

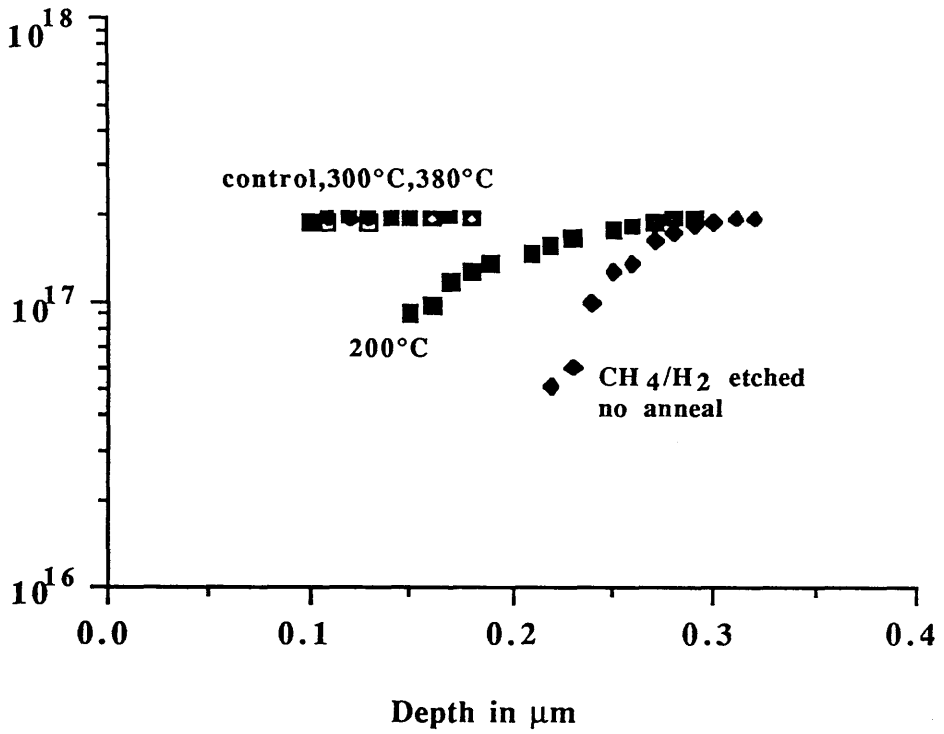


Figure 4.6 Carrier concentration profiles at different annealing temperatures for 2 mins. in GaAs (Si) after CH₄ /H₂ etching

	Control	CH4/H2 etched	200C anneal	380C anneal
Ideality factor	1.04	1.06	1.07	1.06
Barrier height	0.75eV	0.99eV	0.81eV	0.76eV
Reverse breakdown voltage	-9V	-12V	-11V	-8V
Turn on voltage	0.6±0.05V	1.1±0.05V	0.9±0.05V	0.5±0.05V
Reverse leakage current at -2V	-21pA	-2.435nA	-2.255nA	-2.935nA

Table 4.1 Summary of measurements derived from I-V characteristics as a function of anneal temperature (for 2 minutes)

Ideality factor (n)

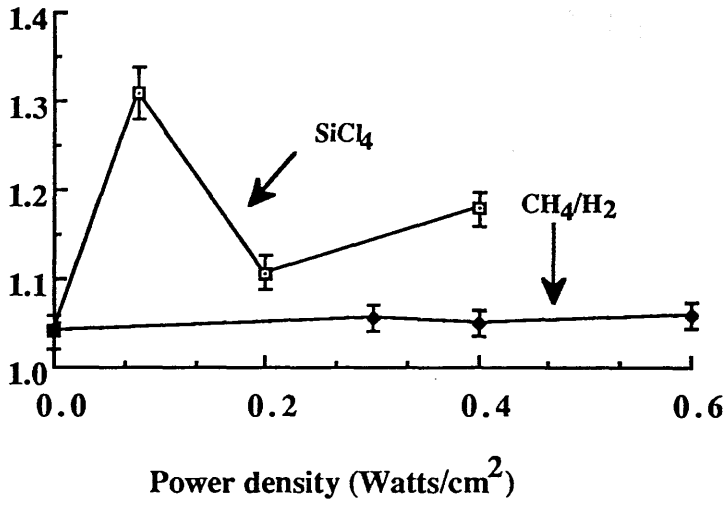


Figure 4.7 Comparison of ideality factors as a function of power density for GaAs surfaces after CH₄/H₂ and SiCl₄ RIE

Normalised PL intensity

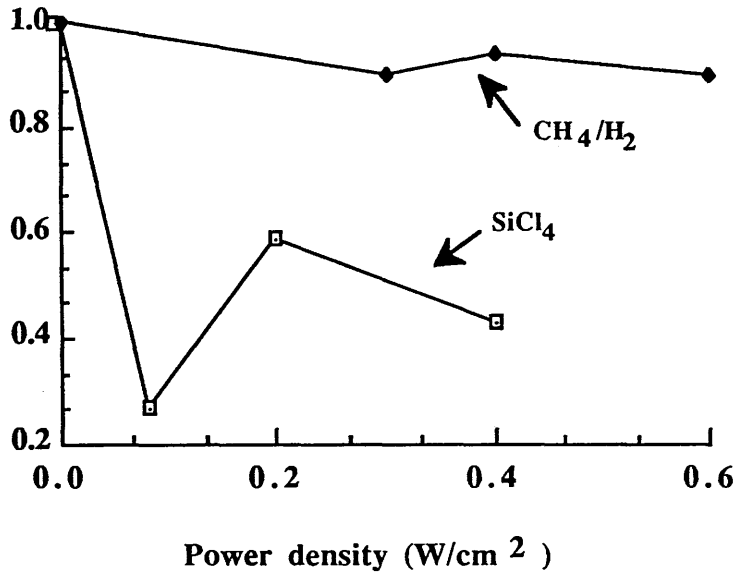
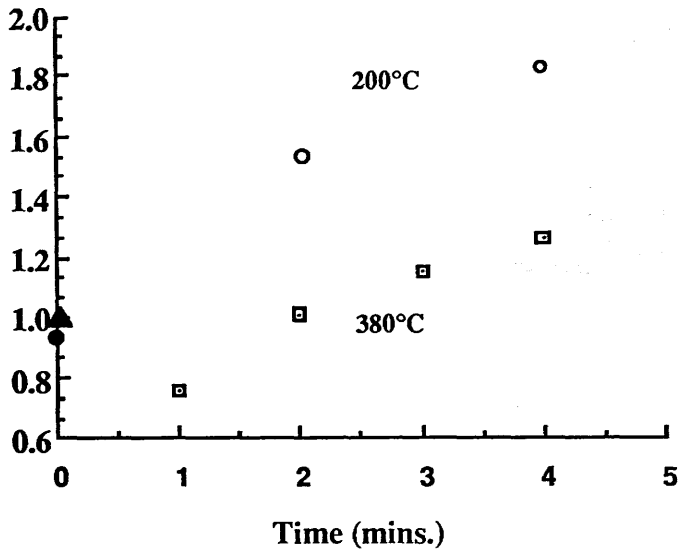


Figure 4.8 Graph of integrated PL intensity vs. power density for GaAs surfaces reactive ion etched in SiCl₄ and CH₄/H₂

Normalized PL intensity



- ▲ unetched; unetched and annealed samples
- CH₄/H₂ etched
- CH₄/H₂ etched and annealed at 200°C
- ◻ CH₄/H₂ etched and annealed at 380°C

Figure 4.9 showing normalised PL intensity vs. anneal time for the hydrogenated samples at anneal temperatures of 200°C and 380°C

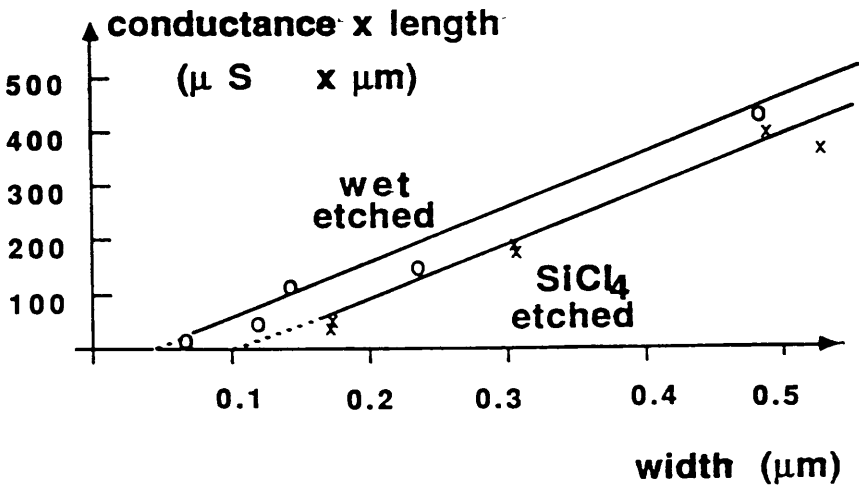
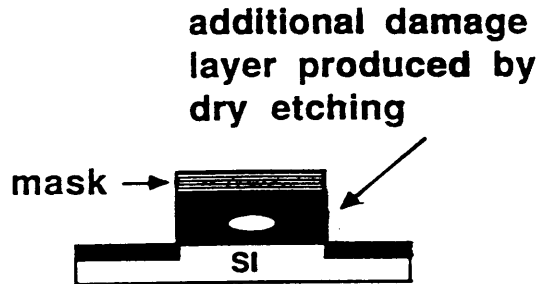
Wet etched



Conducting region

Cut-off wire width
= 2 x depletion width

Dry etched



Epilayer 65nm thick ,doping $1.2 \times 10^{18} \text{ cm}^{-3}$
etched at a dc bias of 300V

Figure 4.10 Schematic diagram of a wet and dry etched wire, and a graph of conductance vs. width. (After S. Thoms. et. al. ref. 4.37)

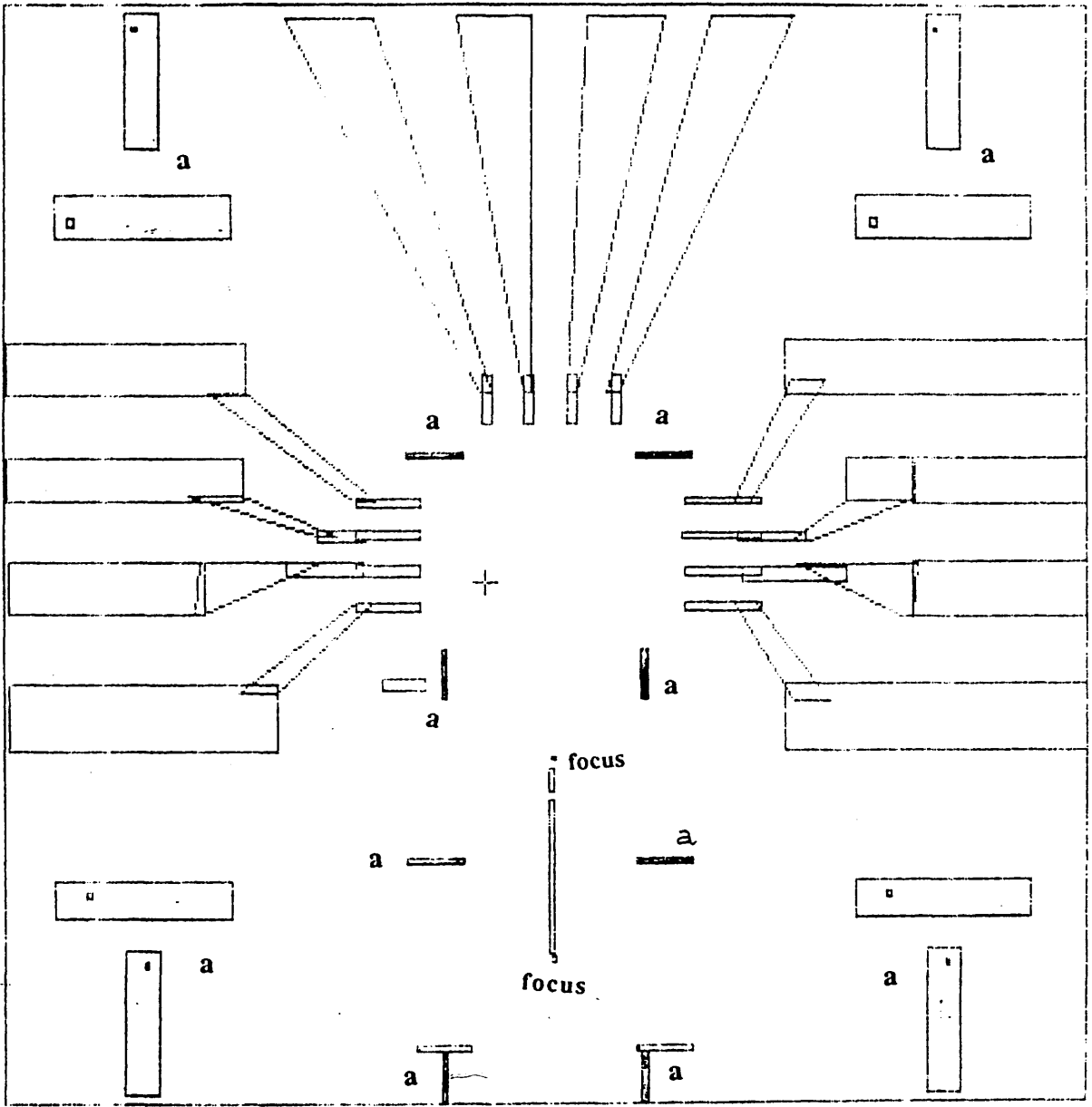
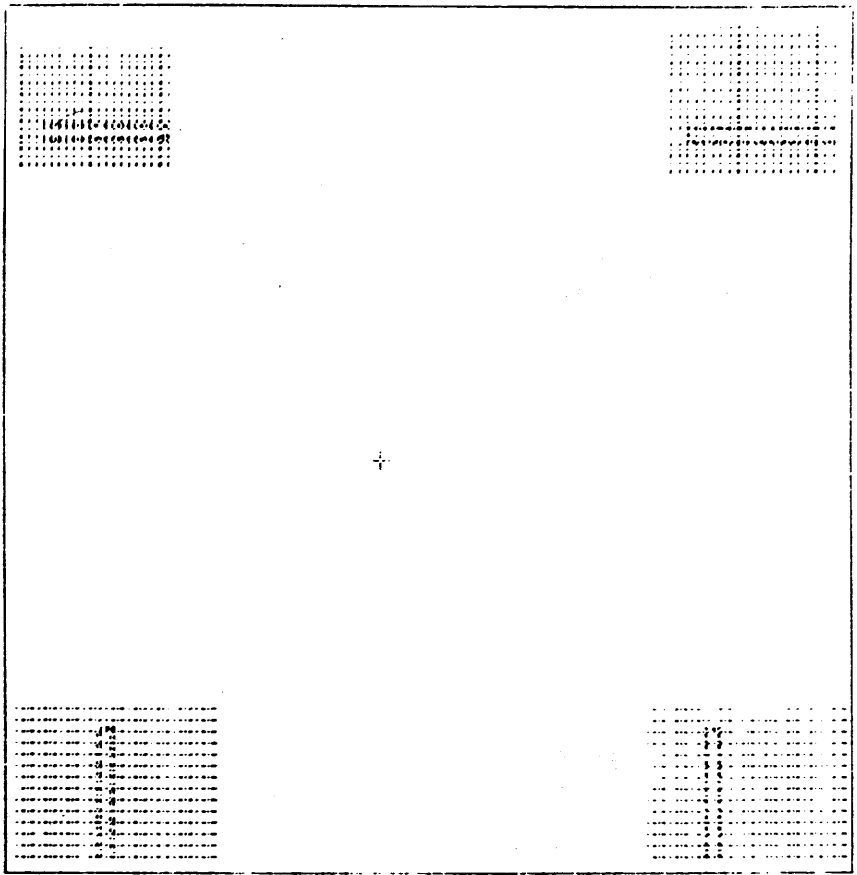
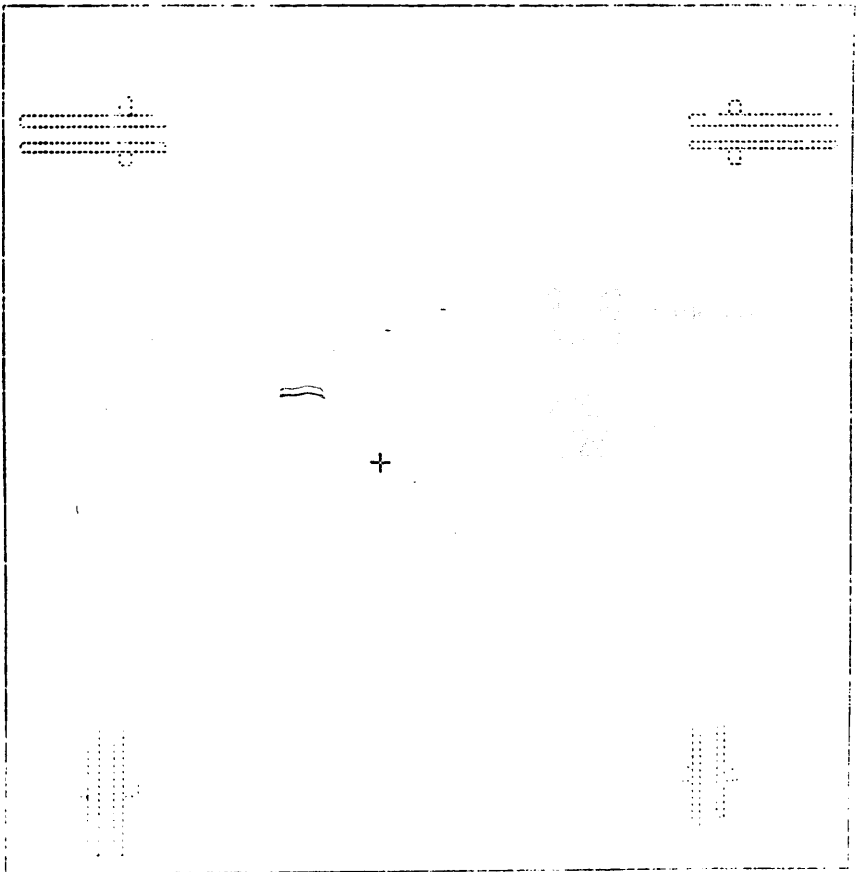


Figure 4.11 showing ohmic, alignment (a) and focussing patterns



a)



b)

Figure 4.12a) and b) showing alignment scans used for aligning

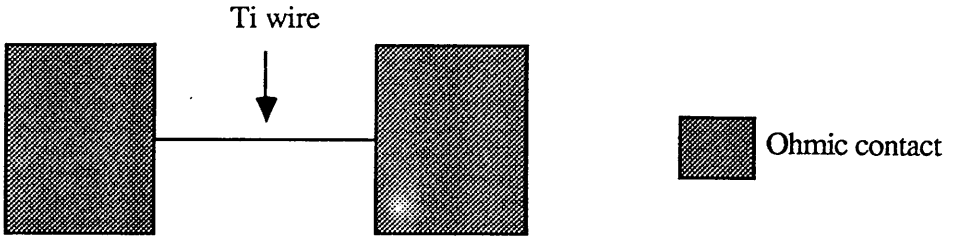


Figure 4.13

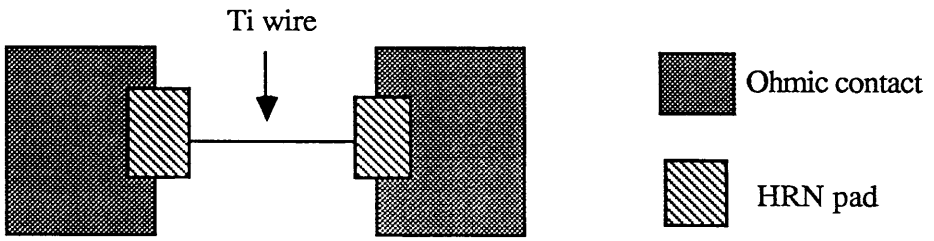


Figure 4.14

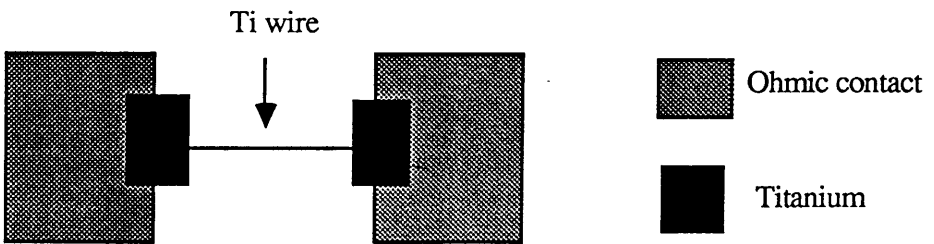
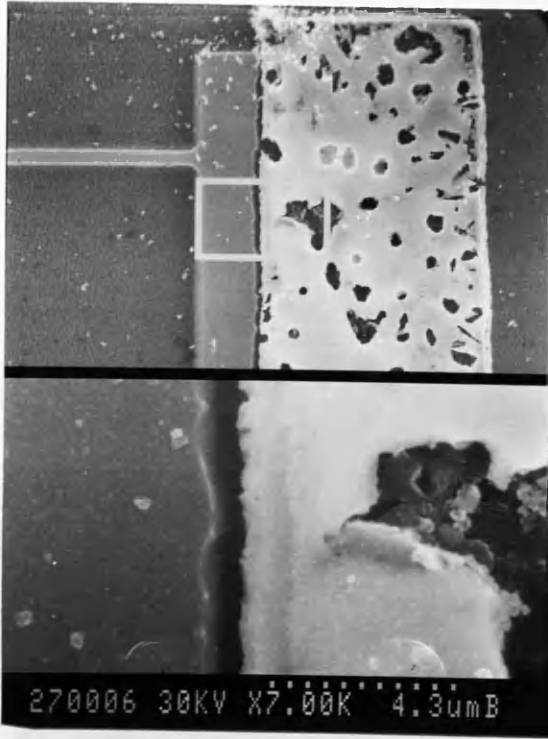
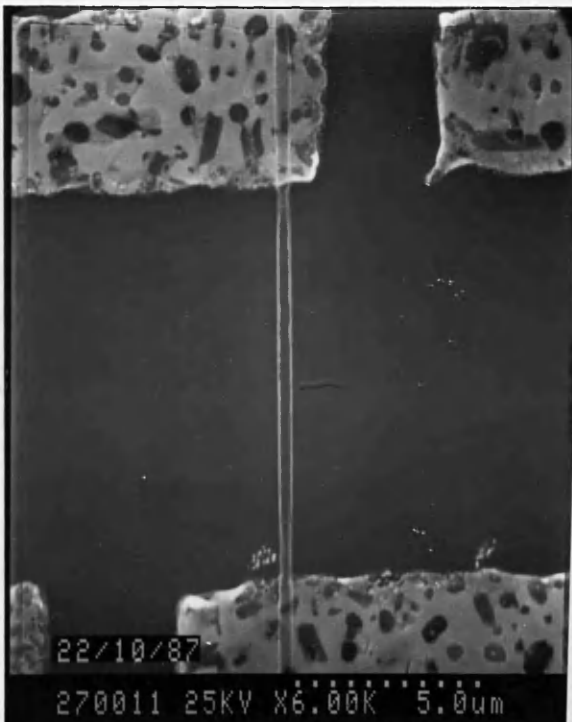


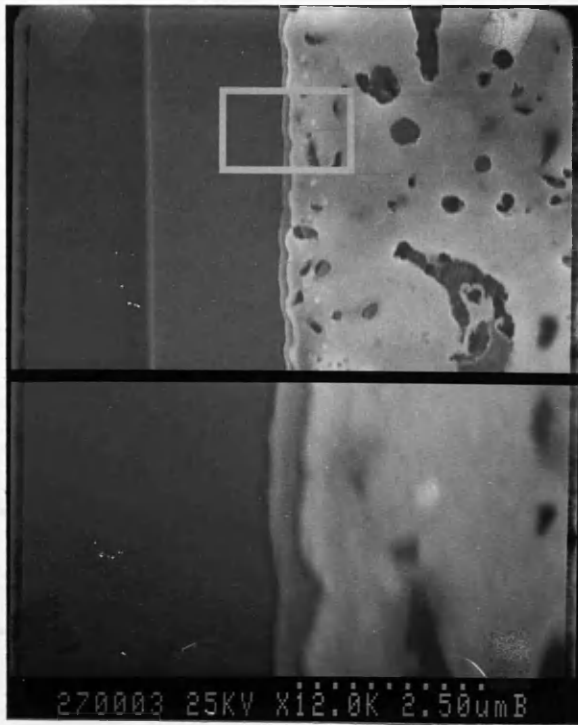
Figure 4.15



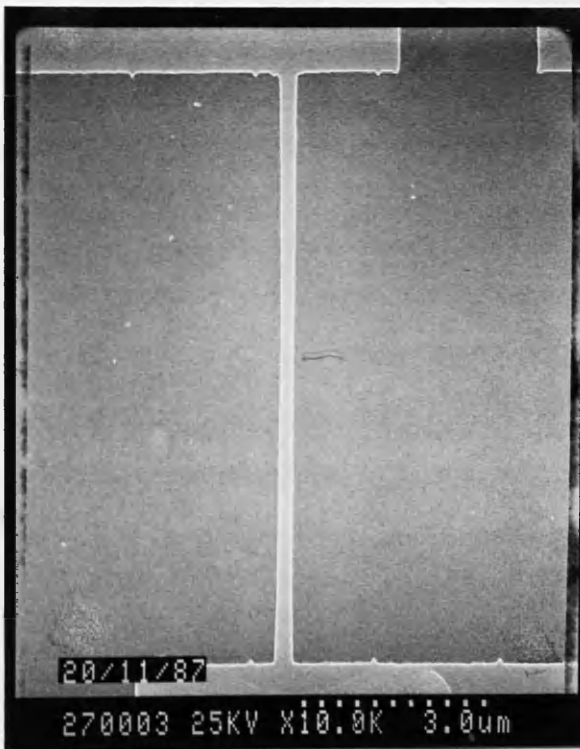
SEM 4.4 showing discontinuity between the Ti wire and ohmic contact in design 4) using a single Ti evaporation



SEM 4.5 The presence of wire-width fluctuation near the wire-ohmic junction in design 1)



SEM 4.6 showing the absence of discontinuity between the wire and ohmic junction using a double Ti evaporation in design 4)



SEM 4.7 The absence of fluctuation of wire width in design 4)

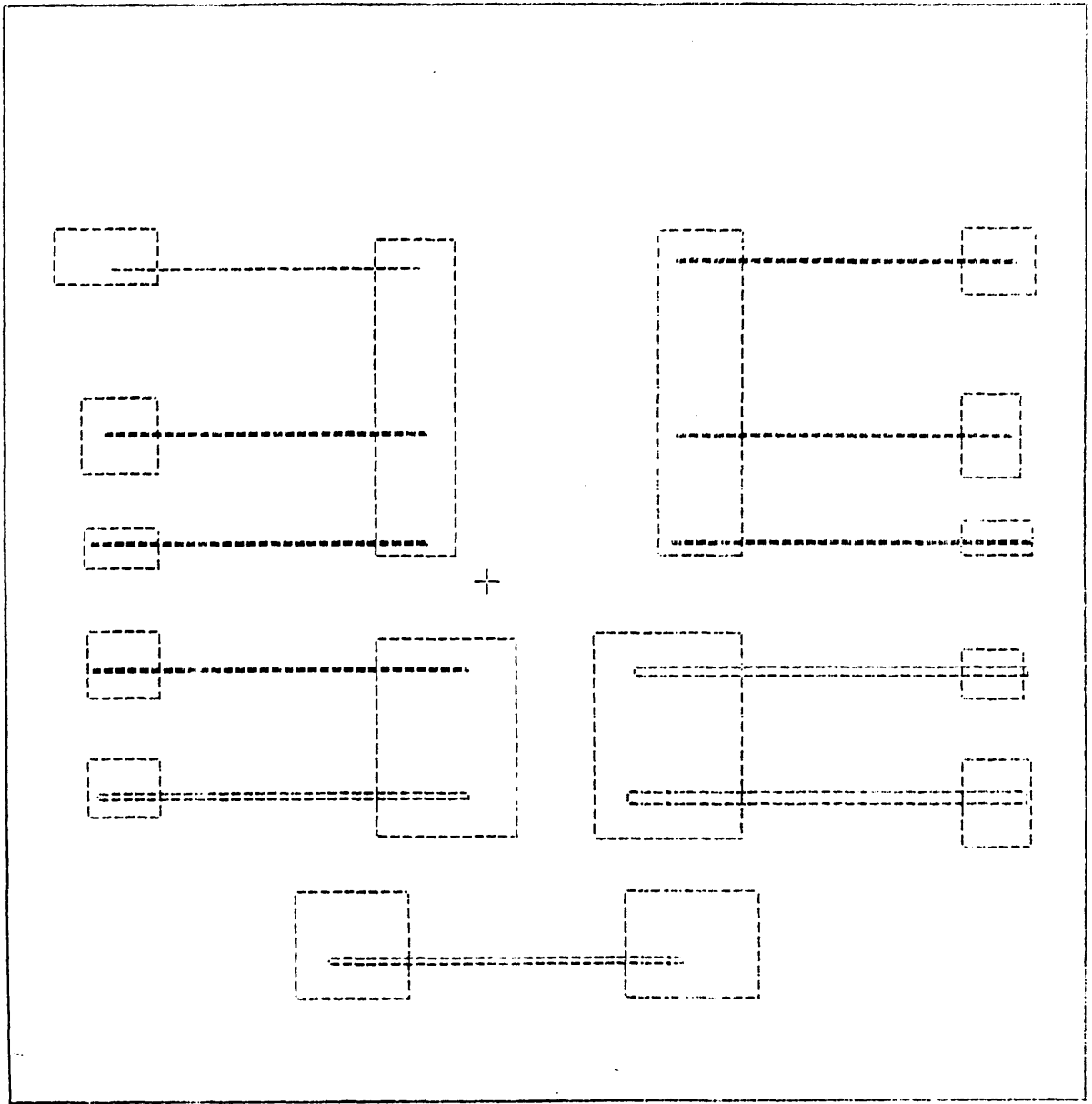
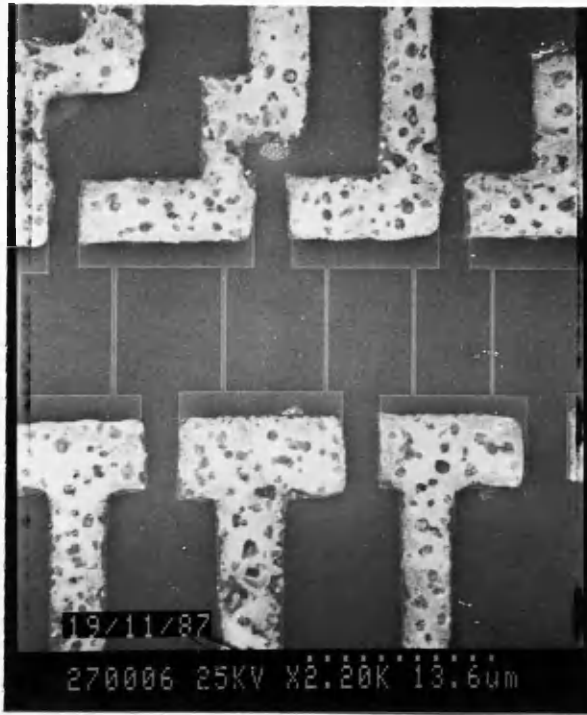
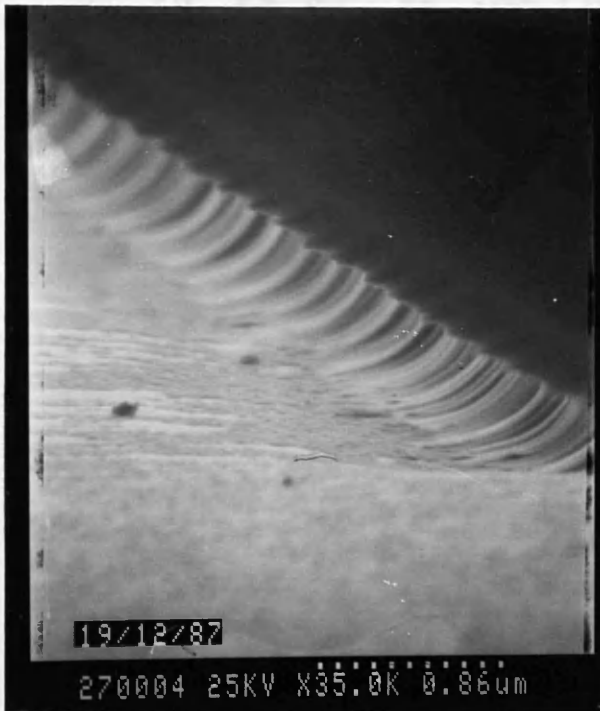


Figure 4.16 showing the entire wire design



SEM 4.8 Wire pattern of varying widths using the optimum design



SEM 4.9 GaAs wet etched in a HCl:KClO₃ (aq.) 50:1 mixture using a HRN mask

Etch depth (nm)

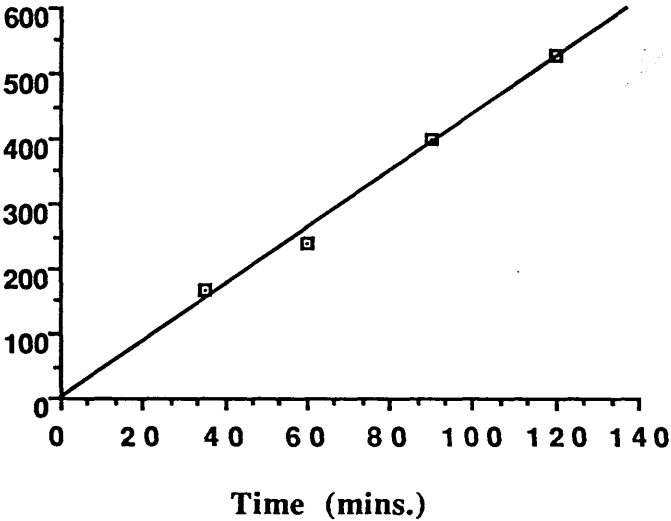


Figure 4.17 Graph of etch depth vs. time for the wet etching of GaAs using KClO_3 solution

Conductance (μS)

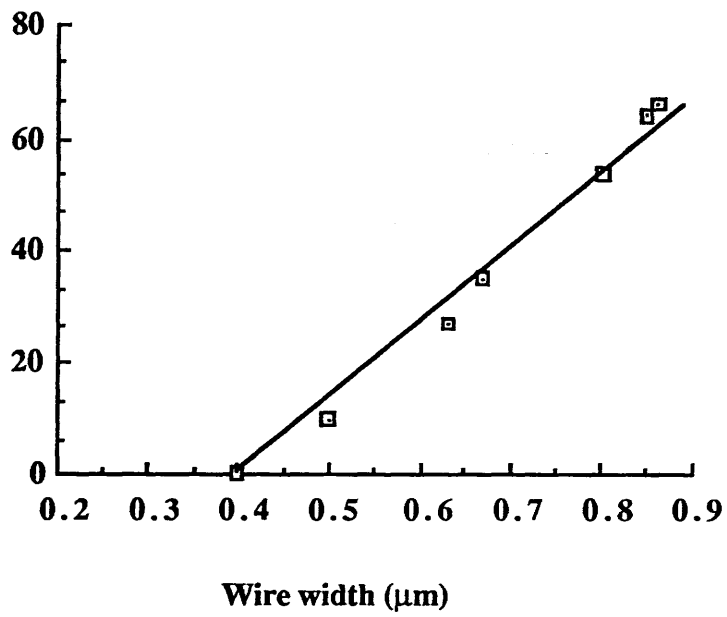
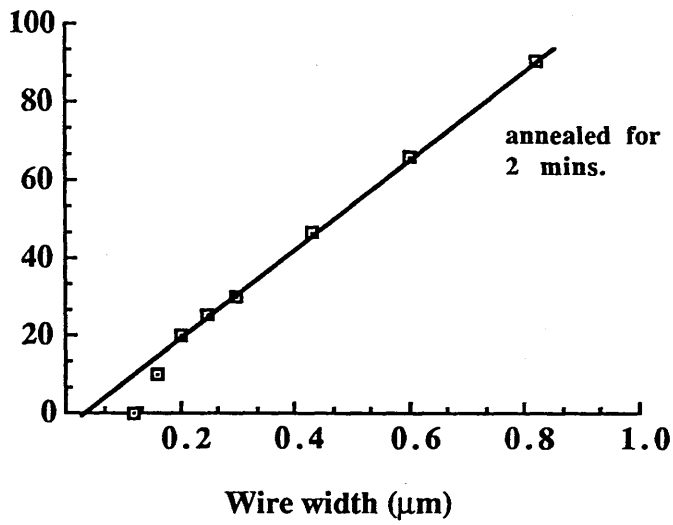


Figure 4.18 showing plot of conductance vs. wire width for the CH_4/H_2 etched wires using design 3)

Conductance (μS)



Conductance (μS)

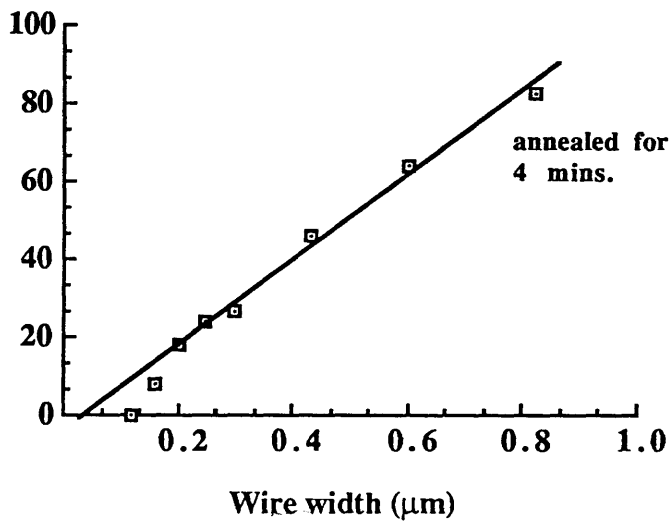
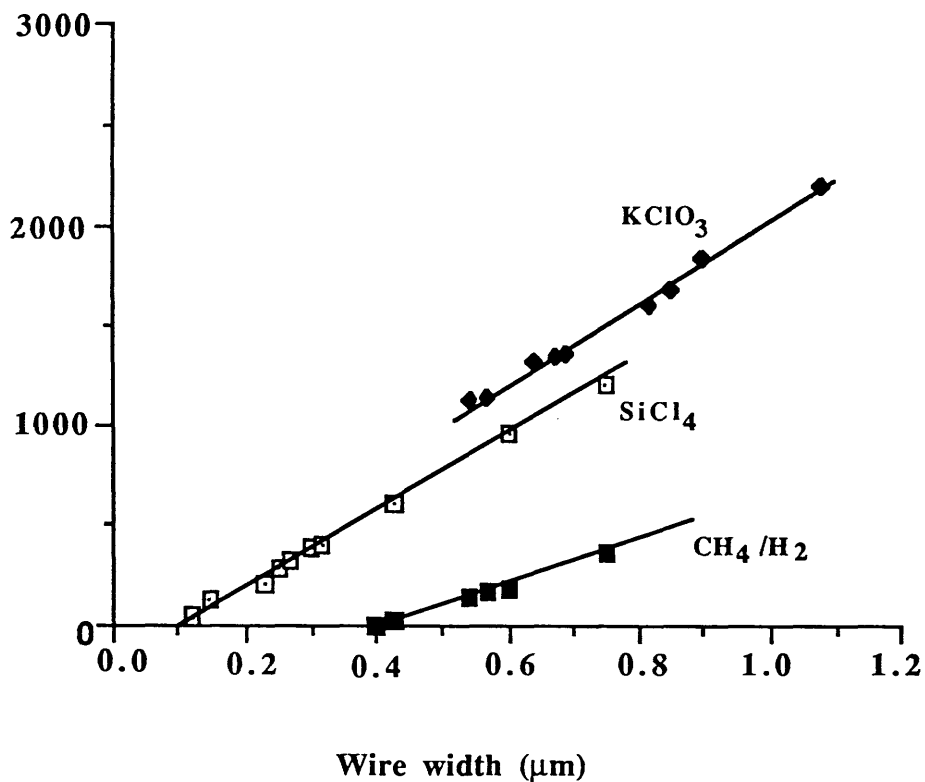


Figure 4.19 showing conductance vs. wire width plots for CH_4/H_2 etched GaAs wires annealed for a) 2 mins.
b) 4 mins. using design 1)

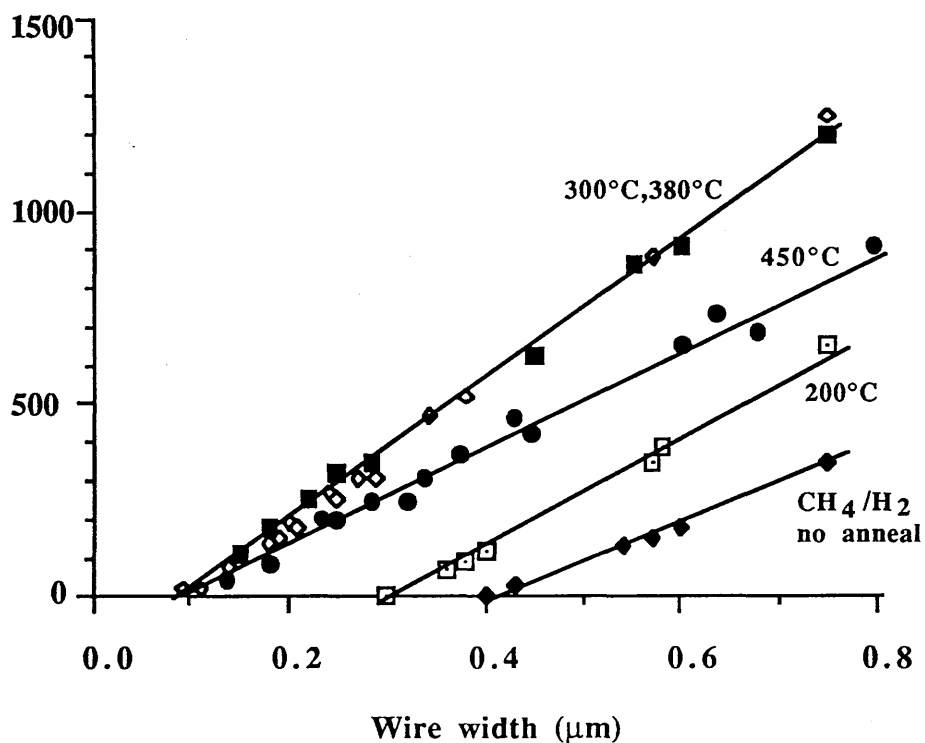
Conductance x width
 $\mu\text{S} \times \mu\text{m}$



- ◆ KClO₃ wet etch
- SiCl₄ RIE
- CH₄/H₂ RIE

Figure 4.20 Increase in cut-off width after CH₄/H₂ RIE in $1.5 \times 10^{18} \text{ cm}^{-3}$ Si-doped GaAs wires

Conductance x length
 $\mu\text{S} \times \mu\text{m}$



- ◆ no anneal
- anneal at 200°C
- ◇ anneal at 300°C for 2 minutes
- anneal at 380°C
- anneal at 450°C

Figure 4.21 showing CH_4/H_2 etched Si-doped n^+ GaAs wires annealed at different temperatures

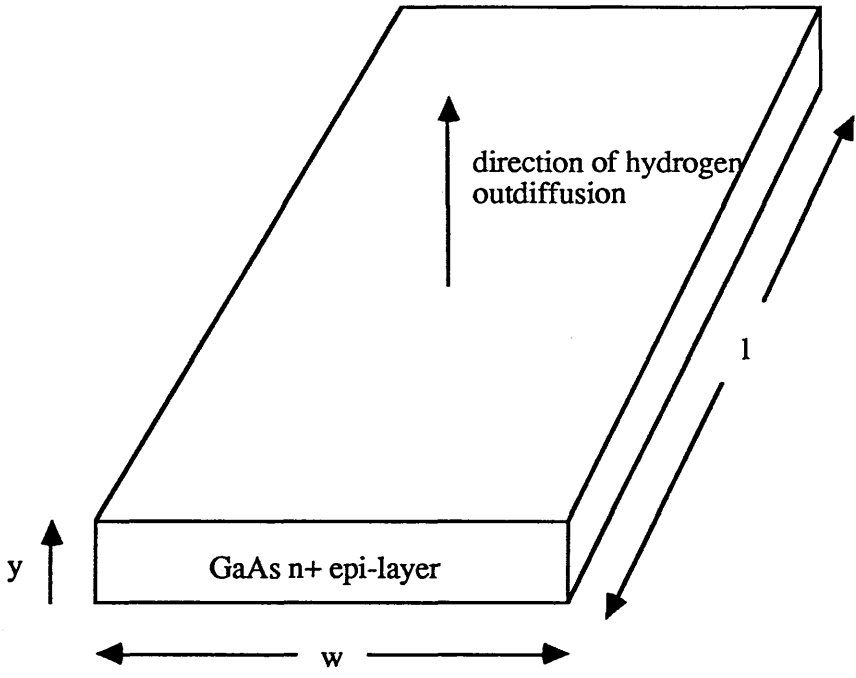


Figure 4.22 Schematic diagram of a GaAs n+ quantum wire with dimensions w, y, and l

Chapter 5 Development and damage characterisation of magnetron and electron cyclotron resonance radio frequency (rf) reactive ion etching using $\text{CCl}_2\text{F}_2/\text{He}$

5.1 Introduction

This chapter describes the work carried out in IBM Thomas J. Watson Research Centre, Yorktown Heights for four months during the course of this project. This particular study is concerned with the development of electron cyclotron resonance reactive ion etching using optical emission spectroscopy. The surface and sidewall damage induced after electron cyclotron resonance, magnetron reactive ion etching were investigated and compared with conventional reactive ion etching.

5.2 Dry etching

The various dry etching techniques available have already been discussed in section 2.4. In this section, the development of magnetron radio frequency reactive ion etching (MAG RF RIE) and electron cyclotron resonance radio frequency reactive ion etching (ECR RF RIE) of GaAs using $\text{CCl}_2\text{F}_2/\text{He}$ will be presented.

5.2.1 Magnetron (MAG) RF and Electron Cyclotron Resonance (ECR) RF reactive ion etching

In magnetron rf reactive ion etching, the plasma configuration is very similar to the conventional rf case, (see section 2.4.4), but an additional electromagnet provides a magnetic field across the cathode, see figure 5.1. The presence of the magnetic field confines the electrons in the plasma to the central region of the chamber, thus decreasing the main source of electron loss through recombination at the chamber walls. As a result, the density of the ions and reactive radicals excited from the gas molecules is enhanced and the plasma density is

proportional to the magnetic field strength. In general, the feed-gas ionization efficiency is measured to be around 0.1% and 0.01% in the MAG RF RIE and RF RIE modes giving plasma densities of 10^{10}cm^{-3} and 10^9cm^{-3} respectively^{5.1}. The use of this plasma configuration has been applied to the RIE of silicon employing bromine^{5.2}.

In electron cyclotron resonance rf reactive ion etching, in addition to the presence of the d.c.magnetic field, microwave power at 2.45GHz is delivered to the reactor, see figure 5.2. This microwave power is absorbed in the magnetized plasma. The absorption coefficient $A(\omega)$ can be written as:

$$A(\omega) = A(0) \frac{\xi}{(\omega - \omega_c)^2 + \xi^2} \quad (5.1)$$

where ξ is the collision frequency which is proportional to the pressure and $\omega_c = eB/m$ is the cyclotron frequency of electron. Resonance absorption occurs at $\omega_c = \omega$, that is, for $B = 0.0875\text{T}$. Under these conditions, the ionization by the microwave power is at its most efficient point and about 1% of the feed-gas is ionised, giving a plasma density of 10^{11}cm^{-3} (^{5.1}). During etching, the RF field is used to extract the ions from the plasma established by ECR. The ξ term in equation 5.1 represents electron-ion collisions which lead to a broadening of the cyclotron resonance. Since the electron-ion collision rate increases with pressure, the cyclotron resonance is diminished at higher pressure where ξ dominates. The plasma parameters in an ECR RF reactor including the plasma density, resonance width, space potential and the electron energy distribution can be characterised using Langmuir probe measurements, and ECR enhancement has been found to be more effective below 10mTorr and has no practical advantage over conventional microwave plasma excitation above 100mTorr^{5.1}. However, a useful characteristic of RIE using ECR excitation is that the d.c. self bias (see section 2.4.4) can be made very low ($\approx 20\text{V}$) by controlling the RF power, since the RF power level no longer determines the degree of ionisation of the gas.

The advantages which make ECR RF RIE potentially more attractive than other RIE configurations comprise of the highly efficient excitation rate which enables a high degree of ionisation at low gas pressures, consequently, recombination reactions among the species are minimised and the ions and reactive

radicals generated in the plasma are used effectively; in addition, the low plasma potential developed, resulting in low energetic ion bombardment, can be expected to minimise the induced damage on the substrate surface. While the reactive ion etching of silicon in this configuration and in a microwave plasma has been reported by a number of workers^{5.2-5.8}, relatively little work has been carried out for the etching of GaAs^{5.9,10}. It is also worth noting that RIBE and RBIBE (see section 2.4) employing an ECR plasma source^{5.11,12} have been used to etch GaAs and in particular, a low level of damage was observed with RIBE^{5.11}.

5.2.2 Development of MAG and ECR reactive ion etching of GaAs using CCl₂F₂/He

5.2.2.1 Reactor Configuration

The ECR-RF hybrid plasma reactor used in this work was provided by Dr. Y.H.Lee in the Silicon technology group of IBM, Yorktown Heights and is shown schematically in figure 5.3. Wafers are placed on the capacitively coupled electrode as in a conventional reactive ion etching system. An electromagnet provides a magnetic field of 50 gauss ($\pm 20\%$) across the 25 cm diameter aluminium electrode. Microwave power (up to 3kW at 2.45 GHz) can be delivered to the ECR reactor at the top of the system through a brass waveguide system, which includes a circulator and four stub tuner. A quartz window separates the waveguide from the ECR reactor and the plasma is extracted by a 13.56MHz rf field. Forward and reflected powers can be measured for both rf and microwave excitation. The pumping system consists of a turbomolecular pump (1500l/s), Roots blower (100cfm) and rotary vane pump (37 cfm). The system is pumped down to a base pressure of $\approx 2 \times 10^{-5}$ Torr before the samples were loaded. An optical spectrometer is fitted to the etch chamber so that the types of molecules and atomic species present in the plasma can be detected by monitoring the wavelength of light emitted.

5.2.2.2 Experimental

Initially, an understanding of the etch characteristics such as etch rate, surface roughness, and the degree of anisotropy both in the MAG RF RIE and ECR RF RIE modes employing $\text{CCl}_2\text{F}_2/\text{He}$ as the etch gas was desired. For the characterisation of etch rate and surface roughness, bulk GaAs wafers were patterned over half the surface with 10% PMMA (2010 Elvacite) and after etching, the resist was removed in acetone and the etch depth was measured using a Talystep. Surface roughness and the degree of anisotropy of etching were characterised using a Hitachi S800 SEM. To determine the degree of anisotropy of etching, NiCr masked ridges were made on bulk GaAs using electron beam lithography exposure of a double layer resist, see sections 2.2 and 2.3, followed by lift-off and subsequently ECR and MAG RF reactive ion etched.

5.2.2.3 Results and discussion

Samples etched in the ECR RF RIE mode using $\text{CCl}_2\text{F}_2/\text{He}$ gas ratio of 1:1 at 200W microwave power, 5mT pressure, $0.1\text{W}/\text{cm}^2$ rf power density and 90V dc bias produced very rough surfaces, see SEM 5.1. A number of other etch conditions were tried but with no further success, see table 5.1. On the other hand, samples etched in the MAG RF RIE mode at $0.36\text{W}/\text{cm}^2$, 5mT, 300V dc bias displayed very smooth surfaces as shown in SEM 5.2. It was clear that there was a need to understand the fundamental etch chemistry involved. One way of doing this is to analyse the optical spectrum of the light emitted by the plasma. Using a grating spectrometer with a multichannel analyser to record the intensity in each wavelength band, the spectra from a He (fig. 5.4a) and a CCl_2F_2 ECR RF excited plasma (fig. 5.4b) were recorded. In the He plasma, the major specie detected was neutral $\text{HeI}^{5.13}$; in the CCl_2F_2 plasma, Cl and CF_x^* radicals were the major species present^{5.13}, where the Cl radicals are mainly responsible for the etching of GaAs to form the relatively volatile gallium chlorides (GaCl_2 , GaCl_3) and arsenic chloride (AsCl_3)^{5.14-16}. Moreover, the fluorine present in a CCl_2F_2 plasma can also react with the GaAs leading to the formation of the volatile arsenic fluorides (AsF_3 , AsF_5) and the involatile high boiling point solid gallium fluoride (GaF_3) and it has been reported that the rate limiting step to this process is the ion induced removal of GaF_3 while the removal rate of GaCl_x also benefit significantly from ion

bombardment^{5.16}.

The spectra emitted by a plasma excited in the MAG RF RIE and ECR RF RIE modes using a $\text{CCl}_2\text{F}_2/\text{He}$ gas ratio of 1:1 are shown in figures 5.5a) and b). It is evident that in the MAG RF RIE mode, a high concentration of the neutral HeI specie is present whereas in the ECR RF RIE mode, a high level of CF_x^* radicals are detected, which masks the trace of any HeI specie. It is likely that this is a result of the relative ionisation efficiency of the plasmas, since the plasma densities generated in the MAG RF RIE (10^{10} cm^{-3}) mode is ten times lower than the ECR RF RIE (10^{11} cm^{-3}) mode.

However, the increased concentration of CF_x^* radicals present in the ECR RF RIE mode is highly undesirable since this would lead to the formation of involatile products such as GaF_3 , AlF_3 (from the Al cathode), and carbon-containing polymers (C_2F_6) which may easily deposit on the substrate surface thus inhibiting the etching process by forming some sort of "micromasks" on the surface. This would account for the surface roughness, the relatively slow etch rate and the long induction period (4 minutes) observed, see figure 5.6.

A solution to this problem would be to try to decrease the amount of CF_x^* radicals present and to eliminate the Al cathode. Therefore, silicon wafers were mounted on the cathode covering about 43% of the electrode. The optical emission spectra in this configuration reveal a high level of Si-F species^{5.62} and a reduction of the CF_x^* radicals, see figure 5.7. This suggests that the Si scavenges the CF_x^* radicals through the formation of SiF_x compounds^{5.5}, thus reducing the major source of polymer formation. Furthermore, the generation of Al-based involatile species like AlF_3 may be suppressed due to the smaller area of the exposed Al electrode. GaAs etched under such conditions gives very smooth surfaces, see SEM 5.3. The measured etch rate also increases by a factor of 2 with an induction time of 15s as shown in figure 5.6. It is possible that this induction time is due to the presence of the native oxide as has been observed by others in GaAs/ $\text{Al}_x\text{Ga}_{1-x}$ As etching^{5.17,18}. Also plotted in figure 5.6 is the etch depth measured for the MAG RF reactive ion etched samples. Although the a.c. bias is higher in MAG RF RIE than ECR RF RIE, a slower etch rate is observed. It is possible that this is a

result of the lower ionisation efficiency, hence a smaller plasma density generated in MAG RF RIE, which also suggests the dominant role of chemical mechanism in the etching process. Thereafter, experiments were carried out in the presence of the silicon wafers.

The next step was to obtain the correct etch condition to produce the required anisotropy. Using the lift-off technique, NiCr lines were fabricated on bulk GaAs using electron beam lithography exposed on a double layer resist. The lines were etched in the ECR RF RIE and MAG RF RIE modes with the same etch conditions as before and both give very vertical sidewalls and smooth surfaces. See SEMs 5.4 (ECR RF RIE) and 5.5 (MAG RF RIE).

In order to find the lowest d.c. self bias in the ECR RF RIE mode which would still satisfy the requirements of surface smoothness and anisotropy, two other etch conditions were tried:

1) 200W μ wave power, 5mT, 0.1W/cm² rf power, 50V self bias - see SEM 5.6; a rough surface was obtained. This may be because there is too little ion bombardment to remove any involatile products on the substrate.

2) 200W μ wave power, 0.17W/cm² rf power, 2mT, 100V dc bias - see SEM 5.7; the surface obtained was smooth, but a kind of 'foot' - overcut profile was observed at the bottom of the wire. This is a general occurrence in conventional RIE when there is not enough reactive species generated at lower pressures to react with the GaAs.

5.2.3 Conventional Radio Frequency reactive ion etching of GaAs using CCl₂F₂/He

The reactive ion etching of GaAs/Al_xGa_{1-x}As using CCl₂F₂/He is well established^{5.19-21}. In this experiment, a conventional 13.56MHz parallel plate reactive ion etcher (Plasma Therm 2484) was used. (This system was provided by Dr. C. M.Knoedler from IBM Yorktown Heights). The system is equipped with a cryopump and a turbomolecular pump. The chamber and the electrodes are made of Al and the electrode separation and diameter are 7cm and 56cm respectively. The

etch chamber was pumped down to a base pressure of 1.1×10^{-6} Torr before the samples were loaded. The nominal etch rate for GaAs in this etcher is 200nm/min. for $\text{CCl}_2\text{F}_2/\text{He}$ ratio of 1:1, 5:5sccm $0.06\text{W}/\text{cm}^2$, 200V d.c. bias, 5mT total pressure^{5.19}. No induction time was observed for these samples as they were etched in $\text{HCl}:\text{H}_2\text{O}$ 1:1 for 30s to remove the native oxide prior to loading into the chamber. (The presence of the native oxide is believed to play an important role in the induction time observed in the ECR RF RIE and MAG RF RIE modes before.) For the actual experiment, the thickness of GaAs etched before reaching the AlGaAs etch stop was detected via a laser interferometer employing a low power He-Ne laser (2mW), see section 5.5.

5.3 Sidewall damage characterisation - n^+ GaAs quantum wires

In order to quantify the amount of sidewall damage after MAG RF, ECR RF and RF reactive ion etching, the cut-off width of n^+ GaAs quantum wires and their conductances at room and low temperatures were measured and compared, see section 4.3.5. In addition, the rms amplitude in the low temperature universal conductance fluctuations of these wires were investigated and appears to be extremely sensitive to the damage layer.

5.3.1 Material design

Quantum wires were fabricated on two different materials in order to examine the dependence of dry etched sidewall damage on the period of time the GaAs was exposed to the plasma. Two molecular beam epitaxy (MBE) grown wafers (provided by Columbia University, New York.) were used as the starting material. The first comprises an 80nm thick Si-doped ($1 \times 10^{18}\text{cm}^{-3}$) GaAs epilayer with an undoped GaAs buffer layer grown on a semi-insulating GaAs substrate. The other has the same configuration but with the undoped GaAs buffer layer replaced by an undoped $\text{Al}_{0.3}\text{Ga}_{0.7}\text{As}$ etch stop layer, see figures 5.8a) and b). Both epilayers were measured to have an electron mobility of $0.2\text{m}^2\text{V}^{-1}\text{s}^{-1}$ at 77K and 4.2K.

5.3.2 Device design

The device patterns were designed using IBM's "Integrated Graphics System", see appendix 1.

The device consists of three levels:

- 1) The first level contains the ohmic contact and alignment marks in an exposure field size of $700\mu\text{m}^2$ as shown in figure 5.9.
- 2) The second level are the wires with Hall bar geometry, the voltage probes are $1.5\mu\text{m}$ apart with probe widths of $0.5\mu\text{m}$ in a field size of $200\mu\text{m}^2$, see figure 5.10.
- 3) The third level are the bonding pads in a field size of $700\mu\text{m}^2$, see figure 5.11.

Figure 5.12 shows a complete layout of the pattern with two devices on each pattern.

5.3.3 Quantum wires fabrication

The device wafers were scribed into 0.3 x 0.4 inch chips using a mechanical scribe and each chip was cleaned in trichloroethylene, followed by acetone, and isopropanol alcohol. Twenty-four (6 x 4) patterns, giving forty-four devices, were defined on each chip using an electron beam. The exposures were carried out in an IBM Vector Scan-6 (VS-6) system^{5.22}. The essential features of the VS-6 system will be described briefly, further details of the machine are described elsewhere^{5.23-25}.

5.3.3.1 Electron beam lithography system (VS-6)

At IBM Yorktown, all the lithographic work was carried out on the VS-6 system, one of the Vector Scan series electron beam machines constructed for lithography in the 100nm regime. The essential features of the VS-6 are:

- a) a single crystal LaB₆ electron gun assembly is used and the minimum spot size is 5nm
- b) the deflection system is optimised for a 20nm spot diameter over a 250µm square field
- c) accelerating voltages from 10 to 100kV
- d) a compact four quadrant, solid state detector is used for SEM operation and registration
- e) the pattern generator uses a 14 bit vector scan exposure system with individual shape-to-shape dose variation as computed by proximity correction programs
- f) the X-Y stage movement is measured by a laser interferometer and mechanical vibrations are eliminated by a piezo-actuated locking substage, which is connected to the X-Y stage by piezoelectric elements
- g) magnetic interference (e.g. 60Hz stray fields) is minimised by magnetically isolating the final lens from the high permeability outer shell (made of nickel:iron 80:20) using non-magnetic stainless steel.

The main components of the VS-6 electron beam lithography system and details of its final lens and substage design are shown in figures 5.13a) and b). The generation and transfer of mask data-sets are described in Appendix 1.

5.3.3.2 Ohmic contact and alignment marks level

10% PMMA (2010 elvacite) in chlorobenzene was spun onto the chip at 4K rpm for 60s to give a resist thickness of 0.7µm and baked overnight at 175°C. The dosage given to each area was corrected for proximity effects using the experimentally deduced parameters^{5.26} at 700µm² field size with 50keV accelerating voltage. The sample was exposed at a nominal 150µC/cm², developed with 2:1 IPA:MIBK for 2 mins.15s; IPA for 15s; followed by inspection under the optical microscope. If the exposure is correct, ohmic contacts were made by evaporating 30nm-germanium, 60nm-gold, 20nm-nickel, capped by 60nm of gold, lifted off by soaking in acetone and annealed at 375°C for 1 minute in a 95%/5% N₂/H₂ ambient.

5.3.3.3 Wires level

Double layer resist was used for this level. The bottom layer was 5% PMMA (2010 elvacite) in xylene with a lower molecular weight (150,000); it was spun at 3K rpm for 60s to give a thickness of 120nm and baked at 175°C for 1 hour. The top layer was 2% PMMA (2041 elvacite) in xylene with a higher molecular weight (360,000); this was spun at 3K rpm for 60s to give a thickness of 40nm and baked at 175°C for 2 hours. For high resolution lithography, this resist system facilitates better lift-off due to the higher sensitivity obtained from the lower molecular weight resist after electron beam exposure^{5.27}.

Wires of various widths from 0.08 μm to 1 μm were exposed with 150 $\mu\text{C}/\text{cm}^2$ dosage (see section 5.3.4) at 50keV after proximity correction in a 200 μm^2 field. The patterns were aligned using the small alignment markers consisting of necked-down crosses of minimum dimension 0.25 μm , the middle ones shown in figure 5.9. The alignment scheme used has adjustments for shift, field size, rotation and orthogonality with a typical accuracy of $\approx 20\text{nm}$ between the levels. After exposure, the chip was developed in 2:1 IPA:MIBK for 60s, followed by IPA for 15s. 30nm of NiCr was evaporated and lift-off was carried out in acetone. The NiCr was then used as a dry etch mask.

It has been demonstrated by Scherer et. al.^{5.28} that strontium fluoride (SrF_2) can be used as a dry etch mask. In the present experiment, it was also tried as an alternative etch mask. While it was possible to fabricate SrF_2 lines with linewidths down to 0.08 μm (see SEM 5.8 and section 5.3.4), the lift off process presented problems due to the similar index of refraction (around 1.3) between the SrF_2 and the available solvents. Therefore, it was decided to use NiCr as a dry etch mask.

After the mask has been defined, the chips were dry etched at different conditions, see section 5.3.4. After dry etching, the metal mask was removed by soaking in HCl:H₂O 1:1 for 2 mins.

5.3.3.4 Bonding pads level

The same type and thickness of resist was used as in the first level with similar exposure and development procedures. The alignment for this level was carried out using all the alignment marks. The size of the patterns were fixed using the $700\mu\text{m}^2\text{FS}$ alignment marks, (diagonal ones), while the rotation and orthogonality were adjusted using the small alignment marks, (middle ones) as shown in figure 5.9. The bonding pads were made from 30\AA nickel to ensure good adhesion and 2000\AA of gold. After lift-off in acetone, each chip was diced into twenty-four samples which were subsequently bonded with gold wire $\approx 50\mu\text{m}$ in diameter. Wires of width $> 0.5\mu\text{m}$ were mounted on non-magnetic headers for room temperature conductivity measurements and those $< 0.5\mu\text{m}$ were mounted on magnetic headers for low temperature measurements.

5.3.4 Experiment

5.3.4.1 Resolution tests

Data sets to be used to generate patterns of lines with different number of pixels corresponding to different widths were prepared using a computer named "Virtual Machine" (VM) (see appendix 1) for exposure tests from dosages $300\mu\text{C}/\text{cm}^2$ - $2000\mu\text{C}/\text{cm}^2$. Using the lift-off technique, strontium fluoride lines were fabricated on bulk GaAs and results seem to indicate that with a constant current of 10^{-10}A at 1MHz, around $450\mu\text{C}/\text{cm}^2$ dosage is needed. SEM 5.8 shows $0.08\mu\text{m}$ lines of strontium fluoride and the whole resolution test pattern is shown in SEM 5.9. However, in order to avoid proximity effects due to backscattering, forward scattering, finite beam distribution and other factors such as secondary electrons around the area between the voltage probes and the wire in the actual device, proximity correction^{5.25} was used for all the wires exposed on the device chip. Using NiCr lines fabricated from the lift-off technique, resolution tests from $100\mu\text{C}/\text{cm}^2$ - $175\mu\text{C}/\text{cm}^2$ dosages indicated that the optimum dosage is around $150\mu\text{C}/\text{cm}^2$, see SEM 5.10.

5.3.4.2 Pattern Layout

Five chips were produced with the chip layout and pattern layout as shown in figure 5.14a) and b). The bonding pad levels were exposed with the ohmic contact and alignment marks level as "dummy" patterns (in sites 1,24) for the testing of ohmic contacts, isolation after etching, mapping positions for alignment and the aligning procedure itself.

5.3.4.3 Dry etching

Once the chips were fabricated as described in section 5.3.3, they were etched under the following conditions before the bonding pads were exposed:

- 1) Chip ECRALG: this sample has an AlGaAs stop layer and was ECR RF reactive ion etched. From the etch rate results obtained in section 5.2.2.3, this chip was etched for 85s in order to ensure electrical isolation between the contact pads. The etch condition was 200W μ wave power, 0.17W/cm² rf power density, 5mT, 80V self bias, CCl₂F₂/He;10sccm:10sccm.
- 2) Chip ECRGa: this sample does not have an AlGaAs stop layer and was ECR RF reactive ion etched. The chip was etched for 2 minutes under the same conditions as above.
- 3) Chip MAGALG: this sample has an AlGaAs stop layer and was etched in the magnetron rf mode. The etch condition was 0.36W/cm² rf power density, 5mT, 300V self bias, 3 mins. to ensure electrical isolation.
- 4) Chip MAGGa: this sample does not have the stop layer and was etched with the same condition as in no.3 for 4mins.
- 5) Chip RIEALG: this sample has an AlGaAs stop layer and was oxide etched by HCl:H₂O 1:1 for 30s before reactive ion etched at 0.06W/cm² rf power density, 5mT total pressure, 200V self bias for 50s by CCl₂F₂/He; 5sccm:5sccm.

5.3.5 Room temperature conductivity measurement

5.3.5.1 Experimental

These measurements were conducted using a Keithley 225 current source and a Keithley 195A digital multimeter used as a voltmeter. Four point measurements were made by passing 1uA through the wires of different widths and their voltages measured. Conductivity was then calculated from these results normalized to the wire length, (taken as the distance between the voltage probes - 1um).

5.3.5.2 Results and Discussion

Initial testing

After the bonding pads were fabricated onto chip MAGGa, all the wires were found to be non-conducting. Some possible explanations were considered for this observation:

- 1) The ohmic contacts may have been damaged by the etching process. This is unlikely since further testing of a pad of area $70\mu\text{m}^2$ indicated a conductance of 200uS. While this confirms the operation of the ohmic contacts, the measured conductance for this area is unexpectedly low.
- 2) A crack may exist between the wire and the ohmic contact. This is possible but close inspection of the area in the SEM showed no such discontinuity.
- 3) The dry etch process has damaged wires of $1\mu\text{m}$ in width, (since there is no conduction even across the voltage probes). This would seem a plausible explanation if the degree of sidewall damage increases with time as will be demonstrated later in this work and has been observed on reactive ion etched surfaces employing the same etch gas^{5.20}, since this chip has been etched for the

longest time - 4 mins. However, this is highly unlikely.

4) A thin layer of polymeric material may have deposited onto the substrate surface after etching which may act as a large series resistance between the ohmic and the bonding pad contact. This appears to be the most likely explanation.

Thereafter, the ohmic contacts on the other chips were tested before the bonding pads were exposed and evaporated. Results showed that the ohmic contacts on chips ECRALG and ECRGa all conducted while the ones on chips MAGALG and RIEALG did not. As explanation 4 seemed to be the most likely cause for the non-conductive behaviour of the wires, it was decided to further process the chips MAGALG, MAGGa and RIEALG in an O₂ plasma. To ensure the samples were not damaged by the O₂ plasma, the following conditions were used: 50sccm, 5mT, 200W μ wave power with no rf power and no self bias voltage for 7 mins. The chips were tested again and all the ohmic contacts conducted. This observation confirms explanation 4).

The existence of the polymeric layer in both the MAG RF RIE and RF RIE modes may be explained by considering their relative feed gas ionization efficiencies and their feed gas - radical recombination rates compared with the ECR RF RIE mode. In the RF RIE mode, only 0.01% of the feed gas is ionized; in the MAG RF RIE mode, 0.1% and in the ECR RF RIE mode, 1%. This implies that the concentration of the dissociated feed gas in the ECR RF RIE mode is about 100 times more than RF RIE. Taking into account of the feed gas - radical and radical - radical collision probabilities, the rate of feed gas - radical recombination, which is a major source of large polymer species, is considerably less in ECR RF RIE than in RF RIE. In particular, the ECR etch chamber in this experiment was loaded with Si wafers (section 5.2.2.3), which would result in further decreases in the formation of polymers.

Device measurements

Figure 5.15 shows the normalized conductance plotted as a function of wire width. The cut-off widths for chips ECRALG, ECRGa, MAGALG, MAGGa and RIEALG are 0.05 μ m, 0.075 μ m, 0.28 μ m, 0.35 μ m, and 0.16 μ m respectively.

As explained in section 4.3.5, a cut-off of conduction is expected when the width of the wire is twice the depletion width due to surface states; assuming the built-in surface potential as 0.6eV, the depletion depth for n^+ GaAs with a donor concentration of $1 \times 10^{18} \text{cm}^{-3}$ is approximately 20nm. These results show that wires etched in MAG RF RIE possess the thickest sidewall damage layer, whereas ECR RF RIE (d.c.bias 80V) results in negligible sidewall damage compared to RF RIE (d.c.bias 200V) and MAG RF RIE (d.c.bias 300V), just as has been found for wet etching^{5.29,30}. The little sidewall damage observed in ECR RF RIE may be attributed to the low d.c.self bias potential developed (80V), and in this particular case, the contamination suppressed environment during etching. It is worth noting that $\text{CCl}_2\text{F}_2/\text{BCl}_3$ RF reactive ion etching at a similar self bias of 80V has been used for matching gate recesses in GaAs MESFETs and that no degradation in transconductance has been observed compared to wet etch samples^{5.31}. A resistivity change is also observed with the MAG RF RIE samples. Similar behaviour resulted when the wires were reactive ion etched in CH_4/H_2 ^{5.30} (see section 4.3.5.4), and in a recent experiment by M. Rahman^{5.32} who also observed a decrease in the conductance of similar quantum wires with increasing etch power (i.e. ion energy) in the RF RIE using SiCl_4 . In the former, the decrease in conductance was attributed to the possibility of hydrogen diffusion through the thin Ti mask thus causing passivation of the silicon donors in the GaAs wire, which was recoverable by annealing; while in the latter, the more severe ion bombardment on and/or penetration through the Ni mask with higher ion energies was believed to be a possible cause for the decrease in conductance observed with higher etch power. In the present experiment, while more helium and other ion bombardment and/or penetration (through the NiCr mask) related to higher ion energies could cause the lower conductance measured in the MAG RF RIE samples, RF RIE at 200V did not exhibit similar behaviour. This is perhaps due to the comparatively small exposure time of the RF RIE samples to the $\text{CCl}_2\text{F}_2/\text{He}$ plasma.

The amount of sidewall damaged material after ECR RF RIE and MAG RF RIE are seen to be dependent on the etch time. This dependence has been observed by Knoedler et. al.^{5.20} when investigating the effect of GaAs surface damage as a function of overetch times with an AlAs etch stop layer in RF RIE employing the same etch gas, the significance of this result has already been discussed in section 3.4.1.3. The 60nm of damage induced on each sidewall of the

wires after RF RIE is a relatively thick damaged layer compared with other dry etchants^{5.29,30}. While an analytical study by Seaward et. al.^{5.33} using X-ray photoelectron spectroscopy indicated that the $\text{CCl}_2\text{F}_2/\text{He}$ RF reactive ion etched GaAs surface was stoichiometric with small quantities of adsorbed F and Cl; in a similar experiment, Ga-rich surfaces contaminated with higher concentrations of carbon and oxygen, with some evidence of Ga-F bonding were found, see section 5.4.2. In addition, it has been reported that GaAs surfaces etched in the presence of helium resulted in an increase in surface depletion width and a decrease in the effective carrier concentration^{5.20,34}. Other possibilities to account for the observation of such a large sidewall damaged layer include the atomic-scale sidewall roughness produced by rf etching and the redeposition of involatile products from the bottom surface onto the sidewalls which was not removed by the O_2 plasma. While the exact cause and nature of the damage layer is unclear, it may be a combination of the above effects that contribute to such a large damage layer observed. In order to obtain more qualitative information of this layer, further characterisation using analytical techniques such as transmission electron microscopy (see section 6.3) is desirable.

5.3.6 Low temperature transport measurement

5.3.6.1 Experimental

The experimental equipment was provided by Dr. T. P. Smith III of IBM Yorktown Heights. In this section, only samples etched in the ECR RF and RF reactive ion etching modes were measured; i.e. samples ECRALG and RIEALG. All measurements were performed in a ^4He cryostat at 1.5K. A schematic diagram of the circuit used is shown in figure 5.16. A power supply controller controls the d.c. current in the magnet which sweeps from 0-76.2A providing a B field of 0-9T. An a.c. current of $0.1\mu\text{A}$ is applied to the sample through the use of an a.c. voltage generated in the Princeton Applied Research (PAR) 5301 lock-in amplifier (phase sensitive detector, PSD), which is fed through a $10\text{M}\Omega$ resistor. In this way, the measured signal may be extracted from any noise background. The value of R_S is chosen to be much larger than the resistance of the device so that all the voltage

from the oscillator appears across it independent of the device resistance. The voltage between the probes is measured using the lock-in amplifier with a built in preamplifier; the data is then recorded in an IBM PC via the lock-in and a digital voltmeter connected to an IEEE 488 bus and is plotted on the chart recorder.

5.3.6.2 Theory

The fluctuations measured in this experiment, referred to as universal conductance fluctuations (UCFs), have been observed in a number of mesoscopic systems including metal wires^{5.35}, conducting channels of Si-MOSFET^{5.36-38}, GaAs wires^{5.29,39,40} and GaAs/AlGaAs heterostructures^{5.28,41} and explained theoretically in terms of magnetically altered quantum interference effects^{5.42,43}. The term "mesoscopic" is commonly used to describe a device whose size is comparable to the phase-coherence length L_ϕ , (defined below), whereby conduction can be described in terms of electron waves, without the effects due to the waves being averaged out over many incoherent regions each of size $\approx L_\phi$. In this respect, the conductance can be seen as a function of the transmission coefficient of the waves through the device^{5.44}, which is determined by the interference of the various partial waves as they propagate randomly, scattering off sites of disorder, such as crystal imperfections and impurities. If many paths contribute to the interference (as in a large device), then, since the phase of each is effectively randomly distributed, the conductance, which is the sum over all the waves will give a well-defined average value and as a result will be insensitive to changes in the phase of individual trajectories. However, if the sample is small enough so that the number of paths which contribute to the interference is also small, then the averaging will not be complete, and the sum will be strongly dependent on the individual phases, and therefore, will be very sensitive to the scatterers present.

Interference effects can only take place between electronic states that are phase-coherent. The length scale, L_ϕ , over which phase coherence occurs is limited by phase-disturbing scattering processes. For a disordered wire, the phase-coherence length is given by $L_\phi = \sqrt{D_e t_\phi}$, where L_ϕ is related to the elastic diffusion constant D_e and the phase coherence time t_ϕ , which includes all phase-breaking processes such as inelastic and spin-flip scattering. However, since elastic

scattering does not disturb the phase, it only limits L_ϕ through its effect on D_e .

Universal conductance fluctuations are in fact the same type of quantum interference phenomena observed in the periodic oscillations in the magnetic-field-dependent conductance of mesoscopic conducting rings, (known as Aharonov-Bohm rings). The oscillations are a signature of the phase change of the interfering electronic wave functions with the application of a magnetic field. This result was derived by Aharonov and Bohm in 1959^{5.45} and can be described as follows: an electron beam propagating around a loop being split into two separate paths and then rejoined is shown in figure 5.17a). The resultant electronic current measured at a point downstream from the loop can be shown to be related to the difference of the phases of the wave functions in the two branches, $\phi_1 - \phi_2$. The result of the application of a magnetic flux ϕ to the interior of the loop causes a phase difference between the two branches of the loop giving:

$$\Delta\phi_1 - \Delta\phi_2 = (e/\hbar)\phi = (e/\hbar) \oint_C \mathbf{A} \cdot d\mathbf{l} \quad (5.2)$$

where \mathbf{A} is the magnetic vector potential and \mathbf{l} is the path that encloses the flux. This implies that the current will show an oscillatory dependence on the applied flux with period h/e , where h is Planck's constant and e is the electronic charge. Figure 5.17b) shows a real, disordered A-B loop with two possible electronic paths scattering off sites of disorder elastically (since elastic collisions are reversible, time-reversed paths are equally probable). It is clear that the electronic trajectories are capable of constituting a large number of A-B loops giving rise to fluctuations (UCFs) (provided that a low number of inelastic scattering i.e. phase-breaking events take place) similar to the A-B oscillations observed in the presence of a magnetic field.

These universal conductance fluctuations have been studied theoretically by Lee^{5.43} and Al'tshuler^{5.42}. By calculating the conductance autocorrelation function:

$$F(\Delta B, \Delta E) = \langle G(B+\Delta B, E_F+\Delta E) G(B, E_F) \rangle - \langle G(B, E_F) \rangle^2 \quad (5.3)$$

where G is the fluctuations in the conductance at magnetic field B and Fermi energy E_F for a completely phase coherent system in which all the dimensions are smaller than L_ϕ , they predicted that the rms magnetoconductance fluctuation amplitude ΔG at absolute zero temperature is given by $\Delta G = \sqrt{F(0,0)}$, which is of the order $e^2/h = G_0$, and is approximately $3.9 \times 10^{-5} S$, where e is the electron charge and h is the Planck constant.

However, in quasi-one-dimensional wires (wires longer than L_ϕ), the phases of electronic waves are broken by inelastic scattering, and the amplitude of the fluctuation in conductance can be approximated by^{5.43}:

$$\Delta G_{\text{rms}} \approx (L_\phi/L)^{3/2} G_0 \quad \text{for } L_\phi \leq L_t \leq L \quad (5.4)$$

where L is the length of the wire, L_ϕ is the phase coherence length, $L_t = \sqrt{\hbar D/kT}$ is the thermal diffusion length where D is the diffusion constant, and $G_0 = e^2/h$ ^{5.43}. This theory predicts that in one-dimensional wires thinner than L_ϕ , the rms amplitude of the fluctuations is directly related to the phase coherence length L_ϕ and the length L of the sample, and is not dependent on its width. If the phase coherence length is comparable to the sample length the conductance fluctuations will be of order e^2/h , but if the phase coherence length is shorter than the channel length their amplitude will be smaller. Since the phase coherence length is sensitive to the type of scatterers present, according to this prediction, ΔG_{rms} is a good measure of the quality of the conducting channel.

5.3.6.3 Results and Discussion

Figure 5.18 shows the magnetoconductance spectra (normalised to e^2/h) of two wires: one reactive ion etched in ECR RF mode, the other reactive ion etched in RF mode; the fluctuations are completely reproducible at a given temperature during one cooling. The lithographic widths of the wires are 100nm and 200nm, respectively, but the effective electrical widths at room temperature are approximately the same (50nm and 40nm) for the two samples. Although these samples had about the same conductance at room temperature, the low temperature conductance of the sample etched in ECR RF RIE is about five times greater than

the conductance of the sample etched by conventional RF RIE. This may be due to the additional freezeout of carriers into the traps produced after RF reactive ion etching.

A tremendous difference in the rms amplitude of the universal conductance fluctuations is observed between the two samples. Despite the fact that the conductance of the ECR RF RIE sample is only five times the conductance of the RF RIE sample at low temperature, the rms amplitude of the UCFs in the spectrum from the former is approximately 50-70 times larger than the rms amplitude of the UCFs in the spectrum from the latter. Since $L_{\phi} = \sqrt{D_e t_{\phi}}$, the difference in L_{ϕ} cannot be fully explained by the change in elastic scattering. One possibility is that this simple analysis is not adequate, and other workers have obtained similarly perplexing results. In a study by Hiramoto et.al.^{5.46}, their quasi-one-dimensional GaAs wires fabricated by focused ion beam implantation exhibit larger amplitude fluctuations than the prediction of equation 5.4 in the wider wires ($w \approx L_{\phi}$), while in the very thin wires ($w < L_{\phi}$), the fluctuations become smaller than the prediction. On the other hand, Ishibashi et.al.^{5.47} observed larger fluctuations than predicted for wires with a narrower width than L_{ϕ} . Moreover, Hansen et.al.^{5.48} reported recently that the nature and configuration of the voltage measurement probes can affect the conductance fluctuations significantly. Another possibility is that the traps and defects produced by RF reactive ion etching may have a larger electronic deficit or surplus changing the carrier density in the channel or giving rise to enhanced spin effects and spin-flip scattering. This type of scattering could reduce L_{ϕ} and might explain the observed dependence on the etching process. Furthermore, some recent conductance data in similar wires fabricated by RF RIE using SiCl_4 (work of M. Rahman, University of Glasgow) measured in the low temperature regime revealed some form of negative differential resistance behaviour in the low field (0-1.2V) I-V characteristics. This was attributed to the possibility of the sidewall damage region (see section 6.3.3.1) behaving as electron traps whereby the detrapping process of the electrons may take longer at low temperatures since they can only escape through tunneling or when enough energy is supplied.

5.4 Surface damage characterisation

The degree of surface modification caused by ECR RF and RF reactive ion etching was studied using Schottky diode contacts; to further identify the chemical composition of the etched surfaces, X-ray photoelectron spectroscopy analysis was carried out on the GaAs surfaces which were etched under the same conditions as the diodes.

5.4.1 Schottky diode characteristics

5.4.1.1 Experimental

The material employed was a $2 \times 10^{17} \text{cm}^{-3}$ Si-doped GaAs epitaxial layer of $1 \mu\text{m}$ thick on an n^+ substrate grown in Glasgow. The experimental procedure for diode fabrication was as in section 3.4.1.2, and the GaAs samples were etched in the ECR RF and RF reactive ion etching modes for 1 minute before diode fabrication. One other unetched GaAs chip was used as a control sample. The etching conditions used were described in section 5.3.4.3.

5.4.1.2 Results and discussion

A summary of the measurements derived from I-V characteristics is shown in table 5.2. The GaAs surface which has been RF reactive ion etched exhibits a higher ideality factor, lower barrier height, lower reverse breakdown voltage and a higher reverse leakage current compared with the ECR RF reactive ion etched surface. Assuming the electron transport mechanism in Schottky junction contacts as thermionic emission described in section 3.4.1.1, these results indicate that more interface traps are introduced after conventional RF reactive ion etching compared with ECR RF reactive ion etching. In a similar study by Knoedler et al.^{5.20}, an increase in ideality factor, surface depletion width and a decrease in effective carrier concentration after $\text{CCl}_2\text{F}_2/\text{He}$ RF RIE resulted. This they speculated to be due to helium ion bombardment and penetration thus creating deep level traps. Decreases in the sheet carrier concentration and mobility of GaAs/AlGaAs heterostructures after helium exposure have also been studied and

used to pattern devices^{5.41,49}. In the present work, the diode characteristics are indicative of the existence of an As-depleted surface acting as a donor defect layer in GaAs after dry etching as has been suggested by a number of workers^{5.50-53}, also see section 3.4.4.3 and below.

5.4.2 X-ray photoelectron spectroscopy (XPS) analysis

An explanation of this technique can be found in section 3.4.4.1.

5.4.2.1 Experimental

The material used for the XPS study was a $2 \times 10^{17} \text{cm}^{-3}$ Si-doped GaAs layer of $1 \mu\text{m}$ thickness grown on an n^+ substrate by molecular beam epitaxy. Two GaAs samples of size $5 \times 5 \text{mm}^2$ were ECR RF and RF reactive ion etched for 1 minute using the etch condition described in section 5.3.4. One other unetched GaAs chip was used as a control sample.

The experimental work for this study was completed in a V.G. ESCALAB MkI electron spectrometer fitted for XPS at Harwell laboratory. The equipment used is briefly described below. The basic system consists of two stainless steel ultra high vacuum chambers separated by a gate valve. Samples are admitted to the preparation chamber by use of a small air lock evacuated by a rotary pump. Since the ingress of damp residual gases will degrade the vacuum during transfer, this chamber provides a buffer between the poor vacuum in the air lock and the high quality vacuum ($\approx 1 \times 10^{-9}$ Torr) in the analysis chamber. Both chambers are pumped by Edwards oil diffusion pumps, in addition, a titanium sublimation pump is provided on the analysis chamber. The spectrometer consists of a 300 Watt X-ray source, a spherical sector electron analyser, and the sample is attached to a manipulator which is maintained at earth potential. An electron flood gun is fitted to neutralise sample charging whenever non-conducting material is being analysed. An $\text{AlK}\alpha$ (1486.6eV) X-ray source operated at 15keV was employed for this experiment. The output electrons from the sample then enter an electron analyser whose energies are determined by their deflection in an electrostatic field. The electron analyser is attached to the analysis chamber by a long focal length electrostatic transfer lens. A life-size electron image of the sample

is projected onto the analyser entrance slit. The electron deflection is caused by the potential difference (set by the analyser control) between the inner and outer hemispheres. The retarding grids (with retard voltages 0-15V) at the analyser entrance are used to scan the spectrum (with kinetic energies in the range 0-2500eV) while the analyser is operated at a constant pass energy in order to maintain a constant energy resolution. The range of voltages, corresponding to the desired kinetic energies to be swept are preset using a computer. The electrons then pass through the exit slits with a current of typically less than 1×10^{-14} A. A pulse counting system based on a very high gain channel electron multiplier is used to detect this low current. Each electron detected gives rise to an avalanche of about 1×10^8 secondary electrons contained in a 10ns pulse. The output pulses are then accumulated and recorded in a computer which is connected to a graph plotter. A schematic diagram of the XPS system is shown in figure 5.19. In the present analysis, both charge compensation and Shirley background level were taken into account^{5.63} and the XPS peaks (measured to ± 0.1 eV) were identified from ref. 5.54,57-61.

5.4.2.2 Results and Discussion

The elemental atomic concentrations (%) determined from the integrated peak intensity and experimental sensitivity factors for the control, ECR RF RIE and RF RIE samples are shown in table 5.3. In general, both carbon and oxygen are present in all samples while higher concentrations are detected on the etched surfaces. This is not surprising since all the samples have been exposed to atmosphere during sample transfer to the XPS chamber, which might have introduced some additional room ambient contamination. Nonetheless, a comparison of the surfaces is still valid. It is worth noting that the effect of increased carbon and oxygen concentrations is more prominent on the GaAs surface etched under conventional RF RIE conditions compared with the ECR RF case. In addition, the presence of fluorine is detected on the same RF RIE sample.

The Ga/As ratios derived from the XPS data indicate that the GaAs surface is considerably more Ga-rich after RF reactive ion etching than after ECR RF reactive ion etching. Ga-rich surfaces have been observed in the reactive ion etching of GaAs using $\text{CCl}_2\text{F}_2/\text{O}_2$ by Pearton et.al.^{5.54} and CCl_2F_2 by Yabumoto

et. al.^{5.55}. This result is significant since an As depleted surface has been suggested to be the cause of diode characteristics similar to those measured in this study^{5.50-53}, see sections 3.4.4.3 and 5.4.1.2. However, from this experiment alone, it cannot be concluded whether the larger carbon and oxygen contamination observed in the RF RIE sample is produced during the etching process or as a result of more susceptible surface reactions from an initial Ga-rich surface after etching. Yabumoto et. al.^{5.55} have also observed an increase in oxygen uptake after reactive sputter etching of GaAs in CCl_2F_2 ; this they believed to be due to the existence of As vacancies after etching.

Figures 5.20a) and b) show the $\text{Ga}(3p_{3/2})$ and $\text{Ga}(3d)$ signals for the control, ECR RF RIE and RF RIE samples, respectively. Little difference is observed between the control and the ECR RF RIE samples in both transitions indicating a well preserved surface after ECR RF reactive ion etching. However, for the RF RIE sample, a shift of the $\text{Ga}(3p_{3/2})$ peak from 104.7eV to 105.5eV is detected implying the presence of Ga_2O_3 , accompanied by a slight shoulder appearing at the original peak (104.7eV, see figure 5.20a). Moreover, the broadening of the shoulder at 108.0eV is suggestive of the presence of Ga-F type bonds. Similar chemical bonding arrangements after RF reactive ion etching are evident from the $\text{Ga}(3d)$ signal taken from the same sample (see figure 5.20b). An extreme broadening and the emergence of possibly two binding states between 20eV and 22eV are observed. Two components may be resolved at 20.3eV and at 21.5eV suggesting the presence of Ga_2O_3 and GaF_3 respectively. In addition, it is possible that the presence of the $\text{F}(1s)$ lineshape at 685.8eV from the RF RIE sample is due to both Ga-F and As-F type bonds, see figure 5.21. However, further analysis of the $\text{As}(3d)$ signal (figure 5.22) rule out the possibility of the existence of As-F bonds on the substrate surface. While Ga-F type bonds appear to exist on the substrate surface after RF reactive ion etching, it is not surprising to find the absence of As-F bonds since AsF_3 is a relatively volatile compound^{5.56}. Moreover, the ion-induced removal of GaF_3 has been reported to be the rate limiting step in this etching process^{5.16}. However, in a similar experiment by Seaward et. al.^{5.57}, Ga-F bonding was not observed; this may be attributed to the different etch conditions used.

5.5 Conclusions

- 1) ECR RF RIE of GaAs using $\text{CCl}_2\text{F}_2/\text{He}$ was developed using optical emission spectroscopy. Due to the high ionisation efficiency of ECR excitation and the Al electrode, silicon wafers were mounted on the cathode in order to produce a contamination suppressed environment.
- 2) By comparing quantum wire cut-off widths, the amount of sidewall damage is found to be dependent on both ion energies and etch time, with the lowest sidewall damage caused by ECR RF RIE, followed by RF RIE and MAG RF RIE.
- 3) The wire conductance and its rms amplitude in the magnetoconductance measured at low temperature appear to be very sensitive to the sidewall damage induced after RIE.
- 4) Comparison of diode characteristics of an ECR RF RIE GaAs surface and RF RIE GaAs surface indicate that more interface traps are introduced after RF RIE.
- 5) XPS data reveal that the ECR RF RIE surface is slightly contaminated with carbon and O_2 while higher concentrations are detected on the RF RIE surface. The RF RIE surface also appear to be Ga-rich with some evidence of Ga-F bonding.

5.6 Appendix 1

At IBM TJW Research Centre in Yorktown Heights, two routines were used to generate mask data sets for the Vecor Scan 6 (VS6) electron beam writing machine:

- 1) From Glives 1 processor (GL1-data): after the design is generated in the Integrated Graphics System (IGS), the data (GL1) is transferred to the Multiple Virtual Storage (MVS)-system (via OUTPUT DATA) into a MVS-dataset. Subsequently, the MVS-dataset has to be converted into a mask dataset for the VS6 e-beam system. This is carried out using the Glives 2 post processor during which

proximity correction may be specified.

2) Prepared on Virtual Machine (VM): X,Y data sets input containing X,Y,DX,DY, shape, code, dose (one record per shape) can be converted into mask data sets by running the program VS6MASK.

After having generated mask data-sets in the MVS system, they were transferred to the VS6 Series/1 for exposure purposes in the VS6 e-beam machine.

5.7 References

- 5.1) Y.H.Lee, J.E.Heidenreich III and G.Fortuno; *J.Vac.Sci.Technol.* **A7** p.903, 1989
- 5.2) A.M.El-Masry, F-O.Fong, J.C.Wolfe and J.N.Randall; *J.Vac.Sci.Technol.* **B6(1)** p.257, 1988
- 5.3) J.Hopwood, D.K.Reinhard and J.Asmussen; *J.Vac.Sci.Technol.* **B6(6)** p.1896, 1988
- 5.4) J.Hopwood, M.Dahimene, D.K.Reinhard and J.Asmussen; *J.Vac.Sci.Technol.* **B6(1)** p.268, 1988
- 5.5) K.Suzuki, S.Okudaira and I.Kanomata; *J. Electrochem.Soc.* **126(6)** p.1024, 1979
- 5.6) K.Suzuki, S.Okudaira, N.Sakudo and I.Kanomata; *Jpn. J. Appl. Phys.* **16(11)** p.1979, 1977
- 5.7) J.Pelletier and M.J.Cooke; *J. Appl. Phys.* **65(2)** p.464, 1989
- 5.8) C.Pomot, B.Mahi, B.Petit, Y.Arnal and J.Pettetier; *J.Vac.Sci.Technol.* **B4(1)** p.1, 1986
- 5.9) R.Cheung, Y.H.Lee, C.M.Knoedler, K.Y.Lee, T.P.SmithIII and D.Kern; *Appl. Phys. Letts.* **54** p.2130, 1989
- 5.10) R.Cheung, Y.H.Lee, K.Y.Lee, T.P.Smith III, D.P.Kern, S.P.Beaumont and C.D.W.Wilkinson; *J.Vac.Sci.Technol.* **B7(6)** p.1462, 1989
- 5.11) K.Asakawa and S.Sugata; *J.Vac.Sci.Technol.* **A4(3)** p.677, 1986
- 5.12) J.A.Skidmore, L.A.Coldren, E.L.Hu, J.L.Merz and K.Asakawa; *J.Vac.Sci.Technol.* **B6(6)** p.1885, 1988
- 5.13) 'Tables of Spectral Lines of Neutral and Ionised Atoms', A.R. Strigaov and N.S.Sventitskii, Plenum, New York, 1968
- 5.14) S.C.McNevin and G.E.Becker; *J. Appl. Phys.* **58(12)** p.4670, 1985
- 5.15) M.Balooch and D.R.Olander; *J.Vac.Sci.Technol.* **B4(4)** p.794, 1986
- 5.16) R.E.Klinger and J.E.Greene; *J. Appl. Phys.* **54(3)** p.1595, 1983
- 5.17) H.Nagasaka, H.Okano and N.Motegi; *Proc. Symp. Dry Process*, p.79, 1982
- 5.18) K.Hikosaka, T.Mimura and K.Joshin; *Jpn. J. of Appl. Phys.* **20(11)** p.L847, 1981
- 5.19) C.M.Knoedler and T.F.Kuech; *J.Vac.Sci.Technol.* **B4(5)** p.1233, 1986
- 5.20) C.M.Knoedler, L.Osterling and H.Shtrikman; *J.Vac.Sci.Technol.* **B6** p.1573, 1988
- 5.21) A.Seabaugh; *J.Vac.Sci.Technol.* **B6(1)** p.77, 1988

- 5.22) D.P.Kern, P.J.Houzeo, P.J.Coane and T.H.P.Chang; *J.Vac.Sci.Technol.* **B1(4)** p.1096, 1983
- 5.23) P.J.Coane, D.P.Kern, A.J.Speth and T.H.P.Chang; in *Proc. of the 10th Conf. on Electron and Ion Beam Sci. and Technol.*, edited by R.Bakish, (Electrochemical Soc., Montreal, 1983)
- 5.24) P.J.Coane, D.P.Kern, A.J.Speth and T.H.P.Chang; *Microcircuit Eng.'82*, Grenoble, p.373, 1982
- 5.25) S.A.Rishton, D.P.Kern, E.Kratschmer and T.H.P.Chang; preprint paper
- 5.26) S.A.Rishton and D.P.Kern; *J.Vac.Sci.Technol.* **B5(1)** p.135, 1987
- 5.27) S.P.Beaumont, T.Tamamura and C.D.W.Wilkinson; in *Proc. Int. Conf. on Microlithography*, Amsterdam, edited by R.P.Kramer, Delft University Press, 1981
- 5.28) A.Scherer, M.L.Roukes, H.G.Craighead, R.M.Ruthen, E.D.Beebe and J.P.Harbison; *Appl. Phys. Letts.* **51(25)** p.2133, 1987
- 5.29) S.Thoms, S.P.Beaumont, C.D.W.Wilkinson, J.Frost and C.R.Stanley; *Microcircuit Engineering 1986*, edited by H.W.Lehmann and Ch. Bleicker (North-Holland, Amsterdam, 1986), p.249
- 5.30) R.Cheung, S.Thoms, I.McIntyre, C.D.W.Wilkinson and S.P.Beaumont; *J.Vac.Sci.Technol.* **B6** p.1911, 1988
- 5.31) D.G.Lishan, H.F.Wong, D.L.Green, E.L.Hu, J.L.Merz and D.Kirillov; preprint paper.
- 5.32) M.Rahman; Private Communication, Glasgow University
- 5.33) K.L.Seaward, N.J.Moll, D.J.Coulman and W.F.Stickle; *J. Appl. Phys.* **61(6)** p.2358, 1987
- 5.34) M.Oren, S.Zemon, P.Norris and T.Emma; *Inst. Phys. Conf. Ser. No.79*, p.361, 1985
- 5.35) C.P.Umbach, S.Washburn, R.B.Laibowitz and R.A.Webb; *Phys. Rev.* **B30** p.4048, 1984
- 5.36) J.C.Licini, D.J.Bishop, M.A.Kastner and J.Melngailis; *Phys. Rev. Letts* **55** p.2987, 1985
- 5.37) S.B.Kaplan and A.Hartstein; *Phys. Rev. Letts.* **56** p.2403, 1986
- 5.38) W.J.Skopol, P.M.Mankiewich, R.E.Howard, L.D.Jackel and D.M.Tennant; *Phys. Rev. Letts.* **56** p.2865, 1986
- 5.39) G.P.Whittington, P.C.Main, L.Eaves, R.P.Tayler, S.Thoms, S.P.Beaumont and C.D.W.Wilkinson; *Int. Conf.Superlattice, Microstructures and*

Microdevices, Gothenburg; in 'Superlattice and Microstructures', 1986

5.40) T.J.Thornton, M.Pepper, G.J.Davis and D.Andrews; 18th Int. Conf. on the Physics in Semiconductor, Stockholm, 1986

5.41) T.L.Cheeks, M.L.Roukes, A.Scherer and H.G.Craighead; Appl. Phys. Letts. **53(20)** p.1964, 1988

5.42) B.L.Al'tshuler, Pis'ma Zh. Eksp. Teor. Fiz. **41** p.530, 1985 [JETP Lett. **41** p.648, 1985]

5.43) P.A.Lee, A.D.Stone and H.Fukuyama; Phys. Rev. **B35** p.1039, 1987

5.44) R.Landauer; Philos. Mag. **21** p.863, 1970

5.45) Y.Aharonov and D.Bohm; Phys. Rev. **115** p.485, 1959

5.46) T.Hiramoto, K.Hirakawa, Y.Iye and T. Ikoma; Appl. Phys. Letts. **51(20)** p.1620, 1987

5.47) K.Ishibashi, K.Nagata, K.Gamo, S.Namba, S.Ishida, K.Murase, M.Kawabe and Y.Aoyagi; Solid State Comm. **61(6)** p.385, 1987

5.48) W.Hansen, T.P.Smith III, D.P.Divincenzo, K.Y.Lee, Y.H.Lee and R.Cheung; preprint paper submitted to EP2DS8 Conference, 1989

5.49) C.M.Knoedler, L.Osterling and M.Heiblum; J. Appl. Phys. **65** p.1800, 1989

5.50) Y.X.Wang and P.H.Holloway; J.Vac.Sci.Technol. **B2(4)** p.613, 1984

5.51) K.Yamasaki, K.Asai, K.Shimada and T.Makimura; J. Electrochem. Soc. **129(12)** p.2760, 1982

5.52) C.S.Wu, D.M.Scott, W.X.Chen and S.S.Lau; J. Electrochem. Soc. **132(4)** p.918, 1985

5.53) F.H.Mullins and A.Brunnschweiler; Solid State Electronics **19** p.47, 1976

5.54) S.J.Pearton, M.J.Vasile, K.S.Jones, K.T.Short, E.Lane, T.R.Fullowan, A.E.Von Neida and N.M.Haegel; J. Appl. Phys. **65(3)** p.1281, 1989

5.55) N.Yabumoto and M.Oshima; J. Electrochem. Soc. **132(9)** p.2224, 1985

5.56) CRC Handbook of Chemistry and Physics, 1986-87

5.57) K.L.Seaward, N.J.Moll, D.J.Coulman and W.F.Stickle; J. Appl. Phys. **61(6)** p.2358, 1987

5.58) C.R.Brundle and D.Seybold; J.Vac.Sci.Technol. **16** p.1186, 1979

5.59) M.K.Bahl, R.D.Woodall, R.L.Watson and K.J.Irgolic; J. Chem. Phys. **64** p.1210, 1976

5.60) G.E.McGuire, G.K.Schweitzer and T.A.Carlson; Inorg. Chem. **12** p.2451, 1973

5.61) G.Leonhardt, A.Berndtsson, J.Hedman, M.Klasson, R.Nilsson and

C.Nordling; Phys. Status Solidi **60** p.241, 1973

5.62) The Identification of Molecular Spectra; R.W.B.Pearse and A.G.Gaydon,
Wiley, New York, 1950

5.63) P.K.Ghosh; 'Photoelectron spectroscopy,' in Chemical Analysis (Wiley,
New York, vol. 67) 1983

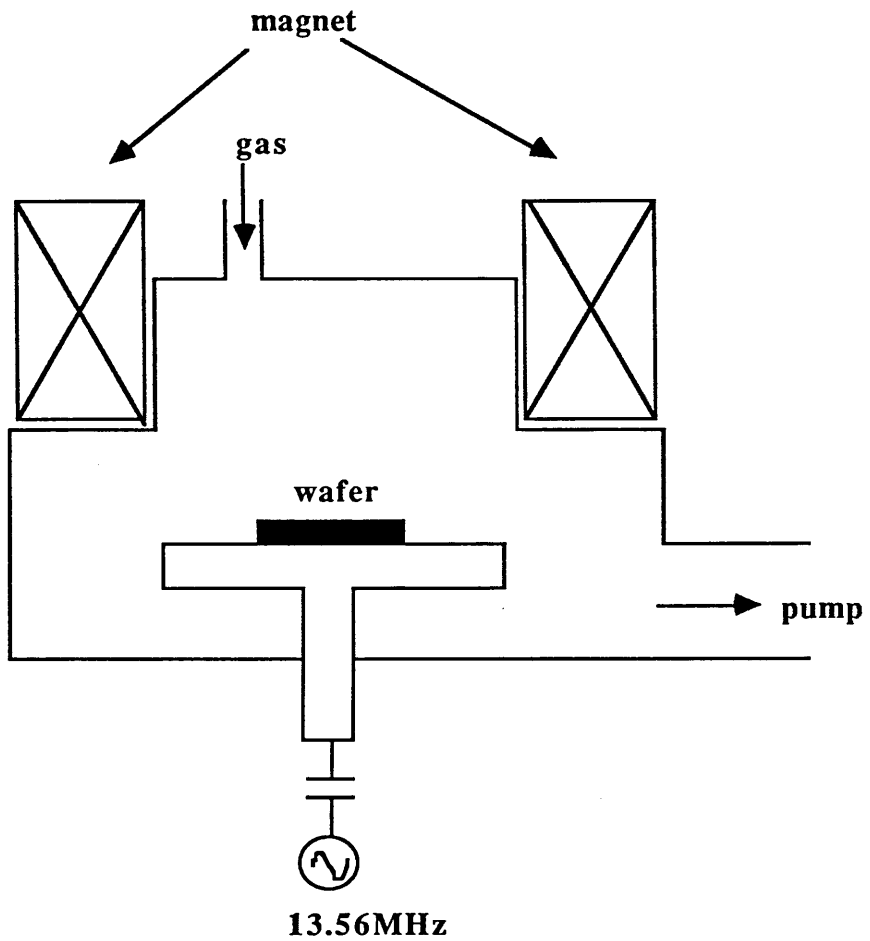


Figure 5.1 Magnetron rf reactive ion etching

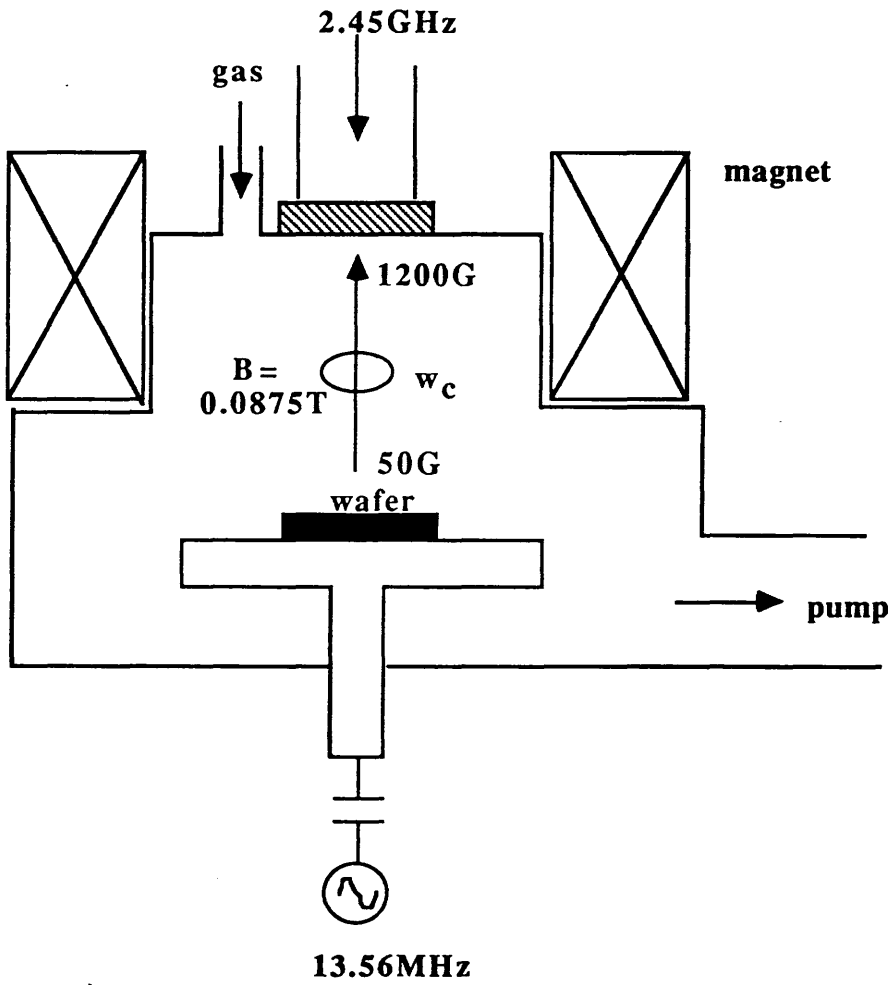


Figure 5.2 Electron cyclotron resonance rf reactive ion etching

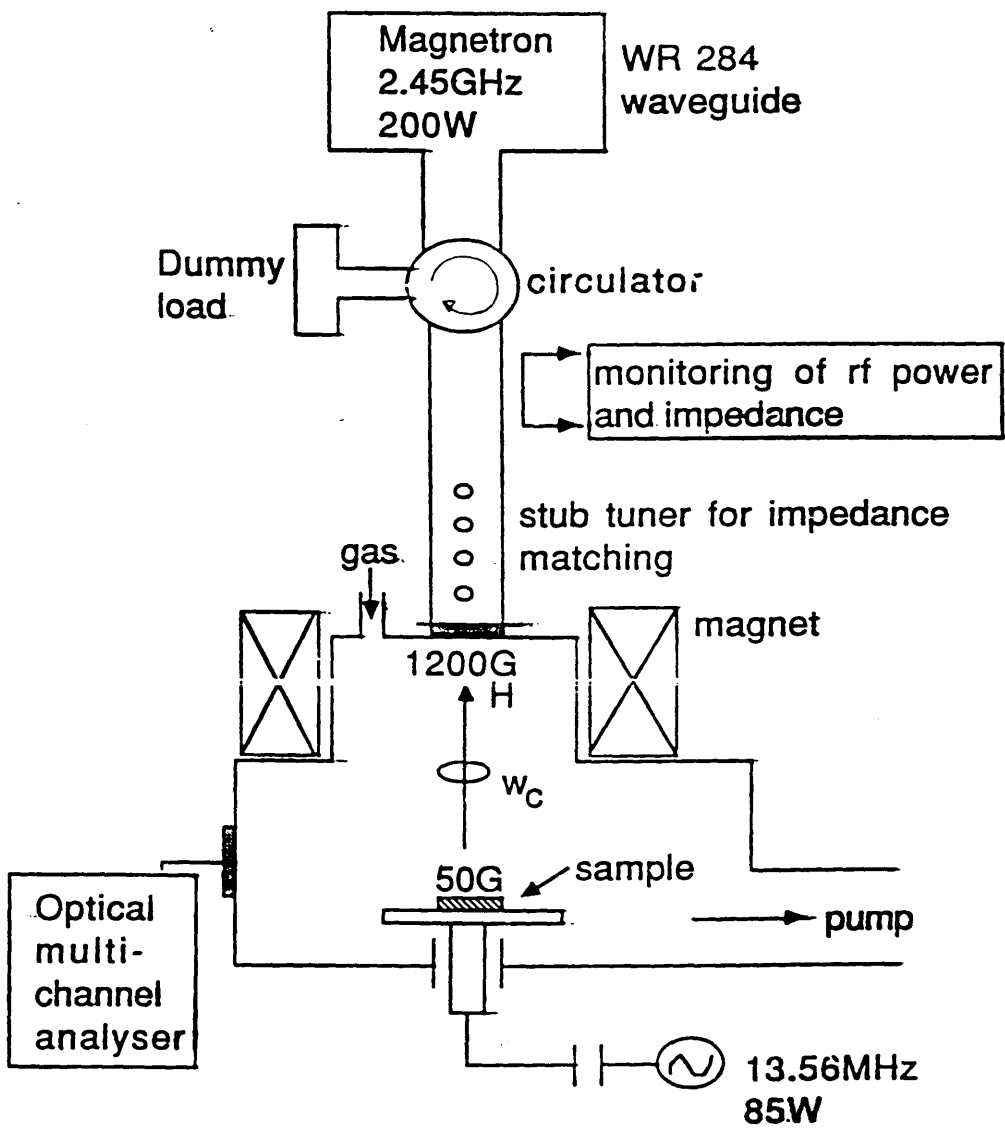
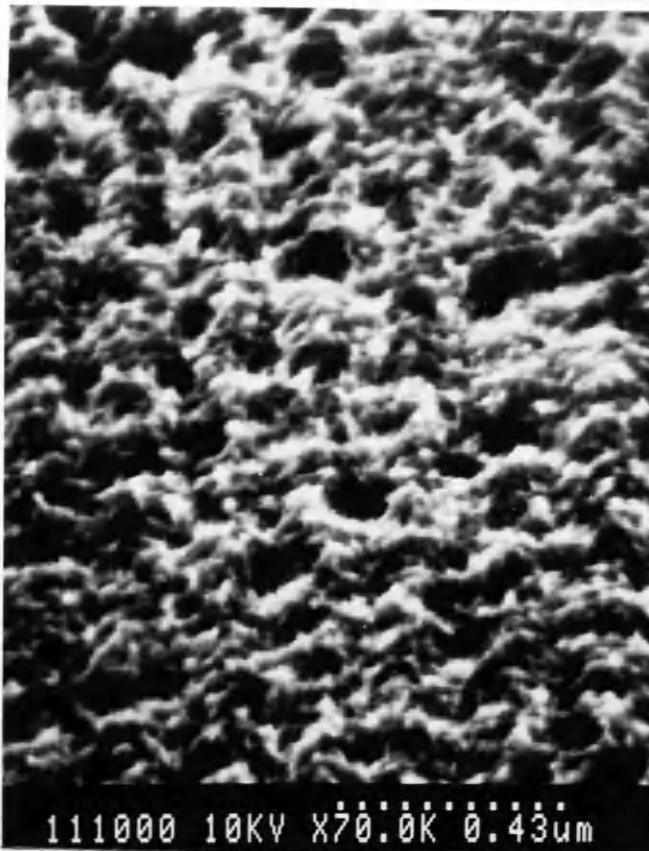


Figure 5.3 Schematic diagram of an ECR-RF hybrid plasma reactor



SEM 5.1 Initial GaAs surface produced after ECR RF RIE in $\text{CCl}_2\text{F}_2/\text{He}$ 1:1 at 200W μ wave power, 5mT total pressure, $0.1\text{W}/\text{cm}^2$ rf power density and 90V dc bias



SEM 5.2 Initial GaAs surface produced after MAG RF RIE in $\text{CCl}_2\text{F}_2/\text{He}$ 1:1 at $0.36\text{W}/\text{cm}^2$ rf power density, 5mT total pressure and 300V dc bias

CCl ₂ F ₂ /He sccm:sccm	μwave power (Watts)	rf power density (W/cm ²)	pressure (mT)	self bias (V)	etch depth (nm/min.)	comment
10:10	200	0.1	5	90	20	no oxide etch
10:10	200	0.1	5	90	41	with acid oxide etch
10:10	200	0.1	5	90	-	with PMMA on Si wafer on Al electrode
10:10	500	0.1	1	100	100	with acid oxide etch
8:8	400	0.3	0.5	80	90	with acid oxide etch plasma very unstable

Table 5.1 Trial etch conditions in the ECR RF RIE of GaAs using

CCl₂F₂/He

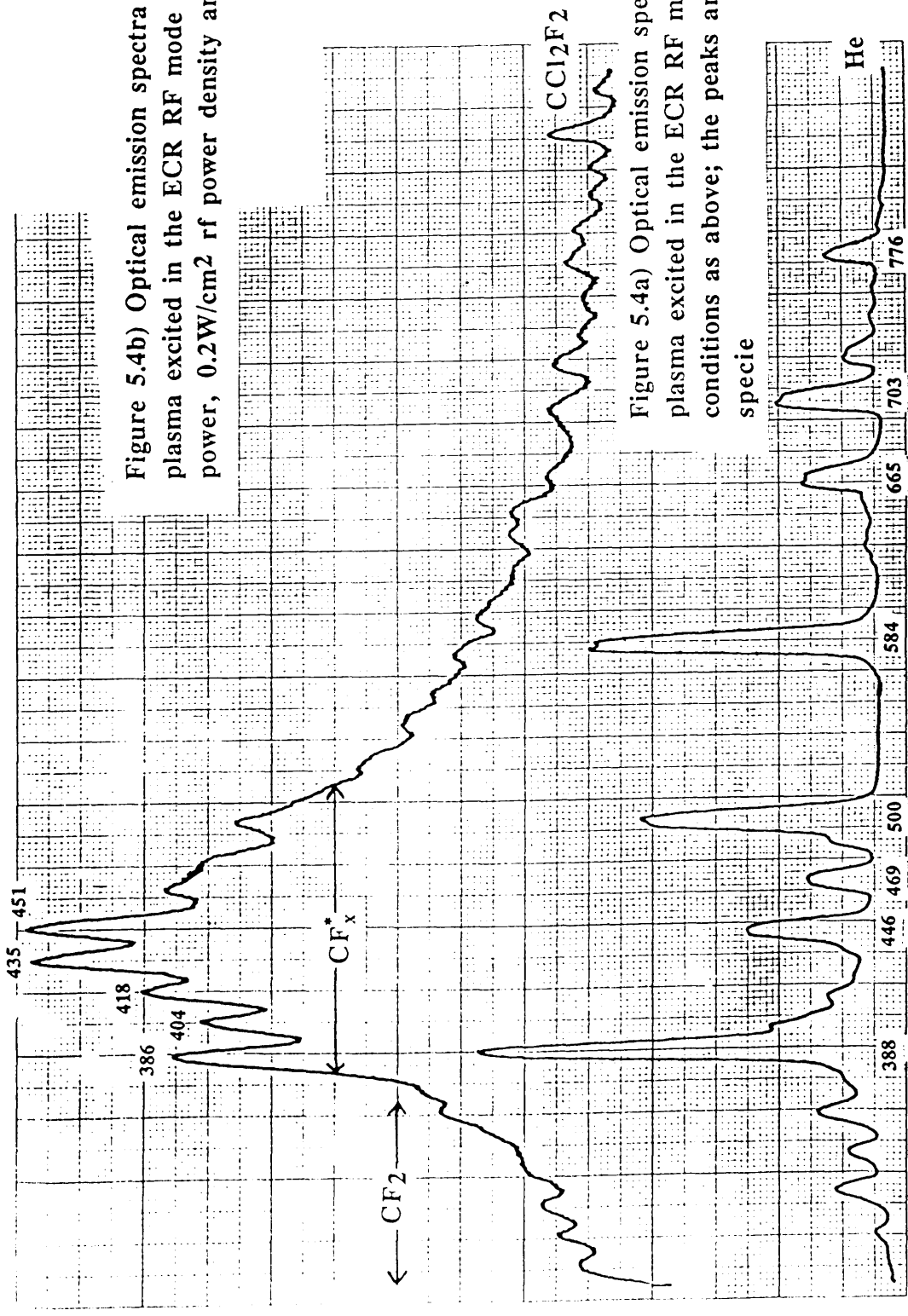


Figure 5.4b) Optical emission spectra of a CCl_2F_2 plasma excited in the ECR RF mode with $200\text{W}\mu\text{wave}$ power, $0.2\text{W}/\text{cm}^2$ rf power density and 5mT pressure

Figure 5.4a) Optical emission spectra of a helium plasma excited in the ECR RF mode with identical conditions as above; the peaks are identified as HeI specie

200nm 800nm

Wavelength (nm)

Figure 5.5a) Optical emission spectra of a $\text{CCl}_2\text{F}_2/\text{He}$ 1:1 MAG RF plasma excited with $0.33\text{W}/\text{cm}^2$ rf power density and 5mT total pressure showing the dominance of HeI lines

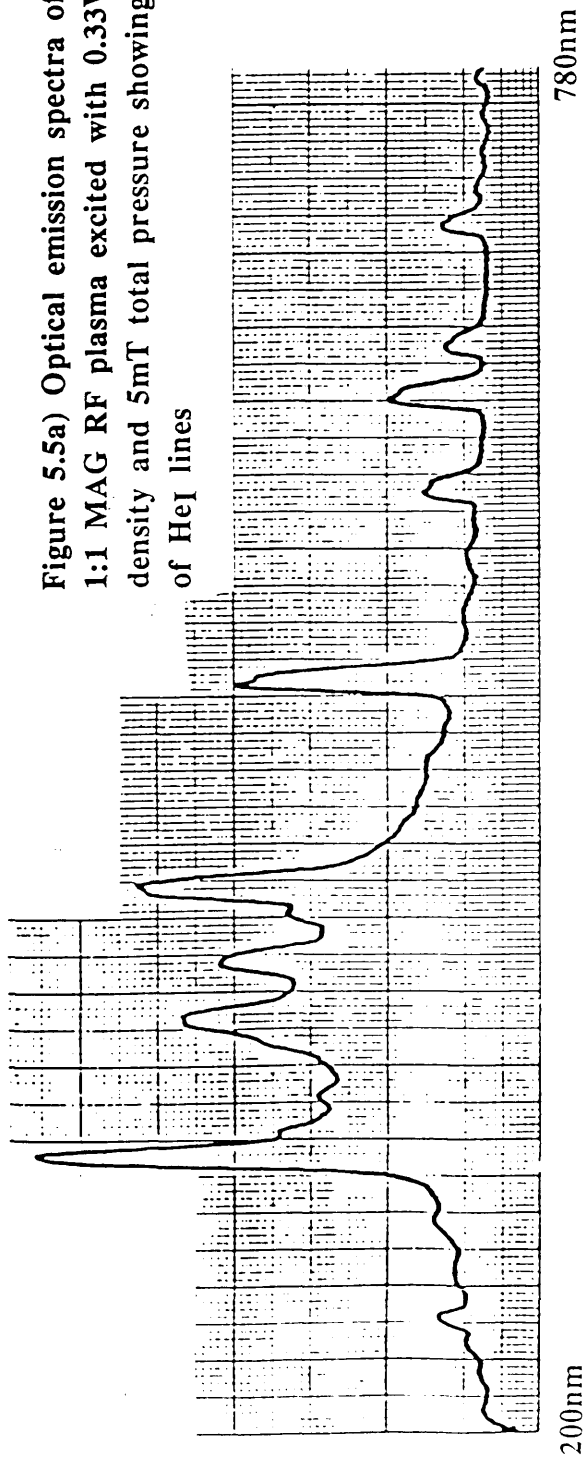
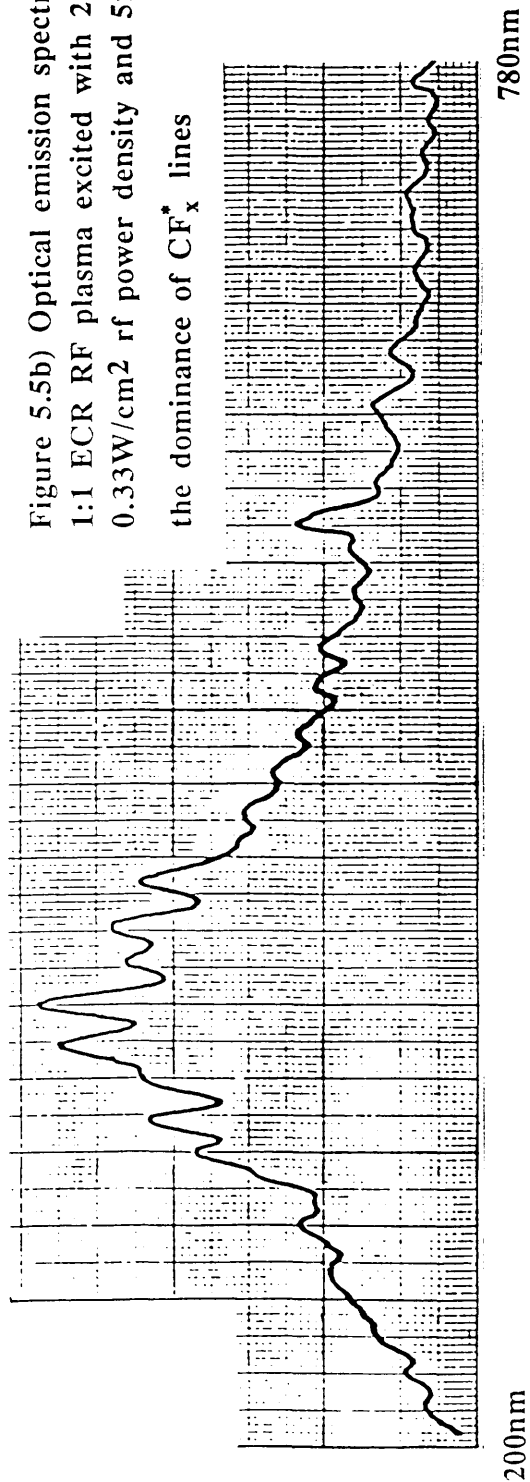


Figure 5.5b) Optical emission spectra of a $\text{CCl}_2\text{F}_2/\text{He}$ 1:1 ECR RF plasma excited with 200W microwave power, $0.33\text{W}/\text{cm}^2$ rf power density and 5mT total pressure showing the dominance of CF_x^* lines



Etch depth (nm)

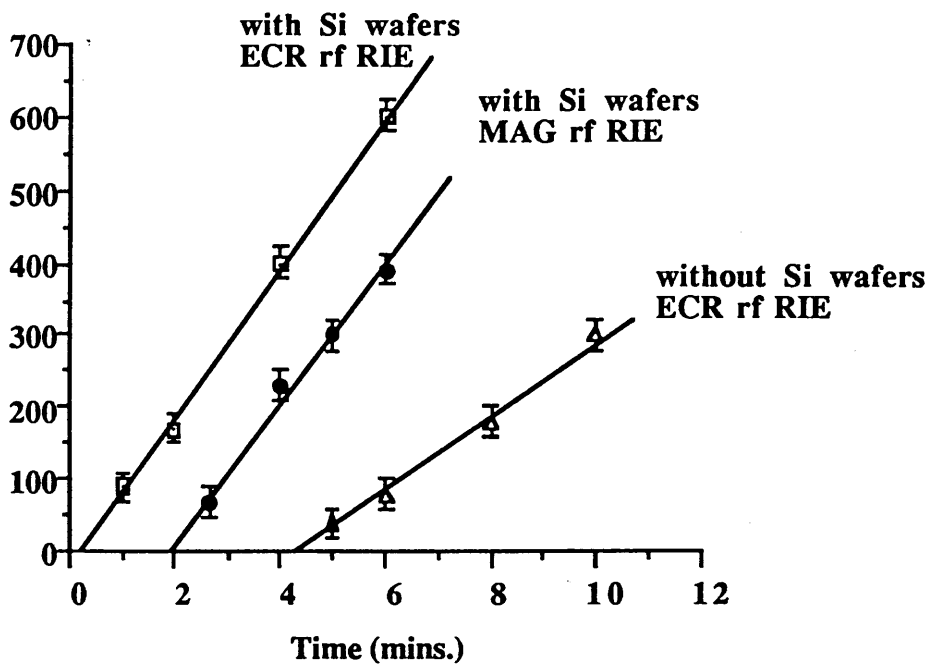


Figure 5.6 Graph of etch depth vs. time for GaAs etched in ECR rf and MAG rf RIE using $\text{CCl}_2\text{F}_2/\text{He}$

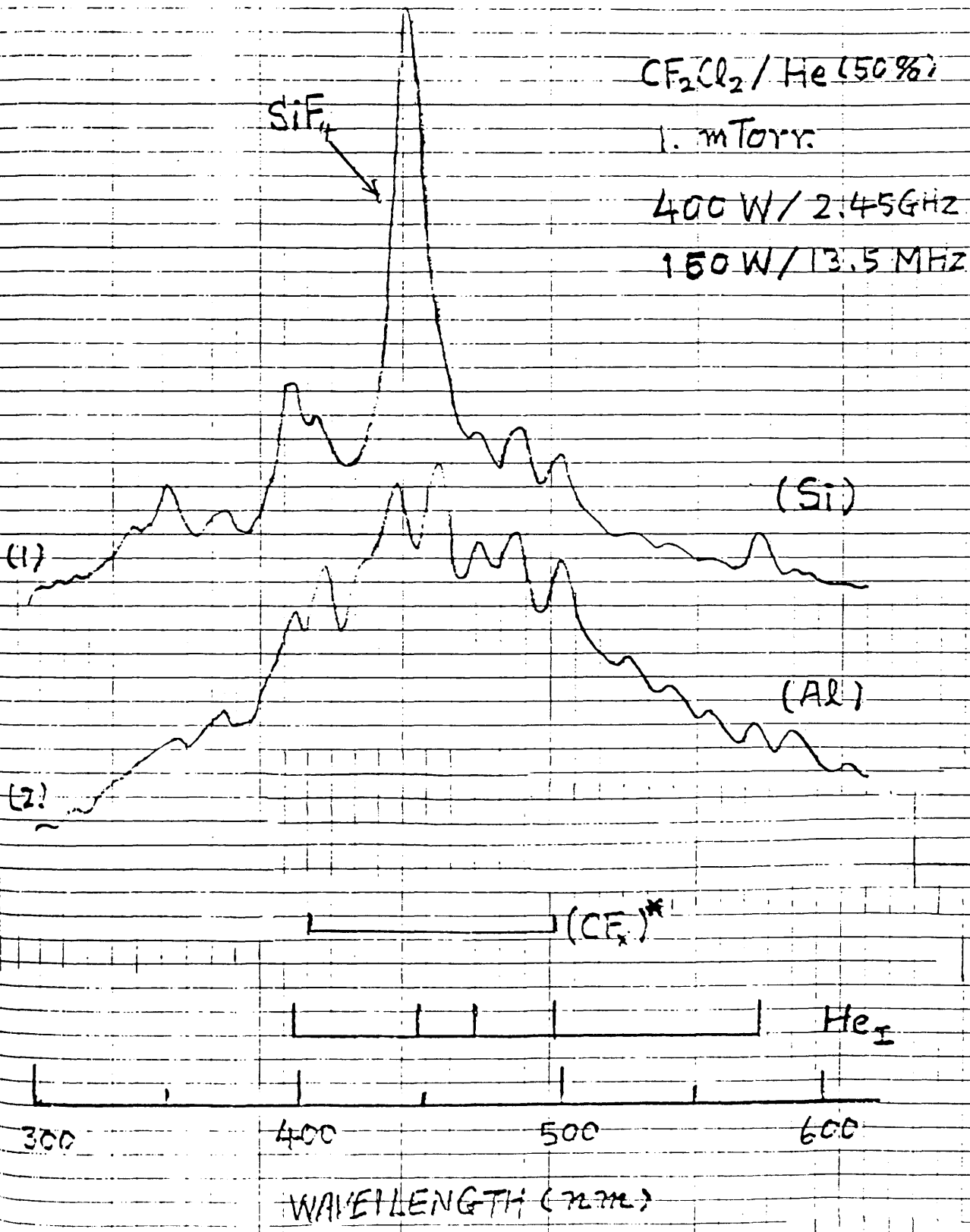
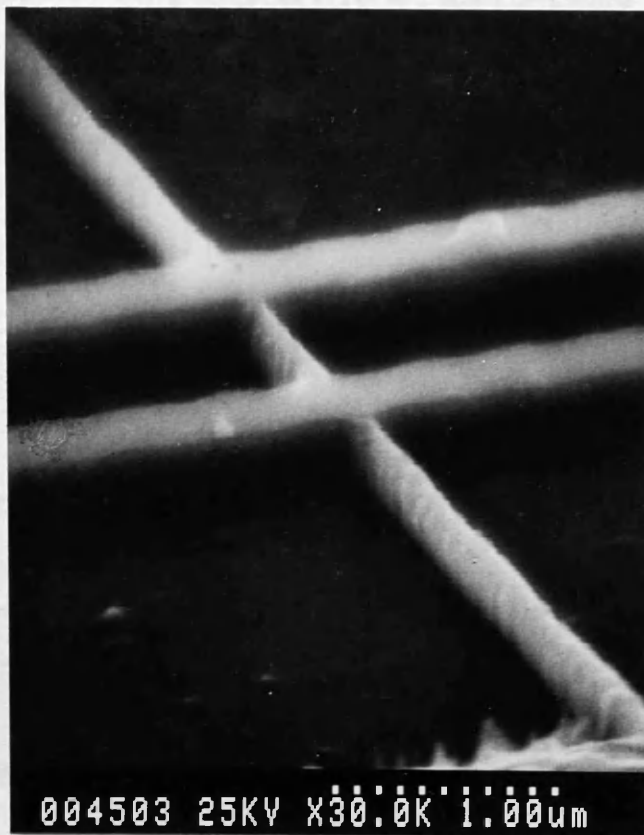


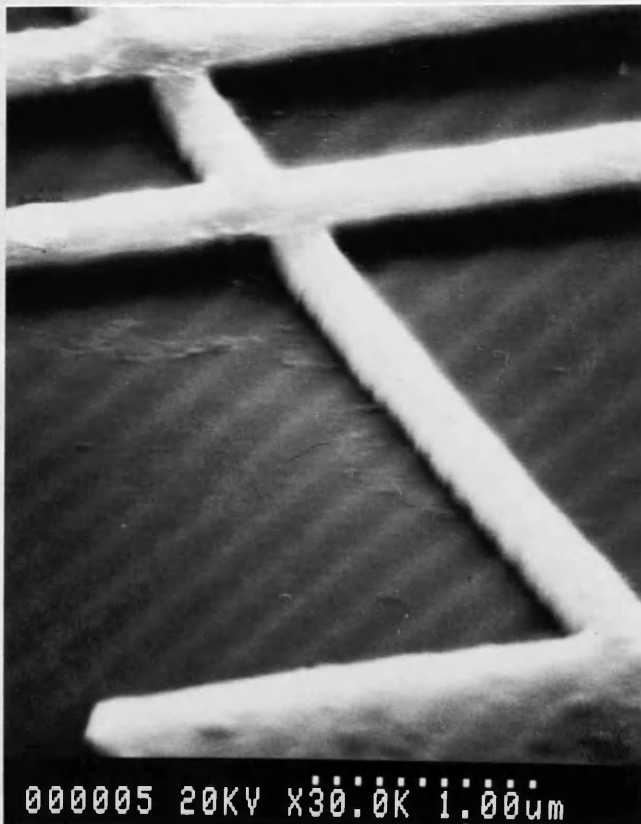
Figure 5.7 showing optical emission spectra of an ECR RF plasma with and without the silicon wafers



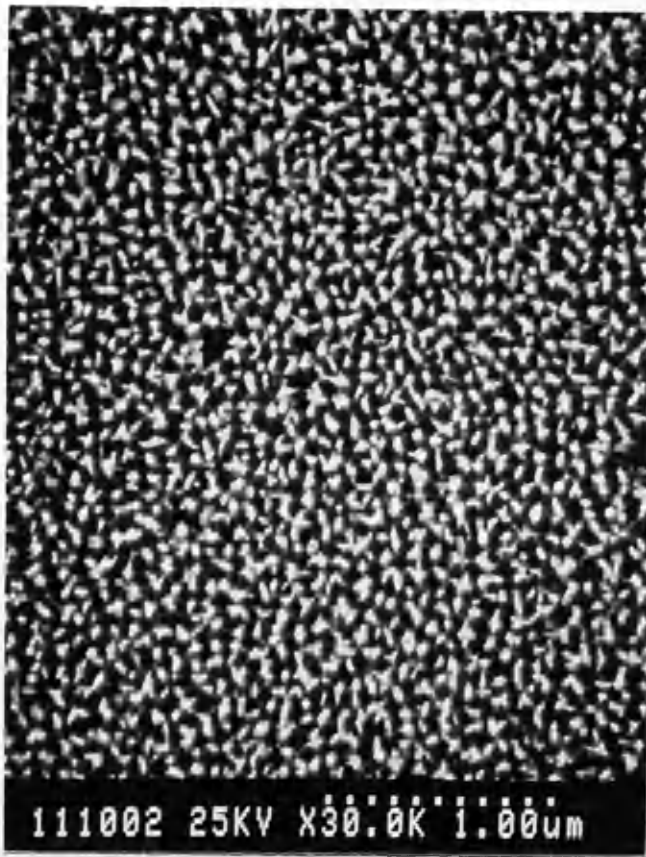
SEM 5.3 GaAs etched under similar conditions as in SEM 5.1 (ECR RF RIE) in the presence of silicon wafers covering about 43% of the Al electrode



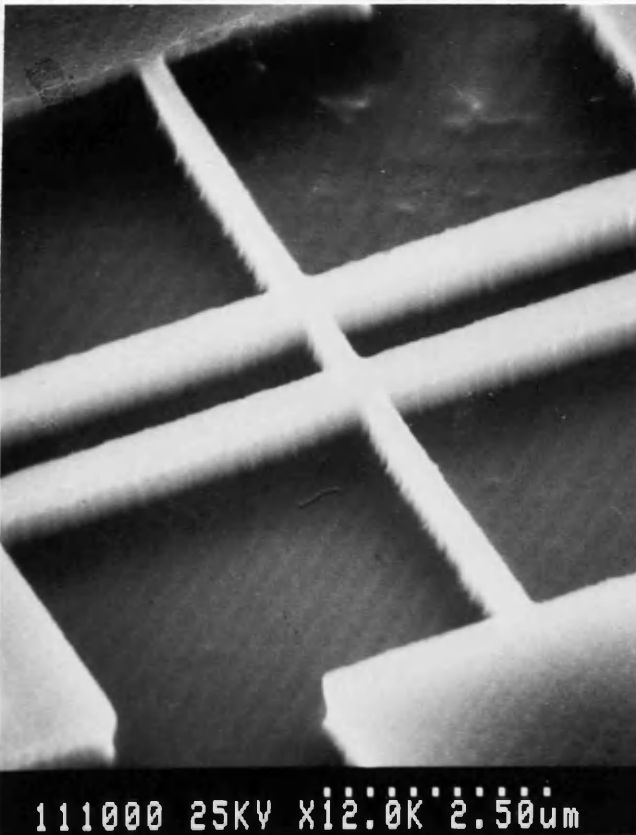
SEM 5.4 A GaAs wire with Hall bar geometry etched under the same conditions as in SEM 5.3 (ECR RF RIE) using NiCr mask



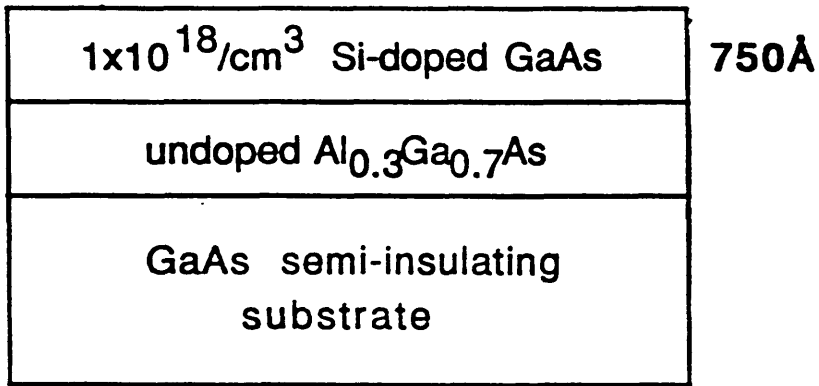
SEM 5.5 A GaAs wire structure with Hall bars etched under the same conditions as in SEM 5.2 (MAG RF RIE) using NiCr mask



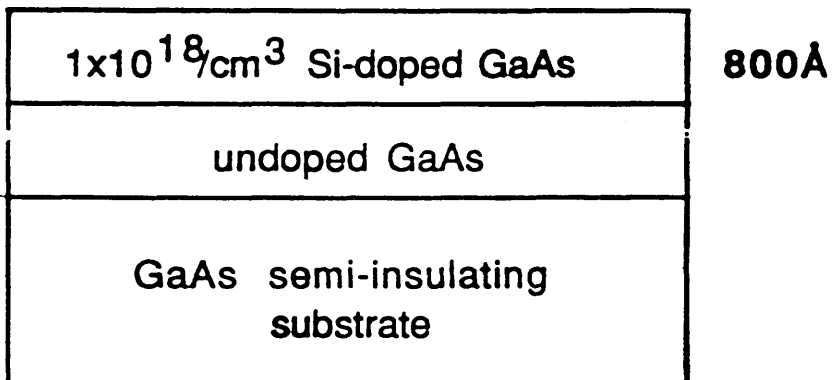
SEM 5.6 GaAs surface ECR RF reactive ion etched in $\text{CCl}_2\text{F}_2/\text{He}$ 1:1 with 200W μ wave power, 5mT total pressure, $0.1\text{W}/\text{cm}^2$ rf power density and 50V dc bias



SEM 5.7 GaAs wire with Hall bar geometry after ECR RF RIE in $\text{CCl}_2\text{F}_2/\text{He}$ 1:1 using 200W μ wave power, 2mT total pressure, $0.17\text{W}/\text{cm}^2$ rf power density and 100V dc bias



a) With AlGaAs etch stop and mobility of $2000 \text{cm}^2 / \text{Vs}$ at 77K



b) Without etch stop and mobility of $2000 \text{cm}^2 / \text{Vs}$ at 77K.

Figure 5.8 Material design

ID: OHM2(1) -400.0 -300.0 700.0 700.0

17November88 at 10:02:41

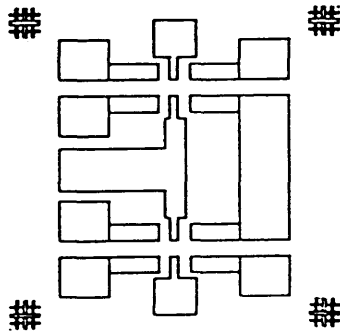


Figure 5.9 First level showing ohmic contact and alignment marks

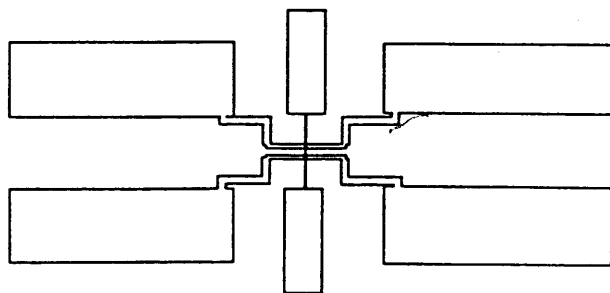
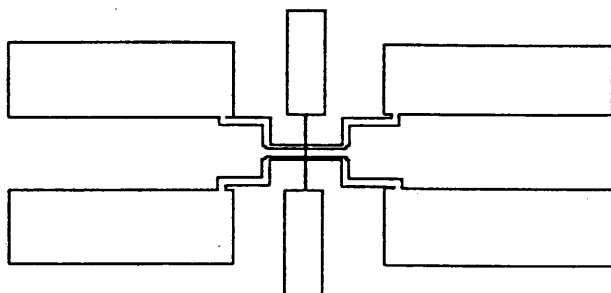


Figure 5.10 Second level showing wires with Hall bar geometry

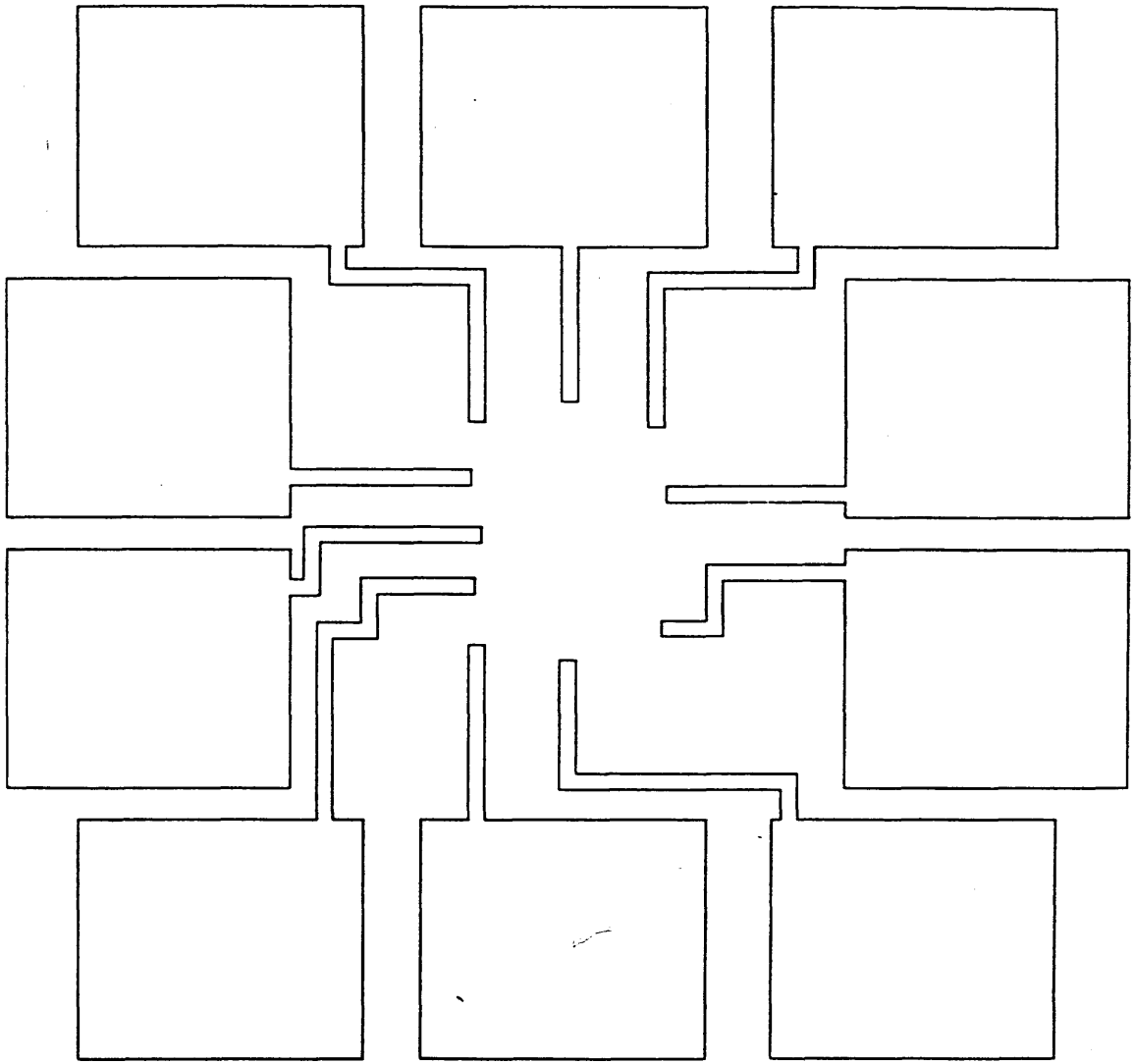


Figure 5.11 Third level showing bonding pads design

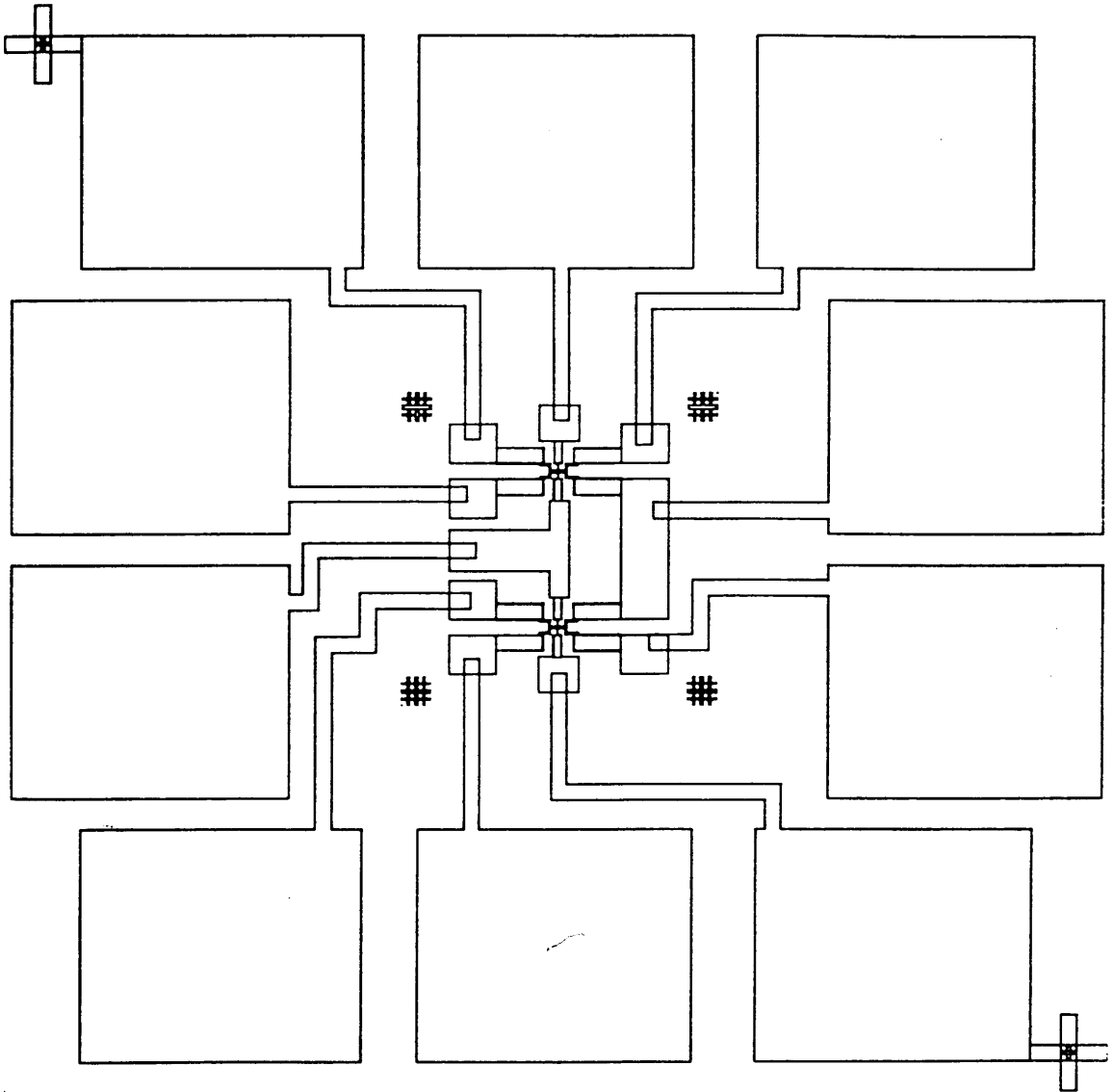


Figure 5.12 Complete layout of exposure pattern

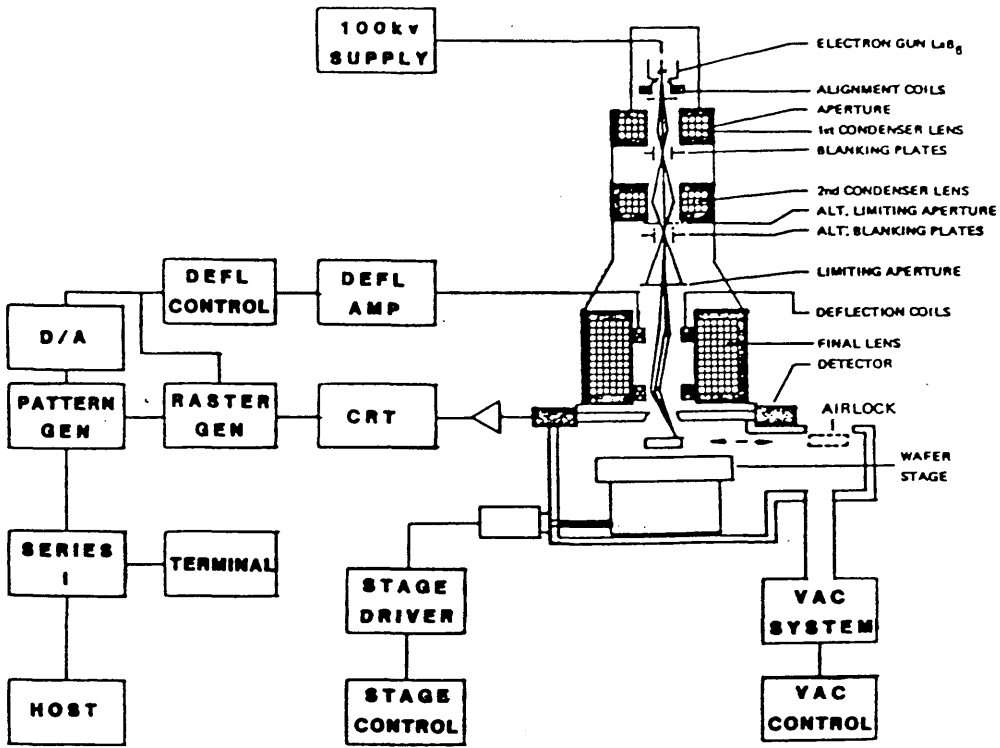


Figure 5.13a) High resolution electron beam fabrication system (After Kern et. al. ref. 5.22)

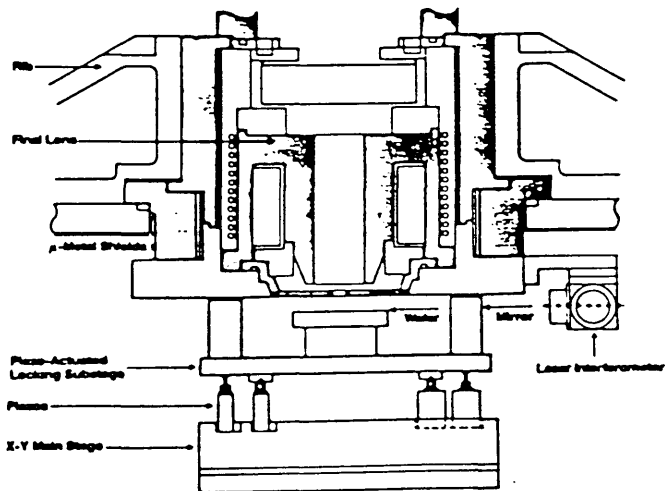
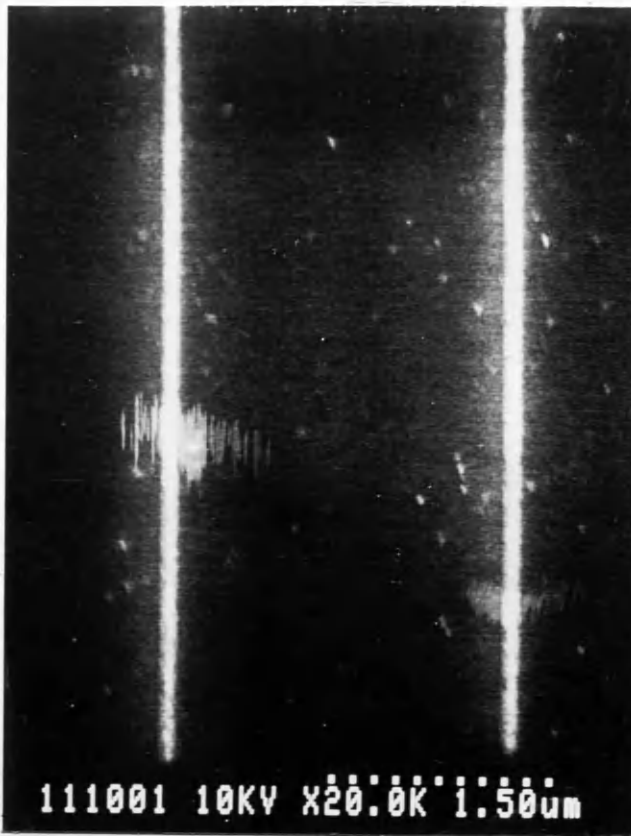
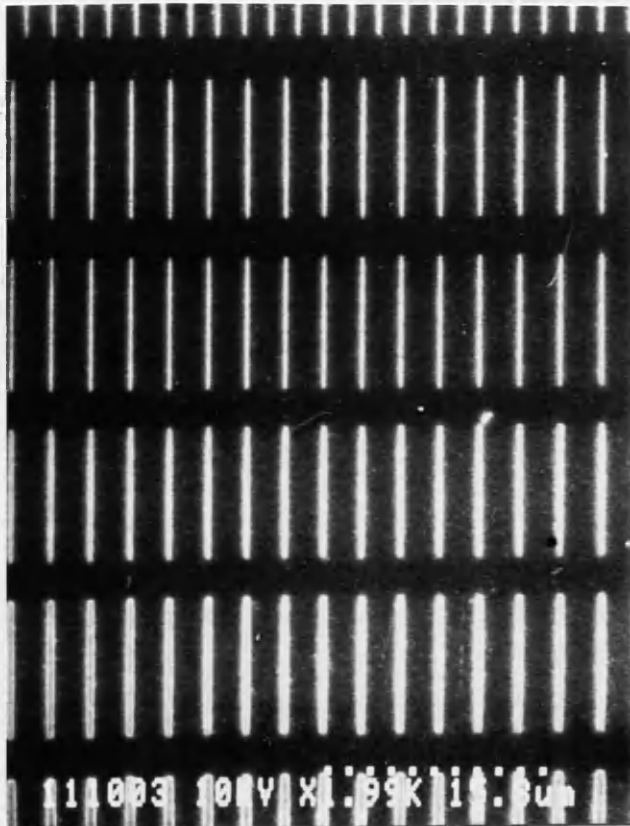


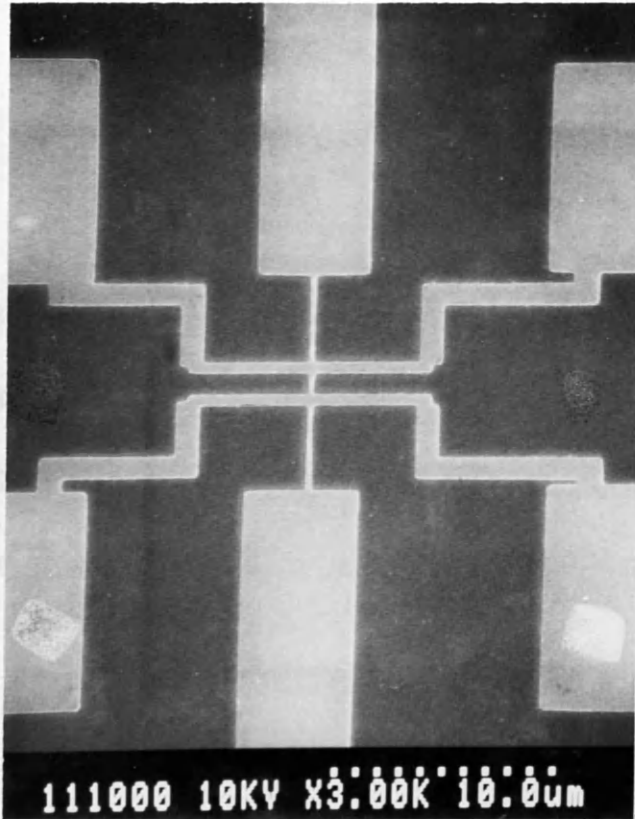
Figure 5.13b) Final lens and substage of the nanolithography system (After Rishton et. al. ref. 5.25)



SEM 5.8 Strontium fluoride lines lifted-off from electron beam exposed double layer PMMA resist on GaAs



SEM 5.9 Resolution test pattern



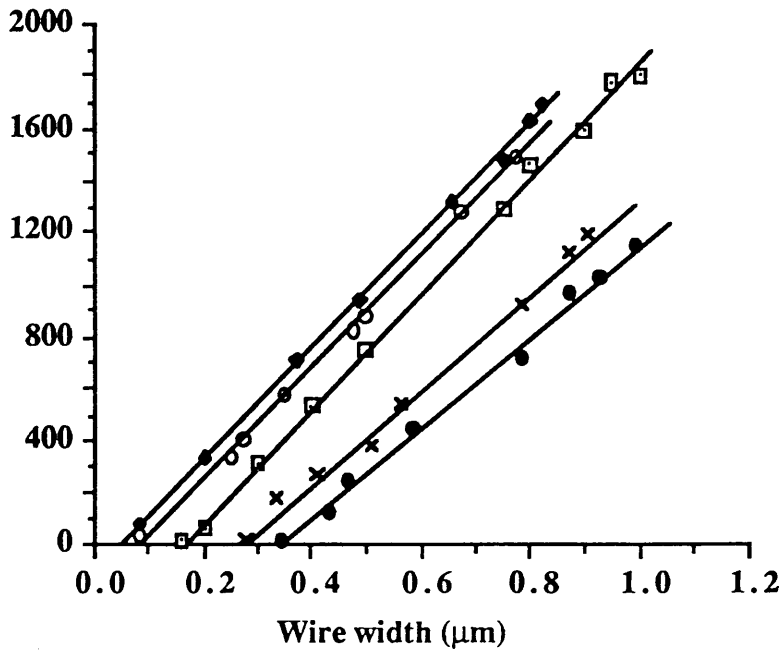
SEM 5.10 Wire pattern defined by exposing an electron beam into double layer PMMA resist after proximity correction and transferred onto GaAs using NiCr lift-off

4	8	12	16	20	24 (test)	
3	7	11	15	19	23	
2	6	10	14	18	22	(a)
(test) 1	5	9	13	17	21	

08A	2A	4A	6A	8A	BOND	
08A	2A	4A	6A	8A	08A	
05A	1A	3A	5A	7A	05A	(b)
BOND 1A	3A	5A	7A	05A		

Figure 5.14 showing a) chip layout and b) pattern files layout

Normalised conductance (μS) \times (μm)



- ◆ ECR RF RIE at 80V for 85s
- ECR RF RIE at 80V for 120s
- × MAG RF RIE at 300V for 3 mins.
- MAG RF RIE at 300V for 4 mins.
- RF RIE at 200V for 50s

Figure 5.15 Room temperature conductance normalised to $1\mu\text{m}$ in length vs. width for $\text{CCl}_2\text{F}_2/\text{He}$ etched GaAs quantum wires

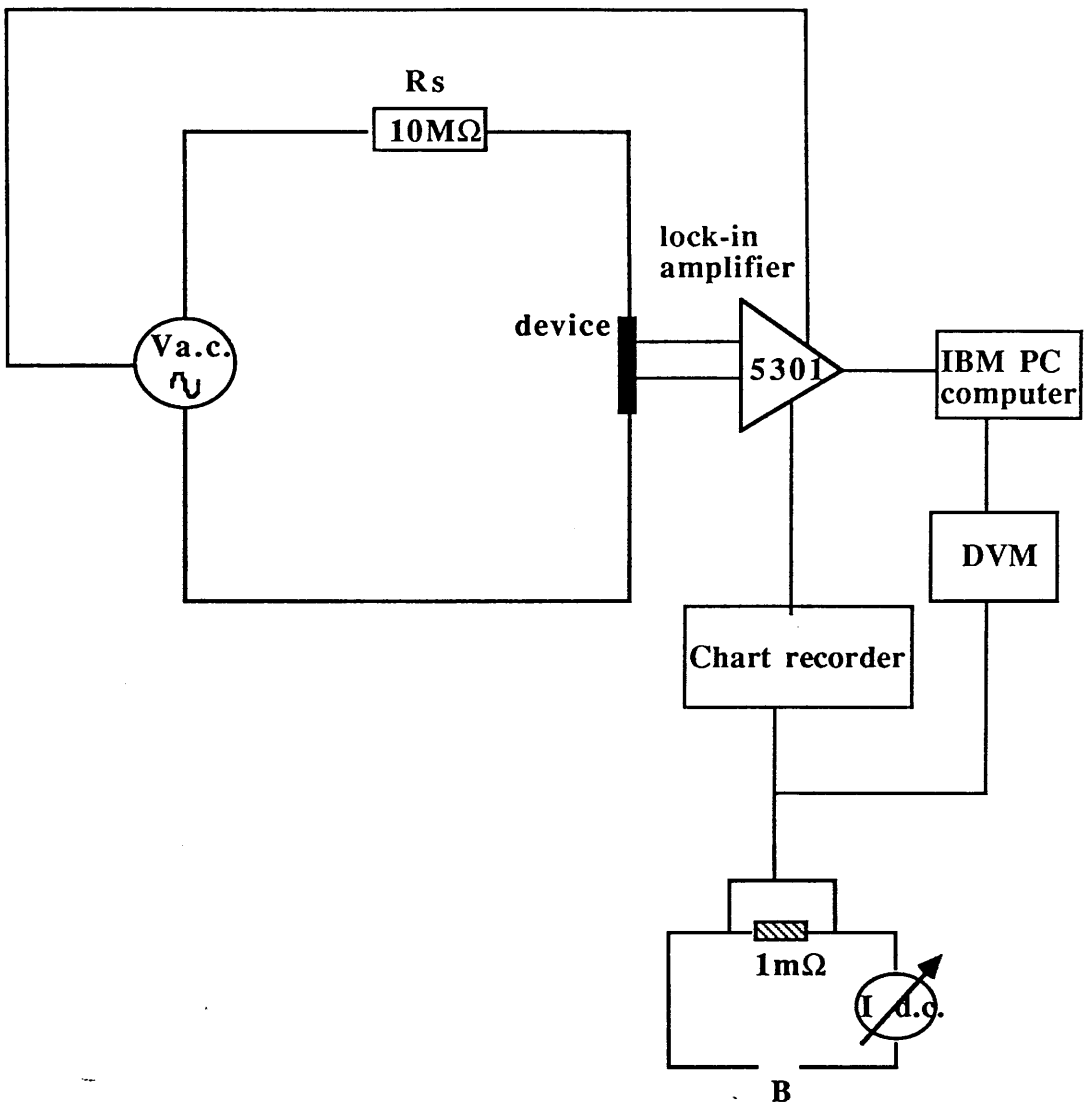


Figure 5.16 Schematic diagram of the circuit used for low temperature transport measurement

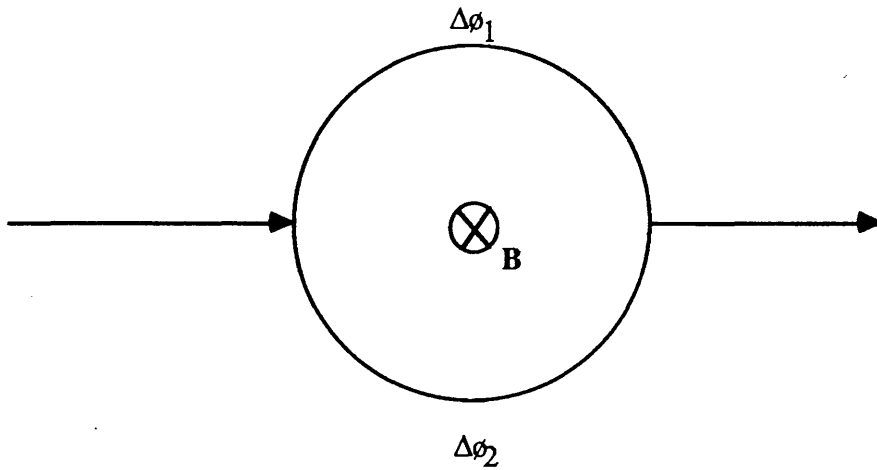


Figure 5.17a) showing an Aharonov-Bohm loop in which an electron beam is split in two and rejoined with the phase change in the two branches in the presence of a magnetic flux

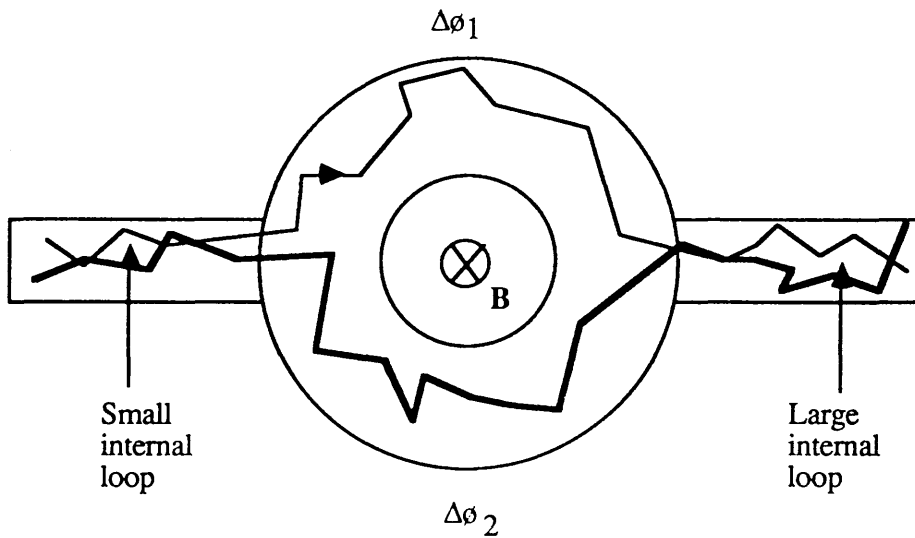


Figure 5.17b) showing a schematic diagram of a disordered A-B loop with two possible electronic paths and two possible enclosed loops which lead to Universal Conductance Fluctuations

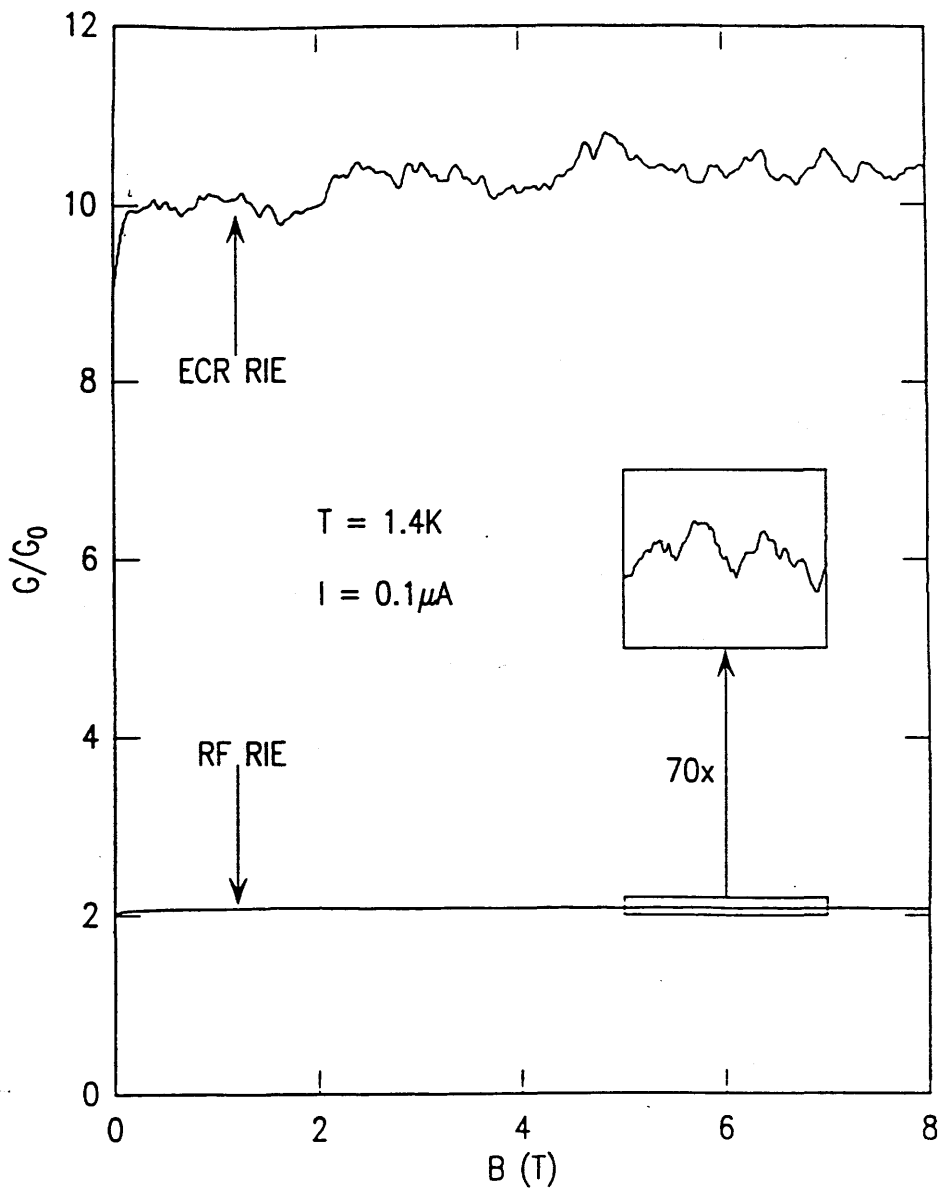


Figure 5.18 showing the magnetoconductance spectra of two wires: one ECR RF reactive ion etched and the other RF reactive ion etched

	Control	ECR-RF	RF RIE
Ideality factor	1.04	1.06	1.12
Barrier height	0.75eV	0.73eV	0.60eV
Reverse breakdown voltage	-9V	-8V	-6V
Reverse leakage current at -2V	-48pA	-850pA	-5.569nA

Table 5.2 Summary of measurements derived from I-V characteristics for Si-doped $2 \times 10^{17}/\text{cm}^3$ Schottky diodes fabricated on unetched, ECR RF reactive ion etched at 80V self bias and RF reactive ion etched at 200V self bias

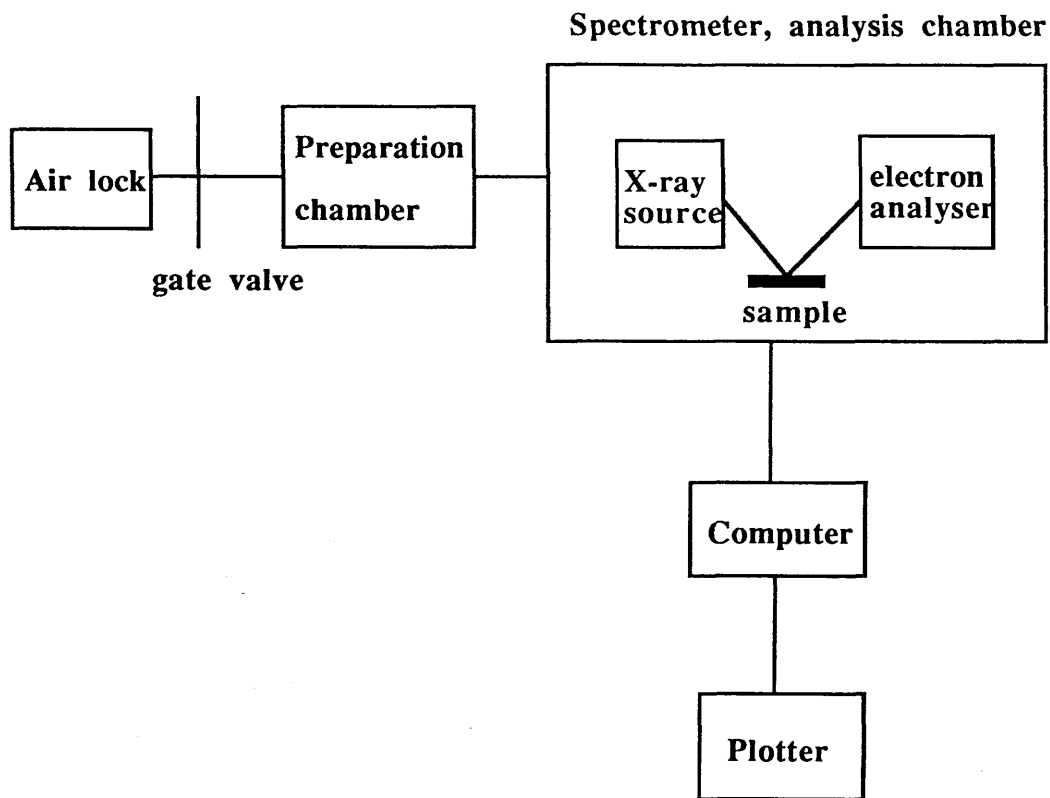


Figure 5.19 Schematic diagram of the XPS system

Atomic concentration (%)

Element	Control	ECR-RF	RF RIE
Ga(3d)	32.2	29.5	18.7
As(3d)	27.6	23.8	11.3
O(1s)	31.7	33.2	43.5
C(1s)	8.5	13.5	20.0
F(1s)	0	0	6.5
Cl(1s)	0	0	0

Table 5.3 Percentage atomic concentrations on the surface of GaAs samples after ECR RF RIE and RF RIE as determined by XPS

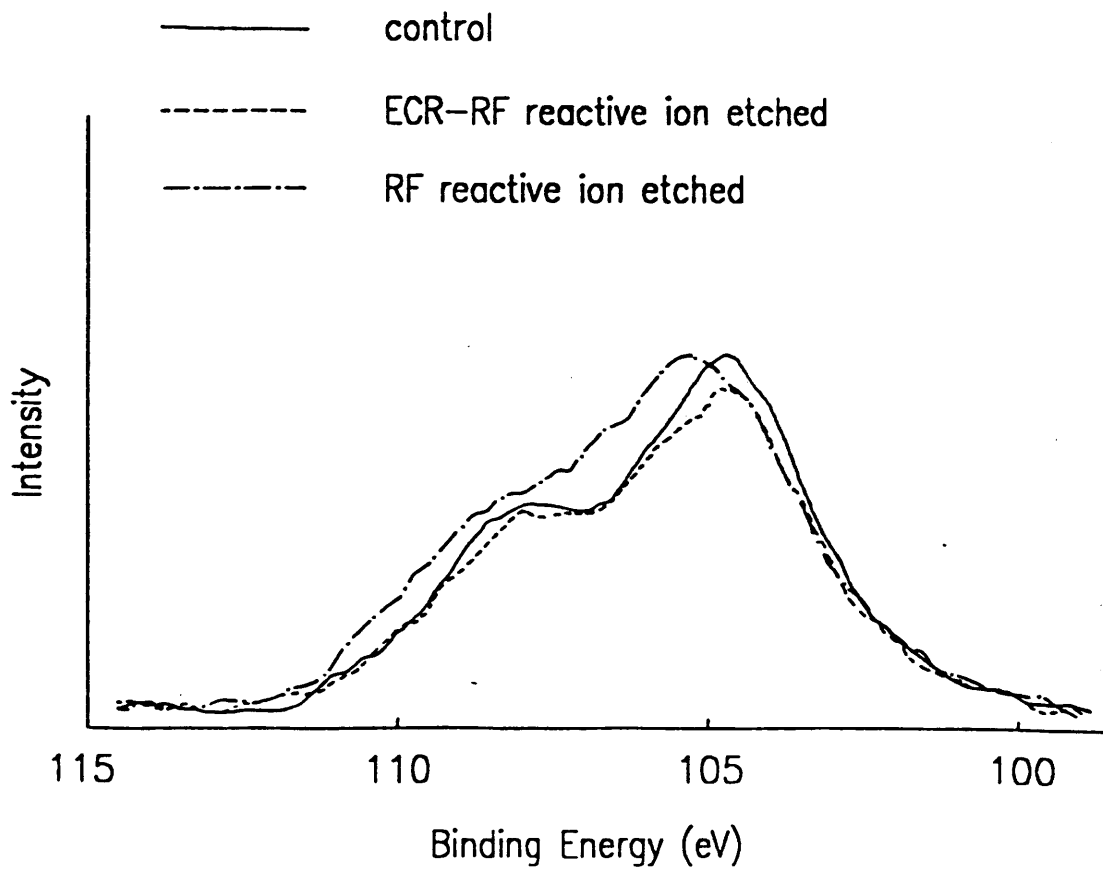


Figure 5.20a) showing the Ga(3p_{3/2}) signal for the control, ECR RF RIE and RF RIE GaAs samples, obtained by XPS

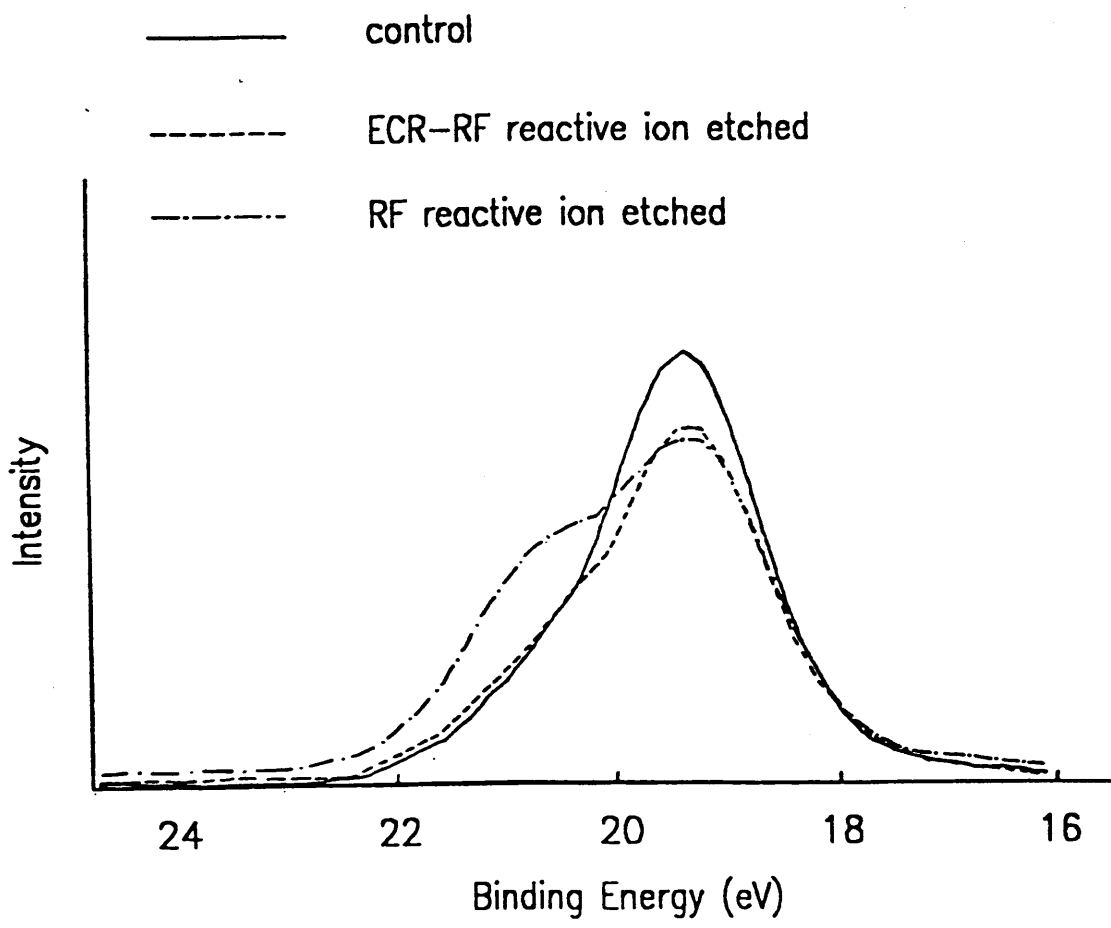


Figure 5.20b) showing the Ga(3d) signal for the control, ECR RF RIE and RF RIE GaAs surfaces, obtained by XPS

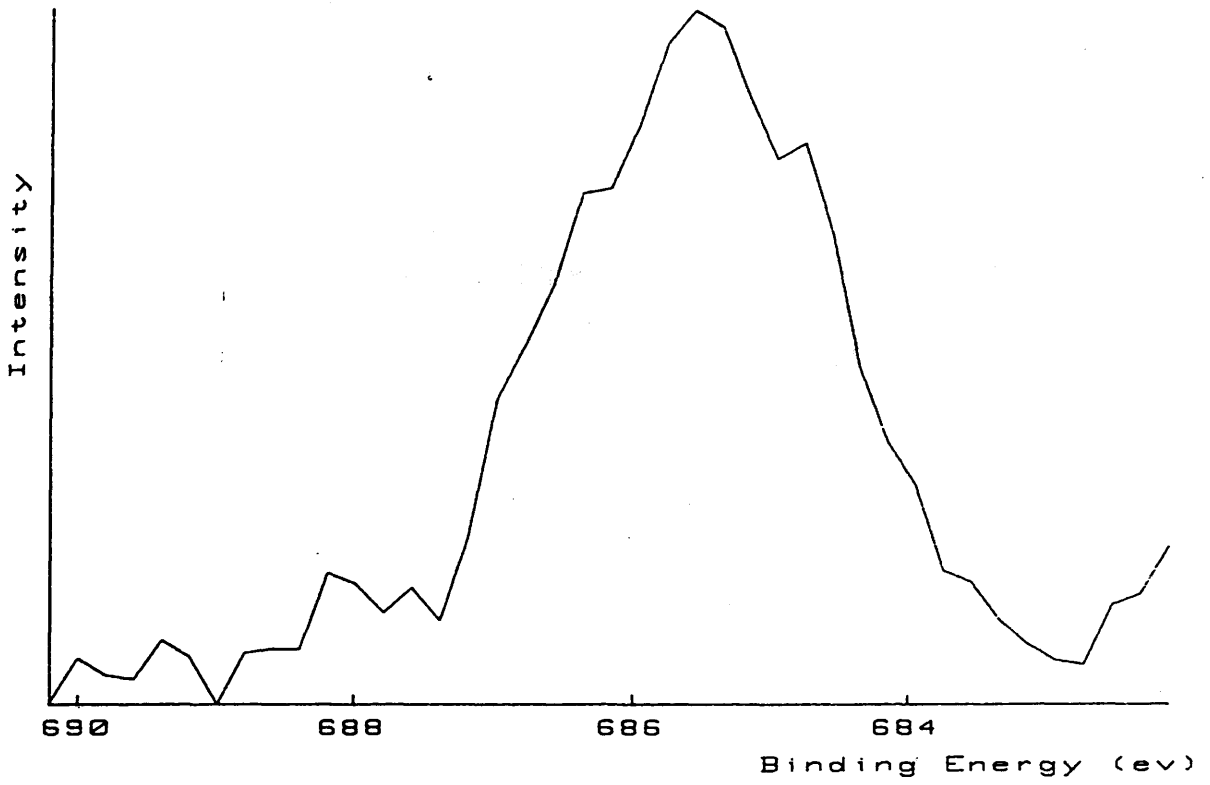


Figure 5.21 showing the F(1s) lineshape from the RF RIE sample

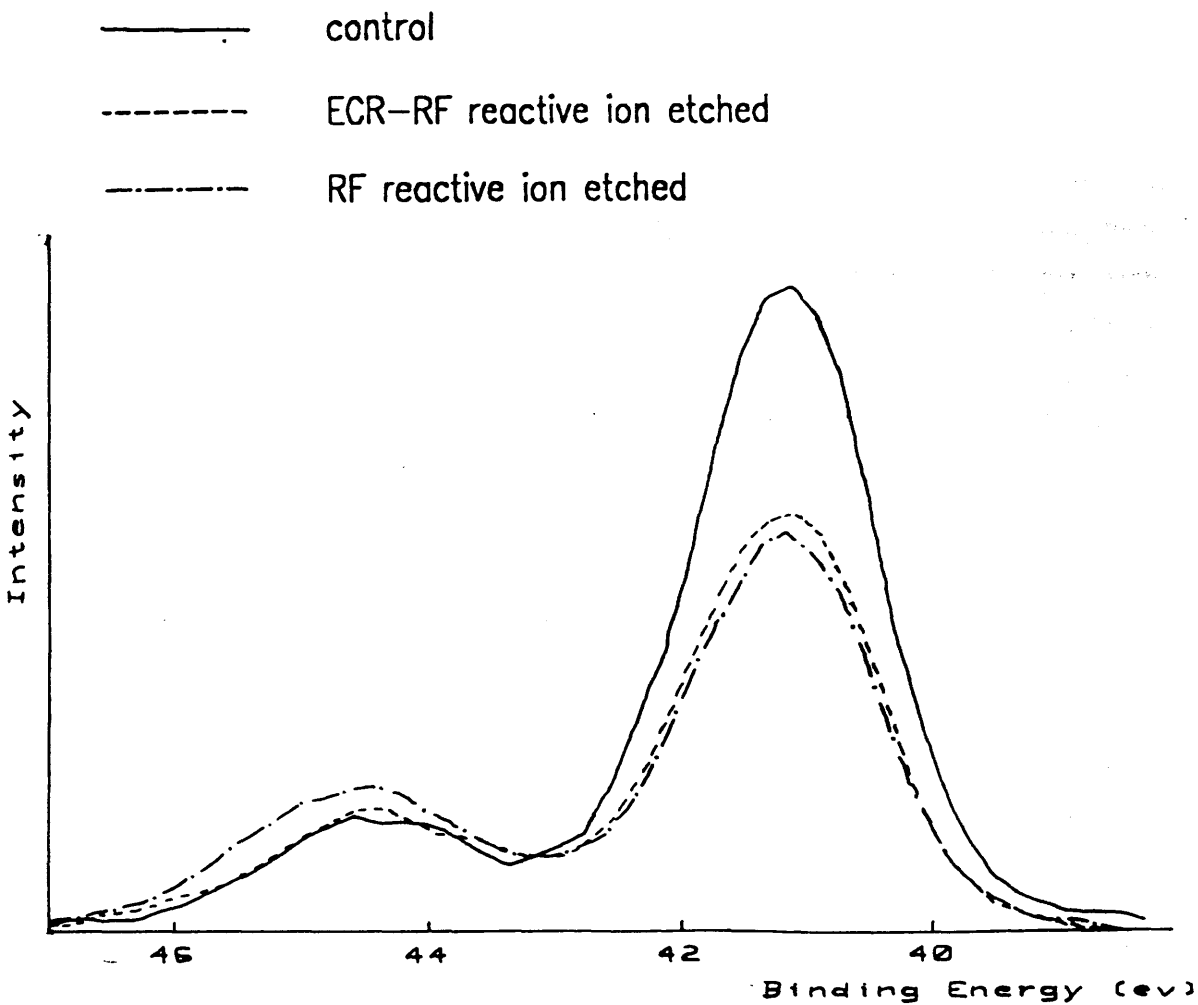


Figure 5.22 showing the As(3d) signal for the control, ECR RF RIE and RF RIE GaAs samples

Chapter 6 Other novel dry etch damage characterisation techniques

6.1 Introduction

In this chapter, studies on the induced surface and sidewall damage after reactive ion etching in SiCl_4 using the analytical techniques available in specular X-ray reflectivity and transmission electron microscopy will be presented. In particular, the high resolution fabrication techniques employed for the development of TEM specimens will be described. It should be mentioned that the experiments on X-ray reflectivity were carried out in collaboration with University of Edinburgh (Dr. U.J. Cox) and the electron microscopy work was collaborated with the Department of Physics at University of Glasgow (Prof. J.N.Chapman) and the TEM images were taken by a final year project student (A. Birnie)^{6.36}.

The basis of both analytical techniques is the Bragg equation which describes the condition for constructive interference for X-rays and electrons diffracted from atomic planes of a crystal. For radiation incident with wavelength λ at an angle θ to the parallel lattice planes spaced d apart, constructive interference of the radiation from successive planes occurs when the path difference is an integral number n of wavelengths λ , so that

$$2d \sin\theta = n\lambda \quad (6.1)$$

This situation is depicted in figure 6.1. Therefore, the Bragg law requires that θ and λ be matched for diffraction. The condition may be satisfied by varying λ , or varying the orientation of a crystal. In the present techniques used, the GaAs crystals are oriented at the angle to satisfy the Bragg condition for diffraction to occur.

6.2 Surface damage - Specular X-ray reflectivity

In this work, the technique of specular X-ray reflectivity using a triple crystal X-ray diffractometer was used to investigate the structural damage caused by

reactive ion etching of GaAs employing SiCl₄ and CH₄/H₂ plasmas. The effect of wet etching before and after dry etching on the GaAs surface has also been examined.

6.2.1 Theory

X-ray scattering is a non-destructive technique which allows accurate characterisation of thin films and surfaces. In particular, X-rays can be totally externally reflected from matter at sufficiently small angles of incidence since the refractive index is less than unity. At these incident angles the X-ray beam penetrates very little into the material and as a result, the measurement of the reflectivity can be used to study amorphous or crystalline films on substrate, and the surface and interfacial roughness. This is because a measurement of the reflectivity as a function of the angle of incidence provides information about the refractive index of the material as a function of depth, and since the difference of the refractive index from unity depends on the electronic density^{6.1}, these measurements will probe that density at and near the surface of a material.

The specular reflectivity of a system consisting of a layer thickness d_1 followed by an infinitely thick bulk is given by Parratt^{6.2} as:

$$R = \frac{r_{01}^2 + r_{01}r_{12}a + r_{12}^2}{1 + ar_{01}r_{12} + r_{01}^2r_{12}^2} \quad (6.2)$$

where $a = 2 \cos(4\pi f_1 d_1 / \lambda)$, and the amplitude reflectivities at the interfaces are

$$r_{01} = \frac{f_0 - f_1}{f_0 + f_1} \quad r_{12} = \frac{f_1 - f_2}{f_1 + f_2} \quad (6.3)$$

$$\text{with } f_1 = (\psi^2 - \psi_c^2(i))^{1/2} \quad (6.4)$$

and where $\psi_c(i)$ is the critical angle for layer i . The critical angles can be converted to give the mass density by using the formula for low atomic number:

$$\Psi_c(i) = 1.64 \times 10^{-3} \lambda \rho(i)^{1/2} \quad (6.5)$$

where Ψ_c is in radians, the wavelength of the incident radiation, λ is in Å, the density, ρ , is in gcm^{-3} , and the fractional difference in the density of the surface layer from that of the bulk is $\Delta\rho/\rho$. For $\Psi \gg \Psi_c$, the interface reflectivities can be written as:

$$r_{01} = \frac{\Psi_c^2(1)}{4\Psi^2} \quad r_{12} = \frac{\Psi_c^2(2) - \Psi_c^2(1)}{4\Psi^2}$$

Consequently, the denominator in the expression for R contains a term Ψ^4 , and the data is represented in the form $T = R\phi^4$ where $\phi = 2\Psi$.

Furthermore, the roughness of the interfaces is incorporated by assuming a gaussian roughness, when the interface reflectivities become:

$$r_{01} = \left(\frac{f_0 - f_1}{f_0 + f_1} \right) \exp -1/2 \left(\frac{4\pi\sigma_1}{\lambda} \sin \Psi \right)^2 \quad (6.6)$$

where σ_1 is the root-mean-square roughness of the air-layer interface, and, since Ψ is small, $\sin\Psi \approx \Psi$. A similar expression can be written for the reflection coefficient r_{12} which depends on σ_2 , the roughness of the layer-bulk interface. For systems more than one layer, expressions can be derived for the reflection amplitudes from each layer with thickness $d(i)$, critical angle $\Psi_c(i)$ and roughness $\sigma(i)$.

The parameters in this model were obtained from least squares fits to the experimental results, with $\Psi_c(\text{bulk})$ held fixed at 0.33° (mass density of 5.33 gcm^{-3}). The model predicts that the angular dependence of T will be modulated by interference fringes, and unambiguous assignment of the model parameters is facilitated when there are many such fringes within the measurable range of angle. However, it will be shown that it is not easy to distinguish between changes in the estimates of electron density and the estimates of the surface roughness by applying the above model to the data taken in this work.

6.2.2 Experimental

In general, measurements can be performed using a double-crystal X-ray spectrometer or a triple-crystal spectrometer. Both techniques have been used to obtain structural information on GaAs/AlInAs/InP^{6.3}, GaInAsP/InP^{6.4}, InGaAs/InP^{6.5}, heteroepitaxial structures^{6.6-6.9}, Cu-Al thin film interfaces^{6.10}, and surface oxide layers on Si^{6.11}. The basic difference between the double-crystal and the triple crystal lies in the fact that in double-crystal, the direction of the scattered X-rays recorded by the detector is defined by spatial collimation (a simple slit) whereas in the latter, angular collimation (by Bragg reflection) is used. In the case of a simple aperture, the direction of the scattered x-rays is also dependent on the exact point on the sample from which they are scattered. On the other hand, an additional analyser crystal serves both to define the direction of the scattered x-rays directly and decouple the scattered direction from the position of the scattered beam. This situation is illustrated in figures 6.2a) and b) with the use of two sources, S1 and S2. Therefore, the operation of a triple crystal spectrometer greatly simplifies the resolution of the instrument and its alignment since it is sensitive only to the direction and energy of the scattered X-ray beam. The double-crystal spectrometer, however, is also sensitive to the position of the scattered beam and the resolution of the instrument will depend upon the source size and the intensity distribution within the source, X-ray beam penetration within the monochromator, sample crystals, sample size and shape effects and beam path lengths. Moreover, the use of an analyser crystal improves the angular resolution of the detector system to (FWHM) 0.003°. To achieve a comparable resolution using spatial collimation would require a 10µm slit at a distance of 200mm from the sample. This would result in an unacceptable loss of signal.

In this work, the experiments were performed at Edinburgh University using an X-ray triple axis spectrometer with CuK α_1 X-rays, collimated by reflection from the (111) planes of a germanium monochromator crystal. The beam scattered from the sample was reflected from a second germanium (111) analyser crystal and measured using a scintillation counter. A schematic diagram of the triple-axis X-ray spectrometer is seen in figure 6.3 showing the two angles measured in the experiment which are the angle of incidence Ψ , and the scattering

angle ϕ . The measurements were performed by choosing some scattering angle ϕ , and scanning the angle of incidence Ψ (which is less than Ψ_c the critical angle) to find the integrated intensity of the specular reflected beam from all parts of the surface. This is analogous to a 'rocking curve' measurement of a Bragg reflection to find the mosaic spread of a sample. The profile of the curve reflects the macroscopic flatness of the surface, on a millimetre or centimetre scale. The reflectivity R is this integrated intensity, which is found as a function of scattering angle ϕ (where ϕ is twice the incident angle, Ψ) from all parts of the surface. It is convenient to describe the results in terms of a function $T = R\phi^4$, for reasons discussed in section 6.2.1.

Since the angle of incidence scanned has to be less than the critical angle for specular reflectance to occur, the GaAs samples studied using this technique were of quarter wafer sizes so that the scattered angle can be received by the analyser. The data presented in this work were from bulk GaAs wafers of $2 \times 10^{17} \text{cm}^{-3}$ doped with Si. Nine GaAs wafers were processed. Five of which were reactive ion etched in SiCl_4 with 9 sccm flow rate, 12mT total pressure, for 30s to produce an etch depth of 100nm, and the power densities were varied from 0.44W/cm^2 (100W) to 0.13W/cm^2 (30W). Two other wafers were used to study the effect of wet etching before and after dry etching. One was wet etched in $\text{H}_2\text{SO}_4/\text{H}_2\text{O}_2/\text{H}_2\text{O}$ 1:8:1 for 20s before reactive ion etched in SiCl_4 with a power density of 0.44W/cm^2 for 30s and for the other wafer, the dry etching was carried out prior to the wet etching. Another GaAs wafer was reactive ion etched in CH_4/H_2 1:5, see section 4.2.3.2, 14mT total pressure with a power density of 0.4W/cm^2 (100W) for 2.5 minutes to produce an etch depth of 50nm. The final wafer served as a control sample. The reactive ion etchers used has been described in sections 2.6.2 and 2.7.2.

6.2.3 Results and discussion

The reflectivity data obtained for the unetched, SiCl_4 reactive ion etched at 0.44W/cm^2 , CH_4/H_2 reactive ion etched at 0.4W/cm^2 , wet etched and subsequently SiCl_4 etched GaAs samples are shown in figures 6.4a), b), c) and d) respectively. The intensity of scattering from figures 6.4a) and c) are qualitatively similar, falling from $T \approx 1.5 \times 10^4$ at $\phi = 0.8^\circ$ to $T \approx 6 \times 10^3$ at $\phi = 1.6^\circ$. In

contrast, the intensity of scattering in figures 6.4b) and d) falls much rapidly with increasing ϕ , to $T \approx 2 \times 10^2$ at $\phi = 1.6^\circ$. This behaviour is indicative of the presence of a rougher surface in the latter two cases, which is confirmed using the present analysis as shown below.

Initially, all the curves were fitted to a single layer model; in addition, a double layer model was used to fit the data obtained from reactive ion etched samples. The parameters obtained from the fits are shown in table 6.1. For the unetched GaAs sample, the analysis suggests that a layer about 26\AA thick and $\approx 5\text{\AA}$ rough is present on the surface, with an electron density about 9% smaller than that of the bulk; the layer-bulk interface is nominally smooth. It is highly possible that this is a native oxide layer due to the exposure of the GaAs to air, since an oxide layer will have an electron density of 5 - 10% less than the bulk and other authors have shown, using ellipsometry, that the thickness of native oxide in GaAs is of the order 24 - 30 \AA ^{6,12,13}. The fit to the data from the SiCl_4 RIE sample suggests that a layer of $\approx 28\text{\AA}$ and surface roughness $\approx 13\text{\AA}$ with an electron density $\approx 15\%$ less than the bulk layer is present on the sample, while the fit to the data from the CH_4/H_2 RIE sample gives a smoother layer with an electron density that is $\approx 13\%$ greater than the bulk. The data sets for both etched samples were additionally fitted to a two layer model, and the parameters obtained are also shown in table 6.1. This model reduces χ^2 for the CH_4/H_2 RIE sample, but increases χ^2 for the SiCl_4 RIE sample. For the CH_4/H_2 etch, the new fit gives an upper layer of about 10\AA thick with an electron density $\approx 18\text{\AA}$ less than the bulk and a surface roughness reduced from 4.5\AA to less than 1\AA , while the lower layer is virtually unchanged. For the SiCl_4 etch, the new fit gives an unphysical result since the upper layer of very low electron density is much thinner than the surface roughness of 19\AA . The lower layer, however, now has an electron density of about 10% greater than the bulk.

Clearly, it is very difficult, from the present analysis, to identify the nature of these layers. The presence of an oxide layer will have an electron density that is 5 - 10% less than the bulk; in addition, the electron density of pure Ga and pure As are both greater than GaAs and therefore, the electron density of such a layer could be greater than the bulk by a few percent. From previous measurements of the reflectivity from semiconductor surfaces, it is also possible for surface contamination from low electron density material such as H_2O to occur^{6.3,6.14}. Nevertheless, it is certain from these results that there is a difference in the surface

roughness caused on the GaAs after SiCl_4 and CH_4/H_2 reactive ion etching. While the root-mean-square roughness of the surface of the control and the CH_4/H_2 RIE samples are less than 5\AA , the roughness of the SiCl_4 RIE samples is considerably greater at $13 - 19\text{\AA}$. The surface roughness obtained with SiCl_4 etch was investigated further by reflectivity measurements on samples etched at different powers for scattering angle $\theta = 0.8^\circ - 1.6^\circ$. The data was fitted with the thickness of the layer held at zero and allowing only the surface roughness to vary. The values obtained are given in table 6.2, which shows that the roughness caused by the dry etch is of the order $17 - 30\text{\AA}$. Measurements made on samples reactive ion etched with CH_4/H_2 plasmas at different powers did not display the same variance, fits to the data gave a surface roughness $< 5\text{\AA}$ in all cases. This result is consistent with the relative degree of surface roughness measured by Carter et. al.^{6.15} using a mechanical stylus after RIE of GaAs in SiCl_4 and CH_4/H_2 , however, their values are greater by about a factor of 10, this is probably a result of the much higher resolution available from the X-ray reflectivity technique.

The effect of wet etching in $\text{H}_2\text{SO}_4:\text{H}_2\text{O}_2:\text{H}_2\text{O}$ 1:8:1 prior to, and after dry etching has also been investigated. Figure 6.4d) shows the reflectivity data for the GaAs sample wet etched in the mixture for 20s, then reactive ion etched in SiCl_4 at $0.44\text{W}/\text{cm}^2$; a surface roughness of $\approx 22\text{\AA}$ and zero layer thickness was obtained, see table 6.2. Comparing this data with the sample which has been etched in SiCl_4 under the same conditions, a rougher surface is evident for the sample with the additional wet etch prior to dry etching. While surface roughness is a common occurrence for GaAs surfaces which have been subjected to aqueous solutions^{6.16}, it is difficult to distinguish whether the cause of this surface roughness was due to the wet etch or the dry etch process, or perhaps a combination of both effects. Another sample was prepared with the wet etch process being carried out after reactive ion etching and a surface roughness of $\approx 38\text{\AA}$ resulted, see table 6.2. Comparing this data with the SiCl_4 etched sample, it appears that the wet etch process has further roughened the dry etched surface.

The limitations of the Gaussian model used to fit the data in this analysis is clearly evident, this is indicative, perhaps of a damaged layer that has a gradient profile. The thickness of this layer is measured in terms of surface roughness, and that the SiCl_4 etched GaAs surface appears to be considerably rougher than the CH_4/H_2 etched surface, but no conclusive information about the nature of the

damage was detectable. Moreover, this characterisation technique does not provide any electrical or optical information about the state of the surface, in the case of CH_4/H_2 etched surfaces, a smooth surface may be passivated by atomic hydrogen and become electrically inactive, see section 4.3, but X-ray reflectivity provides no such information. Therefore, it is essential that a variety of complimentary techniques are employed to study the modified surfaces.

6.3 Sidewall damage - Transmission electron microscopy

Electron diffraction is another analytical technique available to identify the structure of solids. Similar to X-ray diffraction, electron diffraction from a crystal lattice can be described as a kinematic scattering process that meets the electron wave constructive interference conditions given in the Bragg equation. In many applications, the samples under study are thinned to thicknesses of a few thousand Å by chemical etching or ion milling. The images are formed by diffraction of an electron beam (typically 50 - 200 keV) transmitted through the thin sample. Lattice damage induced by reactive ion etching of SiO_2 in CHF_3/O_2 ^{6.17} and by ion bombardment of GaAs using neon ions^{6.18} have been studied using this technique. In particular, Deckman^{6.19} fabricated 2.5 - 500nm sized microstructures suitable for TEM using a submonolayer colloidal particle as mask for reactive ion beam etching, so that effects from RIBE on the etched amorphous semiconductor superlattices can be investigated. In this work, for the first time, using high resolution fabrication techniques, procedures for making thin TEM specimens were developed. This novel structure allows the possible damage induced on the sidewalls of the GaAs after reactive ion etching in SiCl_4 ^{6.20} to be studied through TEM analysis. The idea involves the production of a number of thin (preferably < 100nm thick) wires with supports accompanied with several free ends which sits on top of a mesa, see section 6.3.2.2. The mesa is important for two reasons: 1) to locate the wires; 2) to allow the specimen to be tilted to the Bragg angle without blockage from the large substrate. The wires were fabricated by reactive ion etching using a metal mask lifted-off from PMMA resist (section 2.3) and wet etching was used to produce the mesa. Any damage induced on the sidewalls by the etching process would remain as part of the wire and assuming that this damage is uniform along and around the wire, the material at the end of the wire would be composed

of sidewall damage totally, see figure 6.5a), (as will be verified in section 6.3.3.1 along with an indication of a graded damage profile). In this study, the electron beam has been placed incident at the end as well as in the middle of the wire as shown in figure 6.5b).

6.3.1 Theory

As discussed in section 6.1, the Bragg law is a consequence of the periodicity of the lattice structure, however, it does not refer to the composition of the atoms associated with every lattice point. The incident electrons, rather than suffer physical reflection, are scattered by the atoms, composed of charged nuclei, free and bound electrons. Since a crystal is invariant under any lattice translation, consequently, any local physical property of the crystal such as charge concentration and electron number density is also invariant under any lattice translation and therefore, the electrostatic lattice potential presented to the electrons can be seen to have the periodicity of the crystal lattice. By describing the electrons as waves (more commonly known as Bloch waves), the scattered intensities can be determined by solving the steady-state Schrodinger equation for the periodic lattice potential with the solutions being the electron wave functions with the same translational symmetry. Using this approach, it can be shown that the scattered wave is in the form of a spherical wave, whose amplitude is proportional to the Fourier transform of the potential, giving an atomic scattering amplitude $f(\theta)$ ^{6.21}:

$$f(\theta) = \frac{me^2}{2h^2} \left\{ \frac{\lambda}{\sin\theta} \right\}^2 (Z - f_x(\theta)) \quad (6.7)$$

where m is the rest mass of the electron; e is the electronic charge; h is Planck's constant; Z is the atomic number of the scattering atom and f_x is the atomic scattering factor of X-rays which is a measure of the efficiency of scattering by an atom in a particular direction.

Whereas the scattering from an atom depends on the distribution of its electrons, the scattering from a unit cell, and hence a crystal, depends on the atomic arrangements. An extension of the above analysis results in the scattered wave

amplitude from a unit cell again being proportional to the Fourier transform of the potential giving a structure factor:

$$F(\theta) = \frac{2\pi m e}{h^2} \int_{\text{unit cell}} V(\mathbf{r}_i) \exp(-i \mathbf{K} \cdot \mathbf{r}_i) d\tau_i \quad (6.8)$$

where \mathbf{r}_i are the positions of the atoms in the unit cell; $V(\mathbf{r}_i)$ is the potential at a point \mathbf{r}_i , $d\tau_i$ is element of volume of unit cell and \mathbf{K} is the difference in wavevector between incident and diffracted waves.

From equation 6.8, it can be shown that the scattered wave amplitude is only at a maximum when vector \mathbf{K} coincides with a reciprocal lattice vector^{6.22}. It should be noted that the reciprocal lattice is a lattice in the Fourier space associated with the crystal and has primitive vectors ($\mathbf{b}_1, \mathbf{b}_2, \mathbf{b}_3$) which are related to the

primitive vectors of the crystal lattice ($\mathbf{a}_1, \mathbf{a}_2, \mathbf{a}_3$). { e.g. $\mathbf{b}_1 = 2\pi \frac{\mathbf{a}_2 \times \mathbf{a}_3}{\mathbf{a}_1 \cdot \mathbf{a}_2 \times \mathbf{a}_3}$ }

To extend this analysis further for the description of scattering from an assembly of unit cells, in addition to the scattered amplitudes, it is necessary to account for the phases of the scattered electron waves. Therefore, the scattered amplitude from an assembly of unit cells can be expressed by summing the scattering factors from each unit cell multiplied by the appropriate phase factor. The structure factor for an array of atoms becomes:

$$F(\theta) = \sum_i f_i(\theta) \exp(-i \mathbf{K} \cdot \mathbf{r}_i) \quad (6.9)$$

where $f_i(\theta)$ is the atomic scattering amplitude of atom i ; $\mathbf{K} = v_1 \mathbf{b}_1 + v_2 \mathbf{b}_2 + v_3 \mathbf{b}_3$ since for strong reflection \mathbf{K} is a reciprocal lattice vector and \mathbf{r}_i , the fractional coordinates of the atom in the cell, is given by $\mathbf{r}_i = x_i \mathbf{a}_1 + y_i \mathbf{a}_2 + z_i \mathbf{a}_3$. It should be noted at this point that this treatment is based on the kinematic theory of diffraction, which assumes that the diffracted wave intensities are negligible compared to the incident beam intensity. This method is only applicable for thin crystals since it assumes that the incident electrons suffer only one, if any reflection.

Since $\mathbf{a}_i \cdot \mathbf{b}_j = 2\pi\delta_{ij}$, where $\delta_{ij} = 1$ if $i = j$ and $\delta_{ij} = 0$ if $i \neq j$;

$$F(\theta) = \sum_i f_i(\theta) \exp(-2\pi i (v_1 x_i + v_2 y_i + v_3 z_i)) \quad (6.10)$$

Therefore, the structure factor of GaAs in the (000) and (002) reflections can be determined taking into account that GaAs has a face-centred cubic (FCC) lattice with a basis of 2 atoms (i.e. Ga and As) per lattice point, giving,

$$F(\theta) = F(\text{FCC lattice}) \times F(\text{basis of 2 atoms per lattice point})$$

Since a FCC lattice with 1 atom per lattice point has 4 atoms in each conventional cell at fractional coordinates (0, 0, 0); (0.5, 0.5, 0); (0.5, 0, 0.5); (0, 0.5, 0.5);

$$F(\theta) = 1 + \exp(-i\pi (v_1 + v_2)) + \exp(-i\pi (v_2 + v_3)) + \exp(-i\pi (v_1 + v_3))$$

Therefore, $F(\theta) = 4$ if v_1, v_2, v_3 are all odd or even

$$F(\theta) = 0 \text{ otherwise}$$

For a basis of 2 atoms per lattice point i.e. Ga at (0, 0, 0) and As at (0.25, 0.25, 0.25);

$$F(\theta) = f_{\text{Ga}}(\theta) + f_{\text{As}}(\theta) \exp(-i \frac{\pi}{2} (v_1 + v_2 + v_3)) \quad (6.11)$$

Hence, the finite structure factor of GaAs only exists when the integers (v_1, v_2, v_3) are all odd or all even. If this condition is satisfied, then the structure factor becomes:

$$F_{\text{GaAs}}(\theta) = 4 \left\{ f_{\text{Ga}}(\theta) + f_{\text{As}}(\theta) \exp(-i \frac{\pi}{2} (v_1 + v_2 + v_3)) \right\} \quad (6.12)$$

For the reflection taken along the [000] direction $v_1 = v_2 = v_3 = 0$, therefore,

$$F_{\text{GaAs}}(\theta_{000}) = 4 \left\{ f_{\text{Ga}}(\theta_{000}) + f_{\text{As}}(\theta_{000}) \right\} \quad (6.13)$$

For the [200] reflection:

$$F_{\text{GaAs}}(\theta_{200}) = 4 \left\{ f_{\text{Ga}}(\theta_{200}) - f_{\text{As}}(\theta_{200}) \right\} \quad (6.14)$$

The atomic scattering amplitudes of Ga and As are tabulated values and can be found in ref. 6.21. Therefore, taking the electron wavelength $\lambda = 0.0335\text{\AA}$, the lattice constant of GaAs, $a = 5.6533\text{\AA}$, and determining θ using the following expression:

$$\sin \theta_{200} = \frac{\pi}{ka} \sqrt{(v_1^2 + v_2^2 + v_3^2)} = \frac{\lambda}{a} \quad (\text{Bragg condition for [200] reflection})$$

$f_{\text{Ga}}(\theta_{200})$ is found to be approximately equal to $f_{\text{As}}(\theta_{200})$ giving $F_{\text{GaAs}}(\theta_{200}) \approx 2\text{\AA}$.

So far, kinematic diffraction has been assumed for the analysis. While a substantial amount of interpretation for diffraction can be obtained on the basis of the kinematic theory, quantitative interpretations in many cases lack the desired accuracy, especially where the diffracted intensities are large and the diffracted waves themselves are scattered. Since the wires fabricated in this work were too thick to assume the kinematic theory, it is therefore necessary to improve the accuracy of the analysis with the use of the dynamical theory of diffraction^{6.21} which takes account of repeated scattering, the dynamical interaction of the incident and scattered waves and incorporates the possibility of physical absorption effects. The principles of this theory used in the present work is the two beam approximation although the use of multiple beam dynamical theory is also possible. The idea is illustrated by assuming that the crystal is perfect and that only one set of Bragg reflection planes is near the reflecting position. This gives rise to a pair of coupled first order differential equations linking the incident wave amplitude ϕ_o and the diffracted wave amplitude ϕ_g :

$$\frac{d\phi_o}{dz} = \frac{\pi i}{\xi_g} \phi_g \quad (6.15)$$

$$\frac{d\phi_g}{dz} = \frac{\pi i}{\xi_g} \phi_o + 2\pi i s \phi_g \quad (6.16)$$

where z is the distance into the crystal and s is a measure of deviation from the Bragg reflecting position. It is convenient to introduce a parameter, which is a measure of a 'mean free path' for Bragg reflection, known as the extinction distance ξ_g . It is inversely proportional to the structure factor and therefore is a function of the order of reflection and the atomic number of the scattering atom^{6.21}:

$$\xi_g = \frac{\pi m V_c v \cos\theta}{h F_g} \quad (6.17)$$

where V_c is the volume of the unit cell, m is the mass of electron, v electron velocity, F_g structure factor, and h Planck's constant.

By solving equations 6.15 and 6.16 simultaneously, expressions for the incident and diffracted wave amplitudes at depth z in the crystal can be obtained. In particular, at the bottom of a crystal of thickness ' t ', the intensity of the diffracted beam is given as:

$$I_g = \left| \phi_g(t) \right|^2 = 1 - \left| \phi_o(t) \right|^2 = \sin^2 \beta \sin^2 \left\{ \frac{\pi t \sqrt{1+x^2}}{\xi_g} \right\} \quad \text{where } x = \xi_g = \cot \beta$$

By letting s tend to zero i.e. at exact Bragg position, the intensity of the diffracted beam becomes:

$$I_g = \left(\frac{\pi}{\xi_g} \right)^2 \sin^2 \left(\frac{\pi t}{\xi_g} \right) \quad (6.18)$$

It is evident that from equation 6.18, at the exact Bragg position, the resultant oscillations in the wave intensities are due to a variation in either the thickness of the crystal, t , or the extinction distance, ξ_g , or both. Therefore, having ensured that any change in the diffracted intensity is not a manifestation of thickness variation, information about the composition of the crystal is possible, since the diffracted intensity can then be seen as proportional to the square of the structure factor (from equations 6.17 and 6.18); which in GaAs, is a function of the number density (GaAs being a FCC lattice with a basis of 2 atoms per lattice point) and the atomic scattering amplitudes of the two elements Ga and As.

6.3.2 Experimental

6.3.2.1 Electron microscopy

The transmission electron microscope used in this work was a JEOL 1200EX and is shown schematically in figure 6.6, the electron source was a lanthanum hexaboride crystal which was operated at an accelerating potential of 120kV. This TEM is slightly different from the basic TEM^{6.29} in that it has an improved double condenser lens system, three magnifying intermediate lens stages and a single projector lens. This lens arrangement allows magnification to 500,000 times.

The GaAs samples were mounted in custom-made bulk specimen holders which were machined from copper especially for the specific sample orientation. The chip was mounted such that the wires stand out from the substrate surface and are positioned above a hole in the holder so that the diffracted electrons from the incident electron beam can reach the screen. The wires were aligned to a $[\bar{1}10]$ axis

on a (001) plane so that the electron beam is incident in the [110] direction onto the wires. Experimentally, this can be verified by identifying the characteristic diffraction pattern (from elastically scattered electrons) and Kikuchi band pattern (from inelastically scattered electrons)^{6.21}. The angle of tilt available in this arrangement was by rotating the sample holder rod on its own axis which tilts the sample along its $[\bar{1}10]$ direction. This variable angle allows the specific Bragg reflections to be excited in turn.

Selected area diffraction

The first analytical technique used was selected area diffraction using a convergent electron beam. The basic idea of this technique is to direct a focussed beam of electrons through a small area of the wire, in this case, the spot was 30nm in diameter, and the diffraction pattern recorded from this area. Since the change from imaging to diffraction mode only alters the lenses post-specimen and does not change the electron beam position on the wire, the diffraction pattern will only contain information from the area of the wire which is illuminated by the beam. Identification of the Bragg spots of interest is possible by comparing the diffraction pattern with the mapped reciprocal lattice plan for the FCC crystal^{6.21}.

Imaging

A number of imaging techniques were used in this study including bright field, and dark field imaging of elastically and inelastically scattered electrons. This is possible since a series of interchangeable objective apertures, varying in size, is situated near the back focal plane of the objective lens and can be used to select a particular diffraction spot. If the aperture is positioned so that only the undeviated (000) beam passes through it, the final image formed when the TEM is returned from diffraction to imaging mode, with the aperture unchanged, will be due to the undeviated electrons, see figure 6.7a). When the (000) spot is used to form the image, the technique is known as bright field imaging. However, the objective aperture can be also used to isolate any single chosen diffracted beam other than the undeviated beam. This can be done by displacing the objective aperture, but astigmatism will be produced in the image since the electrons are removed from the optic axis. Consequently, it is more satisfactory to tilt the electron beam so that the desired diffracted beam emerges from the specimen on the optic axis and parallel to

it. This technique is known as dark field imaging and is illustrated in figure 6.7b). In addition to dark field imaging of a diffracted beam, inelastic dark field image (INEL) can be formed by positioning the objective aperture between e.g. the (000) and (002) diffracted spots so that the electrons which form the final image are not elastically scattered (Bragg) but are inelastically scattered. This image is useful in that it is very sensitive to variations in the thickness of the wire.

To investigate the induced sidewall and surface damage by reactive ion etching for the wires fabricated as described in section 6.3.2.2, the three images, namely, (000) bright field image, (002) and INEL dark field images were formed for each wire.

To obtain more quantitative information about the degrees and depths of the induced damage after RIE, a Joyce Loebel Microdensitometer 3CS was also used to measure the intensity of the (002) images as functions of distance from the end of the wires. This was achieved basically by passing a light beam through the negative of the micrograph and measuring the transmitted intensity.

6.3.2.2 Fabrication

As mentioned earlier, this experiment involves fabricating a dry etch damaged structure suitable for the investigation of the induced damage using TEM. The sections below will describe the actual process used to fabricate the present samples under this study. However, before this fabrication process was developed, a few problems were encountered during the development. These problems will be presented briefly, since their contributions to the production of the final process are vital. Finally, improvements on the present process being made currently by a research student (M.A. Foad) will be mentioned.

Fabrication process

Two different materials were used in this study. One of the wafers consisted of a 2 μm thick, $1 \times 10^{17} \text{cm}^{-3}$ Si-doped GaAs epitaxial layer on another

epitaxial layer of GaAs doped with $1 \times 10^{18} \text{cm}^{-3}$ Si of $0.5 \mu\text{m}$ thick on a semi-insulating substrate, and the other was bulk GaAs doped with $2 \times 10^{17} \text{cm}^{-3}$ silicon. The two epitaxial layers were grown by molecular beam epitaxy. The GaAs wafers were scribed into $6 \times 4 \text{ mm}^2$ chips and 3×3 patterns were exposed onto each chip. Two chips from the epitaxial GaAs material and one chip from the bulk GaAs material were processed. Initially, the samples were cleaned in trichloroethylene for 60s, then rinsed thoroughly in acetone and isopropanol. The electron beam lithographic steps consisted of two levels, the wire level and the planarisation (mesa) level, see figures 6.8a) and b). The alignment level was missed out since the patterns were placed exactly 2mm apart (for more practical reasons described later), and therefore, it was more efficient to carry out the exposures by moving the samples manually.

a) Wire level

A double layer 4% BDH PMMA/4% Elvacite PMMA resist system with the spinning, baking and developing conditions as described in section 2.2.3 was used. The resist was exposed using an electron beam (Philips SEM 500 described in section 2.2.2) with a 160nm spot at 50kV in a $194 \times 143 \mu\text{m}$ frame with exposure dosages varying from 900 to $2000 \mu\text{C}/\text{cm}^2$. The wire design is shown in figure 6.8a). After development, chromium of 60nm thick was evaporated onto the samples and lift-off was performed in acetone. The Cr was then used as a mask for reactive ion etching in SiCl_4 with 9 sccm flow rate, 12mT total pressure and a varied power density for different samples for 1.8 minutes to produce a ridge of around $0.6 \mu\text{m}$ deep. For the epitaxial GaAs samples, two power densities of $0.44 \text{W}/\text{cm}^2$ resulting in 300V self bias and $0.75 \text{W}/\text{cm}^2$ with 400V self bias were used while for the bulk GaAs, $0.44 \text{W}/\text{cm}^2$ power density was used. The etching machine used is described in section 2.6.2. SEM6.1 shows a typical TEM wire structure.

b) Planarisation level

This level involves the fabrication of a mesa with the wires on top. The mesa is essential since it serves to locate the position of the wires, and more importantly, to avoid blockage from the large substrate so that the wires can be tilted to the Bragg angle. Before the mesa can be produced by wet etching, the wires have to be

protected from the wet etch. One way of doing this was to use a metal-on-polymer mask^{6.38} and its fabrication involved spinning a layer of 10% polyimide at 6K rpm for 60s to give a thickness of 0.35 μ m and baked at 180°C overnight. Then, a layer of 15% BDH PMMA in chlorobenzene was spun on at 5K rpm for 60s and baked overnight. The pattern for the mesa was then exposed using an electron beam with a 0.125 μ m spot size at 50kV in a 194 x 143 μ m frame. After exposure, the 15% PMMA positive resist was developed in 1:1 MIBK:IPA at 23°C for 45s. Then, NiCr of 0.3 μ m thick was evaporated onto the samples and the unexposed 15% PMMA was removed in acetone. The protected polyimide was subsequently removed in an oxygen plasma for 30 minutes. At this stage, the 6 x 4 mm² samples will be scribed into three 2 x 4 mm² chips, see figure 6.9. The exact dimensions of the chips are important since they have to fit into the custom-made copper specimen holder. The individual chips were then wet etched in H₂SO₄:H₂O₂:H₂O 1:8:1 for 15s to produce a mesa of 6 μ m deep. The metal-on-polymer (MOP) mask was then removed by soaking the chips in N-methylpyrrolid-2-one overnight. This mesa fabrication procedure is illustrated in figures 6.10a)-f). However, the MOP mask process employing NiCr and polyimide was developed initially for the production of the mesa using dry etching, see section below, and it had been kept during the early stages when instead of dry etching, the mesa was produced by wet etching. In fact, when the platform is formed by wet etching, another way of protecting the wires with a large reduction of processing steps is possible by spinning on a much thicker layer of polyimide i.e. 14% instead of the two layers of 10% polyimide and 15% PMMA. The exposures would be carried out as normal except that the unexposed polyimide will be developed in acetophenone:xylene 65:35 at 23°C for 1.5 minutes and the chips will be ready for wet etching. It is important, however, that the 14% polyimide is well baked before exposure to ensure that it will stand up to possible wet etch attacks. SEM 6.2 shows a sample processed in this way, with the 14% polyimide on top of the mesa after wet etching.

Problems encountered during the development of the fabrication process

Initially, alignment marks and only one long wire was fabricated. The problem arose when access of the electrons to the end of the wires at the Bragg angle was blocked by one of the alignment marks. Therefore, the process evolved to the fabrication of four broken wires so that a number of edges will be available.

Since the position of the patterns were laid out precisely 2mm apart, the alignment level became quite inessential and therefore, it was decided to omit this level.

Two other dry etch masks were used for fabricating the wires before Cr was chosen: namely 8% HRN and NiCr. The problem associated with the HRN resist was that it was not as resistant to the etch as the metal masks and as a result, most of the time, the resist did not survive the etch leading to the etching of some parts of the wires; in addition, the wire uniformity defined by the resist was not as good as the metal lines. Therefore, it was decided to change to metal mask. At first, NiCr was chosen since it has been demonstrated to be a good etch mask for the etching of GaAs in SiCl_4 ^{6,24}. The problem with this choice arose at the microscopy stage. While the (002) diffraction pattern taken from the wires showed a very strong spot intensity which had important implications, see section 6.3.3.1, an anonymous ring appeared in the selected area diffraction as the selected area was moved towards the top of the wire and dots were observed in the (002) dark field image in the middle of the wire. The ring observed was believed to be due to the NiCr since it was not removed after the dry etch process. But it was more difficult to identify the origin of the dots. It is possible that they are a consequence of the diffusion of Ni from the NiCr to the arsenic sites during the baking process since Ni diffusion is a common occurrence during the annealing process in the fabrication of ohmic contacts^{6,25-27} at moderate temperatures. Therefore, in order to avoid any further ambiguity concerning Ni diffusion, it was decided to use Cr as a dry etch mask; its etch ratio to GaAs in SiCl_4 is around 1:40.

The final problem was associated with the fabrication of the mesa. Initially, the mesa was formed by reactive ion etching for 30 minutes in SiCl_4 . However, this prolonged etch appeared to have crosslinked the sidewalls of the plasma exposed polyimide rendering it insoluble in any solvent or oxygen plasma. Since this remaining polyimide runs parallel to the wires, see SEM 6.3, they 'block' the access of electrons to the wires when tilted at the Bragg angle. This problem was resolved by the use of wet etching to produce the mesa.

Despite these problems, all the samples investigated suggested a strong spot intensity in the (002) diffraction pattern which was an important preliminary result for the work which followed.

Improvement on existing process

Many improvements can be made on the existing process and these are being carried out by a research student in this department (M.A. Foad). Since the mesa is $20 \times 160 \mu\text{m}^2$ in area, this size of exposure is very compatible with optical lithography and it can be shown that it is possible to replace this electron beam lithographic level by optical lithography provided that an optical mask with the desired mesa dimensions and a suitable uv sensitive resist is used. Other improvements such as producing a longer mesa with the positioning of more wires, a thinner mesa to allow more tilt to the wires with less substrate effects and the fabrication of thinner wires are also feasible^{6.28}.

6.3.3 Results and discussion

6.3.3.1 Sidewall damage

Initially, to obtain information on the degree of crystallinity of the etched GaAs wire, the convergent beam diffraction pattern of the epitaxially grown GaAs sample reactive ion etched in SiCl_4 at $0.44\text{W}/\text{cm}^2$ was taken. Figures 6.11a) and b) show the micrographs of the diffraction pattern obtained from an arbitrary position in the middle of the wire and at the end of the wire respectively. Note that only one half of the diffraction pattern is present as a result of substrate effects at the tilted angle (Bragg). Nevertheless, it is clear that the images are those from a crystalline FCC structure. Thus it appears that the etching process involved does not cause polycrystallinity or amorphisation in the GaAs crystal, since a ring pattern would be observed for a polycrystalline material and a diffuse pattern centred on the optic axis would be present if the crystal was amorphous. Further investigation of the diffraction pattern from mid-wire reveals a brightness from the (002) spot (arrowed), and the same spot from the edge of the wire is significantly brighter. This result is significant since from the dynamical theory of electron diffraction (see section 6.3.1), the intensity of the (002) spot can be shown to be proportional to the (structure factor)² (in the absence of wire thickness variation), where the structure factor is related to the number density and the atomic scattering amplitudes of the

two elements Ga and As. Since the atomic scattering amplitudes of Ga is almost the same as that of As in the [002] reflection, the resultant (002) spot intensity should be very little in pure crystalline GaAs. Therefore, the brightness observed in the (002) spots is indicative of a change in the number densities of Ga to As. In addition, a lower spot intensity was observed for the area in the middle of the wire suggestive of the presence of less damage compared with its end. This is perhaps indicative of the initial assumption that the damaged region lies along the sides and around the end of the wire with the material at the end being totally damaged, in this configuration, the electrons will have to travel through relatively less damaged material in the middle compared with the end of the wire, see figure 6.5a).

In order to obtain more quantitative information about the sidewall damaged layer and the possible variation in wire thickness, the (000) bright and (002 and inelastic) dark field images were taken from the end of the wires, in particular, the intensities of the (002) images were analysed using a microdensitometer and compared amongst the wires. The images taken from the epitaxially grown GaAs sample reactive ion etched with $0.44\text{W}/\text{cm}^2$ power density are shown in figures 6.12a-c). The bright field (000) image (figure 6.12a) shows very little detail of the wire except the mask upon it and an area at the very edge of the wire ($\approx 10\text{nm}$) which is thinner than the rest. On the other hand, the (002) dark field image (figure 6.12b) shows an increase in intensity at the edge which falls off monotonically with distance from the end of the wire indicative of local variations in its structure factor. The inelastic (INEL) dark field image (figure 6.12c) is of very low and uniform intensity suggesting a wire of uniform thickness. It is possible that the bright regions around the mask and at the very end of the wire is due to the remains from the polyimide resist since it is very electron transparent. Similar features were observed from similar images taken from the other two samples, the epitaxial GaAs reactive ion etched at $0.75\text{W}/\text{cm}^2$ and the bulk GaAs reactive ion etched at $0.44\text{W}/\text{cm}^2$ (6.36). The degree and depth of the intensity brightness were quantified using a microdensitometer to measure the intensity of the (002) images as functions of distance from the wire end. Figures 6.13a)-c) show the corresponding graphs for the three samples where the y-axis is a measure of the intensity of the image. The y-axis cannot have a scale since varying exposure times were used for the images, nonetheless, the relative intensities of each wire may be compared. The graphs clearly display similar trends for the images under study. While it is evident, from these graphs, that the degree of damage decreases as the distance from the end

of the wire increases, it appears that the damaged depth can be divided into two regions:

- a) a severely damaged region near the end of the wire with the peaked intensity;
- b) a slightly damaged region where the intensity decreases to background mid-wire level.

If the full width of the severely damaged region is taken at half maximum from the peaked intensity, a summary of the degrees and depths of damage as a function of the etch power density and material may be tabulated and is shown in table 6.1. However, it is clear, from these graphs that there is not a definite division between severely damaged, slightly damaged and undamaged material. The intensity of the (002) reflections, and hence the damage, would appear to decay monotonically with distance from the sidewall. This result is significant since a gradient surface damage profile was also suggested from the X-ray reflectivity data (section 6.2.3). Although from these graphs, comparison of the degrees of damage caused by the different power densities is not possible, reactive ion etching with a higher power density seems to increase the depth of the induced damage. This power density dependence of the inflicted damage on the etched surfaces using the same etch gas have also been observed previously using electrical and optical techniques (see sections 3.4.1-3); however, it was not possible to conclude whether the surface damage was due to a severely damaged or a thicker damage layer. It is also worth noting that the relative intensity of the damaged region in the bulk GaAs is much lower than the epitaxially grown GaAs, this is perhaps indicative of the inherently lower material quality related to bulk GaAs. A similar observation was reported when investigating surface damage after $\text{CCl}_2\text{F}_2/\text{He}$ RIE using electrical measurements conducted on bulk and epitaxial materials^{6.37}.

According to section 6.3.1, the increase in the (002) dark field diffracted intensity observed near the edge of the wire suggests an increase in the structure factor in the GaAs wire. It follows, therefore, that the percentage composition of the Ga to As in the etched GaAs wire has been changed in some way. Since the structure factor of the (002) diffraction is subtractive, on physical grounds, it is only possible to suppose that this change in composition is due to a decrease in the percentage of As atoms rather than an increase in Ga atoms. It is also not difficult to imagine a loss of arsenic resulting from the etching process. Since the reactant

products in the reactive ion etching of GaAs in SiCl_4 are mainly GaCl_x and AsCl_x (see section 2.6.1), and the vapour pressures of AsCl_x products are higher than the GaCl_x products, it is not unlikely that the As products would vapourise faster than the Ga products, leaving a Ga-rich sidewall surface after etching. However, the importance of ion assisted reactions must not be overlooked^{6.30,31}. Surfaces containing As vacancies after the reactive ion etching of GaAs using both SiCl_4 and $\text{CCl}_2\text{F}_2/\text{He}$ have also been observed in this work (see sections 3.4.4 and 5.4.2). Moreover, the presence of As deficiency in the sidewall damage region may act as electron traps which could explain the larger room temperature conductance cut-off (section 4.3.5.4) and the form of negative differential resistance measured in the low field, low temperature regime of n^+ GaAs quantum wires fabricated using SiCl_4 RIE^{6.39}, (see section 5.3.6.3). In RIE, since the etch mechanism is both chemical and physical, it is possible that both surface and sidewalls suffer from ion induced chemical damage (i.e. As deficiency), especially when ion bombardment does not cause sputtering of Ga or As^{6.30,32}. The effect of ion bombardment may cause damage indirectly by inducing a difference in the production and/or desorption rate of the reactant products. In particular, during the RIE of GaAs using SiCl_4 , in addition to the arsenic chlorides being able to desorb much faster than gallium chlorides due to their relative volatility, the role of ion bombardment may be two-fold: while ion assistance can accelerate the production rate of the arsenic chlorides^{6.31}, the less volatile gallium chlorides can also benefit from ion bombardment through stimulated desorption^{6.30,32-34}. This type of etch mechanism involving a different ion induced production and/or desorption rate of the etched products could lead to the presence of a surface layer dominated by As vacancies on the surfaces and sidewalls of etched structures, though the presence of other damage effects such as ion penetration, diffusion and interstitials cannot be ruled out. Similarly in the case of $\text{CCl}_2\text{F}_2/\text{He}$ RIE, whereby the rate limiting step during etching has been found to be the ion induced desorption of the additional GaF_3 reactant product, with a significant ion assisted removal of the gallium chlorides^{6.32}; in particular, the presence of Ga-F bonding on the etched surface has been observed, see section 5.4.2.

6.4 Conclusions

1) Specular X-ray reflectivity was used to study the damage caused in GaAs surfaces after SiCl_4 and CH_4/H_2 RIE. It was highly difficult to apply the Gaussian model assumed in the theoretical curve fit to the experimental data, suggestive of a gradient surface damage profile. Only structural damage in terms of surface roughness was detectable using this characterisation technique. Results of which indicate that SiCl_4 etched surfaces are considerably rougher than CH_4/H_2 etched surfaces.

2) Transmission electron microscopy was employed to study the sidewall and surface damage after RIE using SiCl_4 . Procedures for fabricating thin TEM specimens suitable for this investigation was developed using high resolution fabrication techniques. Results from the diffracted (002) dark field image indicate that the sidewall damage is not amorphous, instead, is due to a composition change in the Ga to As ratio which physically, can only be an As deficiency. A gradient sidewall damage layer, a damage dependence on material and a sidewall damage depth dependence on power density and are also suggested from the intensity brightness analysis of the (002) dark field image.

6.5 References

- 6.1) 'Electricity and Magnetism', B.I.Bleaney and B.Bleaney; Oxford University Press, 1965
- 6.2) L.G.Parratt; Phys. Rev. **95** p.359, 1954
- 6.3) C.A.Lucas, P.D.Hatton, S.Bates, T.W.Ryan, S.Miles and B.K.Tanner; J. Appl. Phys. **63(6)** p.1936, 1988
- 6.4) B.K.Tanner and M.J.Hill; J. Phys. D: Appl. Phys. **19** p.L229, 1986
- 6.5) T.W.Ryan, P.D.Hatton, S.Bates, M.Watt, C.Sotomayor-Torres, P.A.Claxton and J.S.Roberts; Semicond. Sci. Technol. **2** p.241, 1987
- 6.6) X.Chu and B.K.Tanner; Appl. Phys. Letts. **49(26)** p.1773, 1986
- 6.7) B.K.Tanner and M.J.Hill; Advances in X-ray Analysis; **29** p.337, 1986
- 6.8) M.J.Hill, B.K.Tanner, M.A.G.Halliwell and M.H.Lyons; J. Appl. Cryst. **18** p.446, 1985
- 6.9) C.R.Wie; J. Appl. Phys. **65(3)** p.1036, 1989
- 6.10) H.Chen and S.M.Heald; J. Appl. Phys. **66(4)** p.1793, 1989
- 6.11) R.A.Cowley and T.W.Ryan; J. Phys. D: Appl. Phys. **20** p.61, 1987
- 6.12) G.H.Bu-Abbud, S.A.Alterovitz, N.M.Bashara and J.A.Woollam; J.Vac.Sci.Technol. **A1(2)** p.619, 1983
- 6.13) A.C.Adams and B.R.Pruniaux; J. Electrochem. Soc. **120(3)** p.408, 1973
- 6.14) Ryan et. al., unpublished data on Si/SiO₂, 1988
- 6.15) A.J.Carter, B.Thomas, D.V.Morgan, J.K.Bhardwaj, A.M.McQuarrie and M.A.Stephens; IEE Proc. **136 (1)** p.2, 1989
- 6.16) D.E.Aspnes and A.A.Studna; Appl. Phys. Letts. **46(11)** p.1071, 1985
- 6.17) H.Cerva, E.G.Mohr and H.Oppolzer; J.Vac.Sci.Technol. **B5(2)** p.590, 1987
- 6.18) D.J.Mazey and R.S.Nelson; Radiation Effects, **1** p.229, 1969
- 6.19) H.W.Deckman; Mat. Res. Soc. Symp. Proc. **38** p.215, 1985
- 6.20) R.Cheung, A.Birnie, J.N.Chapman, S.Thoms and C.D.W.Wilkinson; paper presented at the 15th international conference on Microlithography, Microcircuit Engineering, Cambridge, 1989
- 6.21) 'Electron Microscopy of Thin Crystals', by P.B.Hirsch, A.Howie, R.B.Nicholson, D.W.Pashley and M.J.Whelan, Butterworths, 1965
- 6.22) 'Introduction to Solid State Physics', by C.Kittel, Wiley, 6th edition, 1986
- 6.23) H.Hashimoto, A.Howie and M.J.Whelan; Proc. Roy. Soc. **A269** p.80, 1962
- 6.24) S.Thoms, S.P.Beaumont, C.D.W.Wilkinson, J.Frost and C.R.Stanley;

Microcircuit Engineering 1986, edited by H.W.Lehmann and Ch. Bleicker (North-Holland, Amsterdam, 1986), p.249

6.25) W.Patrick; Ph.D thesis, 1985

6.26) N.Braslau; Thin Solid Films, **104** p.803, 1981

6.27) N.Braslau; J.Vac.Sci.Technol. **19** p.391, 1981

6.28) M.A.Foad; Private Communication, Glasgow University

6.29) 'Electron Microscopy in the study of Materials', by P.J.Grundy and G.A.Jones, Arnold, 1975

6.30) M.Balooch and D.R.Olander; J.Vac.Sci.Technol. **B4(4)** p.794, 1986

6.31) S.C.McNevin and G.E.Becker; J. Appl. Phys. **58(12)** p.4670, 1985

6.32) R.E.Klinger and J.E.Greene; J. Appl. Phys. **54(3)** p.1595, 1983

6.33) E.L.Hu and R.E.Howard; J.Vac.Sci.Technol. **B2(1)** p.85, 1984

6.34) R.A.Barker, T.M.Mayer and R.H.Burton; Appl. Phys. Letts. **40(7)** p.583, 1982

6.35) H.W.Lehmann, L.Krausbauer and R.Widmer; J.Vac.Sci.Technol. **14(1)** p.281, 1977

6.36) A.Birnie; Final Year Project Report, 1989

6.37) C.M.Knoedler, L.Osterling and H.Shtrikman; J.Vac.Sci.Technol. **B 6** p.1573, 1988

6.38) W.Patrick, W.S.Mackie, S.P.Beaumont and C.D.W.Wilkinson; J.Vac.Sci.Technol. **B4(1)** p.390, 1986

6.39) M.Rahman; Private Communication, Glasgow University

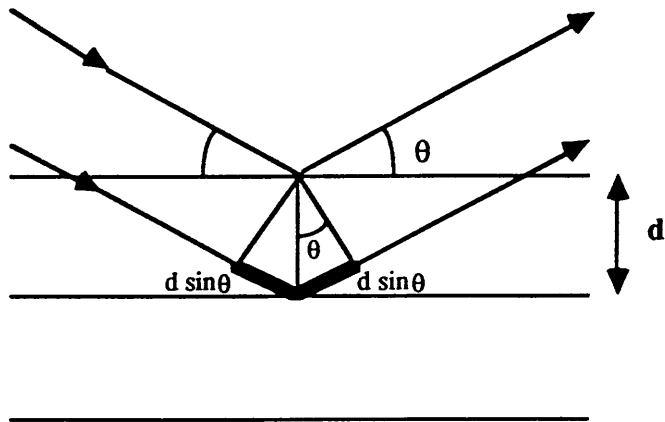


Figure 6.1 Bragg's condition for constructive interference of radiation from successive planes is given by $2d \sin \theta = n \lambda$ see text.

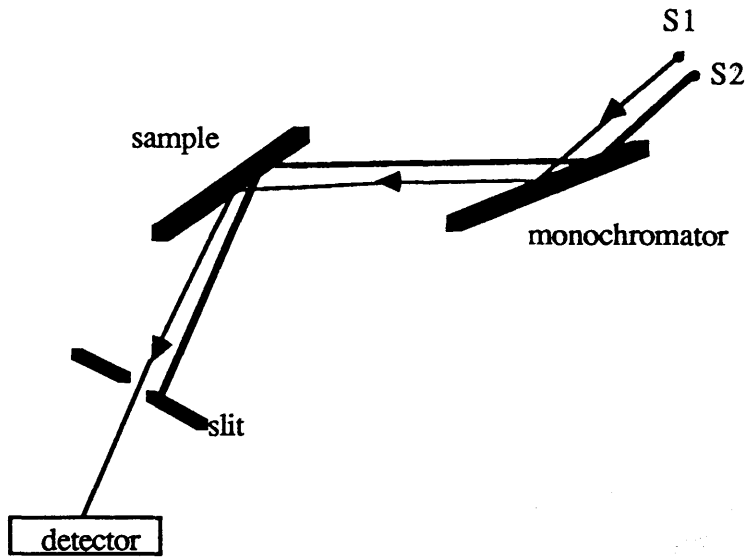


Figure 6.2a) Schematic diagram of a double crystal x-ray diffractometer

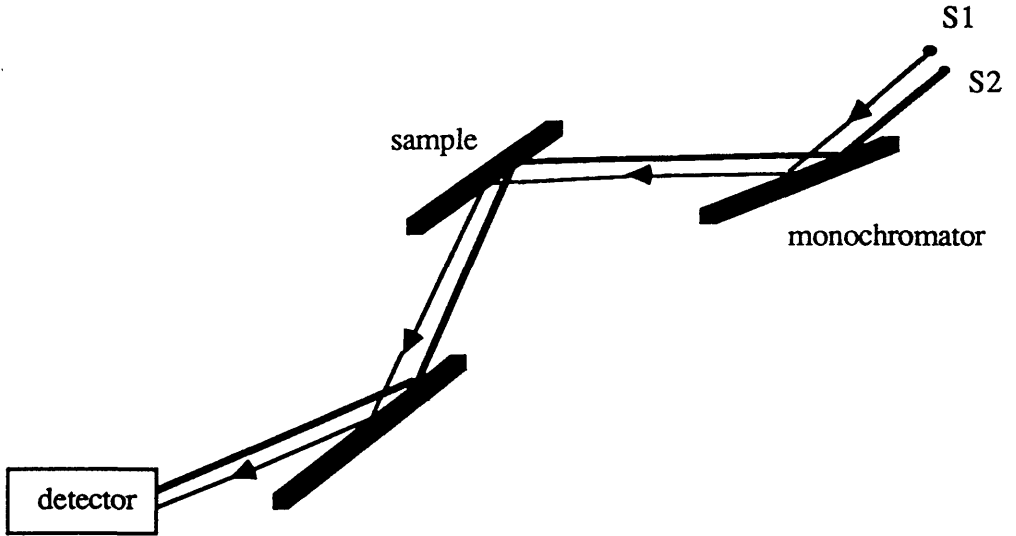


Figure 6.2b) Schematic diagram of a triple crystal x-ray diffractometer

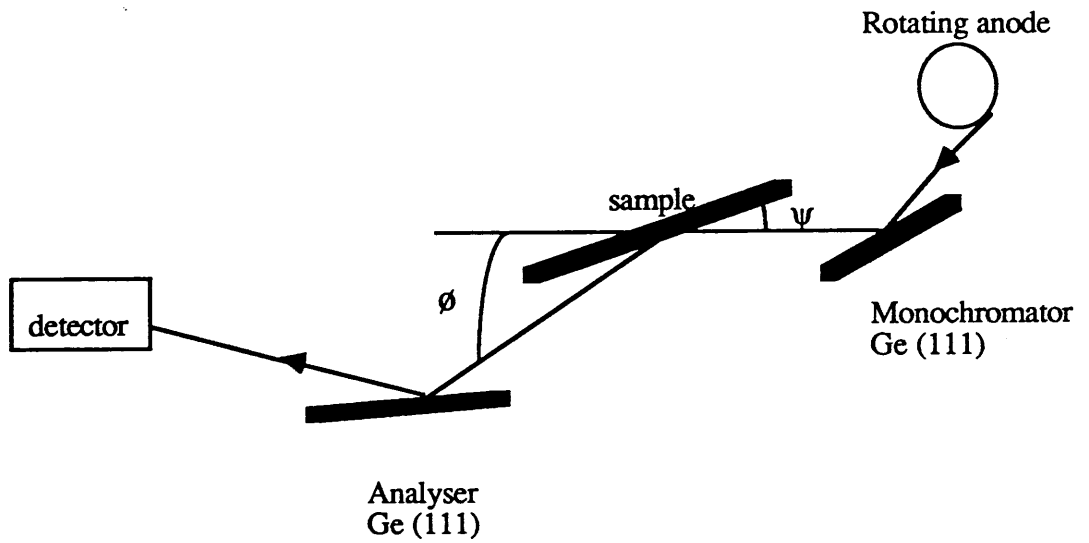


Figure 6.3 Schematic diagram of the triple axis x-ray spectrometer used in the present investigation with angle of incidence ψ and the scattering angle θ

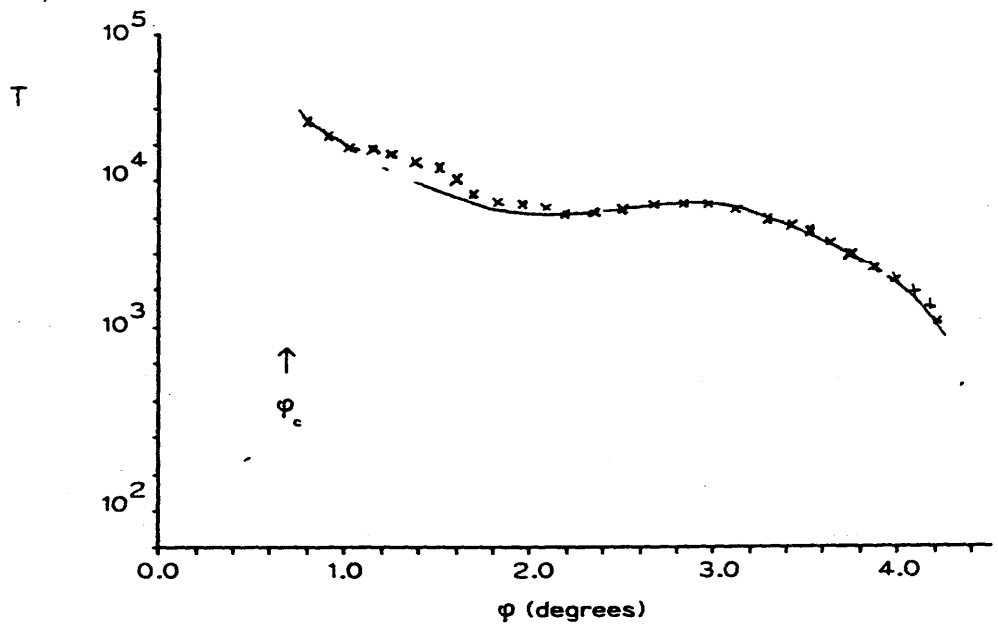


Figure 6.4a) T , the reflectivity R multiplied by ϕ^4 plotted on a logarithmic scale against ϕ for the unetched GaAs sample with the full curve giving fit to the experimental data using a single layer model

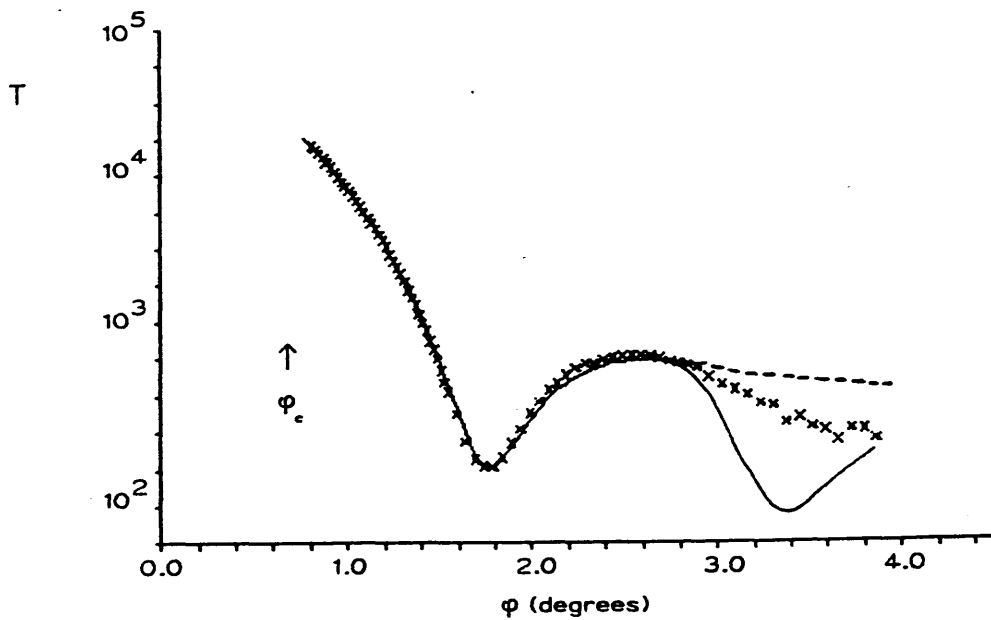


Figure 6.4b) T , the reflectivity R multiplied by ϕ^4 plotted on a logarithmic scale against ϕ for the GaAs sample reactive ion etched in SiCl_4 at 0.44W/cm^2 . The dashed curve gives the fit to a single layer model and the full curve the fit to a double layer model

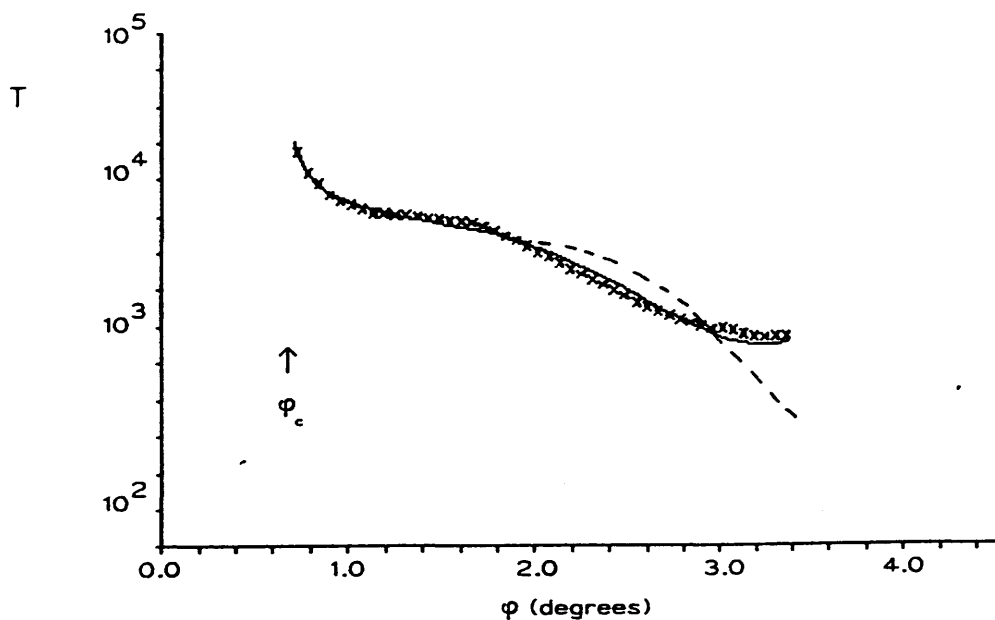


Figure 6.4c) T , the reflectivity R multiplied by ϕ^4 plotted on a logarithmic scale against ϕ for the GaAs sample reactive ion etched in CH_4/H_2 at $0.4\text{W}/\text{cm}^2$. The dashed curve gives the fit to a single layer model and the full curve the fit to a double layer model

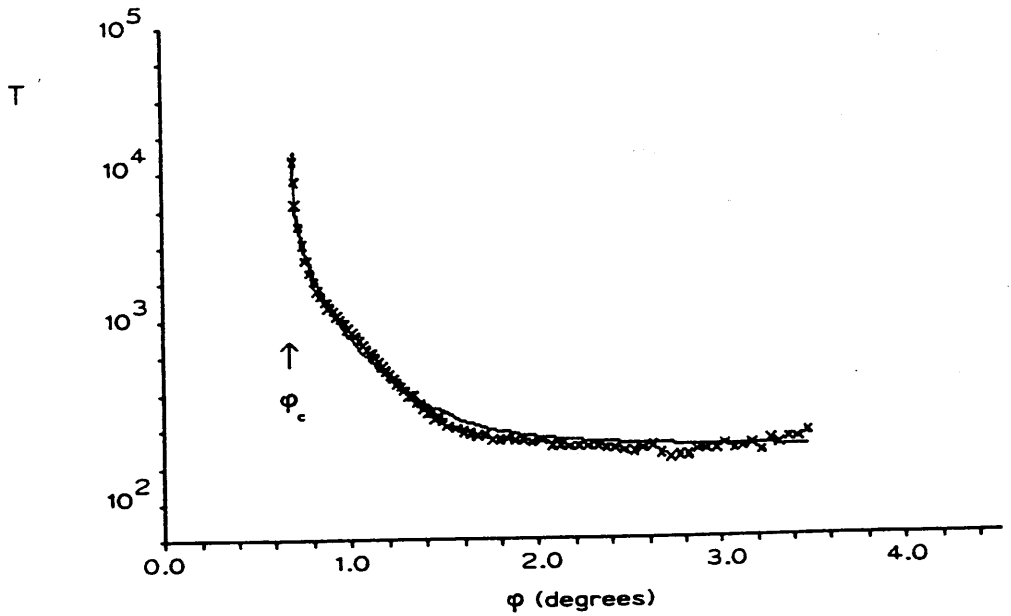


Figure 6.4d) T , the reflectivity R multiplied by ϕ^4 plotted on a logarithmic scale against ϕ for the GaAs sample wet etched and subsequently reactive ion etched in SiCl_4 . The full curve gives the fit to the experimental data using a single layer model

Sample	χ^2	$d_1/\text{\AA}$	$\Delta\rho_1/\rho$	$\sigma_1/\text{\AA}$	$\sigma_2/\text{\AA}$	$d_2/\text{\AA}$	$\Delta\rho_2/\rho$	$\sigma_3/\text{\AA}$
GaAs control	1.25	26.1(5)	-0.09(5)	4.6(3)	0.1(06)			
Si Cl ₄ Fit 1	0.53	28.2(5)	-0.15(3)	13.3(4)	0.4(1)			
(100W) Fit 2	0.75	0.16(3)	-0.83(5)	0.17(2)	18.9(3)	58.7(2)	+0.05(3)	0.1(05)
CH ₄ /H ₂ Fit 1	1.71	21.8(2)	+0.13(5)	4.5(2)	0.0(07)			
(100W) Fit 2	1.31	10.5(4)	-0.18(5)	0.89(4)	0.2(03)	20.8(2)	+0.12(5)	0.1(05)

Table 6.1 Results of least squares fits to the reflectivity data in figures 6.4a) - c): d_1 , d_2 , thickness of layers 1 and 2

$\Delta\rho_1/\rho$, $\Delta\rho_2/\rho$, fractional difference in the density of layers 1 and 2 from that of the bulk

σ_1 , rms roughness of air-layer 1 interface

σ_2 , rms roughness of layer 1-layer 2 interface

σ_3 , rms roughness of layer 2-bulk interface

Sample	χ^2	$\sigma_1 / \text{\AA}$
SiCl ₄ etch at 100W	5.44	17.7(5)
SiCl ₄ etch at 70W	1.35	20.8(3)
SiCl ₄ etch at 50W	1.27	24.8(5)
SiCl ₄ etch at 40W	1.58	32.6(7)
SiCl ₄ etch at 30W	1.67	32.0(6)
Wet etch + SiCl ₄ etch	1.84	22.3(5)
SiCl ₄ etch + Wet etch	1.95	38.2(3)

Table 6.2 Results of least squares fits with zero layer thickness to the reflectivity data obtained for $\theta = 0.8^\circ - 1.6^\circ$ for a) SiCl₄ RIE samples at 0.44W/cm² (100W), 0.3W/cm² (70W), 0.22W/cm² (50W), 0.17W/cm² (40W), 0.1W/cm² (30W), b) wet etched then reactive ion etched in SiCl₄ and c) RIE in SiCl₄ then wet etched; σ_1 , rms roughness of air-bulk interface

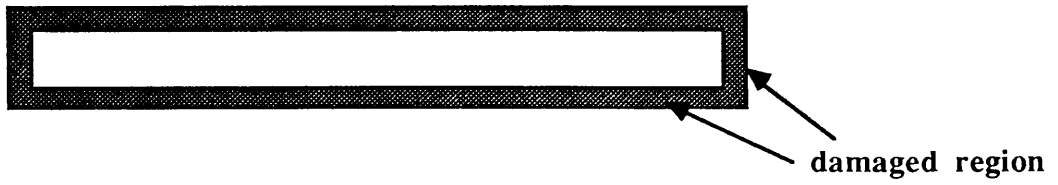


Figure 6.5a) Schematic diagram of the proposed sidewall damage which lies along and around a quantum wire, see text

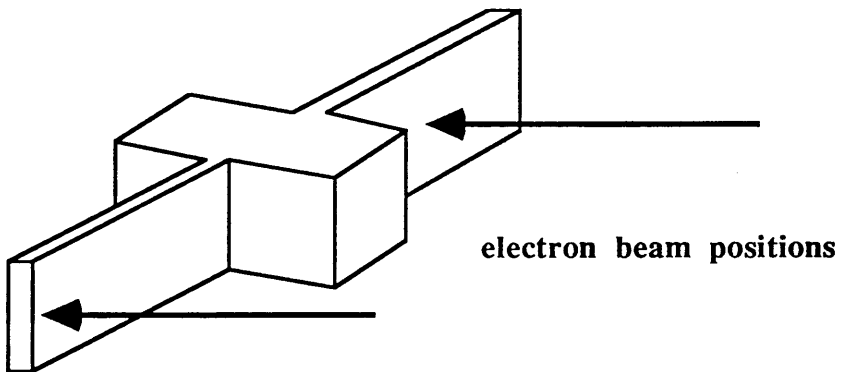


Figure 6.5b) Positioning of the incident electron beam for the study of sidewall damage

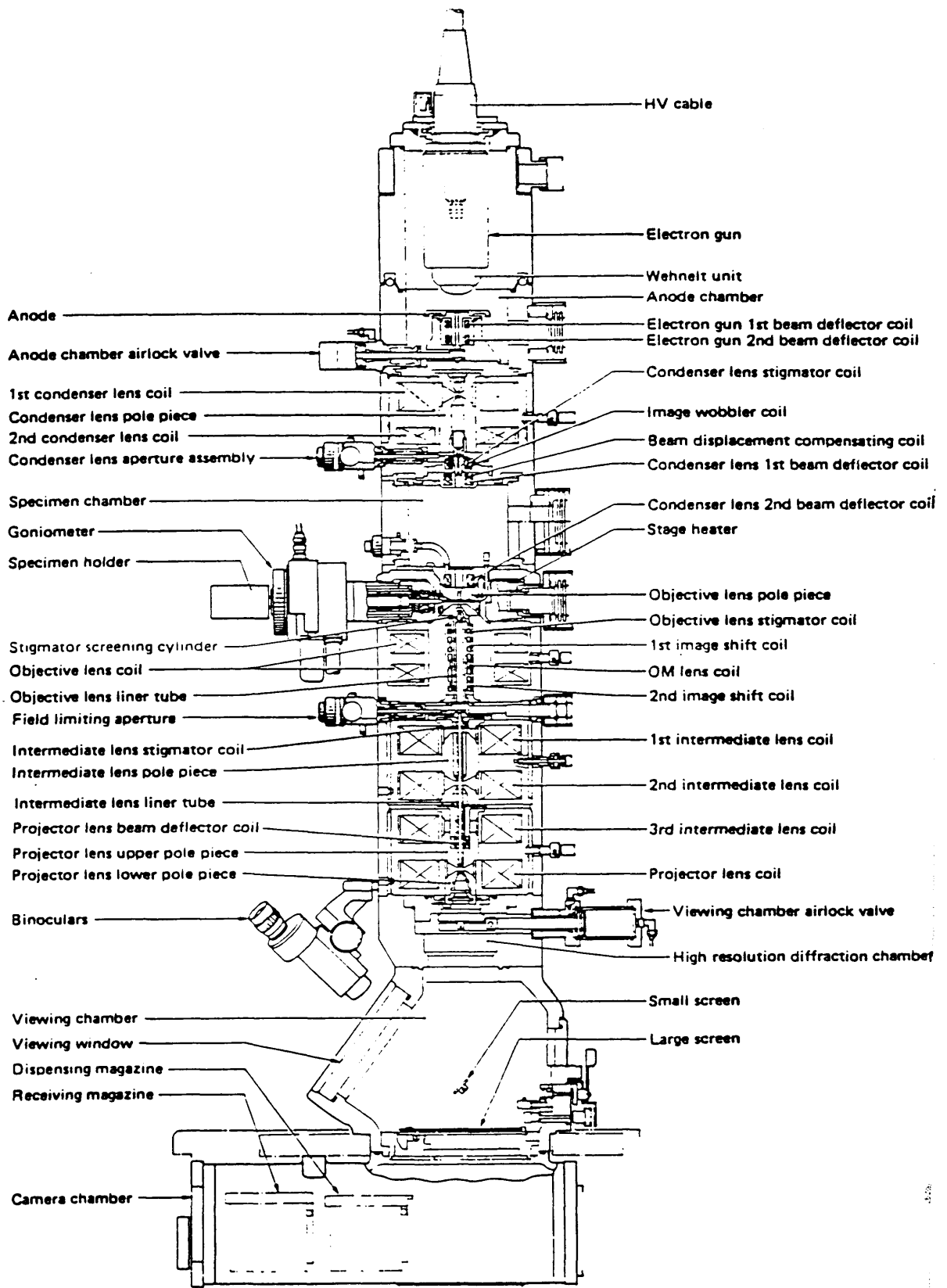


Figure 6.6 Schematic cross-section of a JEOL 1200EX electron microscope

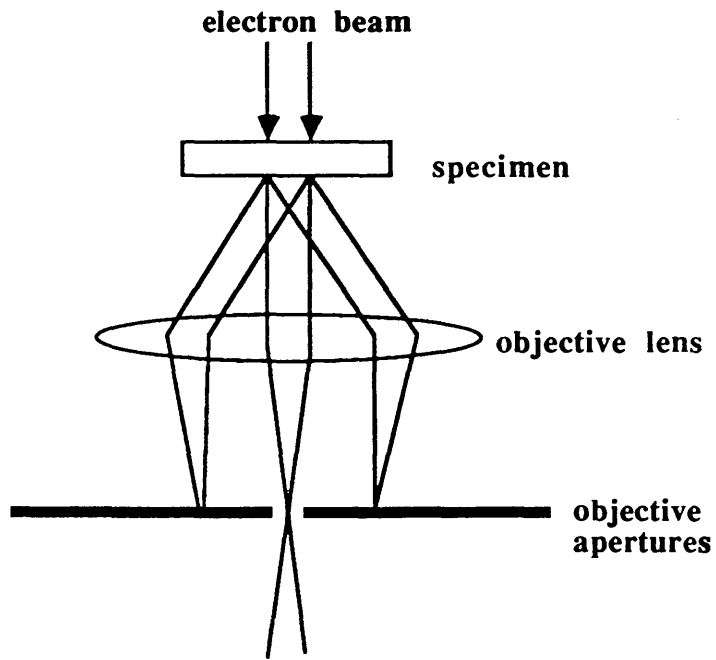


Figure 6.7a) Bright field imaging technique allowing only the direct beam to form the final image

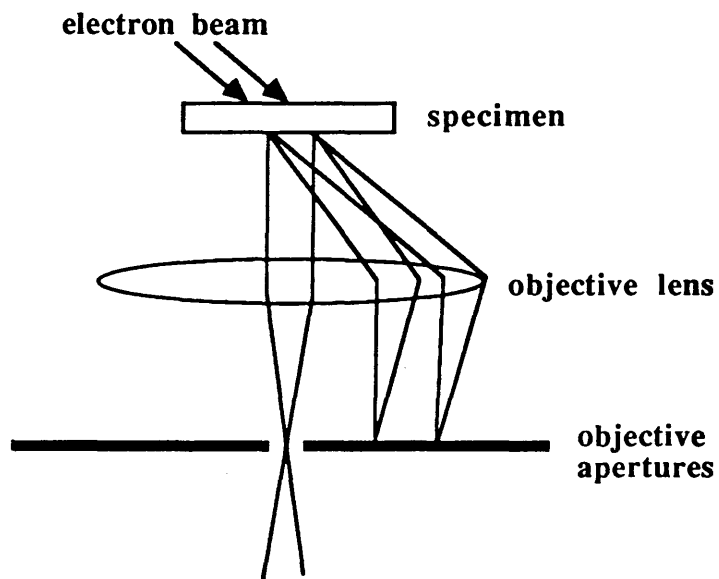


Figure 6.7b) Dark field imaging technique allowing a chosen diffracted beam to form the final image



Figure 6.8a) showing design of the wire level of a TEM structure

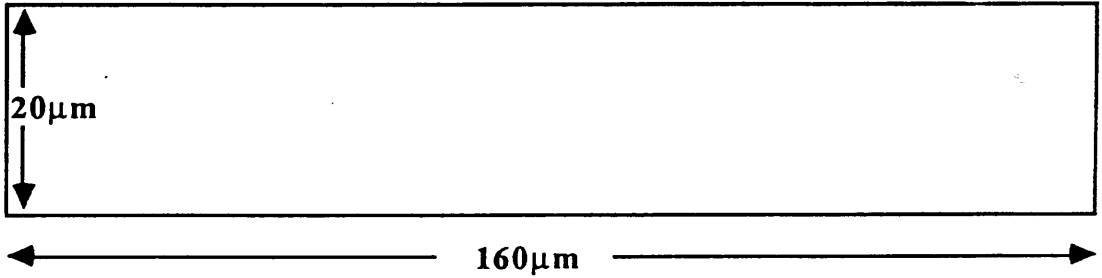


Figure 6.8b) showing the planarisation level of a TEM structure

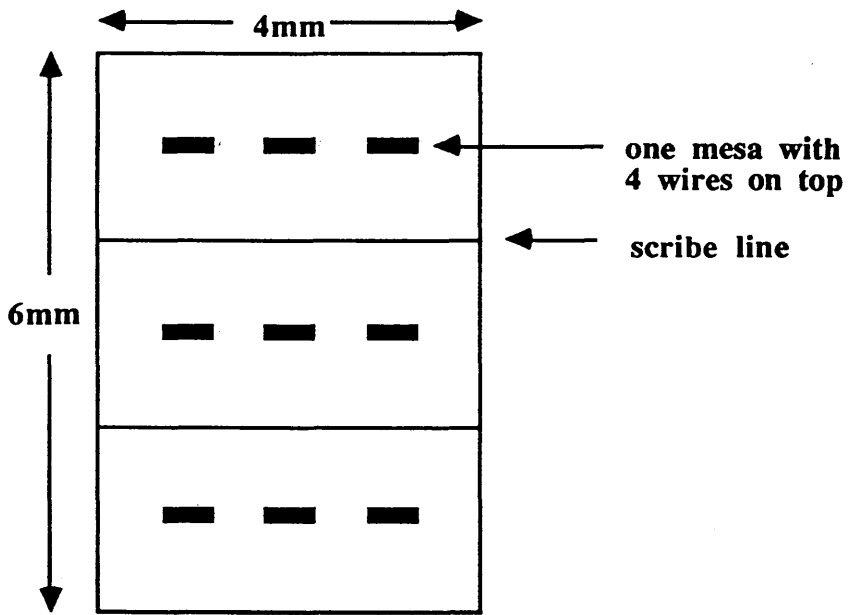
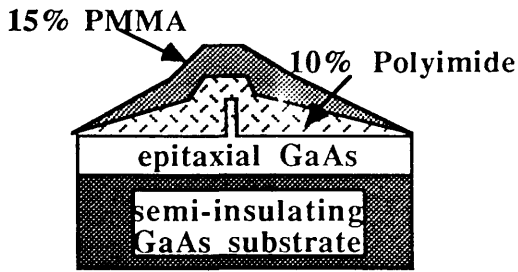
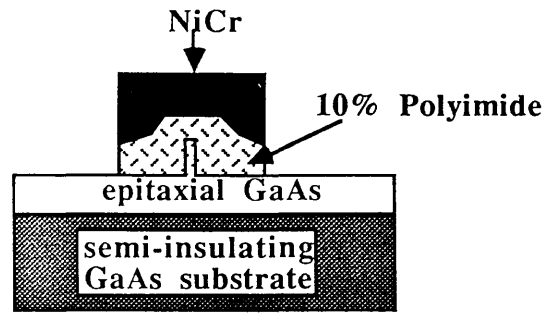


Figure 6.9) showing the pattern layout with the necessary scribing lines to produce exactly $2 \times 4 \text{ mm}^2$ specimen dimensions

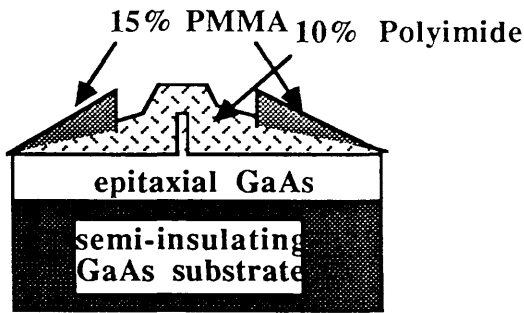
a) Spin resist



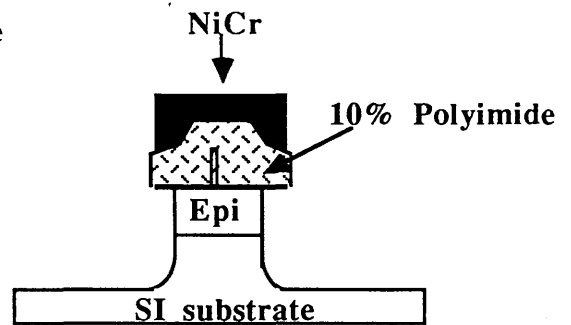
d) Remove polyimide



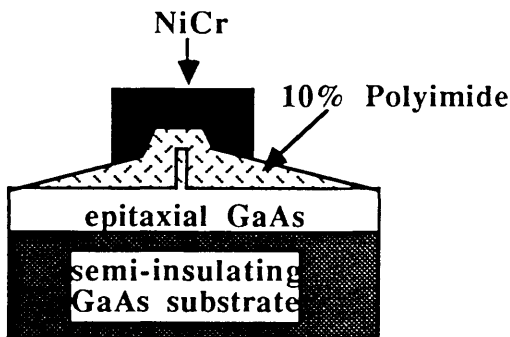
b) Expose and develop



e) Wet etch to produce mesa



c) Evaporate NiCr and lift-off



f) Remove MOP mask producing final TEM structure

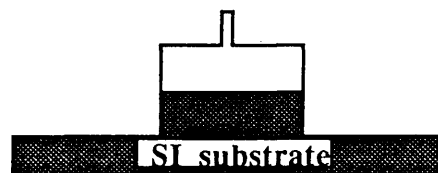
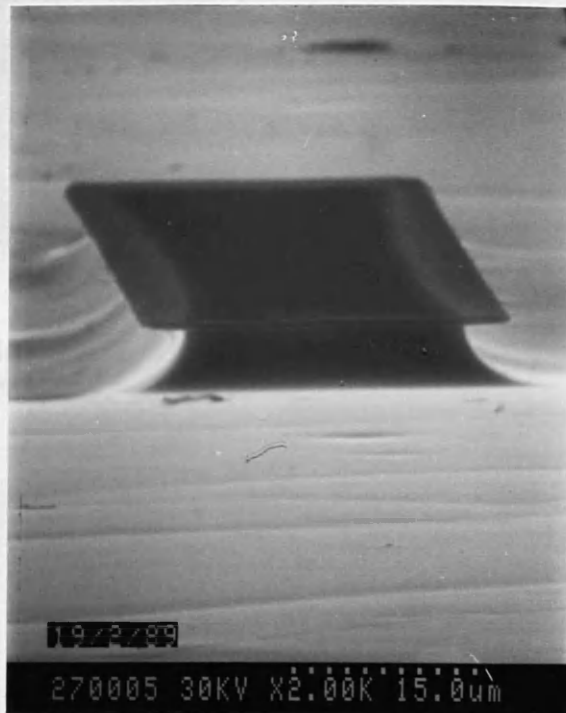


Figure 6.10a)-f) illustrating the fabrication steps of the planarisation level for a TEM structure



SEM 6.1 Typical TEM GaAs wire structure fabricated by reactive ion etching in SiCl_4 with $0.44\text{W}/\text{cm}^2$ power density, 12mT total pressure and 300V dc bias using a 60 nm thick Cr mask



SEM 6.2 GaAs mesa with 14% polyimide remaining on the mesa top after wet etching in $\text{H}_2\text{SO}_4:\text{H}_2\text{O}_2:\text{H}_2\text{O}$ 1:8:1 for 15s



SEM 6.3 showing crosslinked polyimide at both edges of the mesa after reactive ion etching for 30 mins. in SiCl_4



a)



b)

Figure 6.12a) (88)

GaAs wire fabric

A. Birnie Final ye

Figure 6.11a) Convergent beam diffraction pattern from a) the middle and b) the end of a GaAs wire fabricated using SiCl_4 RIE (After A. Birnie Final year report, 1989) Note the relative intensities of the (002) spot (arrowed)



Figure 6.12a) (000) bright field image of the end of an epitaxial GaAs wire fabricated using SiCl_4 RIE at $0.44\text{W}/\text{cm}^2$ (After A.Birnie Final year report, 1989)

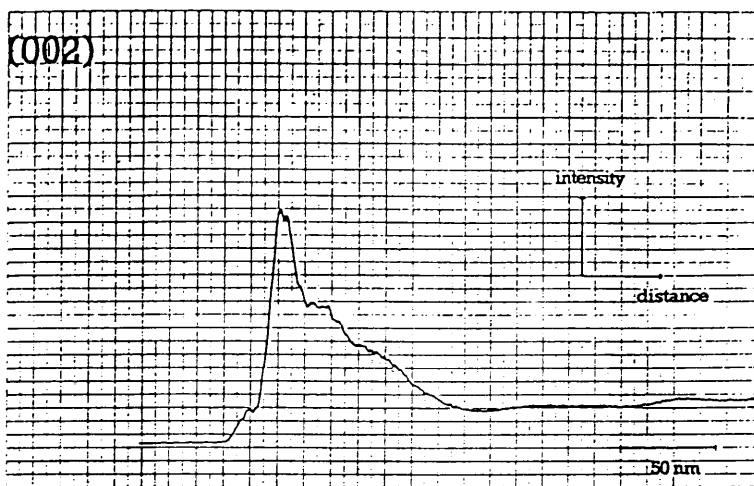


Figure 6.12b) (002) dark field image of the same area as in figure 6.12a) (After A.Birnie Final year report, 1989)

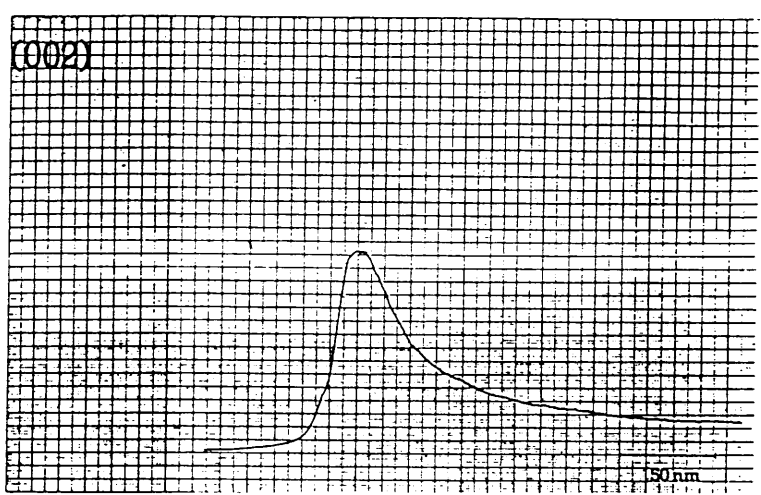


Figure 6.12c) Inelastic dark field image of the same area as in figure 6.12a) (After A.Birnie Final year report, 1989)

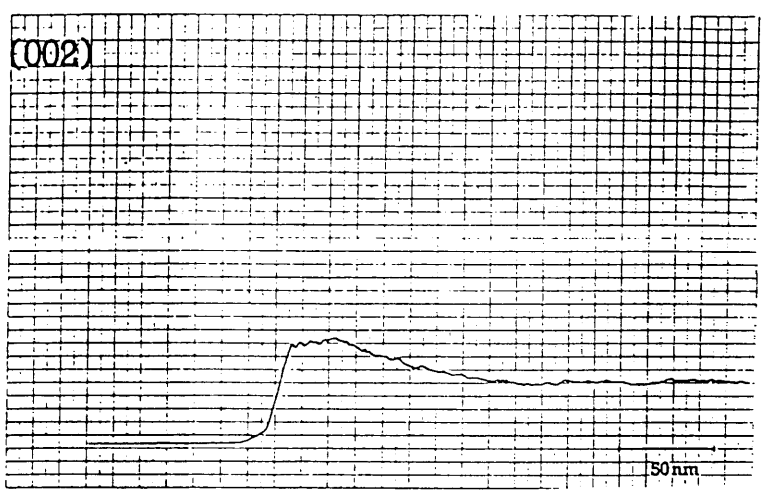
Figure 6.13 Intensity brightness of the (002) spot as a function of distance from the end of a) an epitaxial GaAs wire after RIE in SiCl_4 at 0.44W/cm^2 , b) an epitaxial GaAs wire after RIE in SiCl_4 at 0.75W/cm^2 c) a bulk GaAs wire after RIE in SiCl_4 at 0.44W/cm^2 (After A.Birnie)



a)



b)



c)

Figure 6.13 Intensity brightness of the (002) image as a function of distance from the end of a) an epitaxial GaAs wire after RIE in SiCl_4 at $0.44\text{W}/\text{cm}^2$, b) an epitaxial GaAs wire after RIE in SiCl_4 at $0.75\text{W}/\text{cm}^2$, c) a bulk GaAs wire after RIE in SiCl_4 at $0.44\text{W}/\text{cm}^2$ (After A.Birnie Final year report, 1989)

Etch conditions (Power density)	Depth of severe damage (nm)	Depth of slight damage (nm)
1) 0.44W/cm ² ; epi	≈25	≈130
2) 0.75W/cm ² ; epi	≈35	≈160
3) 0.44W/cm ² ; bulk	-	≈130

Table 6.1 Summary of the degrees and depths of sidewall damage

induced in GaAs after SiCl₄ RIE as a function of power density and material derived from intensity brightness analysis

Chapter 7 Conclusions

In the present work, the importance of the use of a variety of characterisation techniques in order to give a more thorough understanding of the induced 'damage' layer i.e. degree, depth and nature, after reactive ion etching is demonstrated. The difference between surface and sidewall damage is emphasised.

After the RIE of GaAs and $\text{Al}_{0.3}\text{Ga}_{0.7}\text{As}$ using SiCl_4 , it was found that the inflicted surface damage increased with increasing power density. In GaAs, this surface damage was independent on etch time and the depth of the sidewall damage layer was observed to increase with higher etch power. The nature of both surface and sidewall damage layer are dominated by As vacancies and appear to have a gradient profile.

A contamination suppressed environment was developed to etch GaAs in the ECR RF RIE mode using $\text{CCl}_2\text{F}_2/\text{He}$ as the dry etch gas. It was evident that the damage caused in GaAs surfaces and sidewalls etched under suitable ECR RF RIE conditions was lower than RF RIE. The little residual sidewall damage after ECR RF RIE was observed to increase with etch power and etch time. The nature of the surface damage after RF RIE was detected to be Ga-rich with some evidence of Ga-F bonding. Low temperature transport measurements appear to be very sensitive to sidewall damage.

A novel high resolution reactive ion etch process was developed for GaAs using CH_4/H_2 . It was found that the atomic hydrogen in the gas mixture passivated the Si-donors and the non-radiative deep centres in the etched GaAs surfaces and sidewalls. The annealing process was able to recover the donors but the presence of traps and non-radiative deep centres appear to be evident on the etched surface and 20nm of damage remained on each etched sidewall after annealing.

Two novel structures were developed using high resolution fabrication techniques for the study of sidewall damage: sidewall Schottky diode and TEM wire structure.

Much work remains to be done in this area. Improvement on the fabrication process for the TEM specimens to allow the degree of the As deficiency

detected on the SiCl_4 etched sidewalls to be quantified and the application of the sidewall damage characterisation techniques to other etch gases such as CH_4/H_2 and $\text{CCl}_2\text{F}_2/\text{He}$ to reveal more of the nature of the sidewall damage are desirable. To provide a deeper understanding of the surface damage layer, investigation in terms of deep level traps using deep level transient spectroscopy is helpful. Secondary ion mass spectrometry may also be used as a complimentary technique to XPS to measure the composition of the etched surfaces.

